NATIONAL ACADEMY OF SCIENCES OF UKRAINE ● G. V. KURDYUMOV INSTITUTE FOR METAL PHYSICS

A MONTHLY RESEARCH JOURNAL

METALLOPHYSICS AND ADVANCED TECHNOLOGIES

(Metallofizika i Noveishie Tekhnologii)

FOUNDED IN SEPTEMBER, 1979

Volume 48, No. 8; August 2026

CONTENTS

Editorial Announcements	Information for Foreign Subscribers	V
	Information for Contributors	VII
New Metallic Materials and Synthetic Metals	Influence of LaH_x Additions on Characteristics of TiFe-Based Hydrogen-Storage Alloys Manufactured *via* Hydrogen-Assisted Powder Metallurgy *Z. LIU, Y. WANG, T. CHENG, Y. SONG, D. SAVVAKIN, N. LI, and O. IVASISHIN*	775
Amorphous and Liquid States	Influence of Y and Al Addition on the Glass-Forming Ability of Complex Alloyed $Fe_{40–50.4}(TM, Al)_{29.1–37.5}Y_{1.8–2}(Si, C, B)_{19.7–22}$ Alloys *I. K. YEVLASH, M. S. NIZAMEYEV, O. M. SEMYRGA, O. I. BOSHKO, and V. K. NOSENKO*	791
Metallic Surfaces and Films	Patterns of the Relationship between the Limit Potentials of the 06KhN28MDT Alloy and Its Indicators in a Gap with a Chloride-Containing Medium Present in the Operation of Heat Exchangers *A. V. DZHUS, O. E. NARIVSKYI, S. O. SUBBOTIN, G. V. SNIZHNYI, and T. V. PULINA*	807
	Magnetic Post-Processing of Additively-Manufactured Inconel 718 Superalloy: Functional Microrelief Evolution and Surface Strain Hardening *D. A. LESYK, B. M. MORDYUK, O. STAMANN, D. GROCHALA, S. S. SALII, M. M. LYTVYNENKO, M. V. ROMANENKO, M. I. ANYAKIN, and A. LAMIKIZ*	827
	Comparison the Efficiency of High-frequency Impact Surface Hardening of Ti–6Al–4V Titanium Alloy Manufactured by Metallurgical or Additive Routs in Vibration Chambers	

© G. V. Kurdyumov Institute for Metal Physics, N.A.S. of Ukraine, 2026
© Publisher Publishing House 'Akademperiodyka' of the N.A.S. of Ukraine, 2026

	S. M. VOLOSHKO, A. P. BURMAK, B. M. MORDYUK, M. O. VASYLYEV, T. A. KRASOVSKYI, and O. A. VYSLYI	843
Physics of Strength and Plasticity	Microstructural and Phase Evolution of AISI 316 Stainless Steel Produced by Selective Laser Melting and Hot Rolling during Heat Treatment and Ultrasonic Impact Treatment *S. M. VOLOSHKO, I. A. VLADYMYRSKYI, M. I. ANYAKIN, N. A. SHAPOVALOVA, M. M. VORON, and A. P. BURMAK*	865
	Gradient Metals' Microstructure Change under Severe Plastic Deformation: A Review *I. E. VOLOKITINA, A. V. VOLOKITIN, T. D. FEDOROVA, E. N. RESHOTKINA, and G. M. ZHUMANAZAROVA*	889
	Influence of Ti–6Al–4V Alloy Microstructure and Processing Parameters of Hot Deformation (Forging) on the Formation of Cup-Shaped Product *O. M. IVASYSHYN, H. A. BAHLYUK, V. I. BONDARCHUK, S. F. KYRYLYUK, and P. Ye. MARKOVS'KYY*	907

Scientific Editors of Issue—*O. S. Gatsenko, V. A. Tatarenko*
Executive Managing Editor—*O. S. Gatsenko*
Editors—*L. I. Makarenko, M. V. Manilo, I. V. Zagorulko*
The artwork for direct reproduction is made by computer group of EPD of the G. V. Kurdyumov Institute for Metal Physics, N.A.S. of Ukraine

Editorial Office Address:
G. V. Kurdyumov Institute for Metal Physics, N.A.S. of Ukraine, EPD—'MNT',
36 Academician Vernadsky Boulevard, UA-03142 Kyiv, Ukraine
Telephone: +380 44 4249042. Fax: +380 44 4242561. E-mail: mfint@imp.kiev.ua
Media Identifier R30-03171

Approved for publication by the Academic Council of the G. V. Kurdyumov Institute for Metal Physics of the National Academy of Sciences of Ukraine
Published in English or Ukrainian languages according to resolution of Editorial Board of the journal

Printed by Publishing House 'Akademperiodyka', of the NAS of Ukraine
4 Tereshchenkivs'ka Str., UA-01024 Kyiv, Ukraine
Registration Certificate of Publishing Subject: ДК № 544 on 27.07.2001

Journal website: http://mfint.imp.kiev.ua
Journal DOI: https://doi.org/10.15407/mfint

Issue DOI: https://doi.org/10.15407/mfint.48.08

НАЦІОНАЛЬНА АКАДЕМІЯ НАУК УКРАЇНИ ● ІНСТИТУТ МЕТАЛОФІЗИКИ ім. Г. В. Курдюмова

МЕТАЛОФІЗИКА ТА НОВІТНІ ТЕХНОЛОГІЇ

ЩОМІСЯЧНИЙ НАУКОВИЙ ЖУРНАЛ
ЗАСНОВАНИЙ У ВЕРЕСНІ 1979 р.

Том 48, № 8; серпень, 2026

ЗМІСТ

Редакційні оголошення	Інформація для закордонних передплатників	V
	Інформація для авторів	VII
Нові металеві матеріяли та синтетичні метали	Вплив додавання LaH_x на характеристики воднеакумулювальних стопів на основі TiFe, виготовлених методом порошкової металурґії з участю водню *З. ЛЮ, Й. ВАНҐ, Т. ЧЕНҐ, Й. СОНҐ, Д. САВВАКІН, Н. ЛІ, О. ІВАСИШИН*	775
Аморфний і рідкий стани	Вплив додавання Y й Al на здатність щодо утворення скла складних леґованих стопів $Fe_{40-50,4}(ПМ, Al)_{29,1-37,5}Y_{1,8-2}(Si, C, B)_{19,7-22}$ *І. К. ЄВЛАШ, М. С. НІЗАМЕЄВ, О. М. СЕМИРҐА, О. І. БОШКО, В. К. НОСЕНКО*	791
Металічні поверхні та плівки	Зразки взаємозв'язку між граничними потенціялами стопу 06ХН28МДТ і його показниками у зазорі з хлоридвмісним середовищем під час роботи теплообмінників *А. В. ДЖУС, О. Е. НАРІВСЬКИЙ, С. О. СУББОТІН, Г. В. СНІЖНИЙ, Т. В. ПУЛІНА*	807
	Магнетне післяобробляння адитивно виготовленого суперстопу Інконель 718: еволюція функціонального мікрорельєфу та деформаційне зміцнення поверхні *Д. А. ЛЕСИК, Б. М. МОРДЮК, О. СТАМАНН, Д. ГРОХАЛА, С. С. САЛІЙ, М. М. ЛИТВИНЕНКО, М. В. РОМАНЕНКО, М. І. АНЯКІН, А. ЛАМІКІЗ*	827
	Порівняння ефективности високочастотного ударного зміцнення у вібраційних камерах поверхні титанового стопу ВТ6, виготовленого металурґійним та адитивним способами *С. М. ВОЛОШКО, А. П. БУРМАК, Б. М. МОРДЮК, М. О. ВАСИЛЬЄВ, Т. А. КРАСОВСЬКИЙ, О. А. ВИСЛИЙ*	843

© G. V. Kurdyumov Institute for Metal Physics, N.A.S. of Ukraine, 2026
© Publisher Publishing House 'Akademperiodyka' of the N.A.S. of Ukraine, 2026

Фізика міцности та пластичности

Мікроструктурні та фазові зміни неіржавійної криці AISI 316, виготовленої методом селективного лазерного топлення та гарячого вальцювання під час термічного обробляння й ультразвукового ударного оброблення
С. М. ВОЛОШКО, І. А. ВЛАДИМИРСЬКИЙ, М. І. АНЯКІН, Н. А. ШАПОВАЛОВА, М. М. ВОРОН, А. П. БУРМАК 865

Зміни ґрадієнтної мікроструктури металів під час інтенсивного пластичного деформування: огляд
І. Є. ВОЛОКІТІНА, А. В. ВОЛОКІТІН, Т. Д. ФЕДОРОВА, Є. Н. РЕШОТКІНА, Г. М. ЖУМАНАЗАРОВА 889

Вплив мікроструктури стопу Ti–6Al–4V і параметрів гарячої деформації (кування) на формування виробу у вигляді чаші
О. М. ІВАСИШИН, Г. А. БАГЛЮК, В. І. БОНДАРЧУК, С. Ф. КИРИЛЮК, П. Є. МАРКОВСЬКИЙ 907

Наукові редактори випуску: *О. С. Гаценко, В. А. Татаренко*
Відповідальний секретар редакційної колегії *О. С. Гаценко*
Редактор-коректор *О. С. Гаценко*
Технічні редактори: *І. В. Загорулько, Л. І. Макаренко, М. В. Маніло*
Художні редактори: *І. В. Загорулько, Л. І. Макаренко, М. В. Маніло*
Оригінал-макет для прямого репродукування виготовлено комп'ютерною групою РВВ Інституту металофізики ім. Г. В. Курдюмова НАН України

Адреса редакції:
Інститут металофізики ім. Г. В. Курдюмова НАН України, РВВ—Редакція «МНТ»
бульв. Акад. Вернадського, 36; 03142 Київ, Україна
Тел.: +380 44 4249042; факс: +380 44 4242561
Ел. пошта: mfint@imp.kiev.ua
Ідентифікатор медіа R30-03171

Затверджено до друку вченою радою Інституту металофізики ім. Г. В. Курдюмова НАН України
Друкується за постановою редакційної колегії журналу англійською або українською мовами

Підписано до друку 28.08.2026 р. Формат 70×100/16.
Ум. друк. арк. 12,35. Обл.-вид. арк. 11,36.
Тираж 55 пр. Зам. № 0000 від 28.08.2026 р.

Віддруковано ВД «Академперіодика» НАН України
вул. Терещенківська, 4; 01024 Київ, Україна
Свідоцтво суб'єкта видавничої справи ДК № 544 від 27.07.2001 р.

Сайт журналу: http://mfint.imp.kiev.ua
DOI (журналу): https://doi.org/10.15407/mfint
DOI (випуску): https://doi.org/10.15407/mfint.48.08

INFORMATION (GUIDELINES) FOR CONTRIBUTORS

Submission of Manuscripts: Manuscripts should be sent by e-mail (mfint@imp.kiev.ua). Additionally, they can be sent by regular mail to Executive Managing Editor, Editorial Office, G. V. Kurdyumov Institute for Metal Physics, N.A.S. of Ukraine, 36 Academician Vernadsky Boulevard, UA-03142 Kyiv, Ukraine. Manuscripts may also be submitted to a member of the Editorial Advisory Board or to the appropriate Regional Editor who is familiar with the research presented.
Submission of a paper to '*Metallophysics and Advanced Technologies*' (transliteration: '*Metallofizika i Noveishie Tekhnologii*', *i.e.*, '*MfNT*') will be taken to imply that it represents original work not previously published, that it is not being considered for publication elsewhere, and that, if accepted for publication, it will not be republished without the consent of the Editors and Publisher. It is a condition of acceptance by the Editor of a manuscript for publication that the Publishers acquire automatically the copyright in the manuscript throughout the world. Journal '*MfNT*' supports the generally accepted principles described in documents on publication ethics and unacceptable practices, which are presented on the journal website.
Scope of the Journal: *Electronic Structure and Properties, Crystal-Lattice Defects, Phase Transformations, Physics of Strength and Plasticity, Metallic Surfaces and Films, Structure and Properties of Nanoscale and Mesoscopic Materials, Amorphous and Liquid States, Interactions of Radiation and Particles with Condensed Matter, Materials in Extremal Conditions, Reactor and Aerospace Metals Science, Medical Metals Science, New Metallic Materials and Synthetic Metals, Metal-Containing Smart Materials, Physical and Technical Basis of Experiment and Diagnostics, Articles under Discussion*.
Language: The language of publication may be English (preferably) or Ukrainian.
Abstract: Each paper requires an abstract of 200–250 words summarizing the significant coverage and findings (the use of mathematical symbols and expressions in abstract is not recommended).
Keywords and PACS numbers: 5–7 keywords and PACS numbers reflecting the content of the contribution should be supplied (see 'Physics and Astronomy Classification Scheme 2010').
Manuscript Preparation: Papers should be formatted according to the template, which can be downloaded from the Journal's website. The length of **research papers** should not in general exceed 5000 words and 10 figures; **review articles** should not exceed 10000 words and 30 figures, including tables and diagrams. Authors are urged to arrange the subject matter clearly under headings such as: 1. Introduction, 2. Experimental/Theoretical Details, 3. Results, 4. Discussion, 5. Conclusion, References. Subsections should be identified with section and subsection numbers (such as 6.1. Second-Value Subheading).
References and Notes: Notes are indicated in the text by consecutive superior Arabic numbers (without parentheses). References should be numbered consecutively (in square brackets) throughout the text. The full list should be collected and typed at the end of the paper in numerical order. Listed references should be completed in all details including **DOI** (if available) but excluding article titles in journals. **All authors'** initials should precede their names. Examples of references preparation:

1. S. O. Firstov and T. G. Rogul, *Metallofiz. Noveishie Tekhnol.*, **44**, No. 1: 127 (2022) (in Ukrainian). https://doi.org/10.15407/mfint.44.01.0127
2. V. B. Tarelnyk, O. P. Gaponova, and Ye. V. Konoplianchenko, *Prog. Phys. Met.*, **23**, No. 1: 27 (2022). https://doi.org/10.15407/ufm.23.01.027
3. A. Meisel, G. Leonhardt, and R. Szargan, *Röntgenspektren und Chemische Bindung* [X-Ray Spectra and Chemical Bond] (Leipzig: Akademische Verlagsgesellschaft Geest & Portig K.-G.: 1977) (in German).
4. J. M. Ziman, *Printsipy Teorii Tverdogo Tela* [Principles of the Theory of Solids] (Moscow: Mir: 1974) (Russian translation).
5. M. A. Stucke, D. M. Dimiduk, and D. M. Hazzledine, *High Temperature Ordered Intermetallic Alloys. V* (Eds. I. Baker and R. Darolia) (Pittsburgh, PA, USA: MRS: 1993), p. 471.
6. *Handbook of Mathematical Functions with Formulas, Graphs and Mathematical Tables* (Eds. M. Abramowitz and I. A. Stegun), Nat'l Bureau of Standards. Appl. Math. Ser. Vol. **55** (Washington, D.C.: U.S. Govt. Printing Office: 1964).
7. B. B. Karpovych and O. B. Borovkoff, *Proc. of Symp. 'Micromaterials Engineering' (Dec. 25–31, 1999)* (Kyiv: RVV IMF: 2000), vol. **2**, p. 113 (in Russian).
8. A. E. Krug, *Abstr. Int. Conf. Phys. Phenomena (Dec. 25–31, 1991, Alushta)* (Kharkiv: 1991), p. 12.
9. T. M. Radchenko, *Vplyv Uporyadkuvannya Defektnoyi Struktury на Transportni Vlastyvosti Zmishanykh Krystaliv* [Influence of Ordering of the Defect Structure on Transport Properties of the Mixed Crystals] (Thesis of Disser. for the Degree of Dr. Phys.-Math. Sci.) (Kyiv: G. V. Kurdyumov Institute for Metal Physics, N.A.S.U.: 2015) (in Ukrainian). https://doi.org/10.13140/RG.2.2.35430.22089

10. E. M. Gololobov, V. B. Shipilo, N. I. Sedrenok, and A. I. Dudyak, *Sposob Polucheniya Karbonitridov Metallov* [Production Method of Metal Carbonitrides], Authors' Certificate 722341 SSSR (Publ. November 21, 1979) (in Russian).
11. V. G. Trubachev, K. V. Chuistov, V. N. Gorshkov, and A. E. Perekos, *Sposob Polucheniya Metallicheskikh Poroshkov* [The Technology of Metallic Powder Production]: Patent 1639892 SU. MKI, B22 F9/02, 9/14 (Otkrytiya i Izobreteniya, **34**, No. 13: 11) (1991) (in Russian).
12. Yu. M. Koval' and V. V. Nemoshkalenko, *O Prirode Martensitnykh Prevrashcheniy* [On the Nature of Martensitic Transformations] (Kyiv: 1998) (Prepr./N.A.S. of Ukraine. Inst. for Metal Physics. No. 1, 1998) (in Russian).

Journal title abbreviations should conform to generally accepted styles:
https://www.cas.org/support/documentation/references/corejournals;
https://cdn.journals.aps.org/files/rmpguapb.pdf;
https://images.webofknowledge.com/WOK46P9/help/WOS/A_abrvjt.html;
https://mathscinet.ams.org/msnhtml/serials.pdf.

Equations and Formulae: Formulas in the text should be inserted by **MathType**, fully compatible with MS Office. Vectors should be typed in bold without arrows above. Note that complicated formulae, mathematical expressions or (de)notations are not recommended in the title, abstract, and keywords.

Tables: Number tables consecutively with Arabic numerals and give a clear descriptive caption at the top.

Figures: All figures should be numbered with consecutive Arabic numbers, have descriptive captions and be mentioned in the text. Keep figures separate at the end of the text and clearly label each figure with author's name and figure number. The labels at axis should contain the designation (or notation) of quantities and their units.

Preparation: Figures submitted must be of a high enough standard for reproduction with 300–600 dpi resolution (including half-tone illustrations). Redrawing or retouching of unusable figures will be charged to the authors.

Colour Plates: Whenever, the use of colour is an integral part of the research, or where the work is generated in colour, the Journal will publish (in paper version) the colour illustrations with charge to the author. Reprints in colour will carry a surcharge. Please write to the Publisher for details.

Submission of Electronic Text: Authors should submit the electronic version of their paper by e-mail to the Editorial Office. The text file should be saved in the native formats of the MS Word with a name consisting the name of the first author, for example, Hotovchenko.docx. The electronic form of figures (in TIF, EPS, JPG, PNG formats preferably and with name consisting the name of the first author also, for example, Hotovchenko_fig2a.jpg) should be planned so that they reduce to 12.7 cm column width (or less), and keep them separated from the text file. It is desirable to submit additionally all the **figures** within the format of the program, in which they were created.

Proofs: Contributors will receive page proofs for correction by e-mail as a PDF document. These must be returned to Kyiv office (mfint@imp.kiev.ua with subject beginning by word 'mfint') within 5 days of receipt.

Page Charges: There are no page charges to individuals or institutions.

Reprints: Authors can freely download a PDF version of their published article from journal website: https://mfint.imp.kiev.ua. The printed issues may be ordered by completing the appropriate form sent with proofs and prepaid by authors under the terms as for subscription.

Further Information: All questions arising during the **peer review** or after acceptance of manuscripts, especially those relating to reprints, should be directed to G. V. Kurdyumov Institute for Metal Physics, N.A.S. of Ukraine, Executive Managing Editor, Editorial Office, 36 Academician Vernadsky Blvd., UA-03142 Kyiv, Ukraine;
Fax: +380 44 4242561, e-mail: mfint@imp.kiev.ua (with subject beginning by word 'mfint').

We ask the authors to apply with their manuscript Copyright Transfer Agreement form.

Copyright Transfer Agreement

We, the undersigned authors of the manuscript '_____', transfer to the Founders, Publisher, and Editorial Board of the Journal 'Metallophysics and Advanced Technologies' (according to agreements between them) the right to publish this manuscript in original language or in translation to the other languages. We confirm that publication of this manuscript **will not** infringe a copyright of other persons or organizations and publication ethics.

Author(s):_____
(Last Name, First Name, Affiliation)

Correspondence Address:_____

Phone and e-mail: _____

_____ _____
(Signature) *(Date)*

ІНФОРМАЦІЯ (ПРАВИЛА) ДЛЯ АВТОРІВ

Науковий журнал «Металофізика та новітні технології» (МфНТ) щомісяця публікує статті, які раніше ще не публікувалися та не перебувають на розгляді для опублікування в інших виданнях. Статті мають містити результати експериментальних і теоретичних досліджень в області фізики та технологій металів, стопів і сполук з металічними властивостями; рецензії на монографії; інформацію про конференції, семінари; відомості з історії металофізики; рекламу нових технологій, матеріялів, приладів. Журнал дотримується загальноприйнятих принципів, зазначених на його сайті в документах з публікаційної етики та щодо неприйнятних практик.

Тематика журналу: *Електронні структура та властивості, Дефекти кристалічної ґратниці, Фазові перетворення, Фізика міцности та пластичности, Металічні поверхні та плівки, Будова та властивості наномасштабних і мезоскопічних матеріялів, Аморфний і рідкий стани, Взаємодії випромінення та частинок із конденсованою речовиною, Матеріяли в екстремальних умовах, Реакторне й авіакосмічне металознавство, Медичне металознавство, Нові металеві матеріяли та синтетичні метали, Металовмісні смарт-матеріяли, Фізико-технічні основи експерименту та діягностики, Дискусійні повідомлення*.

Статті публікуються однією з двох мов: англійською (віддається перевага) або українською.

Статті, в оформленні яких не дотримано наступних правил для опублікування в МфНТ, повертаються авторам без розгляду по суті. (Датою надходження вважається день повторного надання статті після дотримання зазначених нижче правил.)

1. Стаття має бути підписаною всіма авторами (із зазначенням їхніх адрес електронної пошти); слід вказати прізвище, ім'я та по батькові автора, з яким редакція буде вести листування, його поштову адресу, номери телефону та факсу й адресу електронної пошти.

2. Виклад матеріялу має бути чітким, **структурованим** (розділами, наприклад, «1. Вступ», «2. Експериментальна/Теоретична методика», «3. Результати та їх обговорення», «4. Висновки», «Цитована література»), стислим, без довгих преамбул, відхилень і повторів, а також без дублювання в тексті даних таблиць, рисунків і підписів до них. Анотація та розділ «Висновки» мають не дублювати один одного. Числові дані слід наводити в загальноприйнятих одиницях.

3. Об'єм оригінальної (неоглядової) статті має бути не більше 5000 слів (з урахуванням основного тексту, таблиць, підписів до рисунків, списку використаних джерел) і 10 рисунків. **Об'єм оглядової статті** — до 10000 слів та 30 рисунків.

4. За потреби до редакції може надаватися друкований (А4, подвійний інтервал) примірник рукопису з ілюстраціями.

5. До редакції обов'язково надається (по **e-mail**) файл статті, набраний у текстовому редакторі Microsoft Word, з назвою, що складається з прізвища першого автора (латиницею), наприклад, Hotovchenko.docx.

6. Електронна версія рукопису та його друкований варіянт (в разі його надання) мають бути ідентичними. Вони мають оформлюватися за шаблоном, який можна завантажити з сайту журналу, і містити 5–7 **індексів PACS** в редакції 'Physics and Astronomy Classification Scheme 2010'. Тексти статей мають також містити **назву статті**, **список авторів**, **повні назви** та **поштові адреси установ**, в яких вони працюють, **анотацію статті** (200–250 слів), **5–7 ключових слів** двома мовами (**англійською** та **українською**), а заголовки таблиць і підписи до рисунків мають подаватися **як мовою рукопису, так і англійською мовою**; англомовна анотація може бути представленою в більш розгорнутому варіянті (до 500 слів). Назва статті, її анотація та ключові слова мають не містити складні формули, математичні вирази чи позначення.

7. Електронні версії рисунків мають бути представленими у вигляді окремих файлів (у форматах TIF, EPS, JPG, PNG з розріжненням у 300–600 dpi) з назвами, що складаються з прізвища першого автора (латиницею) та номера рисунка, наприклад, Hotovchenko_fig2a.jpg. Додатково рисунки надаються у форматі програми, в якій вони створювалися.

8. Написи на рисунках (особливо на півтонових) слід по можливості замінити літерними позначеннями (набраними на контрастному фоні), а криві позначити цифрами або різними типами ліній/маркерів, які мають бути роз'ясненими в підписах до рисунків або в тексті. На графіках усі лінії/маркери мають бути достатньої товщини/розміру для якісного відтворення їх у зменшеному в 2–3 рази вигляді (рекомендована початкова ширина рисунка — 12,7 см). Світлини мають бути чіткими та контрастними, а написи та позначення мають не закривати істотні деталі (для чого можна використовувати стрілки). Замість зазначення в підтекстовці збільшення під час зйомки бажано проставити масштаб (на контрастному фоні) на одній з ідентичних світлин. На графіках підписи до осей, **виконані мовою статті**, мають містити позначення (або найменування) величин, що відкладаються вздовж осей, і відділені комою їхні одиниці вимірювання.

9. Формули в текст треба вставляти за допомогою редактора формул **MathType**, сумісного з MS Office. **Вектори** слід набирати напівтовстим шрифтом без стрілок зверху.

10. Рисунки, таблиці, формули, а також підрядкові **примітки (виноски)** мають нумеруватися поспіль по всій статті.

11. Посилання на літературні джерела слід давати у вигляді порядкового номера, надрукованого в рядок у квадратних дужках. Список цитованої літератури складається почергово за першою згадкою джерела. Приклади оформлення посилань наведено нижче (просимо звернути увагу на порядок розташування ініціалів і прізвищ авторів, бібліографічних відомостей і на розділові знаки, а також на необхідність зазначення **всіх** співавторів цитованої роботи та її ідентифікатора **DOI**, якщо він є):

1. S. O. Firstov and T. G. Rogul, *Metallofiz. Noveishie Tekhnol.*, **44**, No. 1: 127 (2022) (in Ukrainian). https://doi.org/10.15407/mfint.44.01.0127
2. V. B. Tarelnyk, O. P. Gaponova, and Ye. V. Konoplianchenko, *Prog. Phys. Met.*, **23**, No. 1: 27 (2022). https://doi.org/10.15407/ufm.23.01.027
3. A. Meisel, G. Leonhardt, and R. Szargan, *Röntgenspektren und Chemische Bindung* [X-Ray Spectra and Chemical Bond] (Leipzig: Akademische Verlagsgesellschaft Geest & Portig K.-G.: 1977) (in German).
4. J. M. Ziman, *Printsipy Teorii Tverdogo Tela* [Principles of the Theory of Solids] (Moscow: Mir: 1974) (Russian translation).
5. M. A. Stucke, D. M. Dimiduk, and D. M. Hazzledine, *High Temperature Ordered Intermetallic Alloys. V* (Eds. I. Baker and R. Darolia) (Pittsburgh, PA, USA: MRS: 1993), p. 471.
6. *Handbook of Mathematical Functions with Formulas, Graphs and Mathematical Tables* (Eds. M. Abramowitz and I. A. Stegun), Nat'l Bureau of Standards. Appl. Math. Ser. Vol. **55** (Washington, D.C.: U.S. Govt. Printing Office: 1964).
7. B. B. Karpovych and O. B. Borovkoff, *Proc. of Symp. 'Micromaterials Engineering' (Dec. 25–31, 1999)* (Kyiv: RVV IMF: 2000), vol. **2**, p. 113 (in Russian).
8. A. Eh. Krug, *Abstr. Int. Conf. Phys. Phenomena (Dec. 25–31, 1991, Alushta)* (Kharkiv: 1991), p. 12.
9. T. M. Radchenko, *Vplyv Uporyadkuvannya Defektnoyi Struktury na Transportni Vlastyvosti Zmishanykh Krystaliv* [Influence of Ordering of the Defect Structure on Transport Properties of the Mixed Crystals] (Thesis of Disser. for the Degree of Dr. Phys.-Math. Sci.) (Kyiv: G. V. Kurdyumov Institute for Metal Physics, N.A.S.U.: 2015) (in Ukrainian). https://doi.org/10.13140/RG.2.2.35430.22089
10. E. M. Gololobov, V. B. Shipilo, N. I. Sedrenok, and A. I. Dudyak, *Sposob Polucheniya Karbonitridov Metallov* [Production Method of Metal Carbonitrides], Authors' Certificate 722341 SSSR (Publ. November 21, 1979) (in Russian).
11. V. G. Trubachev, K. V. Chuistov, V. N. Gorshkov, and A. E. Perekos, *Sposob Polucheniya Metallicheskikh Poroshkov* [The Technology of Metallic Powder Production]: Patent 1639892 SU. MKI, B22 F9/02, 9/14 (Otkrytiya i Izobreteniya, **34**, No. 13: 11) (1991) (in Russian).
12. Yu. M. Koval' and V. V. Nemoshkalenko, *O Prirode Martensitnykh Prevrashcheniy* [On the Nature of Martensitic Transformations] (Kyiv: 1998) (Prepr./N.A.S. of Ukraine. Inst. for Metal Physics. No. 1, 1998) (in Russian).

Слід використовувати загальноприйняті скорочення назв журналів:
https://www.cas.org/support/documentation/references/corejournals;
https://cdn.journals.aps.org/files/rmpguapb.pdf;
https://images.webofknowledge.com/WOK46P9/help/WOS/A_abrvjt.html;
https://mathscinet.ams.org/msnhtml/serials.pdf.

Необхідною вимогою є також надання авторами додаткового списку цитованої літератури (**References**) в **латинській транслітерації** (система **BGN/PCGN**; рекомендовані транслітератори: http://www.slovnyk.ua/services/translit.php; http://ru.translit.net/?account=bgn).

Після транслітерованих назв книг, дисертацій, патентів та ін. слід у квадратних дужках наводити їхній англомовний переклад (див. приклади вище). При транслітерації статей з МфНТ слід використовувати написання П.І.Б. авторів, наведені **лише** в англомовному змісті відповідного випуску, і **офіційну** транслітеровану назву журналу (див. також першу сторінку кожної статті та сайт).

12. Коректура авторам надсилається електронною поштою у вигляді pdf-файлу після завершення етапу **рецензування**. На перевірку коректури авторам відводяться 5 робочих днів. Після закінчення зазначеного терміну стаття автоматично направляється до друку. Виправлення слід відмітити та прокоментувати в самому pdf-файлі або оформити у вигляді переліку виправлень (підписаного уповноваженим представником колективу авторів) і переслати електронною поштою на адресу редакції.

Електронний варіянт статті надсилається на e-mail: mfint@imp.kiev.ua (з темою, що починається словом 'mfint'). Друкована версія рукопису (якщо у ній є потреба) надсилається за адресою: **Інститут металофізики ім. Г. В. Курдюмова НАН України, редакція МфНТ; бульвар Акад. Вернадського, 36; 03142 Київ, Україна** або відповідному реґіональному редактору (див. сайт).

Автори можуть вільно завантажити pdf-файли опублікованих статей з сайту журналу (https://mfint.imp.kiev.ua), а також замовити друковані примірники випуску журналу зі своєю статтею, надіславши до редакції журналу **разом з коректурою відповідну заявку та квитанцію про оплату** друку необхідної кількості примірників випуску на умовах, аналогічних передплатним.

Відповідно до угод між редакцією МфНТ, засновниками та видавцем журналу, редакція вважає, що автори, надсилаючи їй рукопис статті, передають засновникам, видавцю та редколеґії право опублікувати цей рукопис мовою ориґіналу та в перекладі іншими мовами, і просить авторів відразу прикладати до рукопису «Угоду про передачу авторського права».

Угода про передачу авторського права

Ми, що нижче підписалися, автори рукопису «_____», передаємо засновникам, видавцю та редколеґії журналу «Металофізика та новітні технології» (згідно з угодами між ними) право опублікувати цей рукопис мовою ориґіналу та в перекладі іншими мовами. Ми підтверджуємо, що ця публікація **не** порушує авторського права інших осіб або організацій і принципів наукової етики. При цьому за авторами зберігаються всі інші права як власників цього рукопису.

Підписи авторів: _____ (П.І.Б., дата, адреса, тел., e-mail)

Metallophysics and Advanced Technologies
Металофіз. новітні технол.
Metallofiz. Noveishie Tekhnol.
2026, vol. 48, No. 8, pp. 775–789
https://doi.org/10.15407/mfint.48.08.0775
Reprints available directly from the publisher

© 2026 G. V. Kurdyumov Institute for Metal Physics,
National Academy of Sciences of Ukraine
Published by license under
the G. V. Kurdyumov Institute for Metal Physics–
N.A.S. of Ukraine Publishers imprint.
Printed in Ukraine.

PACS numbers: 61.43.Gt, 61.72.sh, 64.75.Lm, 81.05.Rm, 81.20.Ev, 88.30.R-

Influence of LaH_x Additions on Characteristics of TiFe-Based Hydrogen-Storage Alloys Manufactured *via* Hydrogen-Assisted Powder Metallurgy

Z. Liu[*,**], Y. Wang[*,**], T. Cheng[*,**], Y. Song[*,**], D. Savvakin[*,**,***], N. Li[****], and O. Ivasishin[*,**,***]

[*]*College of Materials Science and Engineering,*
Jilin University,
CN-130012 Changchun, China
[**]*International Center of Future Science,*
Jilin University,
CN-130012 Changchun, China
[***]*G. V. Kurdyumov Institute for Metal Physics, N.A.S. of Ukraine,*
36 Academician Vernadsky Blvd.,
UA-03142 Kyiv, Ukraine
[****]*State Key Laboratory of Materials Processing and Die & Mould Technology,*
Huazhong University of Science and Technology,
CN-430074 Wuhan, China

TiFe-based alloys are promising candidates for solid-state hydrogen storage due to their low cost and excellent reversibility near room temperature. However, the conventional powder metallurgy (PM) manufacturing method often induces severe surface oxidation of Ti powders, which significantly hinders the activation and degrades the hydrogen-storage capacity of produced TiFe alloys. In this work, low-cost TiFe-based alloys are synthesized *via* hydrogen-assisted powder-metallurgy route. To mitigate the oxygen impurity issue, La hydride (LaH_x) is introduced as an oxygen scavenger and pore-forming agent. The results indicate that the addition of La plays a dual role: it reacts with

Corresponding author: Orest Mykhaylovych Ivasishin
E-mail: orest.ivasyshyn@gmail.com

Citation: Z. Liu, Y. Wang, T. Cheng, Y. Song, D. Savvakin, N. Li, and O. Ivasishin, Influence of LaH_x Additions on Characteristics of TiFe-Based Hydrogen-Storage Alloys Manufactured *via* Hydrogen-Assisted Powder Metallurgy, *Metallofiz. Noveishie Tekhnol.*, **48**, No. 8: 775–789 (2026). DOI: 10.15407/mfint.48.08.0775

© Publisher PH 'Akademperiodyka' of the NAS of Ukraine, 2026. This is an open access article under the CC BY-ND license (https://creativecommons.org/licenses/by-nd/4.0)

oxygen to form stable La oxides, thereby reducing the oxygen content within the main TiFe matrix, and creates a porous microstructure that facilitates hydrogen redistribution inside the material. Characterization by O/N/H analysis and XRD confirms that, while the total oxygen content increases with La doping, the formation of La-oxide precipitations reduces the concentration of oxygen dissolved in the TiFe matrix. Consequently, the La-doped alloy exhibits superior activation properties and a reversible hydrogen-storage capacity of 0.96% wt. at 40°C compared to 0.58% wt. for the undoped alloy. This study provides a feasible strategy for preparing high-performance TiFe-based alloys *via* a cost-effective PM route.

Key words: TiFe alloy, La hydride, hydrogen-assisted powder metallurgy, pore-forming effect, hydrogen-storage capacity.

Стопи на основі сполуки TiFe є перспективними матеріялами для твердофазного зберігання Гідроґену завдяки їхній низькій вартості та здатності оборотньо взаємодіяти з Гідроґеном за кімнатної температури. Проте, стандартні порошкові технології виготовлення цих стопів часто призводять до надмірного окиснення поверхні порошків, що перешкоджає активації стопу та понижує здатність накопичувати Гідроґен. У цій роботі стопи на основі TiFe було синтезовано методою порошкової металурґії з використанням наводнених порошків. Щоб зменшити проблему з домішкою Оксиґену, гідрид La (LaH_x) був введений як вбирач Оксиґену та пороутворювач. Результати показують, що додавання La відіграє подвійну роль: він реаґує з Оксиґеном, утворюючи стабільні оксиди La, тим самим зменшуючи вміст Оксиґену в основній матриці TiFe, та створює пористу мікроструктуру, яка сприяє перерозподілу Гідроґену всередині матеріялу. Дослідження спеченого стопу за допомогою аналізи O, N, H і рентґенівської дифракції підтверджує, що, хоча загальний вміст Оксиґену збільшується з La-леґуванням, утворення виділень оксиду La зменшує концентрацію Оксиґену, розчиненого в матриці TiFe. Леґований La стоп демонструє чудові активаційні властивості й оборотню водневу місткість (0,96% мас.) за 40°C порівняно з 0,58% мас. для нелеґованого стопу. Це дослідження пропонує можливу стратегію одержання високоефективних стопів на основі TiFe за допомогою економічно ефективного порошкового підходу.

Ключові слова: стоп TiFe, гідрид Лантану, воднева порошкова металурґія, ефект пороутворення, воднева місткість.

(Received 8 July, 2026; in final version, 16 July, 2026)

1. INTRODUCTION

The escalating global energy crisis has propelled the hydrogen industry into the spotlight, driven by hydrogen high energy-density and clean-combustion characteristics [1–8]. Within this sector, hydrogen storage and transportation are pivotal. Conventional methods, such as high-pressure gaseous and cryogenic-liquid storage, are hampered by significant drawbacks, including safety risks and high energy con-

sumption, respectively [3, 6]. Solid-state hydrogen storage emerges as a promising alternative, offering high volumetric capacity and enhanced safety [8–10]. Among various solid-state materials, TiFe-based alloys are particularly attractive due to their low cost and excellent reversibility near ambient temperatures [11, 12].

The synthesis of TiFe alloy is commonly achieved through arc melting, mechanical alloying, and powder metallurgy [13–19]. Arc melting produces an as-cast microstructure with coarse grains, which lengthens the diffusion path of hydrogen and limits the hydrogen-storage kinetic properties of the alloy [15]. Mechanical alloying tends to cause cold welding of powder particles, which requires the addition of organic process-control agents and introduces carbon impurities consequently [16]. In contrast, powder metallurgy, specifically hydrogen-assisted powder sintering, presents distinct advantages, including a simple process and low production cost [18, 20, 21]. The inherent porosity in sintered alloys provides effective pathways for hydrogen diffusion, optimizing kinetic behaviour [19, 22].

However, the powder-metallurgy route faces a critical challenge—the severe surface oxidation of Ti powders during processing. This oxide layer acts as a barrier, hindering hydrogen diffusion, impeding activation, and degrading the overall hydrogen-storage capacity [23]. Previous studies have confirmed that a high oxygen concentration suppresses the formation of the primary TiFe phase and that dissolved oxygen in the TiFe matrix can destabilize the metal hydride by reducing the desorption enthalpy [24]. Therefore, precise control of oxygen content is paramount for enhancing the alloy performance.

To mitigate the detrimental effects of surface oxidation, recent studies have explored the use of La-based additives. Chen *et al.* demonstrated that adding LaH_3 to V–Ti–Cr–Fe alloys decreased the proportion of titanium oxides and improved hydrogen adsorption–desorption capacity [25]. Similarly, Alam *et al.* found that, in mechanically alloyed TiFe, the *in situ* formation of LaH_3 promoted heterogeneous pores' nucleation and provided diffusion channels for hydrogenation [26]. These findings suggest that rare-earth doping is an effective strategy for oxygen control, where the additive reduces the oxygen content in alloy matrix, weakens surface oxide layers, and accelerates hydrogen diffusion *via* the formation of LaH_3.

In this work, we fabricate both pure and La-doped TiFe alloys, using a cost-effective hydrogen-assisted powder-metallurgy route. We introduce La hydride (LaH_x) as a dual-function additive serving as both an oxygen scavenger and a pore-forming agent. A series of characterization tests are conducted to investigate systematically the synergistic regulatory effect of La doping on the microstructure and hydrogen-storage performance. This study aims to clarify the intrinsic modification mechanism of La, focusing on its role in powder activation, phase

formation, and the optimization of hydrogen adsorption/desorption thermodynamics and kinetics. Our findings reveal a cooperative mechanism, wherein La doping constructs hydrogen-diffusion channels, while achieving purification of TiFe lattice, providing practical guidance for optimizing the fabrication of high-performance TiFe-based hydrogen-storage materials.

2. MATERIALS AND METHODS

2.1. Preparation of TiFe Alloys

TiH_2 powder (99.9% purity, < 45 μm) and pure iron powder (99.9% purity, < 38 μm) were adopted as raw materials. The atomic ratio of Ti and Fe was fixed at 1:1 for all samples. 1% wt. La hydride (< 38 μm) was introduced into one group, while the other group contained no additive. The two groups of weighed powders were placed into a container and mixed in a powder-mixing machine at 30 rpm for 6 hours. The as-obtained Ti–Fe mixed powders were loaded into a mould, sealed under vacuum, and then subjected to cold isostatic pressing at 300 MPa with a holding time of 300 s. The green compacts were placed in a vacuum sintering furnace. Upon reaching a vacuum level of $1{\cdot}10^{-3}$ Pa, the furnace was heated at a rate of 10°C/min. After completion of the dehydrogenation stage, the temperature was maintained at 1200°C for 2 hours, followed by furnace cooling to room temperature.

2.2. Characterization

Phase identification was conducted by x-ray diffraction (XRD, PANalytical Empyrean) using CuK_α radiation from 20° to 90° at a scan rate of 10°/min. Oxygen content was measured by an O/N/H analyser (LECO-ONH 836). The microstructure and elemental distribution were observed by scanning electron microscopy (SEM, Thermo Fisher Verios 5 UC) equipped with energy-dispersive x-ray spectroscopy (EDS). Room-temperature compression tests were carried out on a universal testing machine (MTS-E43.104) at a strain rate of 1 mm/min, with specimen dimensions of ∅5 mm×10 mm.

2.3. Hydrogen-Storage Performance Measurement

All samples were activated and tested under equal experimental conditions. To activate hydrogen sorption, vacuum heat treatment was performed at 700°C to reduce the thickness of the surface oxide film. The initial hydrogenation conducted at 700°C under 50 bar hydrogen pressure was adopted to expose the fresh alloy matrix. Ten adsorption–

desorption cycles were subsequently carried out to stabilize the hydrogen-storage capacity. Finally, pressure–composition–temperature (PCT) tests were performed at 40°C on a hydrogen adsorption–desorption instrument (H-Sorb X600PCT-Pro, CIQTEK) to evaluate the hydrogen-storage performance.

3. RESULTS AND DISCUSSION

3.1. Pore-Forming Effect of La Addition

Figure 1 shows the metallographic micrographs of undoped and La-doped TiFe alloys, illustrating the differences in micromorphology and pore structure between the two samples. Low-magnification images show that interconnected macropores exist in both specimens, while the La-doped alloy contains a substantially larger amount of macropores. High-magnification metallographic observations further exhibit the matrix microstructure [27]. Micropores can be found in the undoped sample, yet the La-doped TiFe matrix contains much denser and more abundant micropores. The comparison demonstrates that La-doping promotes the development of both macropores and micropores and produces a well-developed dual-scale porous structure.

Figure 2 shows the SEM morphologies and elemental distribution

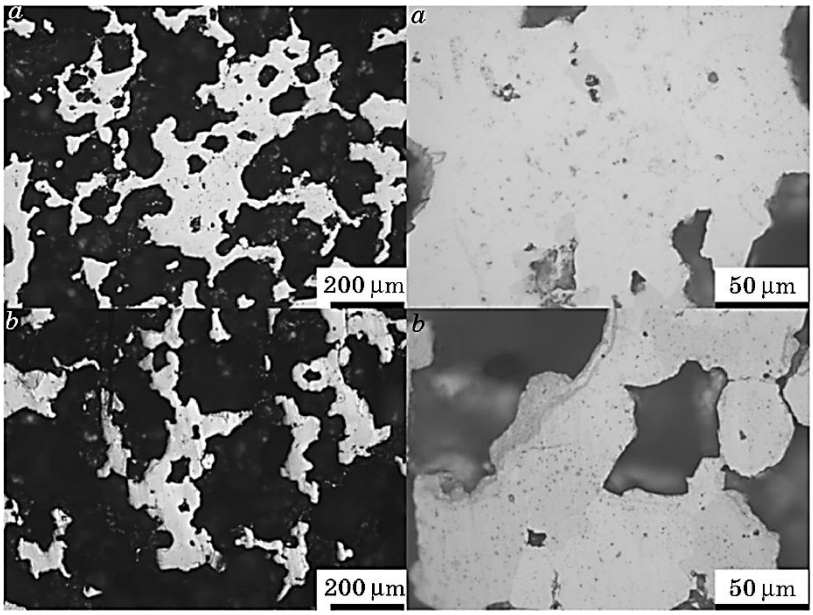


Fig. 1. Metallographic images of undoped and La-doped TiFe alloys at different magnifications: undoped alloy (*a*), La-doped alloy (*b*).

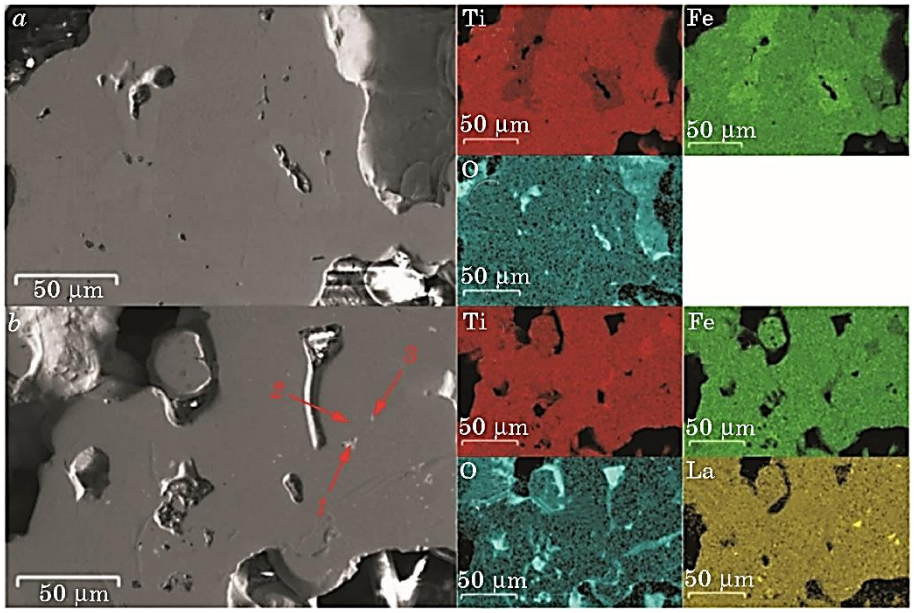


Fig. 2. SEM morphologies and elemental distribution mappings of undoped and La-doped TiFe alloys: undoped alloy (*a*), La-doped alloy (*b*). The marked points in Fig. 2, *b* represent the selected regions for EDS point scanning.

mappings of undoped and La-doped TiFe alloys. Ti and Fe elements exhibit inhomogeneous distribution in both samples. The signal intensity of Ti and Fe declines obviously within the pore areas, indicating low concentrations of Ti and Fe on pore walls and interiors. In contrast, oxygen displays obvious localized enrichment in many pore regions, including large pores and tiny micropores. In the La-doped sample, prominent La signals emerge mainly in partial micropore areas, where oxygen is also enriched. Comparatively, strong La signals are barely observed on large pores that indicates that La-containing phases tend to aggregate preferentially within the micropores rather than large pores.

To further explore the elemental composition difference between micropore regions and dense matrix regions of the La-doped sample, three positions marked in Fig. 2, *b* were selected for EDS point scanning. The atomic percentages of Ti, Fe, O and La at these testing points are summarized in Table 1. Point 1 and point 3 are in micropore regions. The results show extremely low Ti and Fe contents, while O and La account for the overwhelming majority, with combined atomic percentages exceeding 90%. In contrast, point 2 is situated in the dense matrix area away from micropores. This position is dominated by Ti and Fe, and only a small amount of oxygen can be detected; nearly, no

TABLE 1. Elemental composition gained by EDS point scanning at the marked spots in Fig. 2, *b*.

Points	Ti, % at.	Fe, % at.	O, % at.	La, % at.
1	2.1	1.5	61.9	34.5
2	48.2	44.9	6.8	0.0
3	4.2	2.4	60.5	32.9

La element exists in this region. The quantitative data further verify that La and O tend to accumulate within the micropores of the La-doped TiFe alloy forming small precipitations (particles of 2 μm in size).

Combined with metallographic observation, SEM morphology, and EDS elemental analysis results, the effect of La-doping on the microstructure of TiFe alloy can be clarified. The undoped TiFe alloy contains inherent pores after sintering. After La-doping, the macropore size of the alloy increases obviously, while the number of internal micropores rises significantly. SEM and EDS tests confirm that La and O elements preferentially accumulate in micropore regions rather than in dense matrix areas. The enrichment of La and O inside the micropores induces the generation of abundant micropores. In general, La-doping effectively promotes the formation and development of the dual-scale pore structure of sintered TiFe alloy.

3.2. Effect of La Addition on Oxygen Redistribution in the Material

The phase composition of undoped and La-doped TiFe alloys was characterized by XRD, and the corresponding patterns are presented in Fig. 3. Both samples contain the main TiFe phase together with the impurity Ti_4Fe_2O phase [27]. Ti_4Fe_2O forms during high-temperature sintering *via* reactions between the alloy matrix and trace residual oxygen. This impurity phase exerts a poisoning effect on the hydrogen-storage system of TiFe-based alloys [28]. Clear differences in phase constituents are identified between the two samples. Compared with the undoped TiFe alloy, new diffraction peaks belonging to La_2O_3 emerge in the XRD pattern of the La-doped specimen [29]. The appearance of the La_2O_3 phase verifies that the doped La element possesses strong oxygen affinity and consumes partial oxygen impurities in the alloy matrix during the sintering process. Since partial oxygen participates in the formation of La_2O_3, the oxygen source for generating the harmful Ti_4Fe_2O phase is reduced correspondingly [30]. This competitive oxygen-consumption behaviour inhibits the generation of detrimental Ti_4Fe_2O phase with La-doping.

O/N/H analysis was further adopted to characterize quantitatively

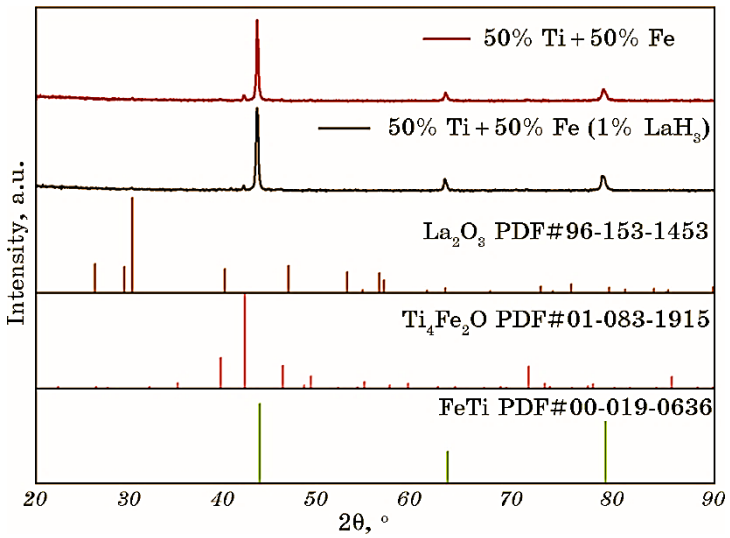


Fig. 3. X-ray diffraction patterns of undoped and La-doped alloys.

TABLE 2. Oxygen, nitrogen and hydrogen contents of undoped and La-doped alloys.

Samples	O, % wt.	N, % wt.	H, % wt.
undoped alloy	0.306	0.00577	0.00426
La-doped alloy	0.472	0.00581	0.0109

the variation of oxygen content, and the measured data are summarized in Table 2. The total oxygen content does not decrease after La-doping, but it shows obvious upward trend. This observation suggests that noticeable part of oxygen impurity can be introduced in the alloy with initial lanthanum hydride powder. What is more important, the effect of La-doping leads to a redistribution of oxygen inside the sintered alloy material. This leads to purification (deoxidization) of the TiFe lattice (matrix) rather than of the sintered material as a whole. This trend can be explained with the support of previous SEM observations and EDS mapping as well as point scanning results.

Multiple characterization results demonstrate jointly that La is not uniformly distributed in the sintered TiFe alloy, but accumulates as small precipitations preferentially within the micropores and grain-boundary regions. Owing to high oxygen affinity, La drives oxygen impurities to migrate out from the TiFe-alloy matrix toward porous and defective zones. The migrated oxygen reacts preferentially with enriched La to generate La_2O_3 precipitations rather than forming Ti_4Fe_2O inside the matrix [31].

Consequently, although La addition increases the statistical total oxygen content of the alloy in macroscopic measurement, the formation of La_2O_3-phase precipitations fundamentally enables the effective deoxidation of the alloy matrix, reducing the oxygen impurity dissolved in the TiFe crystal lattice. The oxygen impurities, which originally poisoned the hydrogen-storage performance, are transferred and consumed in the defect regions that reduces the content of harmful Ti_4Fe_2O phase in the matrix and purifies the alloy microstructure. Furthermore, the *in situ* generation of La_2O_3 particles in pore regions is consistent with the pore-forming effect concluded in the previous section. The oxygen migration and phase-transformation behaviour induced by La-doping achieve simultaneously matrix purification and microstructure optimization, which provides an improved matrix structure for the hydrogen-storage reaction of TiFe alloy.

3.3. Compressive Mechanical Performance

Room-temperature compression tests were carried out to investigate the mechanical performance of undoped and La-doped TiFe alloy. Figure 4 presents the compressive stress–strain curves of the two samples. Table 3 summarizes the corresponding average peak compressive stress and fracture strain. The stress–strain curves show obvious differences between the two alloys. The undoped TiFe alloy achieves a higher peak stress, while the La-doped TiFe alloy exhibits a delayed

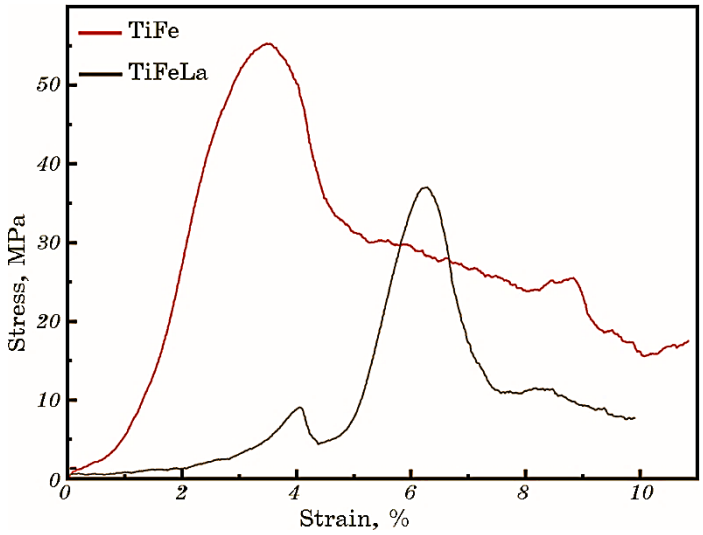


Fig. 4. Representative compressive stress–strain curve of undoped and La-doped TiFe alloys.

TABLE 3. Average peak compressive stress and fracture strain of undoped and La-doped TiFe alloys. Data are expressed as mean ± standard deviation.

Sample	Stress, MPa	Strain, %
undoped alloy	60.1 ± 6.79	8.04 ± 3.96
La-doped alloy	32.25 ± 6.72	11.47 ± 2.23

peak position. Combined with the statistical data in Table 3, the average peak compressive stress of undoped TiFe alloy is of (60.10 ± 6.79) MPa, which reduces to (32.25 ± 6.72) MPa for La-doped TiFe alloy. In terms of fracture strain, undoped TiFe alloy reaches $(8.04 \pm 3.96)\%$, whereas La-doped TiFe alloy increases to $(11.47 \pm 2.23)\%$.

The variation of mechanical properties can be associated with the microstructure evolution induced by La-doping. As discussed above, La addition promotes the *in situ* formation of La_2O_3 particles and generates abundant micropores within the alloy matrix. Under compressive load, these micropores and dispersed La_2O_3 particles act as stress-concentration sites, accelerating crack initiation and propagation and lowering the bearing capacity of the alloy. Meanwhile, the porous microstructure provides space for plastic deformation, which accounts for the larger fracture strain of La-doped TiFe alloy.

These results demonstrate that La-doping reduces the peak compressive strength and improves the deformability of undoped TiFe alloy. From the perspective of practical processing, the decline in compressive strength brings favourable advantages for the hydrogen-storage TiFe alloys. La-doped TiFe alloy can be crushed into fine particles under lower external force, simplifying subsequent pulverization and granulation procedures [32]. Combined with foregoing discussion, La-doping inducing La_2O_3 formation simultaneously realizes TiFe-matrix deoxidation and pore construction, regulating alloy mechanical properties. Such comprehensive modification improves the machinability of TiFe-based alloys and facilitates subsequent activation and hydrogen-storage applications [30].

3.4. PCT Hydrogen-Storage Performance

Figure 5 presents the PCT curves for the undoped and La-doped TiFe alloys at 40°C. The PCT measurements reveal significant differences in both the plateau characteristics and the hydrogen-adsorption capacity between the two samples. The undoped TiFe sample exhibited a sloping-plateau region spanning approximately 10–25 bar (1–2.5 MPa). The hydrogen concentration increased substantially as the pressure was raised. At the end of this plateau region, the hydrogen-adsorption capacity reached approximately 0.58% wt. Upon further pressuriza-

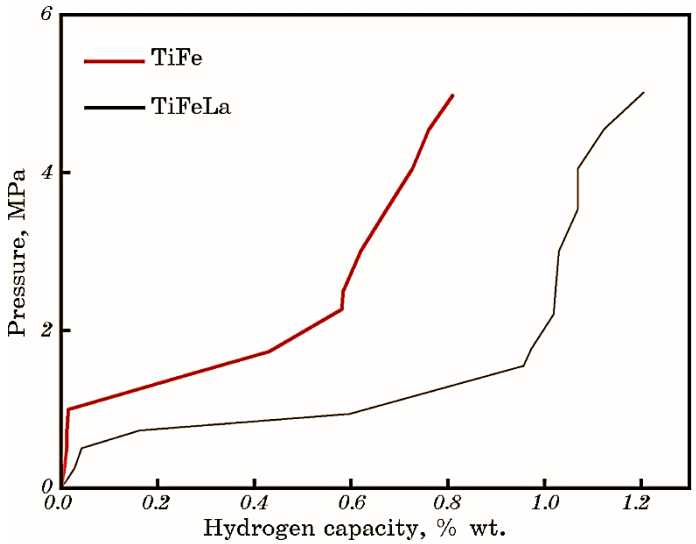


Fig. 5. PCT curves for the undoped and La-doped TiFe alloys at 40°C.

tion to 50 bars, the hydrogen concentration continued to rise gradually, ultimately reaching 0.81% wt. In striking contrast, the La-doped TiFe sample displayed a considerably flatter plateau, with the majority of hydrogen adsorption occurring within the narrow pressure window of 5–15 bars. Within this short interval, the hydrogen concentration increased rapidly to approximately 0.96% wt., exceeding the plateau-end capacity of the undoped sample. Upon further pressurization to 50 bar (5 MPa), the total hydrogen concentration reached approximately 1.20% wt., which is 0.39% wt. higher than the value obtained for the undoped sample.

The markedly improved hydrogen-storage performance of the La-doped sample can be rationalized on the basis of prior XRD, SEM–EDS and O/N/H analyses. The XRD and O/N/H analyses have demonstrated that La-doping reduces the amount of Ti_4Fe_2O phase through preferential oxygen scavenging, preserving the chemical purity of the TiFe matrix [33]. Since Ti_4Fe_2O is an inert phase that does not participate in hydrogen adsorption, its removal is directly contributing to the higher total capacity. Simultaneously, the pore-forming effect of La (increase in total volume of dual-scale pore structure) provides a more extensive network of hydrogen-transport pathways. The enhanced porosity facilitates the infiltration of hydrogen gas into the interior of the sample, accelerating the kinetics of hydrogen uptake and enabling a more complete utilization of the TiFe matrix. The steeper plateau observed in the La-doped sample (5–15 bars *vs.* 10–25 bar) suggests that the improved pore network reduces the pressure hysteresis in sintered TiFe

alloys.

The synergy between the pore-forming and matrix purification of La-doping is therefore evident in the PCT behaviour: the deoxidation effect increases the intrinsic hydrogen-storage capacity of the matrix by reducing the inactive Ti_4Fe_2O phase, while the pore-forming effect enhances the hydrogen accessibility and uptakes kinetics through the creation of a more open microstructural network [19]. This dual mechanism—chemical purification of TiFe matrix coupled with physical channel creation—accounts for the simultaneous increase in both the plateau capacity (0.96% wt. *vs.* 0.58% wt.) and the ultimate capacity (1.20% wt. *vs.* 0.81% wt.) of the La-doped sample.

3.5. Phase Constitution and Impurity Variations after PCT Cycling

To investigate the phase stability and internal elemental variation of undoped alloy and La-doped alloy after long-term hydrogen adsorption and desorption cycling, XRD phase characterization and O/N/H analysis were performed on the cycled alloy samples. The phase structural changes before and after cycling were analysed, based on the XRD results, while the variations of oxygen and hydrogen elements were summarized and discussed, according to the O/N/H test data.

XRD test results shown in Fig. 6 reveal that no new diffraction peaks are observed for the undoped alloy after PCT cycling. In comparison, a new diffraction signal appears for the La-doped alloy, which can

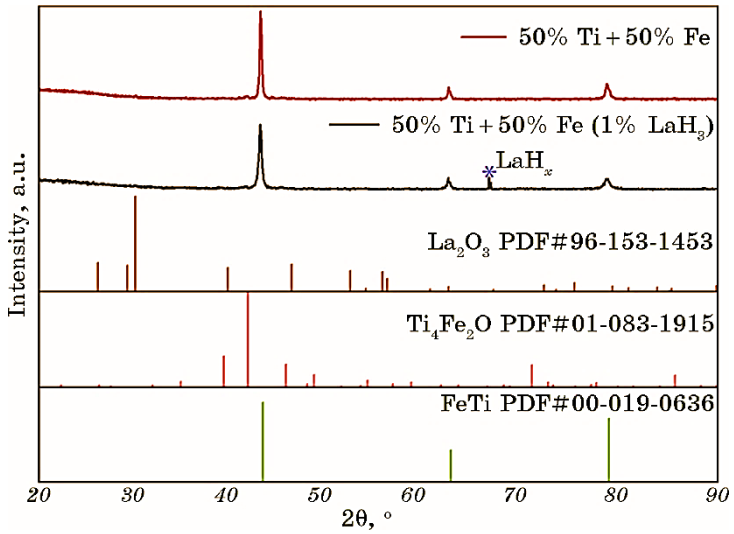


Fig. 6. XRD patterns for the undoped alloy and La-doped alloy after PCT hydrogen absorption–desorption cycling.

TABLE 4. O/N/H elemental contents of alloys before and after PCT cycling.

Samples	O, % wt.	N, % wt.	H, % wt.
undoped alloy	0.760	0.0293	0.0295
La-doped alloy	0.749	0.0357	0.0897

be preliminarily assigned to La-hydride phase (marked in Fig. 6). This indicates that the La-containing phases in the matrix, such as La oxide, can react with hydrogen upon PCT cycling to form La hydride.

As summarized in Table 4, residual hydrogen content rises for both alloys after PCT cycling, while a considerably higher magnitude increase is observed for the La-doped alloy. Accordingly, it may be inferred that La-containing phases (*e.g.*, La oxide) within the La-doped alloy react with hydrogen to produce La hydride. This inference is well supported by the foregoing XRD observations.

Combining the above XRD and O/N/H characterization results, the two sets of experimental evidence jointly indicate that La-bearing constituents inside the La-doped alloy undergo hydrogenation reactions during PCT cycling to produce La hydride.

4. SUMMARY

In this work, we studied comparatively microstructure, mechanical properties and hydrogen-storage performance of TiFe alloy and La-doped TiFe alloy fabricated by hydrogen-assisted powder sintering. The addition of La brought an evident pore-forming effect inside the matrix, modifying the internal pore structure of sintered samples. Moreover, La-doping realized local accumulation of oxygen impurity with formation of lanthanum-oxide precipitations in TiFe matrix, removing harmful Ti_4Fe_2O phase and purifying the TiFe lattice.

Compression-test results demonstrated that the La-doped alloy possessed lower compressive strength relative to the undoped alloy. This reduced strength facilitates crushing the alloy into fine powder particles, which supports subsequent activation and practical application for hydrogen storage.

PCT characterization confirmed the improvement in hydrogen-storage performance derived from La modification. The La-doped alloy exhibited a smoother and more stable hydrogen-adsorption platform. Its hydrogen-storage capacity on the platform was higher than that of the undoped alloy, and the ultimate hydrogen capacity measured at 5 MPa outperformed the undoped counterpart too.

Characterizations after hydrogen adsorption–desorption cycling show increased residual hydrogen content in both alloys. A higher hydrogen increment can be observed for the La-doped alloy. It can be con-

cluded that La hydride is formed through the reaction between La-bearing phases and hydrogen during cycling.

In summary, La-doping optimizes the microscopic structure, crushability and overall hydrogen-storage performance of the TiFe alloys.

This work was financially supported by the National Natural Science Foundation of China (Nos. 52441402 and 52301047), Scientific Research Project of Education Department of Jilin Province (JJKH20261265KJ) and Jilin Province Science and Technology Development Plan Item (20260205066GH). The authors also gratefully acknowledge financial support from Jilin University, China and the National Academy of Sciences of Ukraine.

AUTHORS' CONTRIBUTIONS

Zheyu Liu: experimentation, analysis, drafting; Yuanmeng Wang: analysis, drafting; Yuchao Song: conception and design, provision of resources, supervision, reviewing, and editing; Dmytro Savvakin: data organization, reviewing; Ning Li: data organization, editing; Orest Ivasishin: reviewing, validation.

REFERENCES

1. Z. Li, B. Guan, K. Shu, L. Zhu, T. Zhu, Z. Zhuang, X. Hu, C. Zhu, S. Zhao, J. Chen, J. Gao, H. Dang, L. Zhang, Y. Li, L. Xu, W. Zeng, S. Chen, L. Wang, C. Zhu, J. He, Q. Xian, and Z. Huang, *Int. J. Hydrogen Energy*, **204**: 153160 (2026).
2. S. Kurbanbekov, M. Skakov, V. Tskhe, Y. Amangeldiyeva, A. Gradoboev, A. Tokezhanov, D. Baltabayeva, and N. Raimzhanova, *Metals*, **16**, Iss. 7: 720 (2026).
3. W. Fang, C. Ding, L. Chen, W. Zhou, J. Wang, K. Huang, R. Zhu, J. Wu, B. Liu, Q. Fang, X. Wang, and J. Wang, *Energy and Fuels*, **38**, Iss. 15: 13539 (2024).
4. M. R. Kalibek, A. D. Ospanova, B. Suleimenova, R. Soltan, T. Orazbek, A. M. Makhmet, K. S. Rafikova, and N. Nuraje, *Discover Nano*, **19**: 195 (2024).
5. T. H. Le, M. P. Kim, C. H. Park, and Q. N. Tran, *Materials*, **17**, Iss. 3: 666 (2024).
6. P. K. Panigrahi, B. Chandu, M. R. Motapothula, and N. Puvvada, *Energy and Fuels*, **38**, Iss. 4: 2630 (2024).
7. R. Etezadi, S. Shivaramakrishnan, R. Wang, R. Khalighi, L. Zhao, I. G. Eschrich, F. Aquino, M. Ibrahim, C. Tasser, and T. T. Tsotsis, *Industrial Eng. Chem. Research*, **65**, Iss. 3: 1403 (2026).
8. R. Murugavel, A. A. Rownaghi, P. A. Webley, and F. Rezaei, *Energy and Fuels*, **39**, Iss. 38: 18251 (2025).
9. M. G. Nijkamp, J. E. M. J. Raaymakers, A. J. van Dillen, and K. P. de Jong, *Appl. Phys. A*, **72**: 619 (2001).
10. B. Weinberger and F. D. Lamari, *Int. J. Hydrogen Energy*, **34**: 3058 (2009).

11. H. Liu, J. Zhang, P. Sun, C. Zhou, Y. Liu, and Z. Z. Fang, *J. Energy Storage*, **68**: 107772 (2023).
12. Y. Xu, Y. Deng, W. Liu, X. Zhao, J. Xu, and Z. Yuan, *Sustainable Energy Technologies and Assessments*, **55**: 102974 (2023).
13. E. I. L. Gymez, K. Edalati, F. J. Antiqueira, D. D. Coimbrro, G. Zepon, D. R. Leiva, T. T. Ishikawa, J. M. Cubero-Sesin, and W. J. Botta, *Advanced Eng. Mater.*, **22**, Iss. 10: 2000011 (2020).
14. K. Oishi, S. Takagi, Y. Daikuhara, T. Haraki, H. Uchida, M. Abe, T. Kokaji, and S. Uchida, *J. Advanced Sci.*, **16**, No. 2: 46 (2004).
15. A. Knaislová, P. Novák, J. Kopeček, and F. Průša, *Materials*, **12**, Iss. 19: 3084 (2019).
16. R. B. Falcão, E. D. C. C. Dammann, C. J. da Rocha, and R. M. L. Neto, *Mater. Sci. Forum*, **600–661**: 329 (2010).
17. J. Umeda, T. Tanaka, T. Teramae, S. Kariya, J. Fujita, H. Nishikawa, Y. Shibutani, J. Shen, and K. Kondoh, *Mater. Sci. Eng. A*, **803**: 140708 (2021).
18. A. O. Araoyinbo, F. A. Ishola, E. Y. Salawu, M. B. Biodun, and A. U. Samuel, *AIP Conf. Proc.*, **2437**: 020153 (2022).
19. H. Zhang, Y. Liu, G. Miao, Z. Ma, F. Sun, A. Ju, X. Qu, and P. Li, *Chem. Eng. J.*, **526**: 171450 (2025).
20. J. M. Torralba, *Metals*, **11**, Iss. 10: 1519 (2021).
21. L. Radmann, A. C. Domingos Dias Moraes, L. V. Biehl, R. M. Lima, B. P. d. Silva, M. C. d. Souza, and J. L. B. Medeiros, *Sustainability*, **18**, Iss. 10: 5065 (2026).
22. W. J. Yan, Y. B. Tao, and H. Ye, *Int. J. Hydrogen Energy*, **86**: 1154 (2024).
23. H. Shi, Y. Zhang, Z. Li, F. Gao, X. Wang, Y. Yang, Y. Liu, X. Xiao, F. Fang, and W.-G. Cui, *Int. J. Minerals, Metallurgy Mater.*, **32**: 2743 (2025).
24. H. Liu, J. Zhang, P. Sun, C. Zhou, Y. Liu, and Z. Z. Fang, *J. Energy Storage*, **55**: 105543 (2022).
25. Z. Chen, L. Luo, Z. Su, W. Liu, F. Zhang, and Y. Huang, *Int. J. Hydrogen Energy*, **44**: 13538 (2019).
26. M. M. Alam, P. Sharma, and J. Huot, *Int. J. Hydrogen Energy*, **50**: 261 (2024).
27. Q. Zhao, Z. He, Y. He, Y. Qiu, Z. Wang, and J. Yao, *Intermetallics*, **162**: 108004 (2023).
28. K. Hiebl, E. Tuscher, and H. Bittner, *Chemischer Informationsdienst*, **10**, Iss. 19: 38 (1979).
29. M. M. Alam, P. Sharma, and J. Huot, *Int. J. Hydrogen Energy*, **50**: 727 (2024).
30. X. Wei, W. Chen, X. He, L. Wang, D. Jiao, and Y.-Q. Fu, *Int. J. Hydrogen Energy*, **208**: 153293 (2026).
31. Z. Hou, S. Guo, X. Zhang, L. Xu, Y. Qi, Y. Zhang, P. Li, and D. Zhao, *Int. J. Hydrogen Energy*, **136**: 469 (2025).
32. Y. Xu, Y. Zhou, Y. Li, Y. Hao, P. Wu, and Z. Ding, *Molecules*, **29**, Iss. 11: 2451 (2024).
33. Z. Han, X. Gao, J. Li, Z. Huang, X. Kang, T. Zhai, H. Sun, Z. Yuan, L. Wang, and X. He, *Int. J. Hydrogen Energy*, **239**: 155454 (2026).

Metallophysics and Advanced Technologies
Металофіз. новітні технол.
Metallofiz. Noveishie Tekhnol.
2026, vol. 48, No. 8, pp. 791–805
https://doi.org/10.15407/mfint.48.08.0791
Reprints available directly from the publisher

© 2026 G. V. Kurdyumov Institute for Metal Physics,
National Academy of Sciences of Ukraine
Published by license under
the G. V. Kurdyumov Institute for Metal Physics–
N.A.S. of Ukraine Publishers imprint.
Printed in Ukraine.

PACS numbers: 61.43.Dq, 61.43.Fs, 61.66.Dk, 65.60.+a, 81.05.Bx, 81.07.Bc, 81.70.Pg

Influence of Y and Al Addition on the Glass-Forming Ability of Complex Alloyed $Fe_{40–50.4}(TM, Al)_{29.1–37.5}Y_{1.8–2}(Si, C, B)_{19.7–22}$ Alloys

I. K. Yevlash, M. S. Nizameyev, I. V. Zagorulko, O. M. Semyrga, O. I. Boshko, and V. K. Nosenko

G. V. Kurdyumov Institute for Metal Physics, N.A.S. of Ukraine,
36 Academician Vernadsky Blvd.,
UA-03142 Kyiv, Ukraine

The influence of Y and Al alloying on the glass-forming ability of bulk metallic glasses of the $Fe_{40–50.4}(TM, Al)_{29.1–37.5}Y_{0–2}(Si, C, B)_{19.7–22}$ system alloys with different content of transition metals (TM) and metalloids is investigated. An extensive analysis of the amorphization tendency of the studied alloys is carried out with a comparison of the effectiveness of several criteria. In rapid-quenched bulk samples of the complex alloyed alloys studied in the article, a number of non-equilibrium structures are observed (namely, purely amorphous, amorphous–crystalline (nanocomposite) and nanocrystalline ones) that indicates a significant dependence of the structure of this group of alloys on cooling conditions. As shown, the main factor determining the amorphization tendency of Fe-based alloys is the proximity of the alloy composition to the eutectic. Alloying the alloys with yttrium and aluminium significantly increases the melt amorphization tendency.

Key words: eutectic alloys, nanocrystallization, amorphization, melt quenching, bulk metallic glasses, glass-forming ability.

Досліджено вплив леґування Y і Al на схильність до аморфізації об'ємних металевих стекол стопів системи $Fe_{40–50.4}(TM, Al)_{29.1–37.5}Y_{0–2}(Si, C, B)_{19.7–22}$ з різним вмістом перехідних металів (TM) і металоїдів. Проведено широку

Corresponding author: Igor Yevlash
E-mail: igor.yevlash@gmail.com

Citation: I. K. Yevlash, M. S. Nizameyev, O. M. Semyrga, O. I. Boshko, and V. K. Nosenko, Influence of Y and Al Addition on the Glass Forming Ability of Complex Alloyed $Fe_{40–50.4}(TM, Al)_{29.1–37.5}Y_{1.8–2}(Si, C, B)_{19.7–22}$ Alloys, *Metallofiz. Noveishie Tekhnol.*, **48**, No. 8: 791–805 (2026), DOI: 10.15407/mfint.48.08.0791

© Publisher PH 'Akademperiodyka' of the NAS of Ukraine, 2026. This is an open access article under the CC BY-ND license (https://creativecommons.org/licenses/by-nd/4.0)

аналізу схильности до аморфізації досліджуваних стопів з порівнянням ефективности кількох критеріїв. У швидкозагартованих об'ємних зразках складнолеґованих стопів, досліджених у роботі, спостерігається ряд нерівноважних структур, а саме, повністю аморфні, аморфно-кристалічні (нанокомпозитні) та нанокристалічні, що свідчить про значну залежність структури цієї групи стопів від умов охолодження. Показано, що основним чинником, що визначає схильність до аморфізації стопів на основі Fe, є близькість складу стопу до евтектики. Леґування стопів Ітрієм і Алюмінієм значно підвищує схильність до аморфізації розтопу.

Ключові слова: евтектичні стопи, нанокристалізація, аморфізація, загартування розтопів, об'ємні металеві стекла, здатність до склоутворення.

(Received 21 April, 2025; in final version, 3 March, 2026)

1. INTRODUCTION

The development and use of bulk metallic glasses (BMGs) are of significant interest to modern scientists. Currently, BMGs, which are produced by melt quenching at rates ≤ 100 K/s, have been obtained in alloys based on Zr, Pd, Mg, Ti, Ni, Fe [1, 2]; among these BMGs, iron-based alloys occupy a special place both from a commercial and technological point of view, since they have a unique combination of relatively low cost with high strength characteristics, wear resistance, corrosion resistance, magnetic and even antibacterial properties [3–5]; the competitiveness of bulk amorphous alloys (BAAs) also depends on their amorphization tendency, strength characteristics in combination with satisfactory plasticity, corrosion resistance, thermal stability of the structure, and manufacturing technological regimes, which should be as close as possible to traditional casting technologies.

For the development of BAAs, modern researchers mainly use topological criteria for the glass forming ability of metal melts [6]; one such criterion is a large ($\geq 12\%$) difference in the atomic diameters of the alloy components, number of which there must be at least three [1]; the second criterion emphasizes that the atomic sizes of the alloy components and their concentrations must correspond to certain ratios that provide the densest packing of atoms in the disordered structure [6]; according to Turnbull's thermodynamic criterion [7], the glass forming ability of the alloy increases with increasing normalized glass transition temperature $T_{rg} = T_g/T_l$, where T_g and T_l are the glass transition and liquidus temperatures, respectively; to reduce T_l of iron-based alloys, it is necessary to add metalloid alloy to them, as well as some refractory metals (Zr, Nb, Mo, *etc.*); the addition of refractory metals also contributes to an increase in the glass transition temperature due to an increase in elastic moduli [8]; according to the results of experimental studies of the influence of alloying elements on the glass form-

ing ability of iron-based alloys, it was found that small (1.5–2 at.%) additions of yttrium and other rare earth metals have the most effective effect on reducing the critical cooling rate; thus, the critical thickness of amorphous castings of $Fe_{50}Cr_{14}Mo_{14}C_{14}B_6Y_2$ and $Fe_{50}Cr_{14}Mo_{14}C_{14}B_6Dy_2$ alloys is of 4 mm [9], $Fe_{60}Cr_{10}Mo_9C_{10}B_6Er_2Ni_3$ alloy is of 8 mm [10], $(Fe_{44.3}Cr_5Co_5Mo_{12.8}Mn_{11.2}C_{15.8}B_{5.9})_{98.5}Y_{1.5}$ and $(Fe_{44.3}Cr_{10}Mo_{12.8}Mn_{11.2}C_{15.8}B_{5.9})_{98.5}Y_{1.5}$ alloys is of 12 mm [11], and $Fe_{41}Co_7Cr_{15}Mo_{14}C_{15}B_6Y_2$ alloy is of 16 mm [12]; such critical thickness values of BAAs are record-breaking at the present time; partial replacement of Fe with other transition metals has a less pronounced effect on the amorphization tendency of alloys: the critical thickness of the $Fe_{64}Mo_{14}C_{15}B_7$ alloy casting increases from 2.5 to 4 mm when alloyed with Mn, Cr, and W ($Fe_{49}Mn_{10}Mo_{14}Cr_4W_1C_{16}B_6$) [13], and a change in the Fe/Co ratio from 9:1 in the $[(Fe_{0.9}Co_{0.1})_{0.75}B_{0.2}Si_{0.05}]_{96}Nb_4$ alloy to 1:1 leads to an increase in the critical thickness of the ingots from 2 to 5 mm [14].

The strength properties of BAAs are an important criterion from the competitiveness point of view. As it known, amorphous metal alloys are characterized by a high level of hardness, strength, and wear resistance [15] due to the disordered nature of their structure, in which there are no defects in the crystal structure. Among the known amorphous metal alloys, the strongest are alloys based on the Fe–B system. Their strength limit exceeds 3500 MPa [15]. The level of mechanical properties of amorphous metal alloys largely depends on changes in their chemical composition. For example, an increase in the B content to 17.5 at.% in the $Fe_{75}Si_{10}B_{15}$ alloy instead of Fe causes an increase in the strength limit to 3900 MPa [16]. Therefore, research is focused on finding such combinations of alloying elements that would simultaneously increase the level of both strength properties and the amorphization tendency of alloys. For Fe-based alloys, the optimal alloying elements are Co and Nb, the addition of which made it possible to create a number of high-strength alloys of the $[(Fe_{1-x}Co_x)_{0.75}B_{0.2}Si_{0.5}]_{96}Nb_4$ composition with a compressive strength limit of 3900–4250 MPa, which are amorphized in the form of rods with a diameter of 2 to 5 mm [17, 18].

An additional potential for increasing the strength properties of BAAs is the formation of crystalline phases in the initial amorphous matrix [16, 19], as was observed, for example, in amorphous alloys based on Al [20]. However, currently for Fe-based alloys, this issue remains almost unexplored.

Thus, based on the analysis of literature data, it can be concluded that the problem of creating a new class of structural materials, *i.e.*, bulk amorphous alloys, is extremely relevant, but far from resolved. Further comprehensive research is needed, aimed at finding new alloy compositions with increased characteristics of glass forming ability,

thermal stability, strength, and plasticity, as well as reduced sensitivity to the purity of components and casting conditions.

Based on the above, the main idea of this study was to establish the influence of chemical composition (alloying with yttrium and aluminium) and production conditions on the amorphization and nanocrystallization tendency of complex alloyed iron-based alloys for further development of high-strength composites.

2. EXPERIMENTAL/THEORETICAL DETAILS

Research and development of methods for rapid melt quenching were carried out on alloys of the $Fe_{40-50.4}(TM, Al)_{29.1-37.5}Y_{0-2}(Si, C, B)_{19.7-22}$ system with different content of transition metals and metalloids, the chemical compositions and markings of which are given in Table 1.

The alloys were synthesized (melted) taking into account the physicochemical approach [21] to predict facilitated glass formation, which is based on the properties of the alloy components and the features of their interaction, reflected in the phase diagrams. In particular, the formation of glasses is facilitated by the presence of deep eutectics on binary (Fe–B, Fe–P) and ternary (Fe–B–Si, Fe–P–C) phase diagrams, a significant (not less than 15%) difference in the atomic diameters of the components (transition metals and metalloids), a large difference in their valence [7, 22, 23], as well as the presence in each alloy of significantly more than three components with large negative enthalpies of mixing (ΔH^{mix}). In general, variations in the composition of alloyed alloys were carried out to increase their ability to amorphized and processability during casting (quenching, including ultrafast) on air.

When obtaining bulk amorphized ingots (plates and rods) of new alloys, made by refining from the initial industrial alloys and raw materials, it was shown that the method of casting the melt under excess

TABLE 1. Marking and chemical composition of the studied alloys.

No.	Alloy mark	Chemical composition, at.%	Total metalloid content, at.%
1	HBRM-4	$Fe_{60.6}Cr_{13.8}Mn_{0.3}Mo_{1.9}Nb_2Al_{0.2}Cu_{0.5}B_{16.2}C_2Si_{2.5}$	20.7
2	HBRM-4-1	$Fe_{58.5}Cr_{14.1}Mn_{0.3}W_{1.9}Mo_3Nb_{0.9}Al_{0.1}Cu_{0.5}B_{17.1}C_2Si_{1.6}$	20.7
3	HBCY-1	$Fe_{49.7}Co_{4.5}Cr_{14.7}Mo_{9.3}B_{3.6}C_{13.5}Si_{4.6}Al_{0.1}$	21.7
4	HBCY-1-1	$Fe_{40}Co_{5.3}Cr_{16.6}W_{3.9}Mo_{10.5}Mn_{0.2}B_4C_{14.9}Si_{1.7}Al_1Y_{1.9}$	20.6
5	HBCY-2	$Fe_{50.4}Co_{4.5}Cr_{14.8}Mo_{9.3}Mn_{0.4}B_9C_9Si_{2.5}Al_{0.1}$	20.5
6	HBCY-2-1	$Fe_{43.6}Co_{5.4}Cr_{15.9}W_{3.9}Mo_{7.9}Mn_{0.6}B_{9.8}C_{9.8}Si_{0.1}Al_1Y_2$	19.7
7	HBCY-3	$Fe_{42.4}Co_{6.6}Cr_{15.6}Mo_{13.4}B_{5.8}C_{14.6}Si_{1.6}$	22
8	HBCY-3-1	$Fe_{41.6}Co_{7.1}Cr_{15.3}Mo_{12.8}B_{5.9}C_{14.8}Si_{0.6}Al_{0.1}Y_{1.8}$	21.3

TABLE 2. List of studied samples and their cooling rates calculated using empirical equations from works [26–30].

Alloy mark	Ribbon thickness, μm	Evaluated speed, K/s	Bulk samples	Evaluated speed, K/s
HBRM-4	20	5.85×10^6	Plates–3/5 mm	340/208
HBRM-4-1	19	5.92×10^6	Plates–3/5 mm	340/208
HBCY-1	28	2.06×10^6	Plates–2/5 mm	505/340
HBCY-2	25	2.93×10^6	Plates–2/5 mm	505/340
HBCY-3	28	2.06×10^6	–	–
HBCY-1-1	40	6.82×10^5	Rod–3.8 mm	414
HBCY-2-1	30	1.66×10^6	Rod–3.5 mm	448
HBCY-3-1	–	–	Plate–3.6 mm	448

pressure (higher than 0.5 atm.) into a copper mould with a thickness of 2–3 mm in a protective atmosphere of argon or helium makes it possible to obtain them almost completely in an amorphous state for rods with a diameter of 3–3.5 mm, made of complex alloyed alloys HBCY-1-1 and HBCY-2-1 containing yttrium and aluminium.

Thus, the obtained rapidly cooled samples, the list of which is given in Table 1, had the form of ribbons, plates and rods of various thicknesses.

Using the $R(D)$ dependences [24–27] for different ranges of thicknesses, as well as taking into account the difference in the cooling rate of ingots in the form of plates and rods with the same values of thickness and diameter according to the geometric parameters of all the studied strip and bulk samples studied in this work, the cooling rates were calculated, which, together with the list of samples, are given in Table 2.

3. RESULTS AND DISCUSSION

X-ray studies of rapidly cooled ribbons showed that their diffraction patterns had a form typical of amorphous metal alloys (Fig. 1).

Analysis of the angular positions of the scattering maxima, the heights of the first maximum $I(2\theta)$ and the interatomic distances r_1 showed that for the ribbons of all the studied alloys in the initial state the atomic structure is quite similar. The dimensions of the CSR(L) calculated from these data are within 1.11–1.61 nm (Table 3), which is also typical for metallic glasses. This indicates that the technological parameters of the melt-spinning method used in this work provided cooling rates sufficient to suppress completely the crystallization process in the studied melts. The obtained values of L of the initial amorphous ribbons for different groups of alloys do not correlate with the

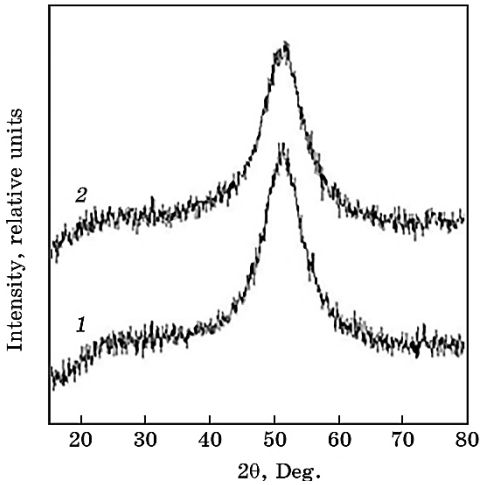


Fig. 1. Diffraction patterns of rapidly cooled ribbons of alloys: HBCY-1 (*1*) and HBCY-2 (*2*).

TABLE 3. Structure parameters of the studied alloys.

Alloy mark	Half-width of halo, deg.	$2\theta_B$, deg.	CSR dimension, L, nm (fraction, X)	Average interatomic distance, nm
HBRM-4	9.28365	52.38	1.23	0.249
HBCY-1	7.05809	51.44	1.61	0.254
HBCY-2	7.62558	51.38	1.49	0.254
HBCY-2-1	10.260	51.123	1.11	0.255

chemical composition and their tendency to amorphization. Thus, the minimum dimensions of the CSR obtained both for ribbons of the yttrium-doped alloy HBCY-2-1 (1.11 nm) with a high and for HBRM-4 (1.23 nm) with a low tendency to amorphization.

From a physical point of view, the most accurate quantitative characteristic of the melt tendency to amorphization (TA) is the minimum (critical) cooling rate, R_c, at which the experimentally detectable fraction of the crystalline phase (usually $\leq 1\%$) does not have time to form in the melt.

However, these measurements are quite complex and to date, experimentally determined R_c for bulk metal alloys (BMAs) based on Fe have been given only in a few works. The data available in the literature on the amorphization of a wide range of metal melts have allowed us to establish empirical correlations between the values of R_c and D_c and a number of thermodynamic criteria characterizing the tendency of melts to glass formation [22]. In particular, qualitative criteria for the

tendency are the relative glass-transition temperature $T_{ra} = T_a/T_l$, the temperature range of the existence of a supercooled melt $T_{ons} - T_a$, and the ratio $y_m = (2T_{ons} - T_a)/T_l$ [31].

By comparing the results of structural studies of a number of obtained alloys, it was found that the use of the γ criterion allows for a qualitative prediction of the critical thickness of ingots. However, the expansion of the range of alloys studied revealed certain discrepancies between the predictions made using this criterion, and further analysis of the TA given in the literature led to the development of a number of new thermodynamic criteria that more correctly characterize the conditions of melt amorphization. Based on this, in this work an extended analysis of the TA of the studied alloys was carried out with a comparison of the effectiveness of several criteria.

As TA criteria, in addition to the γ criterion, two more criteria, $y_m = (2T_{ons} - T_a)/T_l$ and $\omega = T_g/T_{ons} - 2T_g/(T_g + T_l)$, were selected, for which, in Ref. [33], the empirical dependences of the cooling rates [K/s] are given in the form $R_c(\gamma) = 1.333\times10^{21}\exp(-111.138\gamma)$, $R_c(\gamma_m) = 3.947\times10^{14}\exp(-43.802\gamma_m)$ and $R_c(\omega) = 1.833\times10^{-3}\exp(54.639\omega)$.

One of the most important characteristics of amorphous alloys is thermal stability (crystallization onset temperature T_{ons}), since it determines the temperature–time limits in which the physical properties inherent in the amorphous structure are preserved. In addition to the T_{ons} temperature, the value of which was estimated mainly at a heating rate of 10 K/min, the DSC thermograms shown in Fig. 2, contain indirect information regarding the structure of rapidly cooled ribbons and the nature of the transition of amorphous phases to the equilibrium crystalline state. As can be seen from the data presented, the transition of amorphous phases in the studied alloys begins at different temperatures and occurs in two (alloy HBRM-4, Fig. 2, *a*), three (alloys HBCY-1 HBCY-2, HBCY-3 Fig. 2, *b*), four (alloy HBCY-2-1, Fig. 2, *c*) and even in five stages (HBCY-1-1, Fig. 2, *d*).

A common feature of all thermograms of rapidly cooled ribbons of the studied alloys without exception and additional confirmation of the amorphous nature of their structure is the presence of a small endothermic effect immediately before the onset of crystallization, which is a sign of a glass transition, the quantitative characteristic of which is the glass transition temperature, T_g (temperature of the inflection point of the thermogram).

In addition to the temperatures T_g and T_{ons}, the parameter γ also includes T_l, which is an important technological characteristic of the casting process, since it significantly determines the viscosity of the melt.

A common feature of the thermograms of the studied alloys (Fig. 3) is a large endothermic effect, from which melting begins and which, with increasing temperature, is accompanied (except for alloy HBCY-2-1, Fig. 3, *b*) by a number of weaker endothermic reactions.

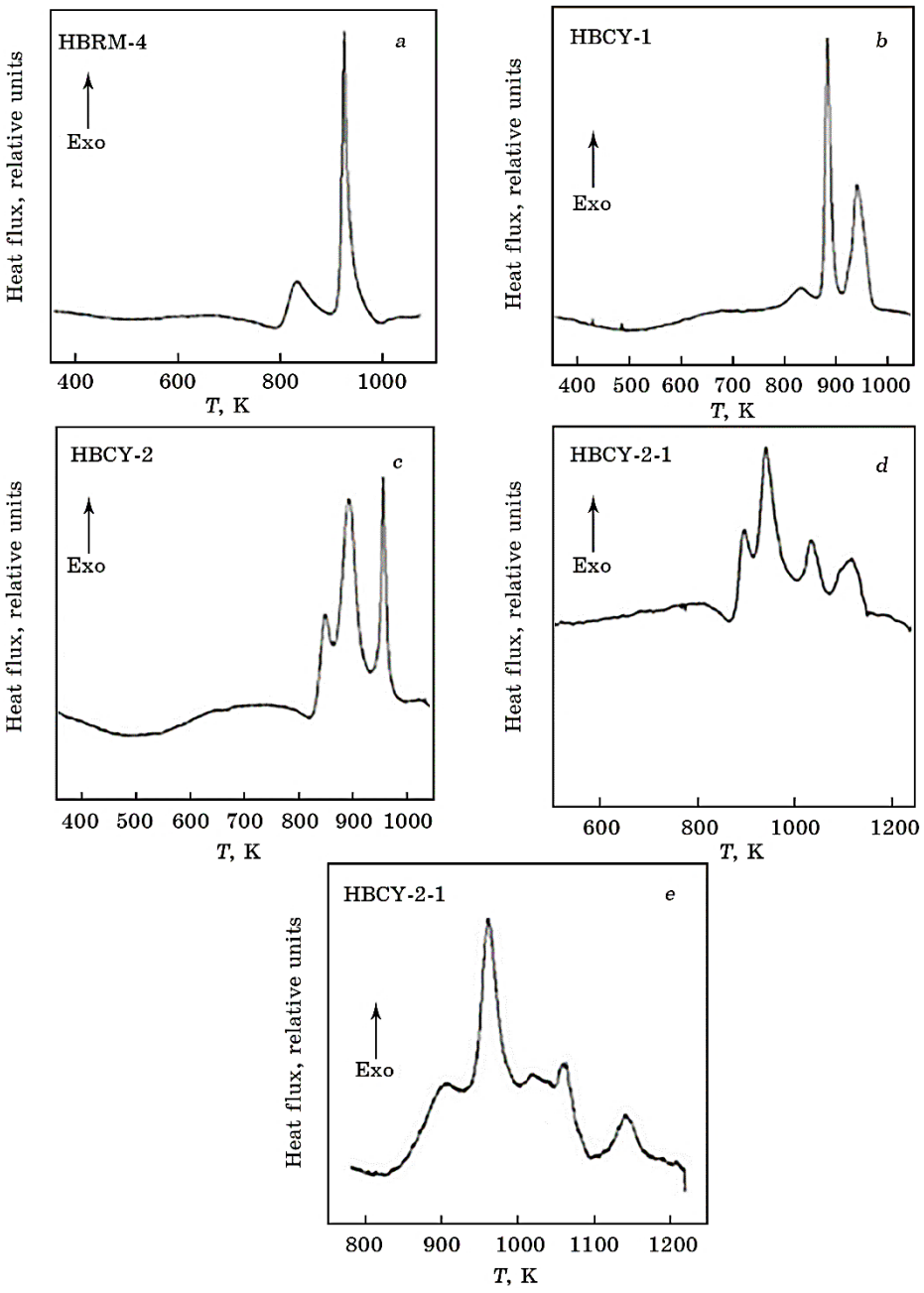


Fig. 2. DSC thermograms of amorphous ribbons of alloys of grades: crystallization in two (alloy HBRM-4) (*a*); three (alloys HBCY-1 (*b*) HBCY-2 (*c*), four (alloy HBCY-2-1) (*d*) and even in five stages (HBCY-1-1) (*e*).

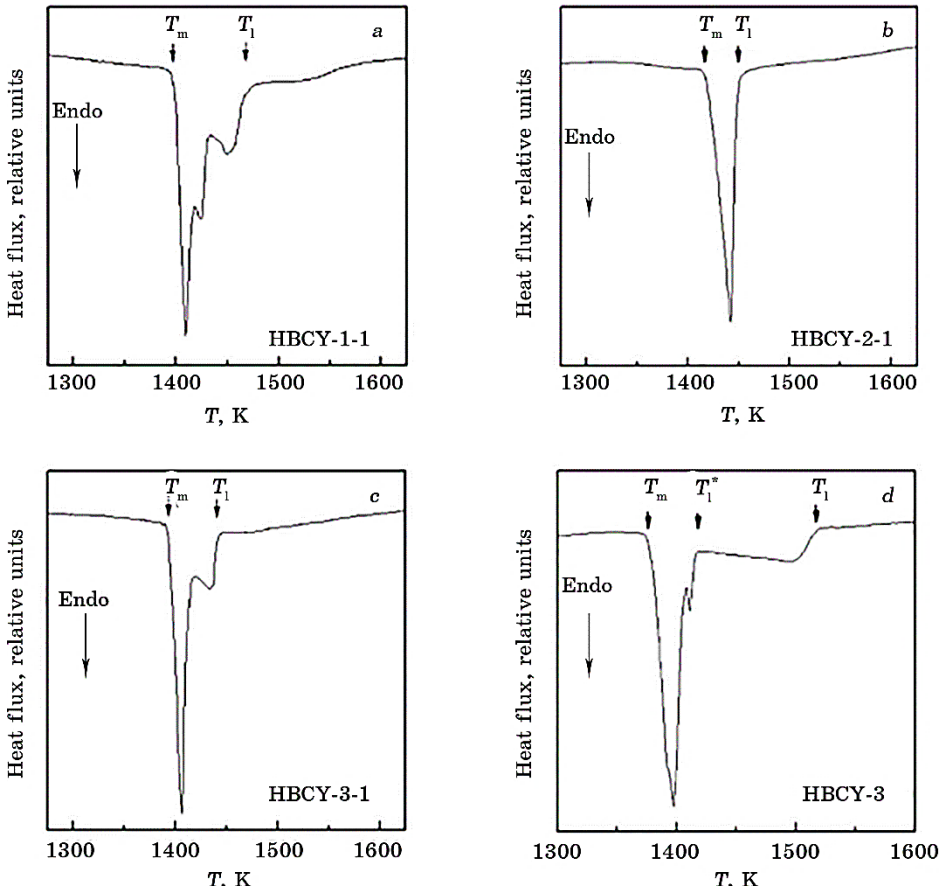


Fig. 3. Melting thermograms measured at a heating rate of 10 K/min., of the initial ingots of the studied alloys: HBCY-1-1 (*a*); HBCY-2-1 (*b*); HBCY-3-1 (c); HBCY-3 (*d*).

Thermal reactions that occur at higher temperatures correspond to the melting of carbide and boride phases, which ends at the liquidus temperature.

The T_L values estimated from these data are given in Table 4 and marked with asterisks, in contrast to the T_L measured using optical pyrometry.

From the above relationships and the data in Table 4, it follows that the differences in the values of the γ and γ_m criteria, which reflect the relative TA of the studied alloys, are due, first of all, to the differences in the liquidus temperatures (Fig. 3), the higher values of which indicate a significant deviation of the alloy composition from the eutectic.

The obtained R_c values for the HBCY-1-1, HBCY-2-1 and HBCY-3-1

TABLE 4. Thermal stability parameters of amorphous phases during continuous heating at a rate of 10 K/min; thermodynamic criteria characterizing the TA of the studied alloys; critical cooling rates and critical thicknesses.

Alloy mark	T_L, K	T_g, K	T_{ons}, K	T_g/T_L	γ	$R_c(\gamma)$, K/s	$D_c(\gamma)$, mm	γ_m	$R_c(\gamma_m)$, K/s	$D_c(\gamma_m)$,mm
HBRM-4	1320	767	798	0.58	0.382	176	2.36	0.637	300	3.417
HBCY-1	1388	762	794	0.549	0.369	813	1.37	0.595	1.89×10^3	0.267
HBCY-2	1438	807	827	0.56	0.368	825	1.34	0.589	2.47×10^3	0.245
HBCY-3	1517	849	875	0.56	0.370	765	1.4	0.594	1.98×10^3	0.263
HBCY-1-1	1467*	866	896	0.59	0.384	150	2.5	0.588	2.62×10^3	0.379
HBCY-2-1	1437*	840	874	0.585	0.384	153	2.5	0.621	614	1.639
HBCY-3-1	1429*	857	879	0.60	0.385	142	2.6	0.631	391.5	1.718

* T_l values measured from DSC thermograms

alloys doped with yttrium and aluminium are noticeably (more than 5 times) higher than for the HBCY-1, HBCY-2 and HBCY-3 alloys.

The estimates of the cooling rates of a 3.5 mm thick bar and a 3.6 mm thick plate, made using the dependence $\lg R = 8.06 - 1.69 \lg D$ [28], give values of 140 and 137 K/s, respectively, which are close to the critical cooling rates R_c for the HBCY-2-1 and HBCY-3-1 alloys (153 and 142 K/s, respectively), calculated using the thermodynamic criterion γ (Table 4). The analysis shows that the thermodynamic criterion γ can be useful for a preliminary assessment of the tendency of alloys to amorphization.

Among the alloys studied that did not contain yttrium and aluminium, both HBCY-1 and HBCY-2 are characterized by a high ability to amorphized and thermal stability of the amorphous state. For a more detailed study of the tendency of these alloys to amorphization, ingots of alloys HBCY-1 and HBCY-2 with a thickness of 2 mm were produced, but their phase compositions were practically identical to those of ingots with a thickness of 5 mm. Figure 4 shows the diffraction patterns obtained from samples cut from the lower parts of ingots with a thickness of 2 mm of alloys HBCY-1 and HBCY-2.

As can be seen from the above data, both samples have a crystal structure consisting of solid solution crystals based on α-Fe, tetragonal phase of the Fe_3B type, $Cr_{23}C_6$ type phase with a complex cubic lattice and Fe_7C_3 phase, the lattice of which belongs to the rhombic system. From the data in Fig. 4, it follows that the redistribution of amorphized elements (increasing the B concentration in the HBCY-2 alloy by 6 at.% due to 5 at.% C and 1 at. % Si) did not lead to significant changes in the phase composition of the ingots, except for a noticeable decrease in the content of Fe_7C_3 carbide.

In addition, a comparison of the diffractograms shown in Fig. 4 shows that the interference lines of α-Fe and carbides and borides

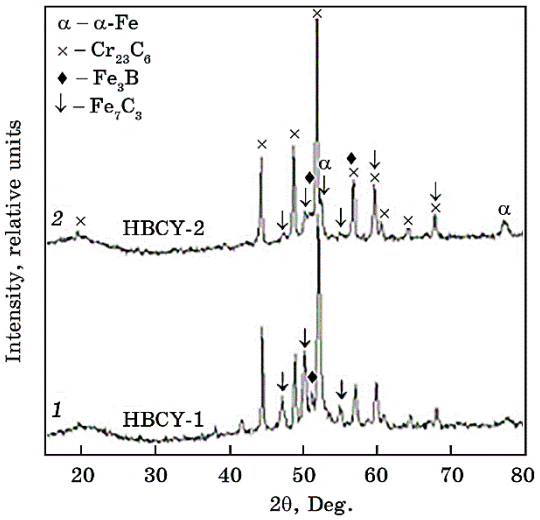


Fig. 4. Diffraction patterns of ingots (bottom) 2 mm thick of alloys HBCY-1 (B-376) (*1*) and HBCY-2 (B-379) (*2*) in the initial state (symbol ♦—lines of the tetragonal phase Fe_3B, α—α-Fe, ×—$Cr_{23}C_6$ phase, ↓—Fe_7C_3-type phase).

formed in the HBCY-1 alloy ingot are noticeably wider than in the HBCY-2 alloy ingot, which indicates a smaller size of nanocrystals in the first of these alloy.

It follows from the diffraction patterns of bulk samples of the HBCY-2-1, HBCY-3-1 and HBRM-4-1 alloy ingots shown in Fig. 5 that, despite the relatively close cooling rates, their structure is noticeably different. If the diffractogram of the HBCY-2-1 alloy ingot (Fig. 5, *a*) contains only a diffuse maximum, which is typical for bulk metallic glasses, then in the diffraction patterns of the remaining samples, reflections from crystalline phases are observed: in the HBCY-3-1 alloy against the background of the maximum from the amorphous phase (Fig. 5, *b*), while in the patterns of the HBRM-4-1 alloy (Fig. 5, *c*) no signs of amorphousness are observed.

Calculations of the relative fraction of the crystalline phase, X, and estimation of the crystal size showed that the structure of the HBCY-3-1 alloy plate contains approximately 10% α-Fe crystals, the average size of which is 12.4 nm, and the bulk density is 10^{23} m^{-3}. Such parameters are typical for the so-called nanocomposite structures that are formed during partial crystallization of amorphous phases upon heating, which was observed, in particular, in amorphous ribbons of the HBRM-4 alloy [33]. The surface layers of the HBCY-3-1 plate contained a small amount of ultrafine (nanosize) carbides and borides identified (marked) on the diffractogram. By gradually grinding the HBCY-3-1 plate, it was possible to establish that all the detected nano-

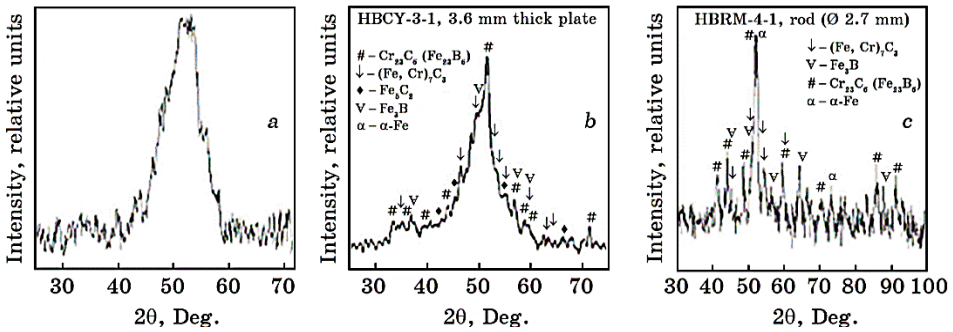


Fig. 5. Diffractograms (CoK_α radiation) of rapidly-cooled bulk alloy samples: *a*—HBCY-2-1 (rod with a diameter of 3.5 mm); *b*—HBCY-3-1 (plate with a thickness of 3.6 mm); *c*—HBRM-4-1 (rod with a diameter of 2.7 mm).

crystals were formed in its surface layer. The presence of an amorphous phase in the inner layers of the ingots and its smaller amount on the surface is at first glance somewhat unexpected, since the surface layers are cooled in direct contact with the walls of the copper casting mould at a higher rate. Nevertheless, a similar effect (formation of crystalline layers on the surface of the castings) was observed in a number of works when obtaining ingots from bulk amorphized alloys based on Fe [34] and Zr [35].

The structure of the HBRM-4-1 alloy ingot consists of α-Fe crystals and phases isomorphic to the borides $Cr_{23}C_6$ ($Fe_{23}B_6$), Fe_3B and $(Fe, Cr)_7C_3$. The estimates showed that the average size of α-Fe crystals and $Fe_{23}B_6$ boride in the structure of the HBRM-4-1 alloy rod is 19.0 and 32.0 nm, respectively.

As a generalization of the results of the structural analysis, we note that in the bulk rapidly cooled samples of complex alloyed alloys of the studied system (Fe, Co)–(Cr, Mo, W, Nb)–Y–(C, B, Si, Al), a number of non-equilibrium structures are observed: purely amorphous (HBCY-2-1), amorphous–crystalline (nanocomposite) (HBCY-1, HBCY-2, HBCY-3-1) and nanocrystalline (HBRM-4, HBRM-4-1), which indicates a significant dependence of the structure of this group of alloys on the cooling conditions. Doping of alloys with Y and Al noticeably increases the tendency of melts to amorphization, which is probably associated both with the optimization of the atomic packing density in the melt due to the addition of large atoms, and with the formation of an oxide protective film on the surface of the solidifying melt.

It is expected that active development of technological processes for casting amorphous Fe-based alloys, close to industrial ones, as well as the use of technical purity components and alloys as starting materials, will reduce the cost of a new class of materials with unique sets of properties to the level of existing tool steels. Further developments in

this direction should be aimed at creating and developing a high-performance technology for the industrial production of highly-alloyed volume-strengthened structural nanostructured materials by controlled crystallization of melts, amorphous ribbons and bulk ingots of developed iron-based alloys; development of a technology for manufacturing electrodes from nanophase powder for applying wear-resistant coatings using existing technologies.

4. CONCLUSIONS

1. The main factor determining the TA of Fe-based alloys is the proximity of the alloy composition to the eutectic one. According to the results of the evaluations, the alloys doped with yttrium and aluminium HBCY-1-1 ($Fe_{40}Co_{5.3}Mn_{0.2}Cr_{16.6}W_{3.9}Mo_{10.5}B_4C_{14.9}Si_{1.7}Al_1Y_{1.9}$), HBCY-2-1 ($Fe_{43.6}Co_{5.4}Mn_{0.6}Cr_{15.9}W_{3.9}Mo_{7.9}B_{9.8}C_{9.8}Si_{0.1}Al_1Y_2$) and HBCY-3-1 ($Fe_{44.85}Co_{7.1}Mn_{0.05}Cr_{15.3}W_{0.01}Mo_{12.8}B_{5.9}C_{14.8}Si_{0.6}Al_{0.1}Y_{1.8}$) have the highest tendency to glass formation, with critical ingot thicknesses of 2.5, 2.5 and 2.6 mm, respectively.
2. The main reason for the presence of nanocrystalline phases in the surface layers of the HBCY-3-1 thin plate and their absence in the inner layers is the intensive heterogeneous nucleation of crystals in the surface layers, caused by their interaction mainly with oxygen residues in the casting atmosphere during a relatively long cooling time. Reducing the influence of heterogeneous nucleation can be achieved by improving the casting conditions (in particular, by choosing the atmosphere), as well as by selecting alloying impurities that reduce the nucleation rate.
3. In the bulk rapidly cooled samples of complex alloyed alloys of the studied system (Fe, Co)–(Cr, Mo, W, Nb)–Y–(C, B, Si, Al), a number of non-equilibrium structures are observed: purely amorphous (HBCY-2-1), amorphous–crystalline (nanocomposite) (HBCY-1, HBCY-2, HBCY-3-1) and nanocrystalline (HBRM-4, HBRM-4-1), which indicates a significant dependence of the structure of this group of alloys on the cooling conditions.

AUTHORS' CONTRIBUTIONS

Y.I.K. wrote the manuscript with input from all authors, performed numerical calculations of x-ray diffractograms. N.M.S. synthesized (melted) initial alloys, carried out rapid quenching of ribbons and bulk samples, reviewed the literature and collected data. Z.I.V. conducted DSC studies of rapidly quenched samples. B.O.I measured the mechanical properties, provided heat treatments. S.O.M. supervised the findings of this work. N.V.K. supervised the project, devised the main con-

ceptual ideas, verified analytical approaches, and provided critical feedback. All authors approved the final version of the manuscript.

REFERENCES

1. J. P. Chu, J. E. Greene, J. S. C. Jang, J. C. Huang, Y.-L. Shen, P. K. Liaw, Y. Yokoyama, A. Inoue, and T.G. Nieh, *Acta Mater.*, **60**, Nos. 6–7: 3226 (2012).
2. M. Chen, L. Zhu, Y. Chen, S. Dai, Q. Liu, N. Xue, W. Li, J. Wang, Y. Huang, K. Yang, and L. Shao, *Materials*, **17**: 1699 (2024).
3. A. Inoue, B. L. Shen, H. Koshiba, H. Kato, and A. R. Yavari, *Acta Mater.*, **52**, No. 6: 1631 (2004).
4. J. Lu, Y. Li, S. Ma, W. Li, F. Bao, Z. Zhu, Q. Zeng, H. Zhang, M. Yao, and W. Zhang, *Acta Metall. Sin. (Engl. Lett.)*, **37**, No. 9: 1 (2024).
5. L. Jiang, X. Fan, Q. Li, X. Li, T. Jiang, and Q. Wei, *Inorganics*, **13**, No. 4: 105 (2025).
6. O. N. Senkov and D. B. Miracle, *Mater. Res. Bull.*, **36**: 2183 (2001).
7. M. Marcus and D. Turnbull, *Mater. Sci. Eng.*, **23**: 211 (1976).
8. T. Egami, *Mater. Sci. Eng. A*, **226–228**: 261 (1997).
9. M. Iqbal, J. I. Akhtar, H. F. Zhang, and Z. Q. Hu, *J. Non-Cryst. Sol.*, **354**: 3284 (2008).
10. Y. H. Zhao, C. Y. Luo, X. K. Xi, D. Q. Zhao, M. X. Pan, and W. H. Wang, *Intermetallics*, **14**: 1107 (2006).
11. Z. Zhang, P. Sharma, and A. Makino, *J. Appl. Phys.*, **112**: 103902 (2012).
12. J. Shen, Q. Chen, J. Sun, H. Fan, and G. Wang, *Appl. Phys. Lett.*, **86**: 151907 (2005).
13. A. Makino, *IEEE Trans. Magn.*, **48**, No. 4: 1331 (2012).
14. A. Makino, T. Kubota, K. Yubuta, and A. Inoue, *J. Appl. Phys.*, **109**: 07A302 (2011).
15. I. V. Zolotukhin, *Fizicheskie Svoistva Amorfnykh Metallicheskikh Materialov* [Physical Properties of Amorphous Metallic Materials] (Moskva: Metallurgiya: 1986) (in Russian).
16. J. Fornell, S. González, E. Rossinyol, S. Suricach, M. D. Bary, D. V. Louzguine-Luzgin, J. H. Perepezko, J. Sort, and A. Inoue, *Acta Mater.*, **58**: 6256 (2010).
17. B. Shen, A. Inoue, and C. Chang, *Appl. Phys. Lett.*, **85**, No. 21: 4911 (2004).
18. A. Inoue, B. L. Shen, and C. T. Chang, *Acta Mater.*, **52**: 4093 (2004).
19. A. V. Sergueeva, N. A. Mara, D. J. Branagan, and A. K. Mukherjee, *Mater. Lett.*, **61**: 1465 (2007).
20. A. Inoue, *Progr. Mater. Sci.*, **43**: 365 (1998).
21. Yu. K. Kovneristy, E. K. Osipov, and E. A. Trofimova, *Fiziko-Khimicheskie Osnovy Sozdaniya Amorfnykh Metallicheskikh Splavov* [Physicochemical Principles of Creating Amorphous Metal Alloys] (Moskva: Nauka: 1983) (in Russian).
22. A. Inoue, *Acta Mater.*, **48**: 279 (2000).
23. S. C. Glade, R. Busch, D. S. Lee, W.L. Johnson, R. K. Wunderlich, and H. J. Fecht, *J. Appl. Phys.*, **87**: 7242 (2000).
24. J. H. Perepezko and K. Hildal, *Phil. Mag.*, **86**, No. 24: 3681 (2006).
25. K. Hildal, N. Sekido, and J. H. Perepezko, *Intermetallics*, **14**: 898 (2006).

26. Zh. Long, H. Wei, Y. Ding, X. Liu, and Z. Liu, *J. Alloys Comp.*, **475**: 207 (2009).
27. A. Inoue and A. Takeuchi, *Mater. Trans.*, **43**, No. 8: 1892 (2002).
28. A. B. Lysenko, G. V. Borisova, and O. L. Kravets, *Fiz. Tekh. Vys. Davl.*, **14**, No. 1: 44 (2007).
29. V. K. Nosenko, A. Yu. Rudenko, T. N. Moiseeva, M. S. Nizameev, A. I. Limanovskii, O. M. Semyrga, and V. I. Tkach, *Metallofiz. Noveishie Tekhnol.*, **37**, No. 12: 1681 (2015).
30. V. I. Tkatch, A. L. Limanovskii, S. N. Denisenko, and S. G. Rassolov, *Mater. Sci. Eng. A*, **323**: 91 (2002).
31. Z. P. Lu and C. T. Liu, *Acta Mater.*, **50**: 3501 (2002).
32. Zh. Long, H. Wei, Y. Ding, X. Liu, and Z. Liu, *J. Alloys Comp.*, **475**: 207 (2009).
33. A. Yu. Rudenko, V. K. Nosenko, V. I. Tkach, and M. S. Nizameev, *Metallofiz. Noveishie Tekhnol.*, **34**, No. 6: 771 (2012).
34. C. Y. Luo, Y. H. Zhao, X. K. Xi, G. Wang, D. Q. Zhao, M. X. Pan, W. H. Wang, and S. Z. Kou, *J. Non-Cryst. Sol.*, **352**: 185 (2006).
35. G. E. Abrosimova, A. S. Aronin, Yu. V. Kir'yanov, D. V. Matveev, V. V. Molokanov, and I. I. Zver'kova, *J. Non-Cryst. Sol.*, **288**: 121 (2001).

Metallophysics and Advanced Technologies
Металофіз. новітні технол.
Metallofiz. Noveishie Tekhnol.
2026, vol. 48, No. 8, pp. 807–826
https://doi.org/10.15407/mfint.48.08.0807
Reprints available directly from the publisher

© 2026 G. V. Kurdyumov Institute for Metal Physics,
National Academy of Sciences of Ukraine
Published by license under
the G. V. Kurdyumov Institute for Metal Physics–
N.A.S. of Ukraine Publishers imprint.
Printed in Ukraine.

PACS numbers: 68.47.Gh, 81.05.Ni, 81.40.-z, 81.65.Kn, 81.65.Lp, 81.65.Rv, 82.45.Bb

Patterns of the Relationship between the Limit Potentials of the 06KhN28MDT Alloy and Its Indicators in a Gap with a Chloride-Containing Medium Present in the Operation of Heat Exchangers

A. V. Dzhus[*], O. E. Narivskyi[**], S. O. Subbotin[*], G. V. Snizhnyi[*], and T. V. Pulina[*]

[*]*National University 'Zaporizhzhia Polytechnic',*
64 Universytetska Str.,
UA-69011 Zaporizhzhia, Ukraine
[**]*Ukrspetsmash LLC,*
7 Haharina Str., Zaporizka Reg.,
UA-71100 Berdiansk, Ukraine

The article develops mathematical models based on regression trees to study the relationship between the repassivation potential (E_{rep}), free corrosion potential (E_{cor}) of the 06KhN28MDT alloy in a chloride-containing media, its chemical composition, and structure. As established, E_{rep} shifts in the positive side with an increase in Cr and Cu contents. Specifically, E_{rep} shifts by 192.4 mV within the Cr content range of 23.12–23.68 wt.% and reaches 0.5 V with Cu content up to 2.73 wt.% and Cr content up to 23.125 wt.%. A reduction in the mean austenite grain diameter from 16.5 to 11 μm shifts E_{rep} to the most negative side of 0.287 V. Additionally, when the Cu content exceeds 2.73 wt.% and Cr exceeds 23.125 wt.%, E_{rep} shifts further by 0.265 and 0.23 V, respectively. The hypothesis suggests that Cr forms dense oxide films, while Cu provides anodic protection to grain boundaries. The E_{cor} potential of the alloy shifts to the most negative side of –0.4557 V as the Cr content decreases from 22.215 down to 21.84 wt.% and Mn decreases from 0.455 down

Corresponding author: Anna Dzhus
E-mail: dzhus_anna@zp.edu.ua

Citation: A. V. Dzhus, O. E. Narivskyi, S. O. Subbotin, G. V. Snizhnyi, and T. V. Pulina, Patterns of the Relationship between the Limit Potentials of the 06KhN28MDT Alloy and Its Indicators in a Gap with a Chloride-Containing Medium Present in the Operation of Heat Exchangers, *Metallofiz. Noveishie Tekhnol.*, **48**, No. 8: 807–826 (2026), DOI: 10.15407/mfint.48.08.0807

© Publisher PH 'Akademperiodyka' of the NAS of Ukraine, 2026. This is an open access article under the CC BY-ND license (https://creativecommons.org/licenses/by-nd/4.0)

to 0.31 wt.%. With carbon content below 0.053 wt.%, E_{cor} is of –0.41 V, while the precipitation of Cr and Mo carbides from the austenite solid solution causes only a slight shift in the negative direction. The most positive E_{cor} value (–0.38 V) is achieved, when the mean austenite grain diameter exceeds 15.5 μm. An increase in Ni content from 27.675 up to 27.730 wt.% shifts E_{cor} in the negative side by 0.17 V, indicating that Ni has a stronger effect on E_{cor} compared to Cr and Cu. As found, a decrease in Cr, Mn, and Ni contents in the alloy accelerates general corrosion, but slows down crevice corrosion due to the redistribution of anodic currents. This trend is caused by the redistribution of anodic currents among a large number of dissolution centres of metal atoms in the alloy composition. The constructed mathematical models are recommended for enterprises, which produce plate-like heat exchangers from this alloy to use to select optimal melts in terms of chemical composition and structure, which will ensure maximum resistance of heat exchanger plates to crevice corrosion in the recycled waters of enterprises.

Key words: 06KhN28MDT alloy, crevice corrosion, resistance to crevice corrosion, repassivation potential, free corrosion potential.

У статті розроблено математичні моделі на основі дерев реґресій для дослідження взаємозв'язку між потенціялами репасивації (E_{rep}), вільної корозії (E_{cor}) стопу 06ХН28МДТ у хлоридовмісному середовищі, його хемічним складом і структурою. Встановлено, що E_{rep} зсувається в позитивний бік зі збільшенням вмісту Cr і Cu. Зокрема, E_{rep} зміщується на 192,4 мВ у діяпазоні вмісту Cr від 23,12 до 23,68 мас.% і сягає 0,5 В за наявности Cu до 2,73 мас.% і Cr до 23,125 мас.%. Зменшення середнього діяметра зерна аустеніту від 16,5 до 11 мкм зміщує E_{rep} до найвід'ємнішого значення у 0,287 В. Водночас, за вмісту Cu > 2,73 мас.% і Cr > 23,125 мас.% E_{rep} зсувається ще на 0,265 В і 0,23 В відповідно. Гіпотеза пояснює, що Cr формує щільні оксидні плівки, а Cu анодно захищає межі зерен. Потенціял E_{cor} стопу зсувається до максимально від'ємного значення у –0,4557 В зі зменшенням вмісту Cr від 22,215 до 21,84 мас.% і Mn від 0,455 до 0,31 мас.%. За вмісту C менше 0,053 мас.% E_{cor} становить –0,41 В, а випадіння карбідів Cr і Mo лише незначно зміщує його у від'ємний бік. Найпозитивніше значення E_{cor} (–0,38 В) досягається за середнього діяметра зерна аустеніту понад 15,5 мкм. Збільшення вмісту Ni від 27,675 до 27,730 мас.% зсуває E_{cor} у від'ємний бік на 0,17 В, що свідчить про сильніший вплив Ni на E_{cor} порівняно з Cr і Cu. З'ясовано, що зменшення вмісту Cr, Mn та Ni у стопі пришвидшує загальну, але уповільнює щілинну корозію через перерозподіл анодних струмів. Таку тенденцію зумовлено перерозподілом анодних струмів між великою кількістю центрів розчинення атомів металів у складі стопу. Побудовані математичні моделі рекомендовано підприємствам, які виробляють пластинчасті теплообмінники з цього стопу, застосовувати для вибору оптимальних топлень за хемічним складом і структурою, які забезпечать максимальний опір пластин теплообмінників щілинній корозії в оборотніх водах підприємств.

Ключові слова: стоп 06ХН28МДТ, щілинна корозія, опір щілинній корозії, потенціял репасивації, потенціял вільної корозії.

(Received 13 January, 2025; in final version, 15 May, 2026)

1. INTRODUCTION

The design features of plate-like heat exchangers can contribute to crevice corrosion during their operation in the circulating systems of enterprises [1, 2]. In particular, work [2] recorded localized corrosion damage at the tops of corrugations between adjacent heat transfer plates, on their surfaces under the recycled water sediment, and at the ends of the groove for the rubber gasket. It is known [3, 4] that, under such conditions, chloride-containing media can be acidified due to the hydrolysis of corrosion products, accumulate chlorides, and locally increase the temperature. The authors of studies [5–9] found that the parameters of model-recycled waters, characterized by pH and chloride concentration, have the most intense effect on the pitting resistance of AISI 304 [5, 6], AISI 321 [7, 8] steels, and 06KhN28MDT alloy [9]. The effect of their structural heterogeneity on critical pitting temperatures is half that of the media parameters, but higher than the chromium content. Taking into account such dependences, some scientists [10–14] propose protective coatings on the surface of heat transfer elements of heat exchangers to prevent their pitting and crevice corrosion in the recycled waters of enterprises. In particular, coatings based on composite [10, 11], polymeric [12, 13], and nanostructured films [14] are considered promising today, as they reliably prevent the contact of passivated steels and alloys with chloride-containing media. This approach provides reliable protection of steels and alloys against local corrosion, but it is quite expensive and time-consuming. At the same time, papers [5–9] used a different approach to prevent such problems; in particular, they developed mathematical models that establish the relationship between the CPT of steels and alloys and their chemical composition, structure components, and parameters of model-recycled waters. This approach does not require additional resources, and therefore is promising. Therefore, the article establishes the dependence between the limit potentials of the 06KhN28MDT alloy and its indicators in a gap with a chloride-containing medium present during the operation of plate-like heat exchangers.

2. EXPERIMENTAL/THEORETICAL DETAILS

In this paper, five industrial melts of 06KhN28MDT alloy (analogous to AISI 904L steel), which is used for the production of heat exchangers, have been studied.

The chemical composition of the alloy has been previously determined [15] by chemical analytical and XRD methods using the SRM-25 installation. It is given in Table 1. In this Table: x_1—C, carbon content in steel, wt.% (≤ 0.06); x_2—Mn, manganese content in steel, wt.%

TABLE 1. A real sample of dependences based on the results of the sample studies.

Nos. alloy melts	x_1	x_2	x_3	x_4	x_5	x_6	x_7	x_8	x_9	x_{10}	x_{11}	E_{cor}, V	E_{rep}, V	ΔE, V
1	0.05	0.32	0.6	24.31	27.39	0.79	2.9	2.75	0.1711	0.0091	11	–0.4	0.8	1.2
2	0.067	0.46	0.57	22.68	27.65	0.59	2.78	2.68	0.1427	0.0036	24	–0.43	0.5	0.93
3	0.068	0.54	0.55	21.84	27.45	0.55	2.55	2.6	0.1918	0.0043	29	–0.42	0.22	0.64
4	0.048	0.57	0.62	22.67	27.73	0.67	2.56	2.53	0.1692	0.0043	31	–0.4	0.55	0.95
5	0.05	0.31	0.57	23.46	27.51	0.89	2.51	2.78	0.0931	0.0036	15	–0.38	0.6	0.98
min	0.048	0.31	0.55	21.84	27.39	0.55	2.51	2.53	0.0931	0.0036	11	–0.5	0.1	
max	0.068	0.57	0.62	24.31	27.73	0.89	2.9	2.78	0.1918	0,0091	29	–0.1	0.7	
multiplicity	0.001	0.01	0.01	0.01	0.01	0.01	0.01	0.01	0.0001	0,0001	1	0.01	0.01	0.01

(< 0.8); x_3—Si, silicon content in steel, wt.% (< 0.8); x_4—Cr, chromium content in steel, wt.% (22.00–25.00); x_5—Ni, nickel content in steel, wt.% (26.00–29.00); x_6—Ti, titanium content in steel, wt.% (0.5–0.9); x_7—Mo, molybdenum content in steel, wt.% (2.5–3.0); x_8—Cu, copper content in steel, wt.% (2.5–3.5); x_9—volume of titanium carbonitrides, vol.% (0.0931–0.1918); x_{10}—volume of titanium sulphides, vol.% (0.0036–0.0091); x_{11}—d_g, mean austenite grain diameter in the alloy, μm (11–31); E_{cor} is the free corrosion potential, V; E_{rep} is the repassivation potential, V; ΔE_{rep} is the criterion, V.

The variances of deviation of the alloy components are: carbon ±0.002, silicon ±0.004, manganese ±0.01, chromium ±0.02, nickel ±0.03, molybdenum ±0.02, copper ±0.02, titanium ±0.02, phosphorus ±0.02, sulphur ±0.003 [wt.%]. The components of the structural heterogeneity of the 06HN28MDT alloy have been determined in [15].

The resistance of 06KhN28MDT alloy to crevice corrosion was evaluated by the ultimate repassivation potentials E_{rep}, free corrosion E_{cor}, and ΔE_{rep} by the criterion determined by the formula

$$\Delta E_{rep} = E_{rep} - E_{cor}. \quad (1)$$

The alloy was considered to be resistant to crevice corrosion, if $\Delta E > 0.05$ V [16]. The real values of the limit potentials E_{rep}, E_{cor}, and ΔE of the 06KhN28MDT alloy criterion are given in Table 1. The generated variable factors (x_1, ..., x_{11}) and output factors E_{cor}, E_{rep}, and ΔE_{rep} are shown in Table 2.

Regression trees were used as the basis for constructing mathematical models (Tables 3, 4), which are the most popular method for solving many practical problems [17], since they automatically select informative features (the most important x_i of the model).

The quality of the mathematical models of Tables 3, 4 was evaluated using the sum of squares of instantaneous mistakes [17]:

TABLE 2. Generated samples.

S	x_1	x_2	x_3	x_4	x_5	x_6	x_7	x_8	x_9	x_{10}	x_{11}	E_{cor}, V	E_{rep}, V
1	0.05	0.32	0.60	24.31	27.39	0.79	2.90	2.75	0.1711	0.0091	11.00	–0.40	0.80
2	0.067	0.46	0.57	22.68	27.65	0.59	2.78	2.68	0.1427	0.0036	24.00	–0.43	0.50
3	0.068	0.54	0.55	21.84	27.45	0.55	2.55	2.60	0.1918	0.0043	29.00	–0.42	0.22
4	0.048	0.57	0.62	22.67	27.73	0.67	2.56	2.53	0.1692	0.0043	31.00	–0.40	0.55
5	0.05	0.31	0.57	23.46	27.51	0.89	2.51	2.78	0.0931	0.0036	15.00	–0.38	0.60
6	0.057	0.31	0.59	23.33	27.61	0.67	2.70	2.71	0.1807	0.0039	13.00	–0.41	0.33
7	0.061	0.51	0.62	22.15	27.51	0.78	2.66	2.75	0.1219	0.0043	23.00	–0.43	0.32
8	0.052	0.54	0.60	22.88	27.39	0.60	2.62	2.75	0.1524	0.0054	16.00	–0.41	0.36
9	0.057	0.54	0.61	23.09	27.60	0.79	2.52	2.67	0.0977	0.0059	19.00	–0.39	0.54
10	0.048	0.33	0.61	23.16	27.51	0.67	2.57	2.57	0.1277	0.0054	25.00	–0.38	0.73
40	0.055	0.43	0.58	23.52	27.58	0.77	2.70	2.63	0.1402	0.0040	18.00	–0.40	0.65
41	0.067	0.51	0.60	23.73	27.65	0.84	2.81	2.77	0.1041	0.0058	20.00	–0.40	0.87
42	0.053	0.32	0.60	23.63	27.44	0.60	2.78	2.63	0.1006	0.0059	14.00	–0.40	0.73
43	0.064	0.55	0.55	23.45	27.62	0.64	2.84	2.60	0.0958	0.0041	25.00	–0.41	0.95
44	0.062	0.51	0.59	23.88	27.40	0.69	2.61	2.65	0.1800	0.0051	22.00	–0.37	0.85
45	0.049	0.35	0.61	22.32	27.67	0.66	2.77	2.54	0.1656	0.0063	28.00	–0.44	0.42
46	0.054	0.41	0.56	24.22	27.54	0.5800	2.79	2.66	0.1255	0.0077	26.00	–0.37	1.22
47	0.053	0.45	0.58	22.23	27.59	0.87	2.55	2.75	0.1474	0.0060	14.00	–0.43	0.03
48	0.053	0.43	0.59	22.72	27.65	0.85	2.80	2.63	0.1527	0.0071	13.00	–0.45	0.18
49	0.058	0.39	0.59	24.17	27.54	0.56	2.87	2.76	0.1285	0.0050	25.00	–0.39	1.19
50	0.058	0.46	0.60	22.07	27.69	0.87	2.55	2.74	0.1829	0.0037	20.00	–0.43	–0.02

$$E = \sum_{S=1}^{S} (y^S - y^{S*})^2 . \quad (2)$$

The sum of the squared mistakes for the potential: $E_{cor} = 0.0027$ V, $E_{rep} = 0.2894$ V; the standard deviation: $E_{cor} = 0.0001$ V, $E_{rep} = 0.0058$ V.

3. RESULTS AND DISCUSSION

According to the results of the analysis of the constructed mathematical model (Table 2), which is based on the defined regression trees (Fig. 1), the following trend was established, in particular, if the parameter of the 06KhN28MDT alloy x_4(Cr) < 23.055 wt.%, then, we move to node 2, where, if x_2(Mn) < 0.455 wt.%, then we move to node 4, then, provided that x_4(Cr) < 22.215 wt.%, the free corrosion potential of the alloy E_{cor} is of –0.455714 V (node 3). It turns out that the most negative value of the potential E_{cor} of the alloy in the gap correlates with a low content of chromium and manganese within the standard for its production (Table 1). It should be noted that under such conditions, the resistance of the studied alloy to crevice corrosion in the model chlo-

TABLE 3. Mathematical model that establishes the relationship between the corrosion potential E_{cor} of 06KhN28MDT alloy and its chemical composition and structure components, based on regression trees.

Item No.	Dependences
1	if $x_4 < 23.055$ then node 2 else; if $x_4 >= 23.055$ then node 3 else –0.4126
2	if $x_4 < 23.055$ then node 2 else; if $x_4 >= 23.055$ then node 3 else –0.4126
3	if $x_5 < 27.575$ then node 6 else; if $x_5 >= 27.575$ then node 7 else –0.38875
4	if $x_4 < 22.215$ then node 8 else; if $x_4 >= 22.215$ then node 9 else –0.444
5	if $x_1 < 0.053$ then node 10 else; if $x_1 >= 0.053$ then node 11 else –0.421818
6	if $x_{11} < 14.5$ then node 12 else; if $x_{11} >= 14.5$ then node 13 else –0.379286
7	if $x_5 < 27.675$ then node 14 else; if $x_5 >= 27.675$ then node 15 else –0.402
8	fit = –0.455714
9	fit = –0.43375
10	fit = –0.41
11	fit = –0.42625
12	fit = –0.4
13	if $x_8 < 2.755$ then node 16 else; if $x_8 >= 2.755$ then node 17 else –0.375833
14	fit = –0.3975
15	fit = –0.42
16	fit = –0.37125
17	fit = –0.385

ride-containing media increases as its ΔE criterion, which was determined by Eq. (1), increases [16]. This is due to the fact that the lower the potential E_{cor} of the alloy, the easier it is to give up electrons, contributing to the ionization of metals in its composition at the anode sites. Under such conditions, the density of anode currents in them decreases due to their redistribution among a larger number of anode sites. This is consistent with the information presented in Refs. [18, 19]. This tendency 'slows down' the transformation of metastable local corrosion damage into stable damage.

A decrease in the content of manganese, as a surface-active chemical element, most likely contributes to the depletion of the oxide film on the surface of the 06HN28MDT alloy by chromium, which leads to a shift its potential E_{cor} to the negative side. Our hypothesis is based on the information that Mn and Cu contribute to the formation of a passive film enriched in chromium [20].

From the analysis of the mathematical model (Table 3), it follows that, if the chromium content in the alloy under study $x_4(\mathrm{Cr}) \geq 23.055$ V, then, its potential E_{cor} shifts to a positive side to –0.4126 V (item 1, Table 3). However, provided that $x_5(\mathrm{Ni}) < 27.57$ wt.% (item 3, Table 3), and $x_{11}[d_g] < 14.5$ μm (item 6, Table 3), its potential E_{cor} is of –0.4 V (item 12, Table 3). These dependences between the potential E_{cor} of

TABLE 4. Mathematical model that establishes the relationship between the repassivation potential E_{rep} of 06KhN28MDT alloy and its chemical composition and structure components based on regression trees.

Item No.	Dependences
1	if $x_4 < 23.43$ then node 2 else; if $x_4 >= 23.43$ then node 3 else 0.5538
2	if $x_4 < 22.315$ then node 4 else; if $x_4 >= 22.315$ then node 5 else 0.336774
3	if $x_{11} < 22.5$ then node 6 else; if $x_{11} >= 22.5$ then node 7 else 0.907895
4	if $x_{11} < 22$ then node 8 else; if $x_{11} >= 22$ then node 9 else 0.150769
5	if $x_{11} < 16.5$ then node 10 else; if $x_{11} >= 16.5$ then node 11 else 0.471111
6	if $x_4 < 23.68$ then node 12 else; if $x_4 >= 23.68$ then node 13 else 0.786364
7	fit = 1.075
8	fit = 0.07875
9	fit = 0.266
10	fit = 0.286667
11	if $x_8 < 2.73$ then node 14 else; if $x_8 >= 2.73$ then node 15 else 0.563333
12	fit = 0.6725
13	fit = 0.851429
14	if $x_4 < 23.125$ then node 16 else; if $x_4 >= 23.125$ then node 17 else 0.523
15	fit = 0.765
16	fit = 0.5
17	fit = 0.73

06KhN28MDT alloy in a gap with a model chloride-containing medium and the content of nickel in it and the size of the austenite grain show that the smaller they are, the more positive it is. Under such conditions, the ionization of metals in its composition that are in contact with the medium becomes more difficult. At the same time, it should be noted that the finer the grain of the alloy austenite, the lower the degree of incoherence between adjacent crystal-lattice atoms, and the higher the resistance of metal atoms located at the grain boundaries to ionization when in contact with a chloride-containing medium. This helps to increase the potential E_{cor} of the alloy and reduce its resistance to crevice corrosion in a chloride-containing media.

The influence of nickel on the resistance of 06HN28MDT alloy to crevice corrosion in a chloride-containing media cannot be assessed only by the above dependences (E_{cor}–Ni content). After all, in Ref. [21], it was found that steel consisting of 21 wt.% Cr, 6 wt.% Ni, and 2 wt.% Mo has high pitting resistance in chloride-containing media because of its pitting potential E_{pit} is of 0.56 V. However, in 0Kh21N5T steel, it is equal to 0.428 V, which is due to the absence of molybdenum and a decrease in nickel content by 0.7 wt.%.

A further decrease in nickel content to 3.2 wt.% accelerates the shift of the potential to the negative side. In addition, the role of nickel in

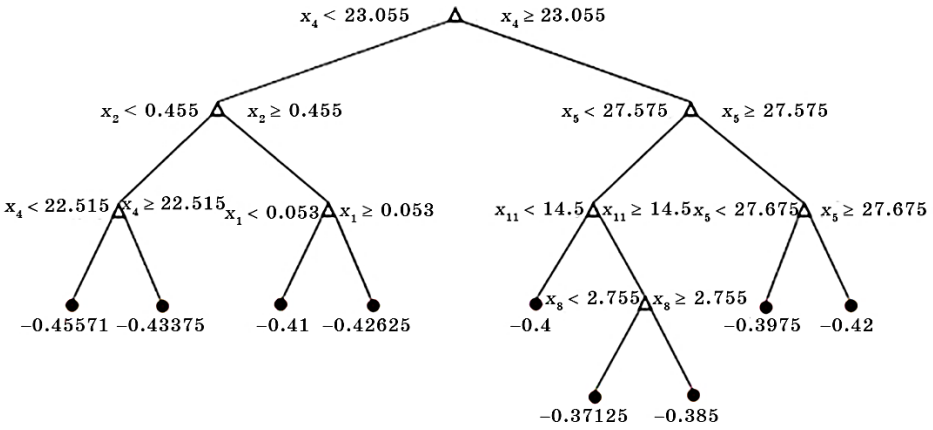


Fig. 1. Regression tree showing the relationship between the free corrosion potential E_{cor} of 06KhN28MDT alloy in a gap with a chloride-containing solution and its chemical composition and structural components.

the pitting resistance of stainless steels is evidenced by the higher value of the potential E_{pit} (0.23V) of Kh14Mn14N3T steel at its content of 3.1 wt.%, than Kh17AMn14 with higher chromium content. At the same time, it should be noted that the pitting resistance of the stainless steel 12Kh18N10T in chloride-containing media is much higher than that of these steels. This information shows that a decrease in the chromium content in steels reduces their pitting resistance more intensively than that of nickel, even in the presence of a two-phase structure [21, 22].

It should be noted that the mechanisms of pitting and crevice corrosion of stainless steels and alloys in chloride-containing media are very similar, so, the effect of nickel on their limit potentials is likely to be the same. Obviously, it is not associated with compensating for the negative effect of MnS inclusions on the pitting resistance of the alloy, as is believed in Refs. [23, 24] for the chromium-nickel-molybdenum steel 13Kh17N11M3, since only carbonitrides (Fig. 2) and titanium sulphides (Fig. 3), which are even insoluble in solutions of many acids, have been recorded in the 06KhN28MDT alloy [25]. However, the potential E_{cor} of the 06KhN28MDT alloy depends on the chromium content in the alloy and its grain size.

After all, from the analysis of items 1, 3, 6, 12 of the mathematical model (Table 3), it was found that the potential E_{cor} of the 06KhN28MDT alloy shifts by 0.0126 V in the positive direction if the chromium content in it is more than 23.055 wt.%, nickel less than 27.575 wt.%, provided that the mean austenite grain diameter is less than 14.5 μm. It was found that the potential E_{cor} of the studied alloy shifts to the negative side to –0.434615 V with an increase in the man-

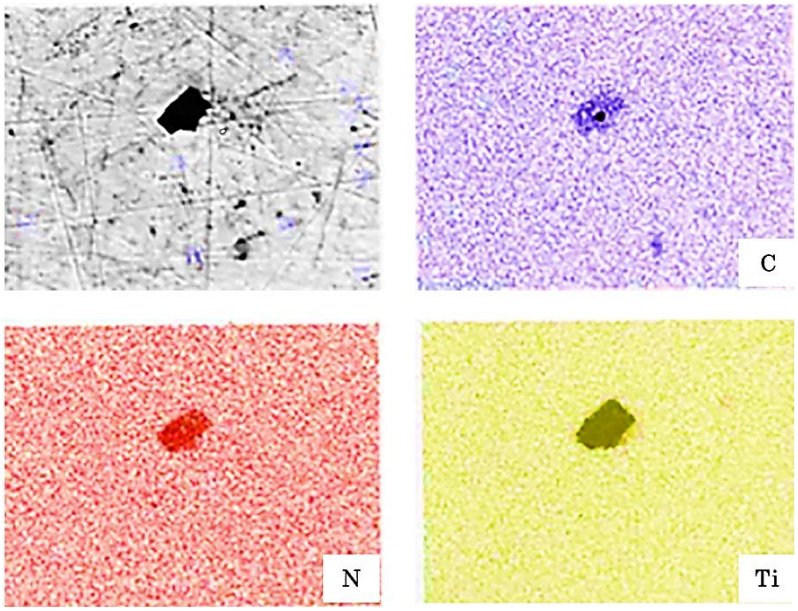


Fig. 2. Titanium carbonitrides in alloy 06HN28MDT (×550).

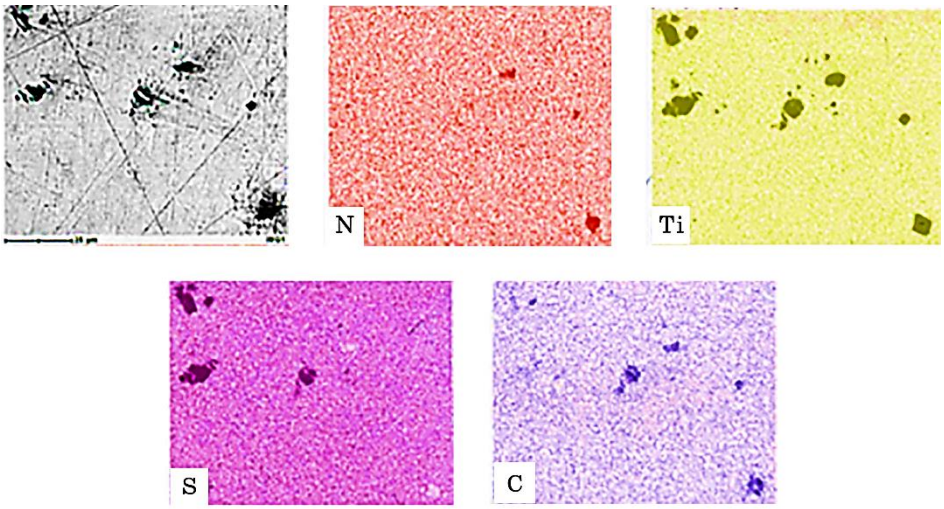


Fig. 3. Titanium sulphides and carbonitrides in 06HN28MDT alloy (×550).

ganese content from 0.455 up to 0.57 wt.% (item 2 of Table 3).

However, under the same conditions, when the carbon content (x_1)) less than 0.053 wt.%, its potential E_{cor} is of –0.41 V (items 5, 10 of Table 3). Thus, it can be noted that the potential E_{cor} of the alloy under

study shifts to the positive side by 0.0246 V (see items 1, 10 of Table 3), which reduces the rate of general corrosion but increases the probability of crevice corrosion. The mechanisms of this process were mentioned above. In addition, at such carbon content in the alloy, according to Ref. [25], it is almost completely dissolved in the austenite solid solution. Under such conditions, the length of the boundaries of inclusions with the austenitic matrix decreases due to a decrease in the volume of the carbide phase in the vicinity of titanium nitrides and a decrease in the total length of the boundaries of austenite grains and inclusions with its solid solution.

From the analysis of the mathematical model (item 3 of Table 3), it was found that if the nickel content (x_5) in the alloy is greater than or equal to 27.575 wt.%, then, its potential E_{cor} is of –0.38878 V. Consequently, under such conditions, it has practically the most positive value, which contributes to a decrease in ΔE criterion of the alloy and its resistance to crevice corrosion. This is due to the fact that the critical passivation potential of Ni (+0.15 V) is much more negative than that of Fe (+0.46 V) [26]. However, when the nickel content in the alloy under study is less than 27.675 wt.% (item 7 of Table 3), its potential E_{cor} is of –0.3975 V (item 14 of Table 3). These dependences indicate that the corrosion potential E_{cor} of the 06KhN28MDT alloy is of about –0.39 V, when the nickel content in it varies in the range from 27.575 up to 27.675 wt.%. It has been recorded that chromium contributes to the shift of the potential E_{cor} of the studied alloy in the negative direction to –0.444 V (item 4 of Table 3). However, according to the information (items 4, 9 of Table 3), under some conditions it can have a slightly more positive value ($E_{cor} = -0.43375$ V). Thus, according to the results of data analysis (items 4, 9 of Table 3), it turns out that the corrosion potential E_{cor} of 06KhN28MDT alloy has the most negative value when the chromium content in it is higher than 22.215 wt.%. This is due to the fact that under such conditions, according to Gerasimov [27], the surface of the alloy is covered with a monolayer of chromium atoms. It is known [26] that the critical passivation potential of chromium is even more negative (–0.35 V) than that of molybdenum (–0.20 V) and titanium (–0.25 V). This tendency contributes to the fact that the ΔE criterion of the 06KhN28MDT alloy increases, since its corrosion potential E_{cor} shifts significantly to the negative side when it contains more than 22.215 wt.% chromium. The mechanisms of increasing the resistance of the studied alloy to crevice corrosion in a chloride-containing media under the condition of a negative shift in the potential E_{cor} were mentioned above.

It was mentioned above (item 2 of Table 3) that the potential E_{cor} of the 06KhN28MDT alloy was –0.434615 V, if the manganese content in it was less than 0.455 wt.%, or –0.41 V, provided that $x_1(\mathrm{C}) < 0.053$ wt.% (items 5, 10 of Table 3). However, with an increase in the carbon

content in the alloy above 0.053 wt.%, a shift of its corrosion potential E_{cor} in the negative direction to –0.421818 V (item 5 of Table 3) or to –0.42625 V (item 11 of Table 3) has been recorded. This tendency is most likely due to the fact that manganese increases the solubility of carbon in the solid solution of austenite of 06KhN28MDT alloy, since there is information that it and chromium [28] thus affect the solubility of nitrogen, which, like carbon, is a chemical element of the introduction in the crystal lattice of a solid solution of austenite of stainless steels and alloys. This contributes to the growth of its parameters and, obviously, facilitates the ionization of chromium atoms on the surface of the 06KhN28MDT alloy. Under such conditions, the released electrons accumulate on its surface, shifting the free corrosion potential E_{cor} to the negative side. This contributes to an increase in the ΔE criterion of the studied alloy in a crevice with a chloride-containing medium and, taking into account information from [16], increases its resistance to crevice corrosion.

It was mentioned above that the free corrosion potential E_{cor} of the 06KhN28MDT alloy in the gap with a model chloride-containing medium was –0.4 V (see item 12 of Table 3) if its mean austenite grain diameter (x_{11}) was less than 11.4 μm (item 6 of Table 3). However, with its growth over 14.5 μm, a shift in the potential E_{cor} of the alloy to the positive side to –0.379286 V has been recorded (item 6 of Table 3). This corrosion behaviour of the studied alloy in a chloride-containing medium is due to the segregation of copper, as a surface-active chemical element, by the boundaries of austenite grains. Indeed, from the analysis of the dependences, it was found that, if $x_{11}[d_g] \geq 14.5$ μm (item 6 of Table 3), then, provided $x_8(\text{Cu}) < 2.755$ wt.% (item 11 of Table 3), the potential E_{cor} of the 06KhN28MDT alloy is of –0.37125 V (item 16 of Table 3). At the same time, if the copper content in the alloy was higher than 2.765 wt.%, it ranged from –0.375833 (item 13 of Table 3) to –0.385 V (item 17 of Table 3). Thus, summarizing this information, it should be noted that the potential E_{cor} of the 06KhN28MDT alloy shifts to the negative side by 9.2 mV with an increase in its copper content from 2.755 up to 2.78 wt.% (melt 2 of Table 1). At the same time, it shifts in the same direction by 20.7 mV with an increase in the mean austenite grain diameter from 14.5 up to 31 μm (item 6 of Table 3). Thus, it can be noted that the effect of the mean austenite grain diameter of the 06KhN28MDT alloy on its potential E_{cor} is more than twice as great as the copper content. However, in general, the higher the copper content in the alloy and its mean austenite grain diameter, the more negative the value of the E_{cor} potential. This positively affects the alloy resistance to crevice corrosion in a chloride-containing media by the above mechanisms.

It was mentioned above about the effect of nickel in the composition of the 06KhN28MDT alloy on its corrosion potential E_{cor} in a gap with a

chloride-containing medium (item 3 of Table 3). In particular, it was found that it is of –0.4 V (item 12 of Table 3), when the nickel content in the alloy is less than 27.575 wt.%, and the mean austenite grain diameter is of 14.5 μm. It should be noted that the potential E_{cor} of the studied alloy shifts to the negative side to –0.379286 V (item 6 of Table 3) with an increase in the mean austenite grain diameter (x_{11}) from 14.5 up to 31 μm and to –0.402 V (item 7 of Table 3) or –0.42 V (item 15 of Table 3) with an increase in the nickel content from 27.675 up to 27.75 wt.% (Table 1). Under such conditions, the potential E_{cor} of the 06KhN28MDT alloy shifts in the negative direction by 20.7 mV with an increase in the mean austenite grain diameter by 16.5 μm (items 6, 12 of Table 3) and by 4.5 (item 7 of Table 3) or 22.5 V (item 15 of Table 3) in the positive direction with an increase in its nickel content by 0.055 wt.%. Thus, it turns out that nickel has a much stronger effect on the potential E_{cor} of the 06KhN28MDT alloy in the gap than the mean austenite grain diameter. At the same time, it should be noted that the joint effect of these alloy parameters on its E_{cor} potential is manifested when x_5(Ni) < 27.575 wt.% (items 3, 6 of Table 3), since it shifts to the negative side by 20.7 mV with an increase in the mean austenite grain diameter from 14.5 up to 31 μm.

Summarizing the above, it can be noted that the corrosion potential E_{cor} of 06KhN28MDT alloy in a crevice with a chloride-containing solution depends on the content of chromium, manganese, nickel, carbon, copper, and the mean diameter of the austenite grain. In particular, the synergistic effect of chromium and manganese on this potential was revealed, since it has a maximum negative value (–0.455714 V), when the chromium content is less than 22.215 wt.%, and manganese 0.455 wt.%. This contributes to the growth of the ΔE criterion of the alloy and its resistance to crevice corrosion. At the same time, it was found that the potential E_{cor} of the studied alloy decreases to –0.4126 V when the chromium content in it is greater than 23.055 wt.%. This is due to the difficulty of ionization of metal atoms in the alloy, since its surface consists of a monolayer of chromium atoms that form a dense passive film.

In addition, with such chromium content in the alloy, provided that the nickel content is less than 27.575 wt.% and the mean austenite grain diameter is of 14.5 μm, its potential E_{cor} is further shifted to the positive side to –0.4 V. This leads to a decrease in the ΔE criterion of the 06KhN28MDT alloy and its resistance to crevice corrosion. This tendency is due to the fact that at the minimum austenite grain diameter in the alloy, the lowest degree of incoherence between the atoms of adjacent crystal lattices is recorded at its boundaries, which complicates the ionization of metal atoms in these areas of the alloy. Meanwhile, the less nickel in the alloy than the above-mentioned amount, the more positive the value of the potential E_{cor}, since the lower the

nickel content in it, the more iron, whose critical ionization potential (+0.46 V) is more than three times more positive than that of nickel (+0.15 V). At the same time, it was found that the larger the mean grain diameter of the austenite of the 06KhN28MDT alloy is over 14.5 μm, the more positive the value of its corrosion potential E_{cor}. At the same time, it is of 13.8 mV more positive when the copper content in the alloy is less than 2.755 wt.%. This is most likely due to the fact that copper, as a surface-active chemical element, can segregate at the grain boundaries of austenite, which increases the potential gradient between the austenite solid solution and its grain boundaries, promoting the ionization of metal atoms and the accumulation of electrons on the alloy surface.

The analysis (Fig. 4) showed that the repassivation potential E_{rep} of the 06KhN28MDT alloy, which is characterized by its ability to restore protective passive films in local corrosion damage, depends on the content of chromium (x_4), copper (x_8), and the mean austenite grain diameter (x_{11}). It should be noted that, unlike the corrosion potential E_{cor} of the alloy under study, it does not depend on the content of manganese and nickel, which, as established above, significantly affect the ability of metal atoms in its composition to ionize.

From the analysis of the mathematical model (Table 4), it follows

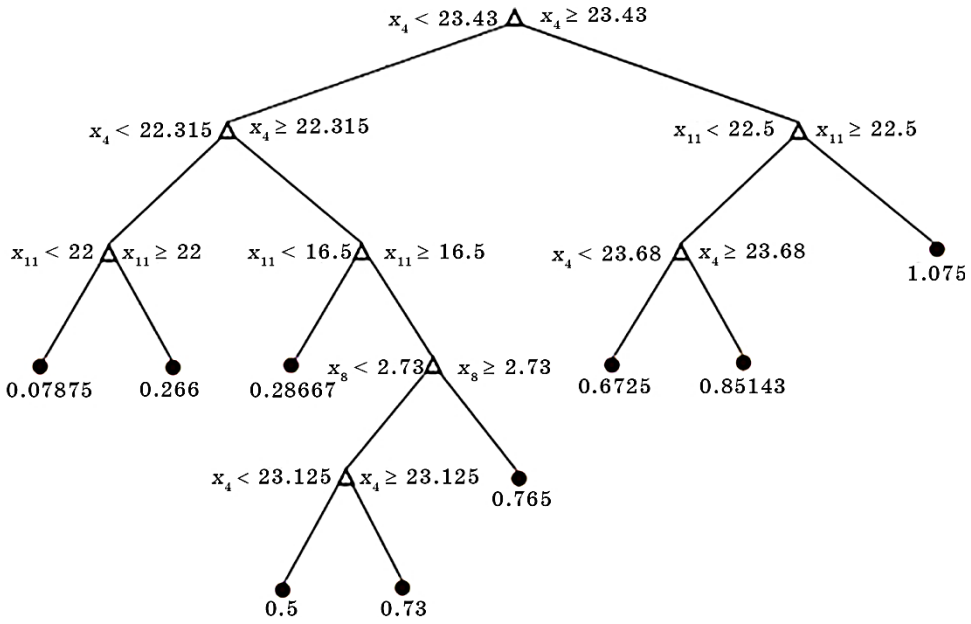


Fig. 4. Regression tree showing the relationship between the repassivation potential E_{rep} of 06KhN28MDT alloy in a gap with a chloride-containing solution and its chemical composition and structure components.

that if $x_4(\mathrm{Cr}) < 23.43$ wt.% (item 1 of Table 4), then, it is necessary to consider the dependences when $x_4(\mathrm{Cr}) < 22.315$ wt.% and $x_{11}[d_g] < 22$ μm (items 2, 4 of Table 4). Under such conditions, the repassivation potential E_{rep} of the 06KhN28MDT alloy in the gap will be 0.07875 V (item 8 of Table 4). However, if the chromium content in the studied alloy is greater than or equal to 23.43 wt.%, then it shifts intensively towards the positive side to 0.5538 V (item 1 of Table 4). This contributes to an increase in the ΔE criterion of the 06KhN28MDT alloy (see Eq. (1)) and its resistance to crevice corrosion in a chloride-containing media.

It should be noted that, as established above, the corrosion potential E_{cor} of the studied alloy does not significantly shift to the positive side with an increase in its chromium content in this interval (Tables 3, 4). This trend suggests that chromium helps to reduce the intensity of general corrosion. Taking into account the intensity of chromium's influence on these potentials, we can note the positive role of chromium in the alloy resistance to crevice corrosion in a chloride-containing media. This is consistent with the information presented in Refs. [5–9, 27–31] about the effectiveness of alloying stainless steels and alloys with chromium to increase their resistance to local corrosion.

The analysis of the developed mathematical model (items 2, 5, 10 of Table 4) showed that the effect of chromium (x_4) on the repassivation potential E_{rep} of 06KhN28MDT alloy is closely related to the mean austenite grain diameter (x_{11}). In particular, it was found that it is 0.336774 V, when the chromium content (x_4) is greater than or equal to 22.315 wt.% (item 2 of Table 4). It should be noted that under such conditions, the repassivation potential E_{rep} of the studied alloy is 0.217 V more negative than when the chromium (x_4) content is greater than or equal to 23.43 wt.% (items 1, 2 of Table 4). This shows that even the chromium (x_4) content in the alloy in this interval itself significantly affects its E_{rep} potential. At the same time, it was found that at such a chromium content in the alloy ($x_4 \geq 22.315$ wt.%; item 2 of Table 4), when the mean austenite grain diameter (x_{11}) is less than 16.5 μm (see item 5 of Table 4), its E_{rep} potential is even lower and amounts to 0.286667 V (item 10 of Table 4). This proves that the grain boundaries strongly affect the potential E_{rep} of the 06KhN28MDT alloy in a chloride-containing medium, shifting it to the negative side. This complicates the repassivation of local corrosion damage to the alloy in the gap with a chloride-containing media, which is associated with structural defects at the austenite grain boundaries. It should be noted that even at the maximum chromium content in the alloy under study within the production standard (Table 1), the effect of the mean austenite grain diameter on the repassivation potential E_{rep} is stronger than the chromium content. This generalization is confirmed by the identified dependences between these indicators. In particular, it was recorded that

the repassivation potential E_{rep} of the 06KhN28MDT alloy is 0.6725 V (item 12 of Table 4), if the mean austenite grain diameter (x_{11}) is less than 22.5 μm (item 3 of Table 4) and the chromium content is of 23.68 wt.% (item 6 of Table 4). At the same time, it becomes very positive (0.907895 V, item 3 of Table 3), when the mean austenite grain diameter (x_{11}) of the alloy under study is greater than or equal to 22.5 μm. This once again proves that defects in the alloy structure along the austenite grain boundaries have a stronger effect on its potential E_{rep} in a gap with a chloride-containing medium than the ability of chromium to form passive films on the surface of local damage on it. After all, it was also found that under such conditions ($x_{11} > 22.5$ μm, item 3 of Table 4), the repassivation potential E_{rep} of the 06KhN28MDT alloy is 1.075 V (item 7 of Table 4). However, even a slight decrease in the mean austenite grain diameter by 0.5 μm (x_{11}) > 22 μm (item 4 of Table 4) can lead to a very intense shift in the potential E_{rep} of the alloy in the positive direction from 0.10266 V (item 9 of Table 4) to 0.150769 V (item 4 of Table 4). The influence of the mean austenite grain diameter (x_{11}) and chromium content (x_4) in the alloy 06HN28MDT on its E_{rep} potential in a gap with a chloride-containing medium was mentioned above. At the same time, the analysis of the developed mathematical model (Fig. 4) showed that this structure indicator (x_{11}) of the alloy and its copper content also affect its ability to repassivate local corrosion damage in the gap. In particular, it was found that the repassivation potential E_{rep} of the 06KhN28MDT alloy in the crevice is 0.471111 V (item 5 of Table 4), when its mean austenite grain diameter (x_{11}) is greater than or equal to 16.5 μm. At the same time, it was found that it does not significantly shift to the positive side up to 0.5 V (item 16 of Table 4), if the copper content (x_8) is less than 2.73 wt.% (see item 11 of Table 4) and chromium 23.125 wt.% (item 14 of Table 4). Thus, taking into account the dependence between the potential E_{rep} and the content of chromium, copper, and the mean grain diameter of austenite, when it is in the range from 16.5 up to 22.5 μm, and the content of copper and chromium is less than the mentioned values, it can be noted that these indicators do not greatly affect it. At the same time, it was found that the potential E_{rep} of the studied alloy varies from 0.786364 (item 6 of Table 4) to 0.851429 V (item 13 Table 4), if the chromium content (x_4) in it is greater than 23.68 wt.% (item 6 of Table 4) and from 0.563333 (item 11 of Table 4) to 0.765 V (item 15 of Table 4), if the copper content (x_8) is greater than 2.73 wt.% (item 11 of Table 4). It should be noted that at such a content of chromium and copper in the 06KhN28MDT alloy, the effect of chromium on its repassivation potential is by 1.23 times more significant than that of copper. This may be due to the fact that copper contributes to the enrichment of the passive oxide film with chromium in local corrosion damage [32].

According to the results of the analysis of dependences (item 4 of

Table 4), it was found that the repassivation potential E_{rep} of the 06KhN28MDT alloy in a gap with a chloride-containing medium varies in the range from 0.523 to 0.73 V, if the chromium content in it is greater than or equal to 23.121 wt.%. At the same time, as mentioned above (items 6, 13 of Table 4), it varies in the range from 0.786364 to 0.851429 V if the chromium content is greater than 23.68 wt.%. Thus, it can be noted that the potential E_{rep} of the 06KhN28MDT alloy shifts rapidly towards the positive side by 192.4 mV with an increase in its chromium content from 23.125 up to 23.68 wt.%. This leads to an increase in the alloy resistance to crevice corrosion in a chloride-containing media.

Summarizing the above, it can be noted that the repassivation potential E_{rep} of the 06KhN28MDT alloy in a gap with a model chloride-containing medium depends on the content of chromium, copper, and the mean diameter of the austenite grain. It was found that it shifts to the positive side with an increase in the content of chromium and copper. The effect of chromium on the potential E_{rep} of the alloy is stronger than that of copper. In addition, it is manifested by the most intense shift of the E_{rep} potential in the positive direction by 192.4 mV with an increase in the chromium content from 23.121 up to 23.68 wt.%. Under such conditions, it most effectively contributes to the reparation of local corrosion damage on the alloy surface in the gap, forming dense oxide films with a minimum number of pores [33, 34], where chloride ions can adsorb from the media and contact the alloy. Copper is known [32] to contribute to the enrichment of oxide films with chromium. It was found that the potential E_{rep} of the 06KhN28MDT alloy has almost the most negative value of 0.286667 V, if the mean austenite grain diameter is less than 16.5 μm. It has been found that under such conditions it shifts to the positive side to 0.765 V, if the copper content is less than 2.73 wt.%, and to 0.73 V, if the chromium content is less than 23.125 wt.%.

It has been established that the corrosion potential E_{cor} of 06KhN28MDT alloy depends on the content of Cr, Mn, Ni, Cu, and the mean austenite grain diameter. In particular, it has been recorded that it has the most negative value of –0.455714 V, if the content of chromium and manganese is less than 22.215 and 0.455 wt.%, respectively. This shows that the surface of the alloy accumulates electrons due to more intense ionization of metals at the anode areas. Under such conditions, the oxide films on the alloy surface are less dense due to a decrease in its chromium content. Under such conditions, the general corrosion is accelerated, but local corrosion is 'slowed down' due to the redistribution of the anode current density between a larger numbers of anode metal dissolution places on its surface. It was found that the potential E_{cor} of the alloy shifts to the positive side to –0.41 V, if the carbon content in it is less than 0.053 wt.%, *i.e.*, it is dissolved in a solid

solution of austenite. When carbides precipitate from the alloy's austenite solid solution, a slight shift of E_{cor} to the negative side has been recorded. It has been found that the potential E_{cor} of the alloy has the most positive value of –0.3 V, if the mean austenite grain diameter is greater than 15.5 μm. This contributes to a decrease in the ΔE criterion of the 06KhN28MDT alloy and its resistance to crevice corrosion. It was found that the potential E_{cor} of the alloy significantly shifts to the negative side ($\cong$ 0.17 V), if the nickel content in it is more than 27.675 wt.%. This trend improves the alloy resistance to crevice corrosion in a chloride-containing media. This is consistent with the information in Ref. [21].

4. CONCLUSION

Based on the results of the analysis of mathematical models developed on the basis of regression trees, it was found that the repassivation potential E_{rep} of the 06KhN28MDT alloy in the gap with a model chloride-containing medium intensively shifts to the positive side by 192.4 mV with an increase in its chromium content from 23.12 up to 23.68 wt.%. This leads to an increase in the ΔE-criterion of the alloy and its resistance to crevice corrosion due to the formation of a dense chromium-containing oxide film. It has been found that the potential E_{rep} of the alloy has the most negative value of 0.287 V, if the mean austenite grain diameter is less than 16.5 μm. It was found that under such conditions, the potential E_{rep} of the alloy shifts to a positive value of 0.5 V if the content of copper and chromium in it is less than 2.73 and 23.125 wt.%, respectively. It is recorded that this potential shifts further in the positive direction to 0.765 and 0.73 V, if the content of copper and chromium in the alloy is more than 2.73 and 23.125 wt.%, respectively. It is shown that, under such conditions, the effect of copper on the potential E_{rep} is of 0.035 V stronger than that of chromium. This is most likely due to the fact that copper contributes to the enrichment of the passive oxide film on the surface of the 06KhN28MDT alloy with chromium, which increases its resistance to crevice corrosion. It has been established that the corrosion potential E_{cor} of the alloy has the most negative value of –0.4557 V, if the content of chromium and manganese in it is less than 22.215 and 0.455 wt.%, respectively. This contributes to the accumulation of electrons on the alloy surface due to the intensification of general corrosion, which leads to a decrease in the probability of crevice corrosion in a chloride-containing media. It has been shown that the precipitation of carbides (Cr, Mo) from austenite solid solution at a carbon content of more than 0.053 wt.% contributes to a slight shift of the E_{cor} potential to the negative side. It is proved that the potential E_{cor} of the alloy has the most positive value $\cong$ –0.38 V, if the mean austenite grain diameter is greater than 15.5

μm, regardless of the copper content. It was found that this potential shifts to the negative side by $\cong 0.17$ V, if the nickel content in the alloy is more than 27.675 wt.%. This leads to an increase in the alloy resistance to crevice corrosion.

AUTHORS' CONTRIBUTIONS

D.A.V. carried out the experimental corrosion tests of the 06KhN28MDT alloy in model chloride-containing crevice conditions, determined the free corrosion potentials E_{cor}, repassivation potentials E_{rep} and the ΔE-criterion, participated in microstructural examinations, and prepared the initial draft of the manuscript (Introduction, Materials and Methods, Results and Discussion).

N.O.E. devised the main conceptual ideas of the study, formulated the research problem related to crevice corrosion of plate heat exchangers, designed the experimental program and test conditions, interpreted the electrochemical and corrosion behaviour of the alloy, provided a critical review of the manuscript, and supervised the scientific part of the work.

S.O.S. generated the extended dataset based on the experimental results, developed and implemented the regression-tree-based mathematical models linking E_{cor}, E_{rep} and ΔE with the chemical composition and structural parameters of the alloy, performed the statistical analysis of model quality, and contributed substantially to the interpretation of the decision rules (Tables 3 and 4).

S.G.V. was responsible for the graphical material: performed and processed microstructural and metallographic examinations (including the characterization of titanium carbonitrides and sulphides), prepared and annotated the figures (micrographs and regression trees), and designed all tables and graphical elements illustrating the obtained results.

P.T.V. coordinated the overall project activities, including communication between the university and industrial partner, organization of access to materials and equipment, and resolution of general organizational issues; she also participated in structuring the manuscript, editing the text, and preparing the final version for submission.

All authors discussed the results, contributed to the interpretation of the findings, and approved the final version of the manuscript.

REFERENCES

1. O. E. Narivs'kyi, *Mater. Sci.*, **43**, Iss. 1: 124 (2007).
2. O. E. Narivs'kyi, *Fizyko-Khimichna Mekhanika Materialiv*, **41**, No. 1: 104 (2005) (in Ukrainian).
3. R. K. Melekhov, H. M. Krutsan, and O. O. Taburenko, *Problemy Trybolohii*, **3**: 3

(2003).
4. N. Sato, *Corrosion Science*, **37**, Iss. 12: 1947 (1995).
5. O. E. Narivs'kyi, G. V. Snizhnoi, T. V. Pulina, V. L. Snizhnoi, and N. A. Solidor, *Mater. Sci.*, **59**, Iss. 3: 649 (2024).
6. O. E. Narivskyi, S. O. Subbotin, and T. V. Pulina, *Phys. Sci. Technol.*, **10**, Iss. 3–4: 48 (2023).
7. O. E. Narivskyi, S. O. Subbotin, T. V. Pulina, S. D. Leoshchenko, M. S. Khoma, and N. B. Ratska, *Mater. Sci.*, **59**, Iss. 5: 275 (2024).
8. O. E. Narivskyi, S. O. Subbotin, T. V. Pulina, S. O. Leoshchenko, M. S. Khoma, and N. B. Ratska, *Mater. Sci.*, **58**, Iss. 5: 1 (2023).
9. A. V. Dzhus, O. E. Narivskyi, S. A. Subbotin, T. V. Pulina, G. V. Snizhnoi, and S. D. Leoshchenko, *Metallofiz. Noveishie Tekhnol.*, **46**, No. 4: 371 (2024).
10. G.S. Yar-Mukhamedova, *Mater. Sci.*, **36**: 598 (2000).
11. G. Yar-Mukhamedova, A. Muradov, K. Mukashev, and G. Ismailova, *International Multidisciplinary Scientific GeoConference SGEM*, **17**, Iss. 61: 201 (2017).
12. A. Muradov, K. Mukashev, and G. Ismailova, *International Multidisciplinary Scientific GeoConference SGEM*, **17**: 208 (2017).
13. A. D. Muradov, K. M. Mukashev, and N. E. Korobova, *Tech. Phys.*, **62**, No. 11: 1692 (2017).
14. G. Yar-Mukhamedova, M. Ved', I. Yermolenko, A. Karakurkchi, and A. Kemelzhanova, *Eurasian Chemico-Technological Journal*, **22**, No. 1: 19 (2020).
15. A. Narivskiy, G. Yar-Mukhamedova, E. Temirgaliyeva, M. Mukhtarova, and Y. Yar-Mukhamedov, *International Multidisciplinary Scientific GeoConference SGEM*, **1**: 63 (2016).
16. *RTM-26-01-88. Rukovodyashchiy Tekhnicheskiy Material. Metody Korrozionnykh Ispytaniy Metallicheskikh Materialov. Osnovnye Trebovaniya. Otsenki Rezultatov* [Guiding Technical Material. Methods of Corrosion Testing of Metal Materials. Basic Requirements. Evaluation of Results] (Moskva: VNIIkhimmash: 1989) (in Russian).
17. O. A. Freedman, *Statistical Models: Theory and Practice* (Cambridge University Press.: 2005).
18. O. E. Narivskyi, *Mater. Sci.*, **43**, Iss. 2: 256 (2007).
19. V. G. Mishchenko, G. V. Snizhnoi, and O. E. Narivs'kyy, *Metallofiz. Noveishie Tekhnol.*, **33**, No. 6: 769 (2011).
20. A. Bolfrouh, C. Masson, D. Vouagner, A. M. de Becdelievre, N. S. Prakash, and J. P. Audouard, *Corrosion Science*, **38**, Iss. 10: 1639 (1996).
21. N. A. Langer, L. N. Yagupolskaya, N. I. Kakhovsky, and K. A. Yushchenko, *Metallovedenie i Metallurgiya*, **2**: 29 (1966) (in Russian).
22. P. E. Manning, D. Duquette, and W.F. Savage, *Welding Journal*, **59**, No. 9: 260 (1980).
23. L. I. Freiman, Y. M. Kolotyrkin, I. I. Reformatskaya, Y. P. Konnov, and A. E. Volkov, *Zashchita Metallov*, **28**, No. 2: 179 (1992) (in Russian).
24. L. I. Freiman, I. I. Reformatskaya, and T. P. Markova, *Zashchita Metallov*, **27**, No. 4: 617 (1991) (in Russian).
25. E. G. Aftandilianets, O. V. Zazymko, and K. G. Lopatko, *Materialoznavstvo: Pidruchnyk* [Materials Science: Textbook] (Kyiv: Vyshcha Shkola: 2012) (in Ukrainian).
26. Ya. M. Kolotyrkin, *Metall i Korroziya* [Metal and Corrosion] (Moskva: Metal-

lurgiya: 1985) (in Russian).
27. V. V. Gerasimov, *Prognozirovanie Korroziyi Metalla* [Prediction of Metal Corrosion] (Moskva: Metallurgy: 1989) (in Russian).
28. R. A. Perren, P. J. Ugowitzer, and M. O. Speidel, *Proc. of the 5th World Conference on Duplex Stainless Steels* (Maastricht, Netherlands: 1997).
29. P. R. Levey and A. A. Van Bennekom, *Corrosion*, **51**, Iss. 12: 911 (1995).
30. E. Alfonsson and R. Qvarfort, *Materials Science Forum*, **111–112**: 483 (1992).
31. S. Bernhardsson and J. Charlee, *Proc. of Conference 'Duplex Stainless Steels "91"'* (Les Ulis, France: Les Editions de Physique: 1991).
32. J. H. Potgieter, *British Corrosion Journal*, **27**, No. 3: 219 (1992).
33. P. E. Manning, D. Duquette, and W. F. Savage, *Mater. Sci.*, **59**, Iss. 9: 260 (1980).
34. J.-H. Wang, C. C. Su, and Z. Szklarska-Smialowska, *Corrosion*, **44**, Iss. 10: 732 (1988).

Metallophysics and Advanced Technologies
Металофіз. новітні технол.
Metallofiz. Noveishie Tekhnol.
2026, vol. 48, No. 8, pp. 827–841
https://doi.org/10.15407/mfint.48.08.0827
Reprints available directly from the publisher

© 2026 G. V. Kurdyumov Institute for Metal Physics,
National Academy of Sciences of Ukraine
Published by license under
the G. V. Kurdyumov Institute for Metal Physics–
N.A.S. of Ukraine Publishers imprint.
Printed in Ukraine.

PACS numbers: 61.72.Ff, 62.20.Qp, 68.35.Ct, 68.70.+w, 81.40.Wx, 81.65.Ps, 83.60.Np

Magnetic Post-Processing of Additively-Manufactured Inconel 718 Superalloy: Functional Microrelief Evolution and Surface Strain Hardening

D. A. Lesyk[*,**,***], B. M. Mordyuk[***], O. Stamann[****], D. Grochala[*****], S. S. Salii[**], M. M. Lytvynenko[**], M. V. Romanenko[**], M. I. Anyakin[**], A. Lamikiz[*]

[*]*National Technical University of Ukraine 'Igor Sikorsky Kyiv Polytechnic Institute', 37 Beresteiskyi Prosp., UA-03056 Kyiv, Ukraine*
[**]*University of the Basque Country, Barrio de Sarriena, s/n, SP-48940 Leioa, Spain*
[***]*G. V. Kurdyumov Institute for Metal Physics, N.A.S. of Ukraine, 36 Academician Vernadsky Blvd., UA-03142 Kyiv, Ukraine*
[****]*Otto-von-Guericke University Magdeburg, 2 Universitätsplatz, DE-39106 Magdeburg, Germany*
[*****]*West Pomeranian University of Technology, 17 al. Piastyw, PL-70-310 Szczecin, Poland*

Nickel-based superalloys with enhanced operational properties are key materials for producing safety-critical components. Additive manufacturing offers a new way to manufacture critical components, enabling the production of superalloy structures with complex shapes, which are unattainable by con-

Corresponding author: Bohdan Mykolayovych Mordyuk
E-mail: mordyuk@imp.kiev.ua

Citation: D. A. Lesyk, B. M. Mordyuk, O. Stamann, D. Grochala, S. S. Salii, M. M. Lytvynenko, M. V. Romanenko, M. I. Anyakin, and A. Lamikiz, Magnetic Post-Processing of Additively-Manufactured Inconel 718 Superalloy: Functional Microrelief Evolution and Surface Strain Hardening, *Metallofiz. Noveishie Tekhnol.*, **48**, No. 8: 827–841 (2026), DOI: 10.15407/mfint.48.08.0827

© Publisher PH 'Akademperiodyka' of the NAS of Ukraine, 2026. This is an open access article under the CC BY-ND license (https://creativecommons.org/licenses/by-nd/4.0)

ventional manufacturing methods. The laser powder bed fusion (LPBF) process is used for manufacturing superalloy components. Post-processing methods are required to improve the surface integrity, because LPBF parts with complex geometries suffer from various defects located both on the surface and near-surface layers. Today, post-processing methods are being developed to improve surface integrity in LPBF-produced parts. In this work, magnetic needle finishing (MNF) is applied for surface post-processing of Inconel 718 superalloy manufactured *via* LPBF. The effects of magnetic needle finishing under optimised conditions on surface morphology, functional relief performance, microstructure, and hardness are investigated. The results indicate that the surface integrity of the LPBF-manufactured 718 alloy is improved by generating a smoothed surface microrelief with a strain-hardened subsurface layer (the macrohardness increased from $\cong 32\ HRC_{10}$ to $\cong 39\ HRC_{10}$) through the high-energy MNF post-processing. Reducing and levelling the amplitude parameters (the R_a parameter is decreased from $\cong 4.0$ μm to $\cong 2.0$ μm) of microirregularities in the MNF-finished Inconel-alloy samples due to the multiple-angle impact of magnetic pins resulted in a redistribution of surface load, which is favourable for the functional performance of the LPBF-produced parts. A decrease in crystallite size as well as an increase in lattice strain and dislocation density due to the surface plastic deformation of the near-surface layer are confirmed.

Key words: magnetic finishing, Inconel 718, laser powder bed fusion, post-processing, surface integrity, functional relief performance, microstructure.

Ніклеві суперстопи з поліпшеними експлуатаційними властивостями є ключовими матеріялами для виробництва критично важливих деталів, від яких залежить безпека. Адитивне виробництво відкриває новий спосіб виготовлення відповідальних деталів, уможливлюючи одержання конструкцій із суперстопів складної форми, створення яких є неможливим класичними методами оброблення. Для виготовлення деталів із суперстопів застосовується процес лазерного пошарового стоплення порошку (ЛПСП). Однак вироби складної геометрії, виготовлені методою ЛПСП, мають різноманітні дефекти, розташовані як безпосередньо на поверхні, так і в приповерхневих шарах, що зумовлює необхідність застосування методів постоброблення для поліпшення цілісности поверхні. Сьогодні активно розробляються нові методи поверхневого фінішного оброблення деталів, виготовлених методою ЛПСП. У цій роботі для фінішного постоброблення поверхні суперстопу Інконель 718, виготовленого методою ЛПСП, було застосовано магнетне фінішне оброблення (МФО). Досліджено вплив МФО за оптимізованих режимів на морфологію поверхні, функціональні характеристики рельєфу, мікроструктуру та твердість. Результати свідчать, що цілісність поверхні виробленого за ЛПСП-технологією стопу 718 було поліпшено за рахунок формування згладженого мікрорельєфу поверхні та деформаційного зміцнення поверхневого шару (макротвердість збільшилася від $\cong 32\ HRC_{10}$ до $\cong 39\ HRC_{10}$) під дією високоенергетичного МФО. Зменшення та вирівнювання амплітудних параметрів мікронеоднорідностей (параметер R_a зменшився від $\cong 4{,}0$ мкм до $\cong 2{,}0$ мкм) у зразках стопу Інконель 718 після МФО внаслідок багатовекторного ударного впливу магнетних штифтів привели до перерозподілу поверх-

невого навантаження, що є сприятливим чинником для функціональних характеристик ЛПСП-деталів. Унаслідок поверхневої пластичної деформації підтверджено зменшення розміру кристалітів і збільшення деформації ґратниці та густини дислокацій у поверхневому шарі.

Ключові слова: магнетне фінішне оброблення, Інконель 718, лазерне пошарове стоплення порошку, постоброблення, поверхнева цілісність, функціональні характеристики рельєфу, мікроструктура.

(Received July 09, 2026; in final version, September 08, 2026)

1. INTRODUCTION

Laser powder bed fusion (LPBF) technology is one of the advanced additive manufacturing methods for producing complexly shaped nickel-based superalloy components [1, 2]. The metal powder layer of a certain thickness is selectively melted *via* a moving laser beam, generating a layered 3*D* object. As compared to the LPBF process [1, 3–5], an overblown metal powder or metal wire at the direct energy deposition process is placed in a specific place and melted by means of a high-energy laser beam [6–8]. The advanced LPBF 3D printing process offers a new alternative way for manufacturing small-size metallic components with complex geometries. The LPBF technology is a very valuable approach for additive manufacturing heat-resistant alloy (Inconel) products [1, 3, 9–12].

Surface integrity improvement in the nickel-based superalloy parts produced by the LPBF technique is a crucial issue in the additive manufacturing routes. On the one hand, the application of specific heat post-treatments needs to eliminate microstructural anisotropy, improving the mechanical properties [10, 13–15]. On the other hand, surface modification treatments should be applied in combination with thermal post-treatments to improve the surface and structural integrity in nickel-based superalloys [4, 10, 14, 15–17]. Currently, various conventional mechanical and chemical surface post-treatment methods are applied to reduce the surface roughness and enhance the mechanical properties of Inconel alloys. Barrel/vibratory finishing [18, 19] and abrasive finishing [4, 10, 20–22] have been used for the surface post-processing of additively manufactured metal parts. The use of laser polishing is another non-abrasive approach for the significant improvement of surface roughness [23]. Laser shock peening [17, 24], cavitation peening [25], and ultrasonic-based surface finishing [14, 17, 26–29] were also applied, aiming to induce nanostructuring and compressive stresses. The mechanical surface post-treatment by ultrasonic tools is one of the most effective approaches to enhance the surface integrity and properties in the near-surface layers of 3*D*-produced Ni-based alloy parts. At the same time, ultrasonic methods are limited for

surface finishing of complexly shaped and/or small-size geometries compared to abrasive finishing methods. Magnetic-assisted surface finishing, chemical and electrochemical surface modification (polishing) are more flexible processes, which are applied for post-treatment of metal parts with complex geometries manufactured *via* LPBF.

Nowadays, magnetically driven surface finishing methods are considered to improve the surface integrity of the nickel-based superalloy components with complex geometries manufactured through LPBF [16, 30]. During the magnetic abrasive finishing of the LPBF components, the material is uniformly removed from both the external and internal surfaces, eliminating the partially melted powder particles and smoothing the surface (R_a decreased from $\cong 7$ μm to less than 1 μm [31]. Magnetic abrasive finishing combined with vibratory machining significantly reduced the surface roughness (R_a values from 1.21 μm to 0.8 μm under optimal conditions) of the LPBF-fused Inconel 939 components [32]. In work [33], magnetic abrasive finishing was applied for the surface post-processing of the heat-treated Inconel 718 alloy manufactured by LPBF, mainly introducing high-angle grain boundaries and subsequently improving mechanical properties.

Unlike traditional magnetic abrasive finishing, magnetic needle finishing (MNF) uses magnetically driven ferromagnetic needles to induce micropeening alongside surface smoothing. In the MNF process, the material surface undergoes moderate plastic deformation under the high-speed impact of magnetic needles, uniformly distributing impact dimples on the surface [30]. At the same time, attempts to use magnetic needle finishing improving the surface integrity of the nickel-based superalloy parts manufactured by LPBF are practically absent. This research work examines the effect of wet magnetic needle finishing on the functional microrelief, the surface roughness, microstructure and internal defects in the Inconel 718 superalloy parts manufactured by the LPBF additive manufacturing method.

2. EXPERIMENTAL DETAILS

2.1. Powder Material and LPBF Method Description

For post-processing, Inconel 718 (IN718) alloy samples were manufactured using the RENISHAW AM400 machine and a commercial nickel-based pre-alloyed IN718 metal powder (the nominal chemical composition [wt.%] is the following: 50–55% Ni, 17–21% Cr, 4.7–5.5% Nb, 2.8–3.3% Mo, 0.6–1.2% Ti, and 0.2–0.8% Al) with high quality. The powder used contained spherical powder particles in the range of 10–55 μm. IN718 alloy parts were manufactured by LPBF using a layer thickness of 60 μm. The key parameters for manufacturing IN718 alloy parts were a laser power of 200 W and a scanning speed of 700 mm/s, using a

multidirectional scanning strategy with a stripe spacing of 5 mm.

2.2. Post-Processing Method Description

Surface post-processing of the LPBF-manufactured IN718 alloy samples was implemented using a magnetically driven magnetic needle finishing (MNF) method. The MNF post-processing of the LPBF-manufactured small-size parts was conducted under a variable magnetic field using a multicomponent media, consisting of ferromagnetic needles and an abrasive paste enriched with surface-active substances, lowered into a chamber [16]. The MNF system comprised a cylindrical processing chamber with liquid compound, a magnetic disk drive, and an electric motor. The MNF process was performed for 30 min at room temperature.

2.3. Experimental Methods Description

The surface samples before and after post-processing were observed by a Mitutoyo Hyper Quick Vision WLI 3D optical profilometer (ISO 25178-2:2012 and ISO 21920-2:2021 standards) and 3D Taylor Hobson Form Talysurf 120 contact profilometer (ISO 4287:1997 and ISO 21920-2:2021 standards). The bearing area parameters (S_{pk}, S_k, S_{vk}) and functional volume parameters (V_{mc}, V_{mp}, V_{vc}, V_{vv}) obtained from the surface (0.5 mm by 0.5 mm area) were analysed. The profile roughness (R_a, R_p, R_v, R_t) parameters along the 0.8 mm sampling length were also examined in this study.

The microstructure and bulk/surface defects in the build and scan direction cross-sections of the LPBF-manufactured and MNF-processed samples were observed by the Leica MEF4A and Polyvar 2 light optical microscopes (LOM), and the high-resolution TESCAN Mira 3 LMU scanning electron microscope (SEM).

X-ray diffraction (XRD) analysis was performed using a Rigaku Ultima IV diffractometer. The quantitative analysis of residual internal defects was statistically carried out using the cross-sectional optical (unetched) micrographs obtained from the build direction by means of the Image-Pro Plus software through grayscale threshold segmentation. Macrohardness measurements were performed on the unpolished outer surfaces using a DIA-TESTOR 2Rc Rockwell hardness tester under an indenter load of 10 kgf.

3. RESULTS AND DISCUSSION

The surface topography, functional microrelief parameters, and roughness alterations are studied in the first part of this study (Figs.

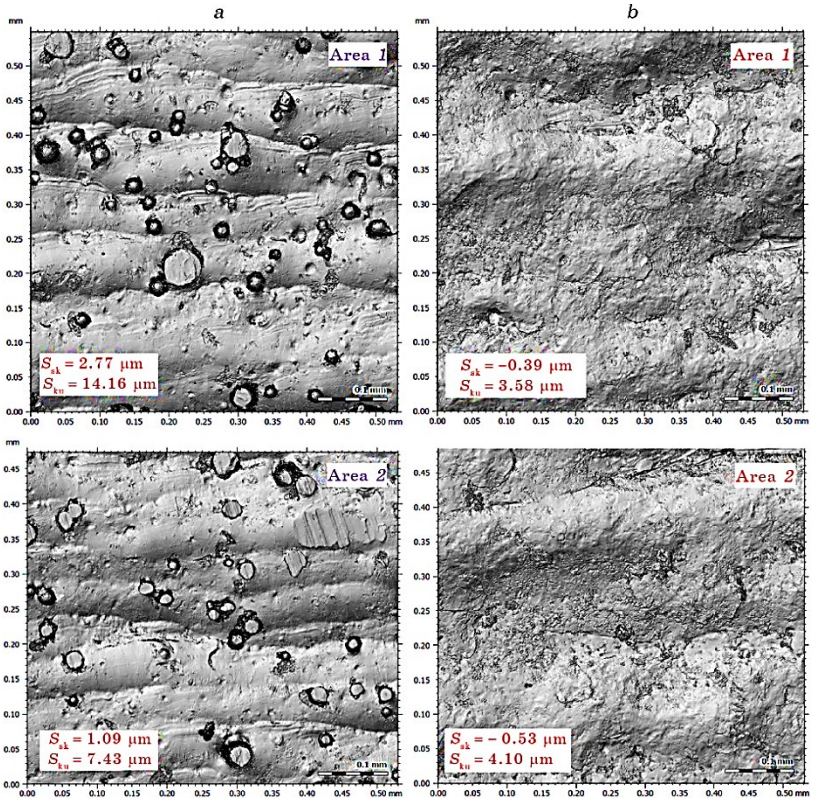


Fig. 1. Surface morphology and height distribution (S_{sk} and S_{ku}) parameters of the LPBF-manufactured (*a*) and MNF-finished (*b*) alloy IN718 samples across Area *1* and Area *2*.

1–3), while the structural–phase state and strain-hardened effect are observed in the second part of this work (Figs. 4–6), clarifying the surface integrity in the IN718 alloy specimens manufactured by LPBF and subsequently post-processed by MNF.

3.1. Surface Microrelief and Morphology

The surface microreliefs/morphologies (Fig. 1), functional bearing capacity (Fig. 2) and material volume parameters of the laser powder bed fused and magnetic needle finished alloy IN718 samples were examined across two representative sample regions (Area *1* and Area *2*) and compared. The MNF process resulted in the removal of partially adhered spherical powder particles due to surface plastic deformation with multiangle collisions of needles, smoothing ($\downarrow S_a$ parameter) and flattening ($\downarrow\downarrow S_p$ parameter) the surface. The MNF finishing slightly

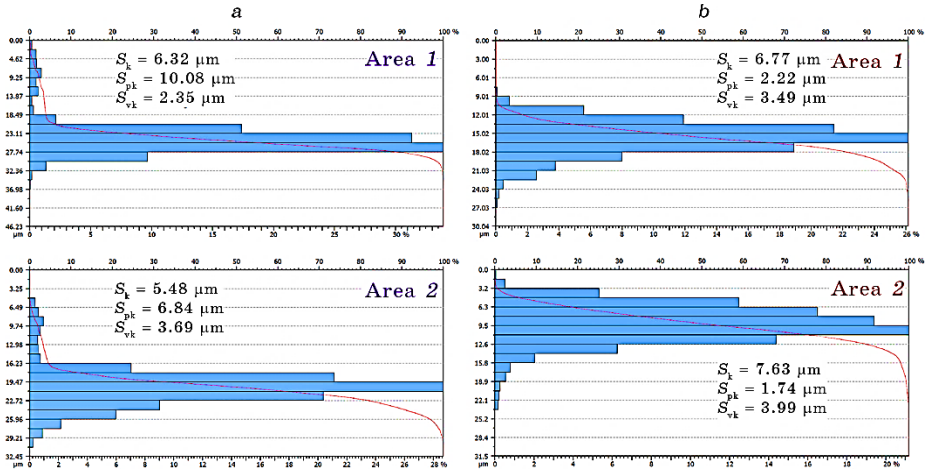


Fig. 2. Load-bearing (S_k, S_{pk}, and S_{vk}) parameters derived from Abbott–Firestone curves for the LPBF-manufactured (*a*) and MNF-finished (*b*) alloy IN718 samples across Area *1* and Area *2*.

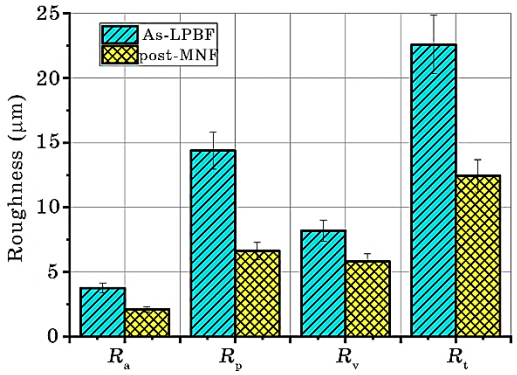


Fig. 3. Surface roughness of the LPBF-manufactured and MNF-finished superalloy IN718 samples.

reduced the arithmetical mean height (S_a = 1.95 μm, 15%-reduction compared to the LPBF sample) parameter, while the maximum peak height (S_p) parameter significantly decreased (from 20–25 μm to 10–15 μm). The maximum valley height (S_v) values in the as-LPBF and post-MNF samples are at the same level, confirming a negligible effect of the high-speed needle impacts on the valley surface.

As illustrated in the topographic images (Fig. 1) of the measured area (500 μm×500 μm), the boundaries of laser tracks were smoothed but not completely removed/erased from the surface because the nickel-based surface samples were subjected to moderate MT conditions.

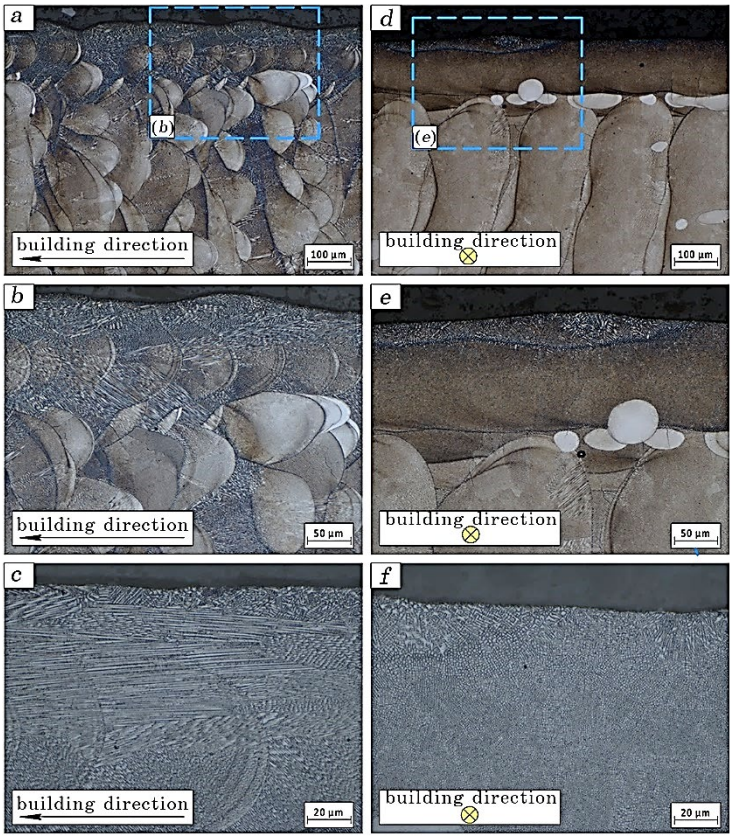


Fig. 4. Macrostructure and microstructure of the LPBF-manufactured (*a*) and MNF-finished (*b*) alloy IN718 samples in the build (*a*–*c*) and scan (*d*–*f*) directions.

Thus, a flattened and wavy surface microrelief with a uniformly distributed dimpled texture (Fig. 1, *b*) due to the individual needle impacts and traces of laser tracks is formed after magnetically driven surface post-processing.

Comparative 2*D* surface morphologies and height distribution (S_{sk} and S_{ku}) parameters that reflect the degree of roughness profile shift, evaluated in the LPBF additive manufacturing conditions (Fig. 1, left) and MNF post-processing conditions (Fig. 1, right), demonstrate that the skewness values are a pronounced positive asymmetry ($S_{sk} > 0$: +2.77 in Area *1* and +1.09 in Area *2*) across both areas in the as-LPBF conditions due to the presence of adhered powder particles and sharp peaks.

Conversely, application of magnetic post-processing using numerous and repetitive pin impacts resulted in negative near-Gaussian skewness values across both areas ($S_{sk} < 0$: –0.39 in Area *1* and –0.53 in

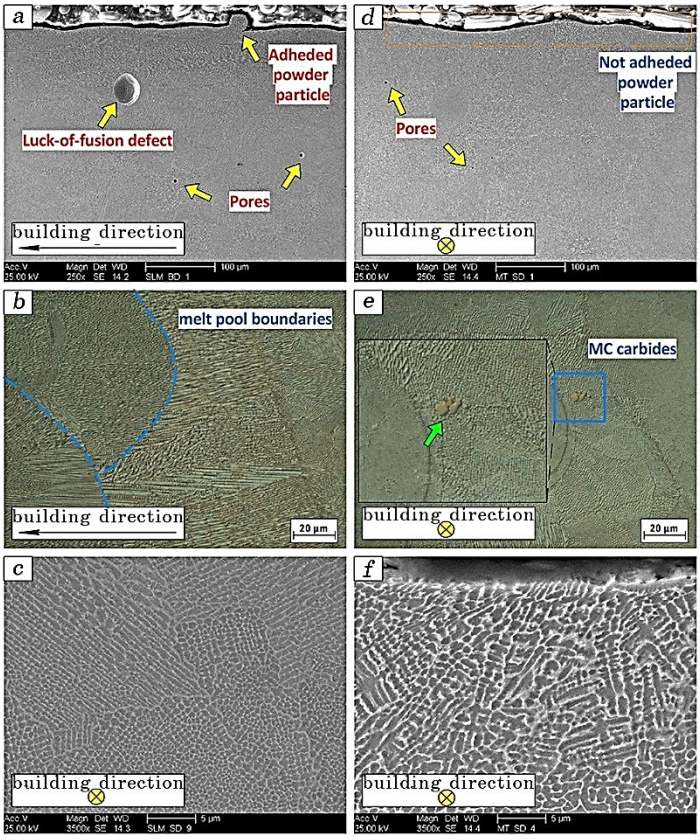


Fig. 5. Microstructure observation by SEM and LOM in the LPBF-manufactured (*a*–*c*) and MNF-finished (*d*–*e*) alloy IN718 samples in the build and scan directions.

Area *2*), which is a relief with a predominance of valleys over peak. The kurtosis (S_{ku}) values that represent the degree of the roughness profile sharpness decreased from 14.16 / 7.43 to 3.58 / 4.10 after the MNF treatment, indicating the elimination of high peaks and the formation of a uniformly smoothed surface texture.

3.2. Functional Microrelief Performance

The functional bearing ratio values and volume parameters with the minimised S_{pk}/V_{mp}, expanded core S_k/V_{mc}, and moderate S_{vk}/V_{vv} alterations demonstrate that the generated surface in the MNF-treated samples possesses the ability to suppress the initial wear during running-in ($\downarrow\downarrow S_{pk}$) and increase the load-bearing capacity due to an increase in the area of actual contact ($\uparrow S_k$) (Fig. 2).

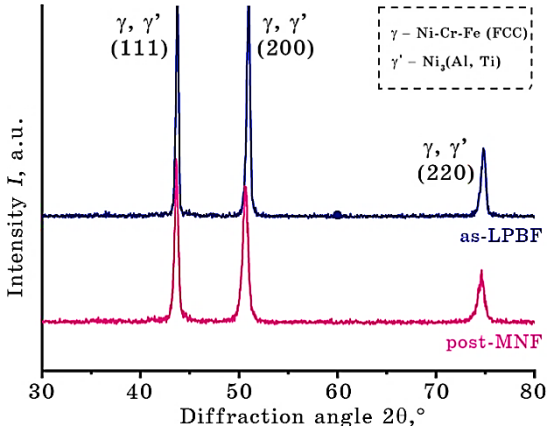


Fig. 6. XRD phase patterns for the LPBF-manufactured and MNF-finished alloy IN718 samples.

In addition, the depth of the valleys does not decrease, but rather increases slightly or remains stable (2.35 μm to 3.49 μm in Area *1* and 3.69 μm to 3.99 μm in Area *2*), confirming that the MNF process deforms the surface locally. The metal pins with multiple microimpacts rotated at high-speed remove high peaks selectively without filling or destroying the intertrack valleys that can create the condition of the microreservoirs to retain lubricant (V_{vv} from 0.0025 mm^3/mm^2 to 0.0036 mm^3/mm^2 in Area *1*).

The surface profile roughness (R_a, R_p, R_v, and R_t) parameters (Fig. 3), estimated from their profiles along the 0.8 mm sampling length, indicate that the magnetically driven surface finishing treatment resulted in a reduction in the surface roughness, correlating well with the area surface roughness. The surface roughness (R_a) parameter was reduced from ≅3.7 μm to ≅2.10 μm after the surface MT post-processing, confirming a significant effect on surface quality improvement. It can be seen that a dramatic reduction in peak height (R_p) was achieved, dropping by over 50% (from ≅14.5 μm to ≅6.5 μm), indicating effective removal of high-peak microasperities in the IN718 alloy through the MT finishing process.

Reducing and levelling the amplitude parameters of micro-irregularities in the MNF-finished Inconel alloy samples due to the high-speed impact of magnetic pins with various collisions leads to a redistribution of surface load, which is favourable for the functional performance of the LPBF-produced parts in extreme conditions. The high-speed needle impacts on the surface ensure micropeening and plastic flattening, rather than just removal of the partially melted/adhered powder particles from the surface. Thus, surface post-processing using the magnetic needle finishing transforms the original

rough and wavy-shaped surface into a smoothed and flattened surface microrelief with a uniformly distributed dimpled texture, resulting in improved surface integrity of Inconel 718 alloy prepared *via* LPBF.

3.3. Microstructure

To examine the near-surface structure, phase composition, and internal/surface defects in as-LPBF IN718 alloy before and after the MT finishing, light optical microscopy, scanning electron microscopy, and x-ray diffraction methods were applied in this study. The macrostructure and microstructure of the LPBF-manufactured and MNF-finished alloy IN718 samples in the build (Fig. 4, *a*–*c*) and scan (Fig. 4, *d*–*f*) directions are presented in Fig. 4 and Fig. 5.

Micrographs of the microstructure of the LPBF-manufactured and surface post-processed IN718 alloy specimens obtained using LOM (Figs. 4 and 5) and SEM (Fig. 5) with high-magnification along build and scan directions demonstrated that the dendritic structure, containing γ [Ni–Cr–Fe] solid solution matrix with a face-centred cubic (f.c.c.) lattice, mainly consists of elongated colonies of cells in the build direction (Fig. 4, *a*–*c*, Fig. 5, *a*, Fig. 5, *b*), oriented parallel to the primary thermal gradient during solidification, while the equiaxed cellular colonies of finely dispersed cells are observed in the scan direction (Fig. 4, *d*–*e*, Fig. 5, *c*–*f*).

The microsegregation of some alloying elements, such as niobium (Nb), molybdenum (Mo), and carbon (C) corresponds to interdendritic Laves phase and carbides (MC) (Fig. 5, *e*), which are uniformly distributed within the intercellular regions [2, 22, 34, 35]. The LPBF-built IN718 alloy specimens with a dendritic structure were characterised by increased macrohardness ($\cong 32\ HRC_{10}$). Finishing by MNF increased the surface macrohardness by $\cong 20\%$ ($\cong 39\ HRC_{10}$) owing to numerous and repetitive pin impacts, which promote near-surface plastic deformation resulting from micropeening and sliding.

Notably, based on the SEM micrographs (Fig. 5, *f*), the dendritic cells were revealed to be precisely located at the subsurface edge of the MNF-processed samples, confirming the lack of interfacial delamination, severe plastic folding or microcracking during the removal of irregularities/peaks on the LPBF-formed surface. This confirms that the numerous dynamic impacts of the metallic needles under the action of an alternating magnetic field promote a controlled removal of metal with the MNF process, in which localised work hardening is generated. Additionally, as seen in Fig. 5, *a* (as-LPBF) and Fig. 5, *b* (post-MNF), compared to the as-built IN718 alloy specimen [31], partially melted powder particles and/or adhered spherical/ellipsoidal balls were removed/reduced from the surface by the MNF finishing.

As noted above, the microstructure comprises the dendritic struc-

ture regardless of the studied condition (as-LPBF and post-MNF), containing γ [Ni–Cr–Fe] solid solution matrix with a face-centred cubic (f.c.c.) lattice, γ' [Ni_3(Al, Ti)], Laves phases [$(Ni, Fe, Cr)_2$(Nb, Mo, Ti)], and MC carbides [(Ti, Nb)C], which are identified in the initial as-LPBF condition (Fig. 6). Primary strengthening elements (such as Nb) remain largely segregated within interdendritic Laves phases and MC carbides and/or trapped in the solid solution matrix due to the extremely high cooling rates in the LPBF process.

The observed XRD patterns show a clear shift of the γ/γ' diffraction peaks toward smaller 2θ-angles after the MNF post-processing (Fig. 6), which is in strong agreement with previously published studies on surface mechanical treatment *via* severe plastic deformation of the Inconel 718 manufactured *via* LPBF [19, 36]. The (220) peak shift (Fig. 6) corresponds to lattice expansion along the normal surface, confirming the induction of beneficial residual compressive macrostresses (≅ 1 GPa) in the subsurface layer instead of the manufacturing induced tensile stresses. Additionally, the moderate broadening of the γ/γ' diffraction (220) peaks aligns with the reduction in crystallite size and the increase in lattice strain (0.32%), providing clear evidence of notable near-surface plastic deformation and dislocation accumulation ($2.41 \cdot 10^{-14}$ m^{-2}) in the parts subjected to the magnetic needle finishing process.

Thus, magnetic needle finishing is an effective method for surface post-processing of IN718 alloy parts manufactured *via* the LPBF technique. In Refs. [37, 38], it was shown that MNF treatment under a spatial composite magnetic field can significantly extend the processing range, increase the effective processing area height by 200%, and improve the uniformity of the workpiece surface morphology. The high-quality MNF finishing is attributed to microcutting material removal, surface smoothing through sliding, and surface hardening *via* micropeening. Compared to barrel finishing [39–41], which is used for the surface post-processing of complexly shaped metal components, magnetic needle finishing is a flexible post-processing method for the LPBF-manufactured small-scale components.

4. CONCLUSION

The current study demonstrated that the high-quality magnetic needle finishing (MNF process applied for surface post-processing of Inconel 718 alloy parts improved surface quality and microstructural characteristics. The surface integrity of the LPBF-manufactured nickel-based superalloy was improved by generating a smoothed surface microrelief with a strain-hardened subsurface layer, creating a synergistic effect of hardening and finishing simultaneously.

The results indicate that the magnetic needle finishing (MNF) flattened surface irregularities (R_p parameter decreased from ≅ 14.5 μm to

$\cong 6.5$ μm) and improved surface finish consistency, eliminating partially melted and adhered powder particles from the surface due to the high-speed impact of magnetic pins with different surface collisions, which promotes near-surface plastic deformation and surface smoothing (R_a decreased from $\cong 4.0$ μm to $\cong 2.0$ μm).

The functional parameters show that the formed surface reliefs in the MNF-treated samples possess the ability to suppress the initial wear during running-in ($\downarrow\downarrow S_{pk}$) and increase the load-bearing capacity due to an increase in the area of actual contact ($\uparrow S_k$).

The observed surface hardening (increased *HRC* value from $\cong 32$ HRC_{10} to $\cong 39$ HRC_{10}) and high lattice microstrain measured by XRD is attributed to the increased dislocation density and grain refinement within the fine dendritic structure of the MNF-processed near-surface layer of the IN718 alloy specimens. In addition, the XRD data confirmed formation of residual compressive macrostresses after applying the MT finishing.

ACKNOWLEDGEMENT

The authors gratefully acknowledge the support of the European Union's HORIZON 2020 Research and Innovation Programme under the Marie Sklodowska-Curie Grant (agreement No. 101034379) and the National Research Foundation of Ukraine under the Science for the Recovery of Ukraine in the War and Post-War Periods Grant (agreement No. 2022.01/0038). The work was also partially supported by the German Academic Exchange Service (DAAD) under the Research Grants for Doctoral Candidates and Young Academics and Scientists program. The authors would like to thank retired professor V. V. Dzhemelinskyi (Igor Sikorsky Kyiv Polytechnic Institute, Ukraine) and Dr. S. Martinez (University of the Basque Country) for the support provided with the MNF-post-processing tests and LPBF-manufacturing samples, respectively. Additionally, the authors would like to thank S. Faust (Otto von Guericke University Magdeburg, Germany) for the support provided with the surface roughness measurements.

AUTHORS' CONTRIBUTIONS

D.A.L. planned this research, performed the MNF experiments, analysed the experimental data, prepared the graphic material, and wrote the manuscript with input from all authors. B.M.M. collected data on integrity properties of Inconel alloys manufactured by LPBF, analysed the XRD data and took part in the preparation of the article text. O.S. reviewed the literature and collected data on advanced mechanical surface post-processing methods, obtained the surface roughness data and

analysed the functional relief performance parameters. D.G. obtained the surface topography data and analysed the functional relief performance parameters. S.S.S. reviewed the literature and collected data on advanced additive manufacturing methods and interpreted the data. M.M.L. prepared the samples for LOM and SEM observations. M.V.R. prepared the samples for LOM and SEM observations. M.I.A. discussed the results obtained. A.L. took part in the preparation of the article text and discussed the results obtained.

REFERENCES

1. G. M. Volpato, U. Tetzlaff, and M. C. Fredel, *Addit. Manuf.*, **55**: 102871 (2022).
2. A. Vafadar, F. Guzzomi, A. Rassau, and K. Hayward, *Appl. Sci.*, **11**: 103729 (2021).
3. K. Li, J. Zhan, Y. Wang, Y. Qin, N. Gong, D. Z. Zhang, S. Tan, L. E. Murr, and Z. Liu, *J. Manuf. Process.*, **133**: 285 (2025).
4. D. A. Lesyk, S. Martinez, A. Lamikiz, O. O. Pedash, and B. N. Mordyuk, *Advanced Manufacturing Processes VI. Lect. Notes Mech. Eng.* (Eds. V. Tonkonogyi *et al.*) (Cham: Springer: 2025).
5. F. Venturi and R. Taylor, *J. Mater. Eng. Perform.*, **32**: 6589 (2023).
6. R. Zhuk, Z. Chen, M. Anyakin, and J. Yao, *Int. J. Adv. Manuf. Technol.*, **108**: 1163 (2020).
7. V. Kovalenko, J. Yao, Q. Zhang, M. Anyakin, X. Hu, and R. Zhuk, *Procedia CIRP*, **42**: 96 (2016).
8. M. Sokolovskyi, O. Siora, Y. Yurchenko, V. Lukashenko, D. Harder, L. Nyrkova, S. Osadchuk, and A. Bernatskyi, *Defect Diffus. Forum*, **448**: 61 (2026).
9. P. Gradl, D. C. Tinker, A. Park, O. R. Mireles, M. Garcia, R. Wilkerson, and C. Mckinney, *J. Mater. Eng. Perform.*, **31**: 6013 (2022).
10. D. A. Lesyk, B. N. Mordyuk, S. Martinez, O. O. Pedash, and A. Lamikiz, *Advanced Manufacturing Processes VI. Lect. Notes Mech. Eng.* (Eds. V. Tonkonogyi *et al.*) (Cham: Springer: 2026).
11. T. Thuneman, K. S. Raja, and I. Charit, *Crystals*, **14**: 89 (2024).
12. D. A. Lesyk, S. Martinez, and A. Lamikiz, *Procedia CIRP*, **124**: 89 (2024).
13. S. Ozer, M. A. Yalçın, G. M. Bilgin, K. Davut, Z. Esen, and A. F. Dericioglu, *J. Alloys Compd.*, **1012**: 178465 (2025).
14. D. A. Lesyk, S. Martinez, V. V. Dzhemelinskyi, O. Stamann, B. N. Mordyuk, and A. Lamikiz, *Advances in Design, Simulation and Manufacturing III. Lect. Notes Mech. Eng.* (Eds. V. Ivanov *et al.*) (Cham: Springer: 2020).
15. D. A. Lesyk, S. Martinez, B. N. Mordyuk, V. V. Dzhemelinskyi, and A. Lamikiz, *Advances in Design, Simulation and Manufacturing VII. Lect. Notes Mech. Eng.* (Eds. V. Ivanov *et al.*) (Cham: Springer: 2024).
16. D. A. Lesyk, S. Martinez, V. V. Dzhemelinskyi, O. Stamann, B. N. Mordyuk, and A. Lamikiz, *Proc. 2020 IEEE 10th Int. Conf. Nanomaterials: Applications & Properties (NAP)* (Sumy: 2020), p. 02SAMA17-1.
17. D. A. Lesyk, A. M. Ralls, B. N. Mordyuk, P. L. Menezes, I. Charit, and A. Lamikiz, *New Technologies, Development and Application VIII. Lect. Notes Networks Syst.* (Eds. I. Karabegović *et al.*) (Cham: Springer: 2025), vol. **1482**, p. 145.
18. A. Boschetto, L. Bottini, L. Macera, and F. Veniali, *Appl. Sci.*, **10**: 138 (2020).

19. D. A. Lesyk, B. N. Mordyuk, S. Martinez, V. V. Dzhemelinskyi, D. Grochala, A. V. Kotko, and A. Lamikiz, *Coatings*, **15**, Iss. 4: 425 (2025).
20. D. A. Lesyk, V. V. Dzhemelinskyi, S. Martinez, D. Grzesiak, and B. N. Mordyuk, *Advanced Manufacturing Processes IV. Lect. Notes Mech. Eng.* (Eds. V. Tonkonogyi *et al.*) (Cham: Springer: 2023).
21. C. S. Bagherifard, N. Beretta, S. Monti, M. Riccio, M. Bandini, and M. Guagliano, *Mater. Des.*, **145**: 28 (2018).
22. D. A. Lesyk, B. N. Mordyuk, S. Martinez, V. V. Dzhemelinskyi, D. Grzesiak, D. Grochala, and A. Lamikiz, *Lasers Manuf. Mater. Process.*, **10**: 702 (2023).
23. L. Beránek, V. Rana, Z. Pitrmuc, S. Pathak, L. Pelikán, Š. Petrášek, L. Hlavůňková, P. Zeman, A. Čermák, J. Kopeček, J. Resl, J. Steklý, O. Gregor, P. Novák, and M. Maštera, *J. Mater. Res. Technol.*, **43**: 2672 (2026).
24. J. A. Banderas-Hernández, C. Rubio-González, and A. Gómez-Ortega, *Int. J. Adv. Manuf. Technol.*, **132**: 669 (2024).
25. H. Soyama, D. Eakins, and A. M. Korsunsky, *Int. J. Fatigue*, **203**: 109342 (2026).
26. L. Chen, J. Xie, Y. Li, G. Yu, X. Zhang, and X. Ren, *J. Mater. Res. Technol.*, **33**: 7668 (2024).
27. D. A. Lesyk, S. Martinez, B. N. Mordyuk, O. O. Pedash, V. V. Dzhemelinskyi, and A. Lamikiz, *Post-Processing Techniques for Additive Manufacturing* (Eds. Z. Alam, F. Iqbal, and D. A. Khan) (Boca Raton: Taylor & Francis: 2023).
28. D. A. Lesyk, B. N. Mordyuk, K. E. Grinkevych, O. O. Pedash, and A. Lamikiz, *Advances in Design, Simulation and Manufacturing VIII. Lect. Notes Mech. Eng.* (Eds. V. Ivanov *et al.*) (Cham: Springer: 2025).
29. D. A. Lesyk, S. Martinez, B. N. Mordyuk, D. Grochala, and A. Lamikiz, *New Technologies, Development and Application VII. Lect. Notes Networks Syst.* (Eds. I. Karabegović *et al.*) (Cham: Springer: 2024), vol. **1069**, p. 201.
30. H. Zou, J. Ying, X. Ma, Y. Chen, B. Han, and J. Zhan, *Surf. Sci. Technol.*, **2**, No. 17: 46 (2024).
31. J. Guo, K. H. Au, C.-N. Sun, M. H. Goh, C. W. Kum, K. Liu, J. Wei, H. Suzuki, and R. Kang, *J. Mater. Process. Technol.*, **264**: 422 (2019).
32. M. Marczak, D. A. Moszczynska, and A. P. Wawrzyszcz, *Appl. Sci.*, **15**, Iss. 15: 8233 (2025).
33. Y. Zhao, J. Ratay, K. Li, H. Yamaguchi, and W. Xiong, *J. Manuf. Mater. Process.*, **6**, Iss. 2: 43 (2022).
34. L. Emanuelli, F. Deirmina, and M. Pellizzari, *Mater. Charact.*, **199**: 112788 (2023).
35. W. Tillmann, C. Schaak, J. Nellesen, M. Schaper, M. E. Aydinöz, and K.-P. Hoyer, *Addit. Manuf.*, **13**: 93 (2017).
36. D. A. Lesyk, S. Martinez, O. O. Pedash, V. V. Dzhemelinskyi, and A. Lamikiz, *MRS Adv.*, **7**: 197 (2022).
37. X. Xu, Q. Shen, B. Han, J. Tang, J. Ying, and H. Yang, *J. Magn. Magn. Mater.*, **630**: 173458 (2025).
38. G. Liu, H. Yang, X. Xu, and B. Han, *JMMM*, **655**: 174353 (2026).
39. Y. Kaynak and E. Tascioglu, *Prog. Addit. Manuf.*, **5**: 221 (2020).
40. M. Ham, S. Park, H. Lee, D. H. Kim, J. H. Sung, G. K. Ahn, G. S. Kim, and B. Lee, *J. Manuf. Process.*, **156A**: 569 (2025).
41. M. Khorasani, A. H. Ghasemi, E. Farabi, M. Leary, I. Gibson, and B. Rolfe, *Int. J. Adv. Manuf. Technol.*, **120**: 3471 (2022).

Metallophysics and Advanced Technologies
Металофіз. новітні технол.
Metallofiz. Noveishie Tekhnol.
2026, vol. 48, No. 8, pp. 843–863
https://doi.org/10.15407/mfint.48.08.0843
Reprints available directly from the publisher

© 2026 G. V. Kurdyumov Institute for Metal Physics,
National Academy of Sciences of Ukraine
Published by license under
the G. V. Kurdyumov Institute for Metal Physics–
N.A.S. of Ukraine Publishers imprint.
Printed in Ukraine.

PACS numbers: 43.35.+d, 61.72.Dd, 61.72.Ff, 62.20.Qp, 68.35.Ct, 81.20.Ev, 81.65.Ps

Порівняння ефективности високочастотного ударного зміцнення у вібраційних камерах поверхні титанового стопу ВТ6, виготовленого металурґійним та адитивним способами

С. М. Волошко, А. П. Бурмак, Б. М. Мордюк*, М. О. Васильєв*, Т. А. Красовський**, О. А. Вислий

НТУ України «КПІ імені Ігоря Сікорського»,
вул. Політехнічна, 35,
03056 Київ, Україна
**Інститут металофізики ім. Г. В. Курдюмова НАН України,*
бульв. Академіка Вернадського, 36,
03142 Київ, Україна
***Київський академічний університет,*
бульв. Академіка Вернадського, 36,
03142, Київ, Україна

Досліджено особливості зміцнення поверхні титанового стопу ВТ6, виготовленого металурґійним (гарячим вальцюванням (ГВ)) та адитивним способом селективного лазерного топлення (СЛТ), із застосуванням двох типів ультразвукових установок, які забезпечують різні моди збудження вібраційної камери, наповненої крицевими кульками, — високочастотно-

Corresponding author: Svitlana Mykhaylivna Voloshko
E-mail: voloshkosvetlana13@gmail.com

National Technical University of Ukraine 'Igor Sikorsky Kyiv Polytechnic Institute',
35 Polytechnic Str., UA-03056 Kyiv, Ukraine
G. V. Kurdyumov Institute for Metal Physics, N.A.S. of Ukraine,
36 Academician Vernadsky Blvd., UA-03142 Kyiv, Ukraine
Kyiv Academic University,
36, Academician Vernadsky Blvd., UA-03142, Kyiv, Ukraine

Citation: S. M. Voloshko, A. P. Burmak, B. M. Mordyuk, M. O. Vasylyev, T. A. Krasovskyi, and O. A. Vyslyi, Comparison the Efficiency of High-frequency Impact Surface Hardening of Ti–6Al–4V Titanium Alloy Manufactured by Metallurgical or Additive Routs in Vibration Chambers, *Metallofiz. Noveishie Tekhnol.*, **48**, No. 8: 843–863 (2026) (in Ukrainian). DOI: 10.15407/mfint.48.08.0843

© Publisher PH 'Akademperiodyka' of the NAS of Ukraine, 2026. This is an open access article under the CC BY-ND license (https://creativecommons.org/licenses/by-nd/4.0)

го зміцнення кульками (ВЧЗК) і віброкамери з коливаннями її дна та стінок. Показано, що пониження шерсткости поверхні, формування стискальних залишкових напружень і значного зміцнення вдається досягти незалежно від схеми ініціювання ударів кульками у використаних ультразвукових віброкамерах за умови вибору певних оптимальних режимів оброблення. Впродовж 4 хв обробляння за допомогою використаних ультразвукових установок ВЧЗК і віброкамери досягнуто зміцнення зразків після гарячого вальцювання на 22,6% (4,72 ГПа) і 24,9% (4,81 ГПа) відповідно. Зміцнення зумовлено формуванням залишкових стискальних напружень (–1560 МПа) під час обробляння у віброкамері порівняно з ВЧЗК (–1240 МПа), подрібненням кристалітів α- (14–19 нм) і β-фаз (36–63 нм) у порівнянні з вихідним станом (150 нм і 174 нм відповідно). СЛТ-зразки після ВЧЗК і віброкамери зазнають зміцнення на 51% (6,61 ГПа) і 46,7% (6,41 ГПа) відповідно порівняно із вихідним станом (4,37 ГПа). У порівнянні з установкою ВЧЗК запропонована віброкамера дає змогу одержати як поздовжні коливання її дна, так і концентричні коливання стінок, що підвищує ефективність стабільного та керованого експрес-обробляння деталів і вузлів складної форми, а також пласких і тонких металевих деталів типу лопатей двигунів.

Ключові слова: селективне лазерне топлення, високочастотне зміцнення поверхні кульками, шерсткість, залишкові напруження, мікротвердість.

The features of the surface hardening of titanium alloy Ti–6Al–4V manufactured by metallurgical (hot rolling (HR)) and additive selective laser melting (SLM) methods are investigated, using two types of ultrasonic installations, which provide different modes of excitation of a vibration chamber filled with steel balls, namely, high-frequency ball hardening, *i.e.*, surface mechanical attrition treatment (SMAT), and a vibration chamber with oscillations of its bottom and walls. It is shown that a surface roughness reduction, the formation of compressive residual stresses and significant hardening can be achieved regardless of the initiating scheme of ball impacts in the used ultrasonic vibration chambers, if certain optimal processing modes are selected. Within 4 minutes of treatment using the SMAT unit and the vibration chamber, the HR samples are strengthened by 22.6% (4.72 GPa) and 24.9% (4.81 GPa), respectively. The strengthening is due to the formation of residual compressive stresses (of –1560 MPa) during processing in the vibration chamber compared to SMAT (of –1240 MPa), the refinement of α- (of 14–19 nm) and β-phase (of 36–63 nm) crystallites compared to the initial state (of 150 nm and 174 nm, respectively). The SLM samples after SMAT and the vibration chamber undergo strengthening by 51% (6.61 GPa) and 46.7% (6.41 GPa), respectively, compared to the initial state (4.37 GPa). Compared to SMAT unit, the proposed vibration chamber allows producing both longitudinal vibrations of its bottom and concentric vibrations of the walls that increases the efficiency of stable and controlled express processing of parts and assemblies of complex shape, as well as flat and thin metal parts such as engine blades.

Key words: selective laser melting, surface mechanical attrition treatment, roughness, residual stresses, microhardness.

(Отримано 26 вересня 2025 р.; остаточн. варіянт — 10 березня 2026 р.)

1. ВСТУП

Титан і його стопи посідають одне з провідних місць серед конструкційних матеріялів для авіяційної, космічної, енергетичної та медичної промисловостей завдяки високому співвідношенню міцности до густини, корозійній стійкості та здатності працювати за екстремальних температурних умов [1, 2]. Одним із найбільш використовуваних стопів у цій групі є стоп Ti–6Al–4V (ВТ6), що характеризується стабільним фазовим складом і придатністю до різних способів термічного та механічного оброблянь [3]. Останнім часом зростає інтерес до адитивного виробництва (АВ) деталів із титанових стопів [4, 5], зокрема методою селективного лазерного топлення (СЛТ), що дає змогу виготовляти вироби складної геометрії з мінімальною кількістю відходів [6].

Разом із тим, відомо, що структура та властивості титанових стопів, одержаних СЛТ, істотно відрізняються від матеріялів традиційної металурґії через високі ґрадієнти температур і швидкість охолодження у процесі формування шарів [7]. Це призводить до утворення текстурованих структур, анізотропії механічних властивостей і високого рівня залишкових напружень, що може неґативно впливати на експлуатаційні характеристики деталів [8]. Для усунення цих недоліків і поліпшення властивостей поверхневого шару перспективним є використання різних високочастотних механічних методів поверхневого модифікування як фінішного постпроцесу [9]. Серед них важливе місце займають поверхневі ультразвукові технології інтенсивної пластичної деформації (ІПД) [10], які мають високу ефективність і дають змогу формувати наноструктурований зміцнений шар металевої поверхні із вигідним розподілом залишкових напружень стиснення [11, 12]. Це повною мірою стосується й адитивно виготовленого титанового стопу ВТ6, властивості й експлуатаційний ресурс якого можна значно поліпшити, наприклад, вдвічі підвищити граничну втомну міцність [13]. Це особливо важливо для виробів, що працюють в умовах циклічного змінного навантаження, таких як лопаті, компресорні диски газотурбінних двигунів літаків та інші деталі складної форми. Оскільки найбільш істотною перевагою АВ є саме можливість виготовляти вироби складної геометричної форми, це потребує вибору відповідного ультразвукового обладнання та прикладеної енергії для забезпечення можливости оброблення великих площ поверхонь складної геометрії.

З цієї точки зору серед низки поверхневих методів ІПД, таких як ультразвукове обкочування поверхні роликами [14], ультразвукове нанокристалічне модифікування поверхні [15], ультразвукове уда-

рне оброблення [16], найбільш придатною є технологія високочастотного зміцнення кульками (ВЧЗК — SMAT—surface mechanical attrition treatment) [17]. Суть такого оброблення полягає в наступному. Оброблюваний зразок складної форми розміщується у камері, оснащеній вібраційним ґенератором, і обробляється крицевими кульками зазвичай із неіржавійної криці. Частота вібрації вакуумної камери може змінюватися в межах від 20 Гц до 20 кГц. В процесі обробляння кульки резонують і вдаряються об поверхню зразка впродовж певного проміжку часу. Швидкість польоту та кінетична енергія кульок залежать від частоти ґенератора, віддалі до поверхні зразка, а також їхнього розміру (маси). Напрямки ударів кульок об поверхню є випадковими та завдяки таким багаторазовим локалізованим механічним ударам із високою частотою досягається інтенсивна пластична деформація, що сприяє подрібненню зеренної структури, закриттю мікродефектів, зменшенню поруватости та підвищенню зносостійкости й втомної міцности [18]. Водночас параметри (частота й амплітуда) ультразвукових коливань, тривалість обробляння чинять істотний вплив на кінцевий результат зміцнення [19].

Незважаючи на значну кількість праць, присвячених ВЧЗК, більшість досліджень стосується титанових стопів традиційного виробництва, зокрема після гарячого вальцювання або штампування [20, 21]. Вплив ВЧЗК на стоп ВТ6, одержаний СЛТ, досліджено недостатньо. З огляду на відмінності структур, кількостей і типів дефектів (дислокації, пори, мікротріщини) та рівнів залишкових напружень, можна припустити, що ефективність ВЧЗК для такого матеріялу матиме свої особливості [22].

Крім того, сучасні дослідження демонструють необхідність оптимізації режимів ультразвукового оброблення залежно від типу вихідної структури матеріялу. Зокрема, роботи [17, 18, 23, 24] вказують, що для адитивних заготівок характерною є вища чутливість до режимів навантаження, що пов’язане з наявністю дрібнозернистих колонних структур і нерівномірного розподілу фаз. Важливим є також тип застосованої вібраційної камери, оскільки за різних конструкцій і методів збудження її різною може бути й оптимальна кінетична енергія кульок, що здійснюють деформаційне модифікування поверхні деталів складної форми. Це створює передумови для більш детального вивчення ефективности різних способів ВЧЗК залежно від технології одержання титанових стопів.

Таким чином, метою даної роботи є дослідження впливу різних способів ВЧЗК за допомогою спеціяльно виготовленого для цього високотехнологічного цифрового ультразвукового обладнання на морфологію поверхні, структуру, фазовий склад і механічні властивості титанового стопу ВТ6, одержаного методою СЛТ. Для порівняння використано також промисловий стоп ВТ6, одержаний га-

рячим вальцюванням (ГВ). Одержані результати дають змогу визначити оптимальні параметри фінішного оброблення адитивно виготовлених деталів зі стопу ВТ6 складної форми для підвищення їхніх експлуатаційних характеристик, що є актуальним завданням задля розвитку сучасних технологій у авіякосмічній, енергетичній і біомедичній галузях.

2. МЕТОДИКА ЕКСПЕРИМЕНТУ

Використовувалися зразки титанового стопу ВТ6 з наступним хемічним складом (ваг.%): Ti — 85,21, Al — 6,18, V — 4,28, одержані гарячим вальцюванням і селективним лазерним топленням.

ГВ-зразки у вигляді пластин довжиною у 20 мм, шириною у 10 мм і товщиною у 5 мм (±0,5 мм) були одержані різанням прутків перпендикулярно напрямку вальцювання.

СЛТ-зразки було виготовлено на 3*D*-принтері Alfa-150D компанії «АЛТ України» («Адитивні лазерні технології України»). Номінальна потужність волоконного ітербійового лазера з довжиною хвилі у 1070 ± 2 нм складала 200 Вт, фокусний діяметер лазерного променя — 45 мкм, швидкість сканування — 500 мм/с, товщина шару — 25 мкм і віддаль штрихування — 150 мкм. Використовували сферичний порошок стопу Ti–6Al–4V дисперсністю у 15–53 мкм. Для запобіження окисненню виготовлення зразків проводилося в інертному середовищі Ar.

Високочастотне ударне зміцнення поверхні зразків стопу ВТ6 без попереднього шліфування проводилось із використанням кульок діяметром у 2 мм із неіржавійної криці з використанням двох різних устатковин. Перша — це камера ВЧЗК (рис. 1, *а*), у якій енергія ультразвукових коливань через торець сонотрода, розміщеного на дні камери, передається металевим кулькам і стимулює їхній рух у обмеженому об’ємі повітряного середовища дослідної камери та високочастотні удари по поверхні зразка (далі — оброблення I-типу). Друга — це віброкамера (рис. 1, *б*), вібрування стінок і дна якої забезпечує кульки кінетичною енергією (далі — оброблення II-типу). За допомогою ВЧЗК за схемою II-типу вдається зменшити кількість технологічних операцій оброблення виробів складної та ножеподібної форми (типу пера лопатки компресора чи газотурбінного двигуна) у порівнянні зі схемою I-типу (рис. 1, *а*), яка передбачає оброблення лише з одного боку плаского або рельєфного виробу та наступну зміну площини оброблення чи то використання двох зустрічних акустичних систем, під’єднаних до однієї камери (рис. 1, *в*), що веде до збільшення економічних витрат.

Камери інтеґруються до ультразвукової вібраційної системи, яка складається з ультразвукового п’єзокерамічного перетворювача, перетворювача швидкости коливань (бустера) та концентратора

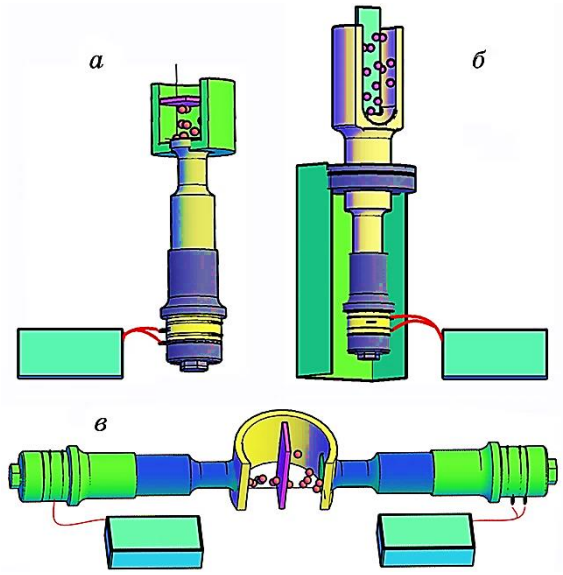


Рис. 1. Схематичне зображення установки ВЧЗК для оброблення I-типу (*а*, *в*) та віброкамери (сонотрод-концентратор) для оброблення II-типу (*б*) [20].

Fig. 1. Schematic view of device for high-frequency ball hardening of I-type treatment (*а*, *в*) and vibrochamber (sonotrode–concentrator) for II-type treatment (*б*) [20].

(сонотрода) й живиться від цифрового електронного ґенератора [20]. Амплітуда ультразвукових механічних коливань (пік-пік) становила 25 мкм, тривалість оброблення змінювалася від 2 хв до 8 хв, віддаль до зразка — 10 мм, кількість кульок — 35.

Перетворювач із високим коефіцієнтом ефективности трансформує високочастотну електричну енергію у потужні ультразвукові механічні коливання з частотою близько 20 кГц, які передаються через бустер і підсилюються сонотродом. Енергія ультразвукових коливань через торець сонотрода передається металевим кулькам і стимулює рух їх у замкненому повітряному об'ємі експериментальної камери та високочастотні удари по поверхні зразка. Задля зменшення дисипативних втрат під час коливань сонотрод устатковини виготовлено з титанового стопу ВТ22.

Електронний ґенератор із повністю цифровим керуванням подає живлення на п'єзокерамічний перетворювач. У схемі ґенератора застосовано сучасні мікропроцесорні технології: синтезу частоти DDS (Direct Digital Synthesis), цифрове фазове автоналаштування резонансного режиму з автоматичною адаптацією до тієї чи іншої акустичної системи. Ґенератор обладнано реґулятором і стабіліза-

тором амплітуди ультразвукових механічних коливань у діяпазоні від 5 до 100% (60 мкм) і реґулятором часу роботи за допомогою цифрового таймера від 0,01 с до 30 хв. Напруга живлення ґенератора становить 220 В, а вихідна потужність — до 2000 Вт.

Мікроструктуру досліджено з використанням оптичного металографічного мікроскопа iScope IS.1053-PLMi, а мікротвердість за методою Віккерса — за допомогою приладу LHVS-1000Z (навантаження у 100 г з витримкою у 10 с).

Морфологію поверхні зразків досліджено за допомогою стереомікроскопа Crystal 45 Konus із збільшенням у діяпазоні від ×7 до ×45 крат залежно від масштабів структурних особливостей і характеру поверхневих дефектів. Для поліпшення контрастности рельєфу використовували реґульоване світлодіодне освітлення стереомікроскопа, змінюючи кут падіння світла.

Для визначення поверхневого рельєфу та макроструктури застосовано профілометер JITAI-8103 Plus.

Для рентґеноструктурних досліджень використано дифрактометр Rigaku Ultima IV (випромінення — $\lambda_{K\alpha}$-Cu): інтервал кутів $2\theta = 20°–120°$, крок реєстрації — 0,04°, час витримки в точці — 2 с. Кількісний фазовий склад стопу ВТ6 розраховувався на основі інтеґральної інтенсивности неперекривних дифракційних максимумів, характерних для кожної фази, за Рітвельдовою методою у програмному забезпеченні PDXL. Уточнення фазового складу здійснювали шляхом підбору структурних моделів α-Ti (ГЩП, 194: $P6_3/mmc$) і β-Ti (ОЦК, 229: $Im–3m$) з бази ICSD (Inorganic Crystal Structure Database) й уточнення масштабних факторів, параметрів ґратниці, профілю дифракційних максимумів і фону. Застосовувалися функція профілю «псевдо-Фогт» і фонове моделювання поліномом. За результатами уточнень визначали кількісний фазовий склад, розмір областей когерентного розсіяння (ОКР) і ступінь деформації кристалічної ґратниці (ε).

Визначення величини напружень 1-го роду проведено методою $\sin2\psi$ за зміною кутового положення дифракційного максимуму α-Ti(110) для значень кутів $\psi = 0°, –5, –10, –15, –20$. Для згладжування профілів дифракційних максимумів використовувалася Savitzky–Golay-функція, а для відокремлення фону — Sonneveld–Vissers-функція. Визначення кутового положення дифракційних максимумів проводилося на основі значень положення центру ваги. Обробку одержаних даних проведено з використанням програмного забезпечення Rigaku Residual Stress Analysis.

3. РЕЗУЛЬТАТИ Й ОБГОВОРЕННЯ

На рисунку 2 показано зміни мікротвердости поверхонь зразків стопу Ti–6Al–4V, оброблених двома різними ультразвуковими

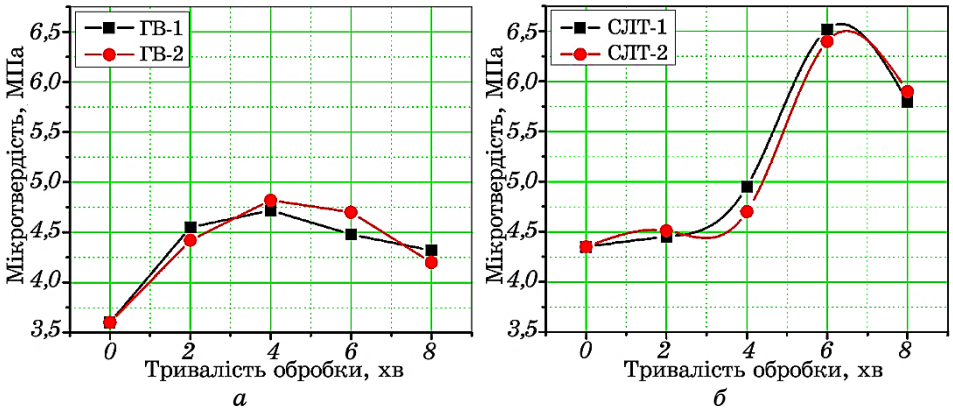


Рис. 2. Зміна мікротвердости ГВ- (*а*) та СЛТ-стопу ВТ6 (*б*) в залежності від тривалости ВЧЗК: 1 — оброблення I-типу, 2 — оброблення II-типу.

Fig. 2. Change of microhardness of HR (*a*) and SLM (*b*) Ti–6Al–4V alloy samples after SMAT (I-type) (1) and vibrochamber (II-type) (2) treatments.

устатковинами впродовж різного часу. Вихідне значення мікротвердости для ГВ-зразка складає 3,93 ГПа, для СЛТ-зразка — 4,37 ГПа. Після різних типів оброблення спостерігається аналогічна тенденція змін мікротвердости з часом, а саме, зростання її величини до максимального значення з наступним зменшенням внаслідок релаксаційних процесів. Для ГВ-зразків максимальні значення мікротвердости досягаються за 4 хв і становлять 4,72 ГПа (+20%) і 4,81 ГПа (+22,4%) після оброблень I-типу та II-типу відповідно. Таким чином, досягається майже однакове зміцнення, зумовлене обома типами оброблення. Після 8 хв деформаційного впливу мікротвердість зменшується до 4,32 ГПа і 4,2 ГПа для оброблення I-типу та II-типу відповідно.

Зміни мікротвердости СЛТ-зразків починають спостерігатися лише після оброблень обох типів упродовж 4 хв. Основна відмінність поведінки мікротвердости СЛТ-зразків від ГВ-зразків полягає в тому, що максимальні значення мікротвердости у 6,61 ГПа і 6,41 ГПа для оброблення I-типу та II-типу відповідно досягаються за час у 6 хв. В даному разі зміцнення становить 51% і 46,7%, а його ефективність є дещо вищою для оброблення I-типу. Надалі спостерігається знеміцнення після 8 хв деформаційного впливу до значень у 5,81 ГПа і 5,92 ГПа для оброблень I-типу і II-типу відповідно.

Вочевидь, наявність певного «інкубаційного» періоду відносно сталої мікротвердости СЛТ-зразків пов'язана з вищими величинами шерсткости їхньої поверхні, елементи якої деформуються впродовж перших 3 хв оброблення (рис. 2, *а*, *б*).

Параметри шерсткости поверхні зразків до та після оброблення

ТАБЛИЦЯ 1. Характеристики шерсткости поверхні стопу ВТ6 після оброблень різних типів.

TABLE 1. Dependences of the surface roughness of Ti–6Al–4V alloy on the time of treatments of different types.

Стан зразка			Параметри шерсткости		
Умови одержання	Тип оброблення	Тривалість оброблення, хв	R_a, мкм	R_q, мкм	R_z, мкм
СЛТ	вихідний	–	5,750	7,190	34,341
СЛТ	I	4	4,072	4,761	21,786
СЛТ	I	6	3,27	4,253	22,707
СЛТ	I	8	3,593	4,437	22,939
СЛТ	II	4	8,024	10,623	54,570
СЛТ	II	6	5,133	6,548	34,115
СЛТ	II	8	4,677	6,069	32,081
ГВ	вихідний	–	1,336	1,681	8,832
ГВ	I	4	1,654	2,321	8,925
ГВ	I	8	2,524	3,234	10,567
ГВ	II	4	1,425	1,743	9,076
ГВ	II	8	3,915	4,787	21,398

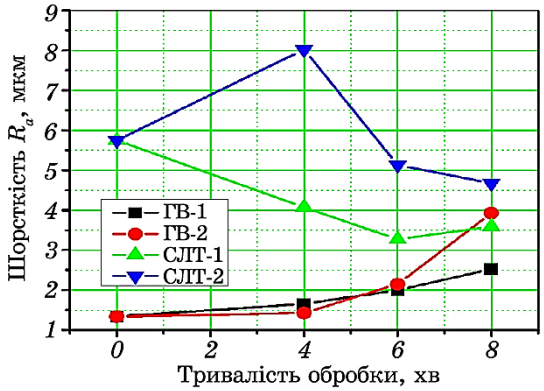


Рис. 3. Залежності шерсткости поверхні стопу ВТ6 від часу оброблень різних типів.

Fig. 3. Dependences of the surface roughness of Ti–6Al–4V alloy on the time of treatments of different types.

наведено в табл. 1.

На рисунку 3 наведено залежності середньоарифметичної шерсткости R_a ГВ- і СЛТ-зразків від тривалости їх оброблень обох типів. У вихідному стані середнє значення шерсткости R_a СЛТ-зразка є у 4,3

рази більшим порівняно із ГВ-зразком. Після оброблення I-типу СЛТ-зразка упродовж 4 хв величина R_a зменшується до 4,072 мкм, а для II-типу — збільшується до $\cong 8$ мкм внаслідок утворення западин і виступів, тоді як для ГВ-зразків істотних змін не відбувається. Збільшення тривалости деформаційного впливу зумовлює поступове зменшення шерсткости поверхні СЛТ-зразка до $\cong 3{,}6$ і $\cong 4{,}7$ мкм залежно від типу оброблення.

Слід зазначити, що після 8 хв оброблення II-типу в деяких ділянках СЛТ-зразка, які вільні від смуг і мають гладку морфологію, значення R_a зменшується (порівняно із 4 хв) практично на порядок величини — до $\cong 0{,}8$ мкм, тоді як для ГВ-зразка R_a навпаки збільшується практично втричі (у 2,75 разів).

Причиною більшої вихідної мікротвердости СЛТ-зразків також є особливості їхньої структури. Результатом циклічної термічної історії, яку зазнає зразок під час СЛТ, є формування шаруватої смугастої макроструктури з α- та β-фази (рис. 4, *а*, *б*), яка забезпечує вищі значення мікротвердости 3*D*-виробів порівняно з будь-якими іншими технологіями виробництва [25]. Дійсно, процес АВ деталів зі стопу Ti–6Al–4V є унікальним через те, що після 3*D*-друку може бути досягнуто надзвичайно дисперсну мікроструктуру, що має подібність до тієї, яка спостерігається після зварювання або гартування [26]. Така дрібнозернистість і значна густина дислокацій, як у АВ-стані, так і після оброблень I-типу та II-типу, забезпечують більші значення мікротвердости СЛТ-зразка, ніж структура після гарячого вальцювання, яка ще й може мати ознаки кристалографічної текстури. Разом з тим, ефект зміцнення ГВ- і СЛТ-зразків за умов оброблень обох типів майже однаковий і складає 1,5 ГПа і 2 ГПа відповідно.

Під час ударної механічної деформації у віброкамері (II-тип обро-

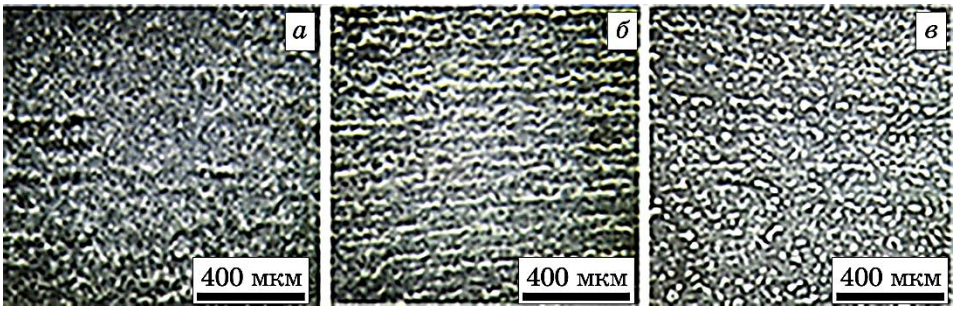


Рис. 4. Дезінтеґрація вихідної шаруватої СЛТ-структури (*а*) після оброблення II-типу упродовж 4 хв (*б*) та 8 хв (*в*) (збільшення ×25 крат).

Fig. 4. Disintegration of the initial layered SLM structure (*а*) after II-type treatment for 4 min. (*б*) and 8 min. (*в*) (magnification ×25).

блення) така шаруватість гальмує внесок напружень з протилежного боку зразка до вислідних напружень в об'ємі і, відповідно, в досліджуваному приповерхневому шарі. Із збільшенням часу оброблення смуги ущільнюються та виконують роль стопора для дислокацій, що ґенеруються в процесі пластичної деформації, і це забезпечує вищий рівень зміцнення СЛТ-зразків порівняно з ГВ-зразками (незалежно від типу оброблення). З подальшим збільшенням часу обробляння накопиченої деформації стає достатньо для переривання смуг і подрібнення їх на окремі фраґменти. Це може стати однією з додаткових причин зменшення значень мікротвердости, що спостерігається для СЛТ-зразків із перевищенням 6 хв оброблення. Такі складні трансформації значно розширюють діяпазон досяжних мікроструктур і механічних властивостей для АВ-деталів зі стопу Ti–6Al–4V (залежно від типів і режимів механічного оброблення).

Розглянемо більш докладно особливості морфології поверхні зразків (рис. 5), оброблених двома різними ультразвуковими устатко-

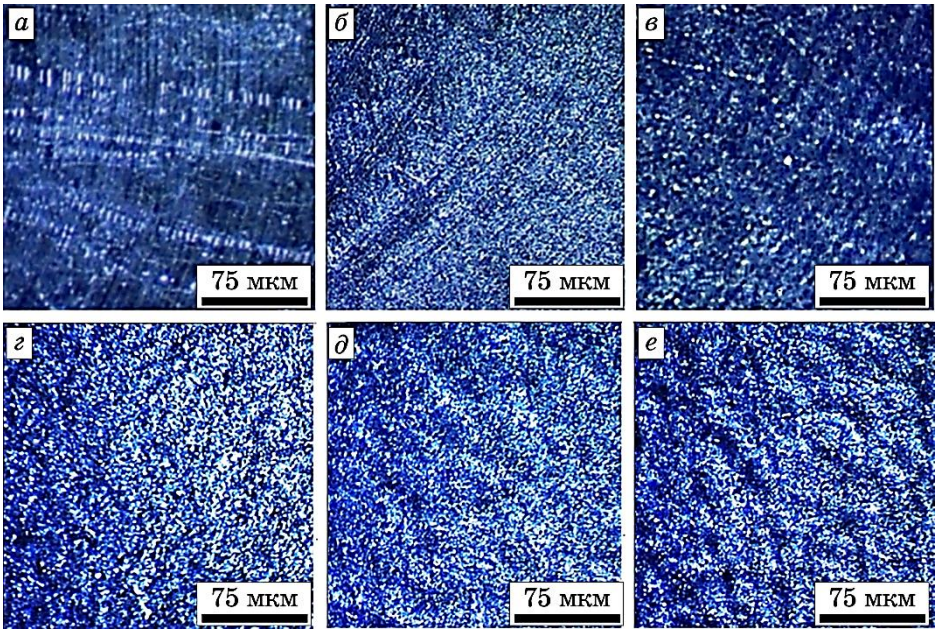


Рис. 5. Морфологія поверхні (*а*–*в*) ГВ- і (*г*–*е*) СЛТ-зразків стопу ВТ6: *а*, *г* — вихідний стан; *б*, *д* — оброблення I-типу, $\tau = 8$ хв; *в*, *е* — оброблення II-типу, $\tau = 8$ хв (×150).

Fig. 5. Surface morphology of HR (*а*–*в*) and SLM (*г*–*е*) samples of Ti–6Al–4V alloy: *а*, *г*—the initial state; *б*, *д*—I-type treatment, $\tau = 8$ min.; *в*, *е*—II-type treatment, $\tau = 8$ min. (×150).

винами. Порівняно з початковим станом, після ударного впливу морфологія поверхні ГВ- і СЛТ-зразків зазнає помітних змін, які проявляються у формуванні характерного ямкового рельєфу, але ступінь цих змін є різним. Після максимального часу оброблення II-типу поверхневий рельєф є більш дрібним і рівномірним для СЛТ-стопу (рис. 5, *е*) порівняно з ГВ-стопом (рис. 5, *в*). Водночас, навіть після максимальної тривалости оброблення, пошкодження поверхні з утворенням мікротріщин або інших дефектів, які можуть неґативно вплинути на механічні характеристики, не відбуваються ані для СЛТ-стопу, ані для ГВ-стопу (рис. 6).

Оскільки для СЛТ-стопу максимальне значення мікротвердости спостерігається після 6 хв інтенсивної пластичної деформації, на рис. 7 додатково наведено порівняння впливу оброблень I-типу та

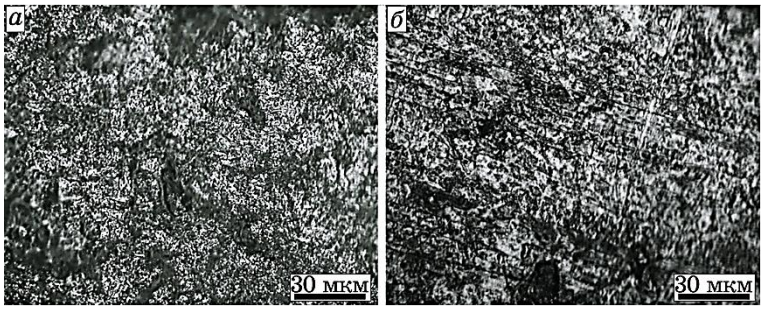


Рис. 6. Мікроструктура поверхні (*а*) СЛТ- і (*б*) ГВ-зразків стопу ВТ6 після оброблення I-типу, $\tau = 8$ хв (×400).

Fig. 6. Microstructure of the surface of SLM (*а*) and HR (*б*) samples of Ti–6Al–4V alloy after I-type treatment, $\tau = 8$ min. (×400).

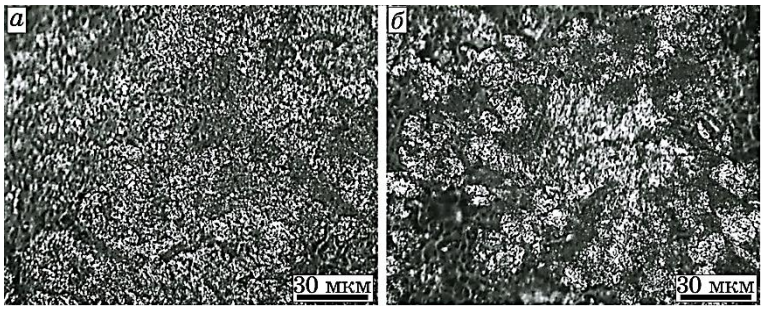


Рис. 7. Мікроструктура поверхні СЛТ-стопу ВТ6 після оброблення упродовж $\tau = 6$ хв: I-типу (*а*) та II-типу (*б*) (×400).

Fig. 7. Microstructure of the surface of SLM samples of Ti–6Al–4V alloy after I-type treatment (*а*) and II-type treatment (*б*) for $\tau = 6$ min. (×400).

II-типу саме такої тривалости на мікроструктуру поверхні. Для II-типу оброблення поверхня виглядає більш подрібненою із більшою глибиною западин.

Для виявлення структурно-фазових змін у стопі ВТ6, одержаному й обробленому різними способами, застосовано рентґеноструктурну аналізу (рис. 8 і 9). Визначено кількісний фазовий склад, розмір областей когерентного розсіяння, ступінь деформації кристалічної ґратниці та макронапруження I роду (табл. 2 і 3). Порівнювався структурно-фазовий стан зразків стопу ВТ6 після оброблення на максимальну твердість ($\tau = 4$ хв для ГВ- і $\tau = 6$ хв для СЛТ-зразка), а також після релаксації напружень ($\tau = 8$ хв).

На рисунку 8, *а* представлено фраґменти дифрактограм для вихідного стану ГВ-зразків і після оброблення I- і II-типу тривалістю у 4 хв і 8 хв. Основні рефлекси відповідають α-фазі титану із ГЩП-ґратницею та β-фазі з ОЦК-ґратницею. У вихідному стані цей двофазний стоп містить більшу кількість об'ємної частки α-фази; об'ємна частка β-фази складає не більше 15%. Після оброблення I- та II-типу тривалістю у 4 хв відбувається формування деформаційної текстури та переорієнтація зерен під дією повторюваних імпу-

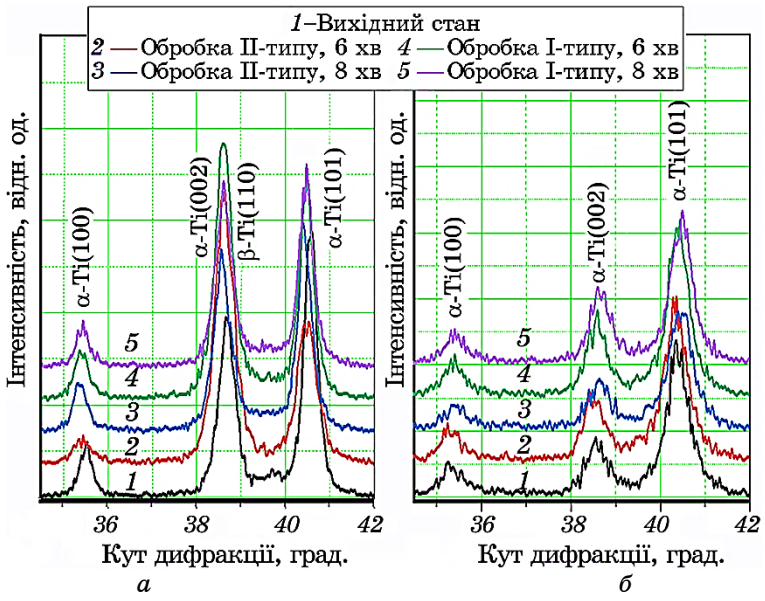


Рис. 8. Фраґменти дифрактограм (*а*) ГВ- і (*б*) СЛТ-зразків стопу ВТ6 у вихідному стані та після оброблення I-типу і II-типу різної тривалости.

Fig. 8. Fragments of x-ray spectra of HR (*а*) and SLM (*б*) samples of Ti–6Al–4V alloy in the initial state and after I-type and II-type treatments for various durations.

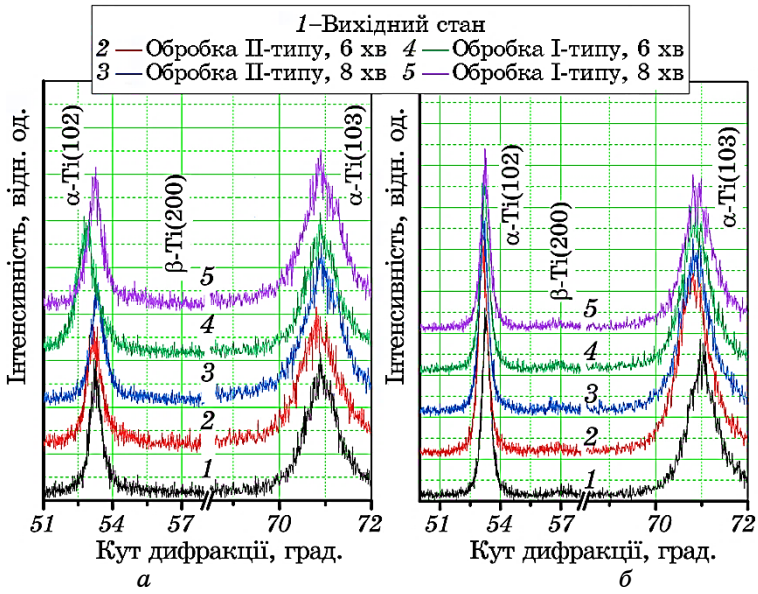


Рис. 9. Фраґменти дифрактограм (*а*) ГВ- і (*б*) СЛТ-зразків стопу ВТ6 у вихідному стані та після оброблення I-типу і II-типу різної тривалости.

Fig. 9. Fragments of x-ray spectra of HR (*а*) and SLM (*б*) samples of Ti–6Al–4V alloy in the initial state and after I-type and II-type treatments for various durations.

льсних ударів, що проявляється в зростанні інтенсивности рефлексу (002) й пониженні інтенсивности рефлексу (101) від α-фази титану. Більш тривале оброблення упродовж 8 хв зумовлює збільшення напівширини дифракційних максимумів і зменшення текстури в напрямку [001]. Кількість β-фази практично не змінюється для оброблення I-типу та дещо зменшується для оброблення II-типу.

На рисунку 8, *б* наведено фраґменти дифрактограм для СЛТ-стопу ВТ6. У порівнянні з ГВ-зразком у структурі СЛТ-стопу спостерігається 93% α-фази. Оскільки α-фаза має більшу мікротвердість, ніж β-фаза, це є ще однією з причин більшої мікротвердости СЛТ-зразка у вихідному стані порівняно з ГВ-зразком.

Після оброблення інтенсивність рефлексу (002) від α-фази дещо зростає у порівнянні з вихідним станом, особливо для випадку оброблення I-типу тривалістю у 8 хв. Це свідчить про переорієнтацію зерен за напрямком переважної текстури під дією багаторазових імпульсних навантажень [27]. Одночасно інтенсивність рефлексу (101) α-фази зменшується, що підтверджує формування деформаційної текстури та переорієнтацію кристалів.

Кількість β-фази після оброблення будь-якого типу дещо збіль-

шується до 10–11% порівняно із вихідним станом, але залишається втричі меншою, ніж у ГВ-зразках. Відсутність змін кількісного фазового складу свідчить, ймовірно, що основні трансформації, які зумовлюють різке збільшення мікротвердости для СЛТ-зразка після 6 хв оброблення стосуються α-фази.

Крім того, після оброблення дифракційні профілі помірно розширюються, що пов'язане із подрібненням зеренної структури та зростанням рівня мікродеформацій кристалічної ґратниці. Подібні ефекти спостерігалися під час ультразвукового ударного зміцнення у роботах [28] і [22], де відзначено, що інтенсивна пластична деформація СЛТ-стопів супроводжується формуванням субзерен з високою густиною дислокацій.

Можна зробити висновок, що всі ультразвукові процеси зумовлюють дроблення кристалітів у приповерхневому шарі ГВ-стопу. Водночас мінімальний розмір кристалітів ГВ-стопу був зафіксований після II-типу оброблення у віброкамері: для α-фази (14 нм) упродовж часу 4 хв, який відповідає максимальному значенню мікротвердости, а для β-фази (17 нм) упродовж 8 хв (табл. 2). Розмір ОКР, як для α-фази, так і для β-фази СЛТ-стопу у вихідному стані, є значно меншим порівняно із ГВ-стопом. Після оброблення як I-, так і II-типу істотних змін розміру ОКР не відбувається. Тобто подрібнення зерен є визначальним чинником змін мікротвердости тільки для ГВ-зразка.

Що стосується мікродеформацій, то значення ε для ГВ-стопу після I-типу оброблення збільшується після 4 хв і дещо зменшується після 8 хв, але залишається більшим, ніж у вихідному стані (табл. 2). Для II-типу оброблення мікродеформація α- та β-фаз відбувається по-різному. Після 4 хв значення ε зменшується для α-фази вдвічі та збільшується для β-фази з 0,77% до 2%. Із збільшен-

ТАБЛИЦЯ 2. Параметри кристалічної структури, кількісний фазовий склад і величина напружень 1-го роду ГВ-стопу ВТ6 у вихідному стані та після оброблення.

TABLE 2. Parameters of crystalline structure, quantitative phase composition, and stresses of first kind for HR Ti–6Al–4V alloy in the initial state and after treatment.

Тип оброблення	Тривалість оброблення, хв	Параметер α/β-фаз			Напруження σ, МПа
		ОКР, нм	ε, %	Вміст, %	
Вихідний стан		150/174	0,33/0,77	90/10	–523/–
I	4	19/63	0,58/1,19	92/8	–1240/–
	8	38/22	0,42/0,86	97/3	–398/–
II	4	14/36	0,15/2,0	95/5	–1560/–
	8	55/17	0,49/0,043	96/4	–762/–

ням часу навпаки більшої деформації зазнає кристалічна ґратниця α-фази (0,5%), а для β-фази ε має мінімальне значення (0,043%). Для СЛТ-стопу (табл. 3) за всіх режимів оброблення ε зростає, як для α-фази, так і для β-фази, порівняно із вихідним станом. Після 6 хв оброблення більші значення ε спостерігаються для II-типу оброблення порівняно з I-типом. Аналіза одержаних даних уможливлює зробити висновок, що в основному деформується ґратниця β-фази, а оскільки її набагато менше, ніж α-фази, цей чинник впливу на мікротвердість не є істотним.

Процес високочастотного механічного оброблення ГВ-стопу сприяє формуванню високого рівня стискальних залишкових макронапружень. Після 4 хв оброблення II-типу (табл. 3) досягається максимальний рівень стискальних напружень (–1560 МПа) порівняно із тим, що утворюється під час аналогічного оброблення I-типу (–1240 МПа), і вихідним станом (–523 МПа). Після 8 хв ці значення зменшуються до –762 МПа і –398 МПа відповідно, що корелює із зменшенням мікротвердости та підтверджує процеси релаксації напружень.

Таким чином, як подрібнення зерен, так і високі значення стискальних напружень є сприятливими чинниками для зміцнення поверхні ГВ-стопу ВТ6.

У вихідному стані СЛТ-зразка напруження є розтягувальними (+175 МПа) і внаслідок високочастотного ударного оброблення змінюють знак [29]. Після 4 хв оброблення I- та II-типу значення σ дорівнюють –1625 МПа і –1413 МПа, а після 6 хв оброблення збільшуються до –1815 МПа і –1642 МПа відповідно. Надалі внаслідок релаксаційних процесів величина σ зменшується, але не настільки

ТАБЛИЦЯ 3. Параметри кристалічної структури, кількісний фазовий склад і величина напружень 1-го роду СЛТ-стопу ВТ6 у вихідному стані та після оброблення.

TABLE 3. Parameters of crystalline structure, quantitative phase composition, and stresses of first kind for SLM Ti–6Al–4V alloy in the initial state and after treatment.

Тип оброблення	Тривалість оброблення, хв	Параметр α/β-фаз			Напруження σ, МПа
		ОКР, нм	ε, %	Вміст, %	
Вихідний стан		11/62	0,18/0,58	93/7	+175/–
I	4	20/36	0,67/0,49	89/11	–1625/–
	6	18/32	0,37/0,79	90/10	–1815/–
	8	28/67	0,7/0,79	89/11	–1153/–
II	4	11/21	0,39/0,19	89/11	–1413/–
	6	17/23	0,55/0,92	95/5	–1642/–
	8	12/39	0,2/0,45	89/11	–1211/–

істотно, як для випадку ГВ-зразків.

Максимальне значення напружень (–1815 МПа) для II-типу оброблення СЛТ-зразка упродовж 6 хв незначно відрізняється від максимального значення для ГВ-зразка (–1560 МПа), досягнутого після 4 хв оброблення. Саме така тривалість ударного впливу відповідає максимальним значенням мікротвердости. Тобто значно більше значення мікротвердости СЛТ-зразка порівняно з ГВ-зразком, скоріш за все, може зумовлюватися не тільки рівнем залишкових макронапружень стиснення та подрібненням зеренної структури.

Тому виявлений ефект зміцнення СЛТ-стопу, ймовірно, слід пов'язувати із фазовими перетвореннями, які стосуються в основному α-фази (оскільки її значно більше і вона має більшу мікротвердість порівняно з β-фазою), а також зі змінами дислокаційної структури.

Спостережувані на рентґенограмах дифракційні рефлекси є суперпозицією рефлексів від α-фази і α'-мартенситу (просторова група $P6_3/mmc$, $a = 0{,}293$ нм, $c = 0{,}467$ нм). Близькі значення параметрів ґратниці цих фаз перешкоджають чіткому розділенню дифракційних максимумів. Згідно з [26], нерівноважні фази та морфології є характерною ознакою СЛТ-стопу ВТ6. Фізичну причину перебігу бездифузійного мартенситного перетворення в процесі 3D-друку забезпечує висока швидкість охолодження та формування дислокацій високої густини.

Як правило, β-стабілізатори мають недостатньо часу для дифундування з новоутвореної α-фази під час $\beta \to \alpha'$-перетворення, яке відбувається за швидкого твердннення. В результаті, з попередніх зерен β-фази утворюється мартенситна α'-фаза в пластинчастих або рейкових морфологіях, розміри яких варіюються від кількох мікрометрів до десятків нанометрів [30]. Ця мартенситна α'-фаза зберігає наявну структуру α-фази, але містить підвищену концентрацію β-стабілізаторів і зазвичай знаходиться всередині попередніх β-зерен.

Автори [31] зазначають, що структура СЛТ-зразків може складатися з двох різних варіянтів метастабільної фази, а саме, не тільки з гексагональної α'-мартенситної фази, а і з невеликої кількости базоцентрованої орторомбічної α''-мартенситної фази (5,45–8,0 мас.% V). Тобто у стопі ВТ6 можуть спостерігатися два типи метастабільних мартенситних перетворень, а саме, $\beta \to \alpha'$ і $\beta \to \alpha''$.

Завдяки пошаровому способу виготовлення СЛТ-стопу попередньо виготовлені шари матеріялу нагріваються й охолоджуються кілька разів, тобто піддаються термоциклуванню, яке відрізняється від традиційного ізотермічного термічного оброблення тим, що час термічного циклу знаходиться в межах мілісекунд. Тому замість β-фази з рівноважною концентрацією Ванадію утворюються нанорозмірні метастабільні області зі збільшеною його концентрацією

[31]. І саме в цих областях, збагачених β-стабілізувальними елементами, зазвичай спостерігається α″-мартенсит. Його утворення не вимагає такого великого переохолодження, як це потрібно для α′-фази.

Під час високочастотного механічного оброблення може відбуватися вирівнювання концентрації V і розкладання α″-мартенситу. Як відомо, на відміну від α′-мартенситу, поява α″-мартенситу приводить до розм'якшення, а його розкладення — до затвердіння титанових стопів [32].

Крім того, може змінюватися морфологія α′-мартенситу; він може набувати голчастої форми і таким чином забезпечувати високий рівень зміцнення. Можливі й інші фазові перетворення та трансформації дислокаційної структури, оскільки пластична деформація стиснення викликає високу щільність дислокацій і накопичення внутрішньої енергії [33]. Кількісна аналіза механізмів зміцнення показала, що є критичний рівень деформації, нижче якого посилення дислокаціями було домінувальним порівняно з посиленням меж зерен [34].

Складний взаємочин між умовами міжшарової деформації та вислідними механічними властивостями адитивно виготовлених матеріялів потребує подальших структурних досліджень із залученням методу високороздільчої електронної мікроскопії.

4. ВИСНОВКИ

1. Незалежно від схеми ініціювання ударів кульками по оброблюваній поверхні, порівнювані ультразвукові устатковини за певних оптимальних режимів оброблення можуть забезпечити пониження шерсткости, формування стискальних залишкових напружень, значне зміцнення, що позитивно впливає на експлуатаційний ресурс оброблених матеріялів і може сприяти довготривалій і безпечній експлуатації металевих виробів і конструкцій в автомобільній, машинобудівній, авіяційній промисловостях та у біомедичних застосуваннях.
2. Запропонована віброкамера уможливлює одержати як поздовжні коливання її дна, так і концентричні коливання стінок, що підвищує ефективність стабільного та керованого оброблення деталів і вузлів складної форми. У порівнянні з устатковиною ВЧЗК віброкамера дає змогу здійснювати експрес-оброблення з обох боків пласких і тонких металевих деталів, наприклад лопатей двигунів або компресорів.
3. Порівняно з мікротвердістю HV_{100} вихідного зразка стопу ВТ6 (3,85 ГПа), одержаного гарячим вальцюванням, використані ультразвукові устатковини забезпечили зміцнення його поверхні на 22,6% (4,72 ГПа) і 24,9% (4,81 ГПа) упродовж 4 хв оброблення для

ВЧЗК і віброкамери відповідно. Така ріжниця пояснюється формуванням максимальних залишкових стискальних напружень (–1560 МПа) під час оброблення у віброкамері порівняно з методою ВЧЗК (–1240 МПа). Подрібнення кристалітів α-фази Ti за 4 хв оброблення відбувається до приблизно однакового розміру у 14–19 нм (у вихідному стані — 150 нм), тоді як β-фаза (у вихідному стані — 174 нм) більш інтенсивно подрібнюється у віброкамері (36 нм), аніж за ВЧЗК (63 нм).

4. Для стопу ВТ6, одержаного селективним лазерним топленням, забезпечується зміцнення на 51% (6,61 ГПа) і 46,7% (6,41 ГПа) порівняно із вихідним станом (4,37 ГПа) для ВЧЗК та віброкамери відповідно, але необхідний час оброблення збільшується до 6 хв через наявність стадії ($\cong$ 3 хв) деформування елементів більш шерсткої поверхні. Дрібнозернистість, шаруватість смугастої структури та наявність α'- й α''-мартенситу, сформованого внаслідок високої швидкости охолодження, забезпечують вищі значення мікротвердости СЛТ-зразка у вихідному стані.

5. Під час оброблення смугаста будова фазових складових і наявні міжфазні межі виконують роль стопорів для дислокацій, які ґенеруються в процесі пластичної деформації, що забезпечує вищий рівень зміцнення та мікротвердости СЛТ-зразків порівняно з ГВ-зразками незалежно від типу застосованого механічного оброблення. Також цілком можливі процеси еволюції морфології α'- та α''-мартенситу з подрібненням або перетворенням цих фазових складових.

ВНЕСОК АВТОРІВ

С. М. Волошко розробила концепцію роботи, виконала аналізу одержаних експериментальних результатів і підготувала перший варіянт рукопису. А. П. Бурмак виконав рентґенівські та мікроскопічні дослідження, а також макетування рукопису. Б. М. Мордюк виконав модифікування поверхні зразків за допомогою УЗУО, взяв участь у аналізі результатів, а також виконав редаґування рукопису. М. О. Васильєв проаналізував літературні дані щодо поверхневого оброблення титанових стопів методами деформування поверхні, взяв участь у аналізі результатів. Т. А. Красовський розробив і виготовив низку ультразвукових інструментів задля проведення модифікування поверхні зразків. О. А. Вислий виготовив зразки та провів дослідження мікротвердости після різних видів оброблення. Усі автори схвалили остаточну версію рукопису.

Роботу виконано за підтримки МОН України в рамках держбюджетної теми (№ держ. реєстрації 0124U001001) і часткової підтримки НАН України (№№ держ. реєстрації: 0123U102368, 0124U000361).

ЦИТОВАНА ЛІТЕРАТУРА—REFERENCES

1. T. DebRoy, H. L. Wei, J. S. Zuback, T. Mukherjee, J. W. Elmer, J. O. Milewski, A. M. Beese, A. Wilson-Heid, A. De, and W. Zhang, *Prog. Mater. Sci.*, **92**: 112 (2018).
2. Q. Zhao, Q. Y. Sun, S. W. Xin, Y. N. Chen, C. Wu, H. Wang, J. W. Xu, M. P. Wan, W. D. Zeng, and Y. Q. Zhao, *Mater. Sci. Eng. A*, **845**: 143260 (2022).
3. Z. Gao, X. Chen, S. Zhu, Y. H. He, and W. Xu, *Int. J. Fatigue*, **172**: 107608 (2023).
4. M. O. Vasylyev, B. M. Mordyuk, and S. M. Voloshko, *Prog. Phys. Met.*, **24**, No. 1: 5 (2023).
5. M. O. Vasylyev, B. M. Mordyuk, and S. M. Voloshko, *Prog. Phys. Met.*, **24**, No. 1: 38 (2023).
6. A. K. Singla, M. Banerjee, and A. Sharma, *J. Manuf. Process.*, **64**: 161 (2021).
7. N. Eshawish, S. Malinov, W. Sha, and P. Walls, *J. Mater. Eng. Perform.*, **30**: 5290 (2021).
8. N. Baskin and C. Yüce, *J. Mater. Res. Technol.*, **30**: 7006 (2024).
9. M. Chen, W. L. Deng, J. S. Li, C. H. Jiang, and V. Ji, *Mater. Today Commun.*, **46**: 112901 (2025).
10. С. М. Волошко, Б. М. Мордюк, М. О. Васильєв, В. І. Закієв, А. П. Бурмак, Н. В. Франчік, *Металофіз. новітні технол.*, **45**, № 2: 217 (2023); S. M. Voloshko, B. M. Mordyuk, M. O. Vasyliev, V. I. Zakiev, A. P. Burmak, and N. V. Franchik, *Metallofiz. Noveishie Tekhnol.*, **45**, No. 2: 217 (2023).
11. G. I. Prokopenko, B. M. Mordyuk, M. O. Vasyliev, and S. M. Voloshko, *Physical Principles for Ultrasonic Impact Hardening of Metallic Surfaces* (Kyiv: Naukova Dumka: 2017); ISBN 978-966-00-1235-6
12. A. I. Dekhtyar, B. N. Mordyuk, D. G. Savvakin, V. I. Bondarchuk, I. V. Moiseeva, and N. I. Khripta, *Mater. Sci. Eng. A*, **641**: 348 (2015).
13. X. C. Yan, S. Yin, C. Y. Chen, R. Jenkins, R. Lupoi, R. Bolot, W. Ma, M. Kuang, H. Liao, J. Lu, and M. Liu, *Mater. Res. Lett.*, **7**, No. 8: 327 (2019).
14. C. S. Liu, D. X. Liu, X. H. Zhang, D. Liu, A. Ma, N. Ao, and X. C. Xu, *J. Mater. Sci. Technol.*, **35**, No. 8: 1555 (2019).
15. A. Amanov, I.-S. Cho, D.-E. Kim, and Y.-S. Pyun, *Surf. Coat. Technol.*, **207**: 135 (2012).
16. М. О. Васильєв, Б. М. Мордюк, Г. І. Прокопенко, С. М. Волошко, Л. Ф. Яценко, Н. І. Хріпта, *Металофіз. новітні технол.*, **40**, № 8: 1029 (2018); M. O. Vasylyev, B. M. Mordyuk, G. I. Prokopenko, S. M. Voloshko, L. F. Yatsenko, and N. I. Khripta, *Metallofiz. Noveishie Tekhnol.*, **40**, No. 8: 1029 (2018).
17. А. П. Бурмак, С. М. Волошко, Б. М. Мордюк, Т. А. Красовський, В. І. Закієв, І. А. Владимирський, М. О. Васильєв, *Металофіз. новітні технол.*, **44**, № 11: 1453 (2022); A. P. Burmak, S. M. Voloshko, B. M. Mordyuk, T. A. Krasovskyi, V. I. Zakiev, I. A. Vladymyrskyi, and M. A. Vasylyev, *Metallofiz. Noveishie Tekhnol.*, **44**, No. 11: 1453 (2022).
18. Q. Zhang, B. B. Duan, Z. Q. Zhang, J. B. Wang, and C. R. Si, *J. Mater. Res. Technol.*, **11**: 106 (2021).
19. J. Cai, H. Wu, Y. Tian, and X. Zhang, *Sci. Rep.*, **15**: 13548 (2025).
20. S. Diachenko, T. Krasovskyi, A. Burmak, S. Voloshko, V. Malinin, and

B. Mordyuk, *Proc. 7th Int. Sci. Pract. Conf. 'Scientific Goals and Purposes in XXI Century' (19–20 Oct. 2024, Seattle, USA)* (InterConf: 2024), p. 388.
21. T. Suzuki, K. Sakamoto, Y. Hirose, T. Okawa, H. Shimanuki, T. Nose, N. Ohta, H. Suzuki, and A. Moriai, *Adv. Mater. Res.*, **996**: 736 (2014).
22. Z. Wang, Z. Xiao, C. Huang, L. Wen, and W. Zhang, *Materials*, **10**, No. 10: 1203 (2017).
23. B. N. Mordyuk, A. I. Dekhtyar, D. G. Savvakin, and N. I. Khripta, *J.Mater. Eng. Perform.*, **31**: 5668 (2022).
24. D. Yuan, L. Zhang, Y. Chen, D. Yuan, S. Shao, C. H. Guo, F. C. Jiang, and J. D. Wang, *Ultrason. Sonochem.*, **73**: 105472 (2021).
25. S. M. Kelly and S. L. Kampe, *Metall. Mater. Trans. A*, **35**: 1861 (2004).
26. E. Eshed and A. Shirizly, *Materials*, **18**, No. 13: 3198 (2025).
27. H. Sun, C. Si, and J. Wang, *Surf. Eng.*, **40**, No. 1: 1 (2024).
28. X. Luo, X. Ren, Q. Jin, H. Qu, H. Hou, and L. Zhang, *J. Mater. Res. Technol.*, **13**, No. 5: 1586 (2021).
29. P. Mercelis and J.-P. Kruth, *Rapid Prototyp. J.*, **12**: 254 (2006).
30. W. Okuniewski, M. Walczak, M. Szala, and D. Chocyk, *Eng. Failure Anal.*, **176**: 109653 (2025).
31. N. Kazantseva, P. Krakhmalev, M. Thuvander, I. Yadroitsev, N. Vinogradova, and I. Ezhov, *Mater. Charact.*, **146**: 101 (2018).
32. O. M. Ivasishin, H. M. Flower, and G. Lutjering, *Titanium'99: Sci. Technol.* (1999), p. 77.
33. M. Zhang, C. Liu, X. Shi, X. Chen, C. Chen, J. Zuo, J. Lu, and S. Ma, *Appl. Sci.*, **6**: 304 (2016).
34. A. Mithal, V. S. Sridharan, N. Y. J. Tan, S. J. Ng, and Y. Chew, *J. Mater. Process. Technol.*, **343**: 118982 (2025).

Metallophysics and Advanced Technologies
Металофіз. новітні технол.
Metallofiz. Noveishie Tekhnol.
2026, vol. 48, No. 8, pp. 865–888
https://doi.org/10.15407/mfint.48.08.0865
Reprints available directly from the publisher

© 2026 G. V. Kurdyumov Institute for Metal Physics,
National Academy of Sciences of Ukraine
Published by license under
the G. V. Kurdyumov Institute for Metal Physics–
N.A.S. of Ukraine Publishers imprint.
Printed in Ukraine.

PACS numbers: 43.35.+d, 61.72.Dd, 61.72.Ff, 61.72.Hh, 62.20.Qp, 81.20.Ev, 81.40.Ef

Microstructural and Phase Evolution of AISI 316 Stainless Steel Produced by Selective Laser Melting and Hot Rolling during Heat Treatment and Ultrasonic Impact Treatment

S. M. Voloshko[*], I. A. Vladymyrskyi[*], M. I. Anyakin[*], N. A. Shapovalova[*], M. M. Voron[*,**], and A. P. Burmak[*]

[*]*National Technical University of Ukraine 'Igor Sikorsky Kyiv Polytechnic Institute', 37 Beresteiskyi Ave., UA-03056 Kyiv, Ukraine*
[**]*Physico-Technological Institute of Metals and Alloys, N.A.S. of Ukraine, 34/1 Academician Vernadsky Blvd., UA-03142 Kyiv, Ukraine*

The effects of fabrication route, heat treatment, and ultrasonic impact treatment (UIT) on the microstructure, phase composition, microhardness, and residual stresses of AISI 316 stainless steel produced by selective laser melting (SLM) and hot rolling (HR) are investigated. The SLM material exhibits a fine cellular structure and higher austenite stability, manifested by a lower susceptibility to the deformation-induced $\gamma \rightarrow \alpha'$ martensitic transformation compared with the hot-rolled steel. Heat treatment promotes microstructural homogenization, residual-stress relaxation, and an increase in the γ-phase fraction. UIT induces intense plastic deformation, refinement of coherent scattering domains, and compressive residual stresses. The maximum microhardness reaches 7.6 GPa for the hot-rolled steel and 6.7 GPa for the SLM material. The stronger hardening of the hot-rolled steel is associated with its greater susceptibility to deformation-induced martensitic transformation. Prior heat treatment significantly affects the response to subsequent

Corresponding author: Svitlana Mykhaylivna Voloshko
E-mail: voloshkosvetlana13@gmail.com

Citation: S. M. Voloshko, I. A. Vladymyrskyi, M. I. Anyakin, N. A. Shapovalova, M. M. Voron, and A. P. Burmak, Microstructural and Phase Evolution of AISI 316 Stainless Steel Produced by Selective Laser Melting and Hot Rolling during Heat Treatment and Ultrasonic Impact Treatment, *Metallofiz. Noveishie Tekhnol.*, **48**, No. 8: 865–888 (2026). DOI: 10.15407/mfint.48.08.0865

© Publisher PH 'Akademperiodyka' of the NAS of Ukraine, 2026. This is an open access article under the CC BY-ND license (https://creativecommons.org/licenses/by-nd/4.0)

UIT, with annealing followed by UIT providing the largest and most stable increase in microhardness. The results demonstrate the effectiveness of combining heat treatment and UIT for controlling the structural and phase state and mechanical characteristics of AISI 316 stainless steel produced by different fabrication routes.

Key words: AISI 316, additive manufacturing, heat treatment, ultrasonic impact treatment, microstructure, phase composition, microhardness.

Досліджено вплив технології виготовлення, термічного оброблення й ультразвукового ударного оброблення (УЗУО) на мікроструктуру, фазовий склад, мікротвердість і рівень залишкових напружень неіржавійної криці AISI 316, одержаної методою селективного лазерного топлення (SLM) та гарячого вальцювання (HR). Матеріял, виготовлений методою SLM, характеризується дрібнодисперсною комірчастою структурою та вищою стабільністю аустенітної γ-фази, що проявляється у меншій схильності до деформаційно-індукованого мартенситного перетворення $\gamma \to \alpha'$ порівняно з гарячекатаною крицею. Термічне оброблення сприяє гомогенізації мікроструктури, релаксації залишкових напружень і збільшенню частки γ-фази. УЗУО забезпечує інтенсивну пластичну деформацію поверхневого шару, зменшення розміру областей когерентного розсіяння та формування стискальних напружень. Максимальна мікротвердість сягає 7,6 ГПа для гарячекатаної криці та 6,7 ГПа для матеріялу, одержаного методою SLM. Вища ефективність зміцнення гарячекатаної криці пов'язана з більшою схильністю її до деформаційно-індукованого мартенситного перетворення. Попереднє термічне оброблення істотно впливає на ефективність подальшого УЗУО, причому найбільше та найбільш стабільне підвищення мікротвердости забезпечує поєднання відпалу з УЗУО. Одержані результати підтверджують ефективність комплексного застосування термічного та поверхневого деформаційного оброблення для керування структурно-фазовим станом, мікротвердістю та залишковими напруженнями криці AISI 316, виготовленої різними технологічними методами.

Ключові слова: AISI 316, адитивне виробництво, термічне оброблення, ультразвукове ударне оброблення, мікроструктура, фазовий склад, мікротвердість.

(Received 3 July, 2026; in final version, 22 July, 2026)

1. INTRODUCTION

Austenitic stainless steels are important structural materials due to their high corrosion resistance, excellent processability and non-magnetic properties [1, 2]. Owing to their high deformability, these steels are used to produce vessels for the chemical, energy and food industries, pipes, capillaries and various complex-shaped components, including critical-purpose products [3].

The main grades of austenitic stainless steels include AISI 304, 306, 316 and 321. These steels are similar in chemical composition and me-

chanical properties, but differ in the alloying additions that determine their service performance. AISI 304, containing 18–20% wt. Cr and 8–11% wt. Ni, is the most widely used base grade in the chemical and food industries. A distinctive feature of AISI 316 is Cr content lower by ≅ 2% wt. and Ni content higher by ≅ 2% wt. together with 2–3% wt. Mo. This composition provides much higher corrosion resistance and a lower susceptibility to intergranular corrosion; therefore, grade 316 is often referred to as 'marine' or 'chemical' stainless steel. AISI 321 is close in composition to AISI 304; however, it contains Ti providing the highest heat resistance without loss of corrosion resistance. Owing to its high resistance at elevated temperatures and improved weldability, it is used for components of military equipment, including aviation parts, heat exchangers and related products [2, 4, 5].

As was already mentioned, these austenitic stainless steels reveal a similar set of mechanical properties. After quenching, their ultimate tensile strength is of 480–580 MPa, yield strength is of 200–250 MPa and elongation is of 35–55% [2, 5, 6]. These properties can be effectively modified by deformation and heat treatment. For example, cold plastic deformation promotes grain refinement, the development of crystallographic texture, and deformation-induced martensite formation, increasing the microhardness from 340 to 540 *HV*. Depending on the processing conditions, the resulting strength reaches 700–1600 MPa, while the elongation decreases to 2–20%, accompanied by deterioration in corrosion resistance [7, 8]. Multiple equal-channel angular pressing of AISI 316 steel refines the grain size to 10–40 nm and increases the yield strength to 1480 MPa; however, these improvements are achieved at the expense of high energy consumption [9]. By combining deformation and heat treatment, the microstructural parameters of austenitic stainless steels can be controlled effectively and their mechanical properties can be varied over a wide range [10].

Despite these advantages and the possibility of controlling structural properties, phase composition and mechanical characteristics, improvement of corrosion resistance remains a key issue for austenitic stainless steels. Various surface treatments of steel products are primarily used for this purpose. For example, in Ref. [11], the effect of laser surface treatment on the chemical composition, surface morphology and corrosion resistance of AISI 304, AISI 316 and AISI 321 steels was investigated. A decrease in the concentrations of Cr and Ni and an increase in O content at the surface were observed, resulting in different corrosion resistance at a certain depth from the surface. The most pronounced positive effect was obtained for AISI 321 owing to Ti migration towards the surface. However, the specimen surface remains continuous only after treatment with low laser energies. When the energy density exceeded 100 J/cm^2, cracks appear on the surface, significantly deteriorating corrosion resistance and fatigue strength. In con-

trast, deformation-induced surface nanostructuring combined with annealing led to Cr enrichment of the treated surface and, consequently, to a substantial improvement in corrosion resistance. Lei *et al.* showed [12] that a preformed gradient nanostructured (GNS) surface layer of 316L stainless steel was subjected to surface mechanical rolling treatment (SMRT) followed by annealing at 700°C. Tensile tests showed that the strength–ductility ratio is higher for the annealed SMRT material, while grain size and hardness of the GNS layer remain sufficiently stable. In addition, significant Cr enrichment was detected for the GNS surface layer after annealing, leading to a considerable corrosion resistance enhancement. In Ref. [13], a $\cong$ 20-μm thick nanostructured surface layer was formed on a low-carbon steel plate by surface mechanical attrition treatment (SMAT). In particular, the authors showed that after SMAT, a much thicker Cr diffusion layer was obtained compared to the coarse-grained specimen after chromizing, especially at low temperatures. For the SMAT material, the temperature of chromium-containing compound formation is considerably lower and the amount of chromium carbides is higher in comparison with its coarse-grained counterpart. Thus, surface mechanical attrition-assisted chromizing of austenitic stainless steels also improves corrosion resistance.

Other methods of surface alloying and strengthening of austenitic stainless steels were actively investigated in recent decades as well, including plasma surface alloying [14], electrolytic coating deposition [15], thermochemical treatment with simultaneous chromizing and nitrocarburizing [16], aluminosiliconizing [17] to name just a few. Austenitic stainless steels exhibit superior mechanical performance, characterized by high yield and tensile strength, good ductility, excellent fracture toughness, and enhanced fatigue and wear resistance, when the modified surface contains a fine-crystalline structure both in the base metal and in the coating phases. In particular, oxides, carbides or nitrides could simultaneously improve fatigue strength, corrosion resistance and wear resistance. However, it should be noted that, under sufficient mechanical loading, such surfaces might fail because of structural anisotropy.

A homogeneous fine-grained microstructure leading to higher corrosion resistance compared to rolled products can be achieved by additive manufacturing of austenitic stainless steel components [18, 19]. For example, wire-arc additive manufacturing (WAAM) of AISI 316L steel increases the material strength by 58% and the fatigue strength by 10% [20]. Alloy produced by selective laser melting (SLM) reveal a finer-grained structure with grain size of 1–5 μm and higher ultimate tensile and yield strengths of 650 MPa and 550 MPa, respectively, albeit with lower ductility compared with the same alloy manufactured by conventional routes such as forging and casting [21]. The reduced

ductility of SLM specimens is compensated by their higher strength.

Therefore, additively manufactured components made of austenitic stainless steels are promising for subsequent surface treatment due to fine-grained and homogeneous microstructure. Such treatment should not promote grain growth but should refine grains, thereby increasing surface hardness and, where possible, enrich the surface with interstitial elements improving the corrosion and wear resistance. Since SLM-fabricated 316L components reveal an anisotropic cellular structure with a high density of dislocations and macrodefects, surface or deformation treatment should be combined with thermal annealing [22].

Since printed components usually have complex geometries, the choice of post-processing approaches is limited. It should also be considered that prolonged exposure to high temperatures might be unfavourable for structural modification of additively produced specimens. So, additive manufacturing followed by heat treatment and subsequent ultrasonic impact treatment represents an effective processing route for producing austenitic stainless-steel components with a homogeneous microstructure and enhanced mechanical and service properties. The efficiency of this approach for surface grain refinement and strengthening was demonstrated for metallurgically produced AISI 321 steel [23]. Another successful example is the combination of recrystallization annealing at 900°C for 1 hour with ultrasonic surface modification of AISI 316 steel, which restore ductility while maintaining an increased surface microhardness of $\cong 400\ HV_{10}$ [24].

Thus, the aim of the present study is to perform a comparative analysis of the structural properties, phase characteristics and hardness changes of 316L steel produced by metallurgical and SLM routes after heat treatment, ultrasonic impact treatment and their combination.

2. MATERIALS AND METHODS

Specimens of AISI 316 austenitic stainless steel with the following chemical composition [% wt.] were used: Cr, 16–18, Ni, 10–14, Mo, 2–3, Mn ≤ 2, Si ≤ 1, Cu ≤ 0.75, Fe—balance. Materials produced by two routes were investigated: SLM and a conventional route (HR) involving melting, formation of rolled stock and production of deformed billets.

SLM specimens in the form of parallelepipeds (15 mm in length, 8 mm in width, and 6.5 mm in height) were fabricated using an Alfa-150D 3*D* printer manufactured by ALT. The printer was equipped with a 200 W ytterbium fibre laser operating at a wavelength of 1070 ± 2 nm, with a focused laser beam diameter of 45 μm. The scanning speed was 500 mm/s, the powder layer thickness was 25 μm, and the hatch spacing was 150 μm. Spherical AISI 316L austenitic stainless-steel powder with a particle size range of 15–53 μm was used. To minimize oxidation, the specimens were fabricated in an inert argon (Ar) atmos-

phere [25].

Specimens of deformed AISI 316 stainless steel were produced by a standard industrial metallurgical route. The starting components were melted in an electric arc furnace, followed by argon-oxygen decarburization refining to ensure the specified chemical composition in accordance with ASTM A240/A240M requirements for steel products in bar form. After refining, the metal was cast into semi-finished products, which were subsequently hot rolled and slowly cooled in air.

Both types of investigated specimens were subjected to heat treatment; the treatment conditions are given in Table 1 in accordance with ASTM A276.

AISI 316 stainless-steel specimens were subjected to ultrasonic impact treatment both in the as-received state and after thermal impact. The ultrasonic impact treatment (UIT) was carried out in air using a UZG-300 device equipped with an impact head containing a cylindrical 10×18 mm striker made of hardened AISI 52100 steel [26]. A single-contact normal impact-loading mode was used [27]. The amplitude at the concentrator end face was 25 μm, and the treatment duration was varied from 30 to 300 s. During loading, each specimen received 10^4–10^5 impacts.

Microstructural studies were performed using an iScope IS.1053-PLMi optical metallographic microscope. Microhardness was measured by the Vickers method using an LHVS-1000Z tester under a 100 g load and a dwell time of 10 s.

X-ray diffraction studies were carried out using a Rigaku Ultima IV diffractometer with radiation CuK_α: 2θ range—20–120°, step size of 0.04° and counting time 2 s per point. The PDXL software package and the ICDD international diffraction database (PDF-2, 2025) were used to analyse the XRD patterns, calculate the coherent scattering domain (CSD) size, lattice microstrain (ε) and perform quantitative phase analysis. The quantitative phase composition was calculated from the integrated intensities of non-overlapping diffraction peaks characteristic of each phase using Rietveld refinement in PDXL.

TABLE 1. Heat-treatment conditions for AISI 316 stainless steel.

	SLM alloy	
1	As-received state	SLM–0
2	Annealing at 1050 ± 10°C for 30 min followed by furnace cooling	SLM–T1
3	Annealing at 1050 ± 10°C for 30 min followed by water quenching	SLM–T2
	Deformed alloy (hot rolling)	
4	Initial state	HR–0
5	Annealing at 1050 ± 10°C for 30 min followed by furnace cooling	HR–T1
6	Annealing at 1050 ± 10°C for 30 min followed by water quenching	HR–T2

First-order residual stresses were determined by the $\sin^2\psi$ method from the change in the angular position of the γ-Fe(311) diffraction peak at $\psi = 0°$, $-10°$, $-20°$, $-30°$ and $-40°$. A Savitzky–Golay function was used to smooth the diffraction-peak profiles, and a Sonneveld–Vissers function was used for background separation. The angular positions of diffraction peaks were determined from the centre-of-gravity positions. The data were processed using Rigaku Residual Stress Analysis software.

3. RESULTS AND DISCUSSION

Figure 1 compares the microhardness and first-order residual-stress level of AISI 316 steel produced by two routes, SLM and HR, in the as-received state (0), after annealing (T1) and after water quenching (T2).

In the as-received state, the microhardness of the SLM and HR specimens is close with a value of ≅ 2.8–3.0 GPa (Fig. 1, *a*). This fact indicates a relatively high strengthening level of both studied materials, although the mechanisms responsible for their structure formation differ substantially.

After heat treatment, the microhardness of the SLM specimen slightly decreases and remains at about 2.5 GPa for both T1 and T2. By contrast, the microhardness of the hot-rolled specimens increases from 2.8 to approximately 3.0 GPa after HR–T1 annealing and to 3.5 GPa after T2 water quenching. This difference can be explained by the distinct microstructures of the two materials. In the as-built condition, the SLM material is characterized by a fine cellular-dendritic microstructure and residual stresses formed during rapid solidification

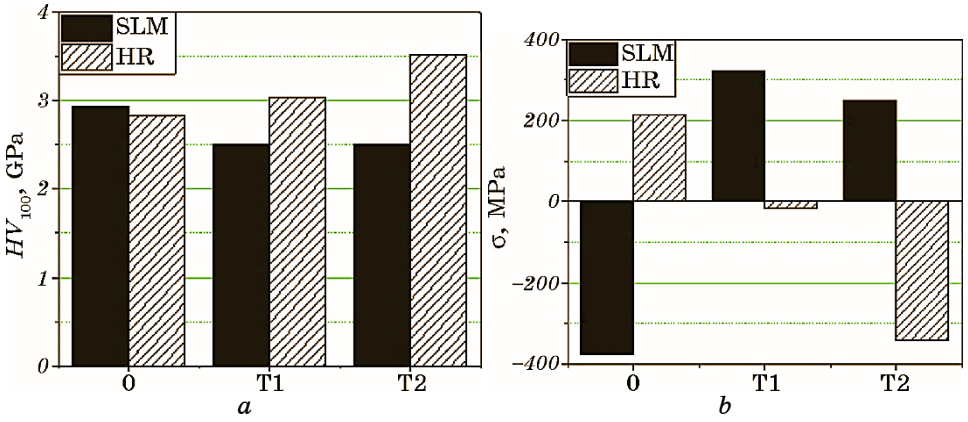


Fig. 1. Microhardness (*a*) and first-order residual stresses (*b*) in AISI 316 stainless steel produced by selective laser melting and hot rolling in the as-received state and after heat treatment.

(Fig. 1, *b*). Heat treatment partially relieves these residual stresses while preserving the refined microstructure, resulting in only a slight decrease in microhardness.

For the hot-rolled state, heat treatment may primarily promote recovery, stabilization of the subgrain structure and, depending on the heat-treatment temperature, recrystallization and precipitation of secondary phases, which increases microhardness. The increase in microhardness after annealing is attributed to the microstructural changes induced by heat treatment. Since the residual stresses are largely relieved after annealing (Fig. 1, *b*), the observed strengthening is likely associated with microstructural refinement rather than residual stress effects. In turn, water quenching preserves the recrystallized microstructure and introduces residual stresses that are subsequently transformed from tensile to compressive during ultrasonic impact treatment. Their magnitude nearly reaches the level typical for the as-received SLM material.

To identify the specific features of microstructural changes in SLM AISI 316 steel in more detail manner, comparison with the conventionally deformed material is required.

Figure 2, *a* shows that, in the as-received state, the SLM structure is characterized by pronounced anisotropy and elongated overlapping melt-pool tracks, which are typical for structure formation during additive manufacturing. The boundaries between individual melt tracks remain clearly visible, indicating the local nature of the thermal effect.

After annealing (Fig. 2, *c*), the microstructure becomes considerably more homogeneous, and the boundaries between individual melt pool regions become less distinct. The pronounced heterogeneity characteristic of the as-built condition is substantially reduced, while localized contrast-rich regions remain visible within the microstructure. These changes indicate significant microstructural evolution during annealing and are consistent with recovery and relaxation of residual stresses.

After water quenching (Fig. 2, *e*), the SLM specimens retain more features of the as-received structure, which is related to the shorter high-temperature exposure. The outlines of the melt pool regions become less visible, and the structure becomes more homogeneous while retaining its fine dispersion. The simultaneous substantial decrease in grain-boundary contrast also indicates the occurrence of polygonization.

Considering the simultaneous changes in microhardness and residual stresses, which will be discussed below, water quenching modifies the microstructural and stress state of the material. The XRD patterns reveal the coexistence of austenite γ-Fe and deformation-induced martensite α'-Fe, indicating a two-phase $\gamma + \alpha'$ structure. The relative intensities of the γ- and α'-phase reflections change with increasing UIT duration, reflecting the progressive $\gamma \rightarrow \alpha'$ deformation-induced mar-

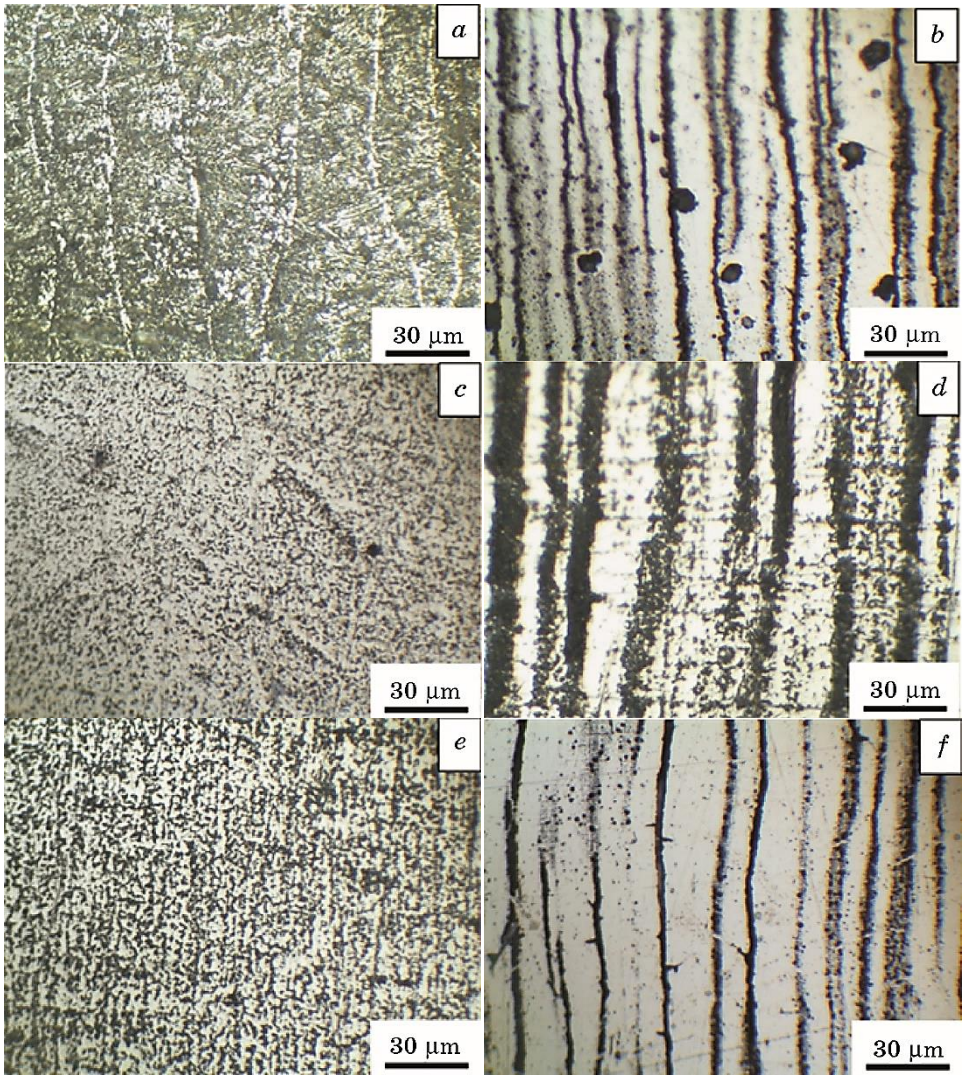


Fig. 2. Microstructure of AISI 316 stainless steel produced by selective laser melting (*a*, *c*, *e*) and hot rolling (*b*, *d*, *f*): as-received state (*a*, *b*), after annealing (*c*, *d*), after water quenching (*e*, *f*).

tensitic transformation. Therefore, the differences in residual stress and microhardness between the heat-treated conditions cannot be attributed solely to residual stress relaxation and are also related to changes in phase composition and microstructure.

The hot-rolled material in the as-received state (Fig. 2, *b*) exhibits a pronounced banded morphology, with elongated grains or structural regions oriented predominantly along the rolling direction. Distinct

dark contrast features are distributed within the elongated regions and locally concentrated near their boundaries.

After annealing (Fig. 2, *d*), the banded structure is largely retained, while the grains remain relatively intact and locally exhibit an increase in size. This is reflected by an approximately 1.5–2-fold increase in the apparent grain width, accompanied by changes in the morphology and continuity of the intergranular regions. The dispersed contrast features observed in the as-received condition become less pronounced after annealing, indicating significant microstructural evolution during heat treatment. The low level of residual stresses after annealing (Fig. 1, *b*) indicates substantial stress relaxation during the heat-treatment process.

After water quenching (Fig. 2, *f*), the microstructure of the AISI 316 stainless steel exhibits features intermediate between those observed in the as-received and annealed conditions. The heat treatment results in an increase in the apparent grain width and makes some grain boundaries more distinct, while regions with less distinct boundaries remain visible. The water-quenched condition is also characterized by a relatively high level of compressive residual stresses, comparable to that measured in the as-received SLM material (Fig. 1, *b*). The simultaneous increase in microhardness and development of compressive residual stresses indicate a pronounced change in the mechanical and stress state of the surface layer after water quenching.

Heat treatment promotes structural changes in both types of the investigated material; however, the effect varies to the different mechanisms of initial microstructure formation. In the SLM material, owing to the higher grain dispersion and the initially high level of compressive stresses, recrystallization processes, particularly grain-growth recrystallization, proceed more rapidly. In the hot-rolled material, these processes occur more slowly and are less pronounced due to the stable textured structure.

Figure 3 shows fragments of XRD spectra and the results of quantitative phase analysis of AISI 316 stainless steel produced by selective laser melting and hot rolling in the as-received state and after heat treatment.

In the as-received state (Fig. 3, *a*), the austenitic γ-phase predominates in the both cases. Its content is $\cong 99\%$ for the HR specimen and $\cong 93\%$ for the SLM specimen. The results indicate partial martensite formation during selective laser melting caused by the high thermal gradients and substantial internal stresses typical for additive manufacturing.

After annealing (Fig. 3, *b*), the SLM material exhibits a pronounced increase in the γ-austenite fraction, reaching approximately 98%. The XRD patterns show a dominant γ-Fe phase, while the contribution of the α'-Fe phase is substantially reduced after annealing. This phase re-

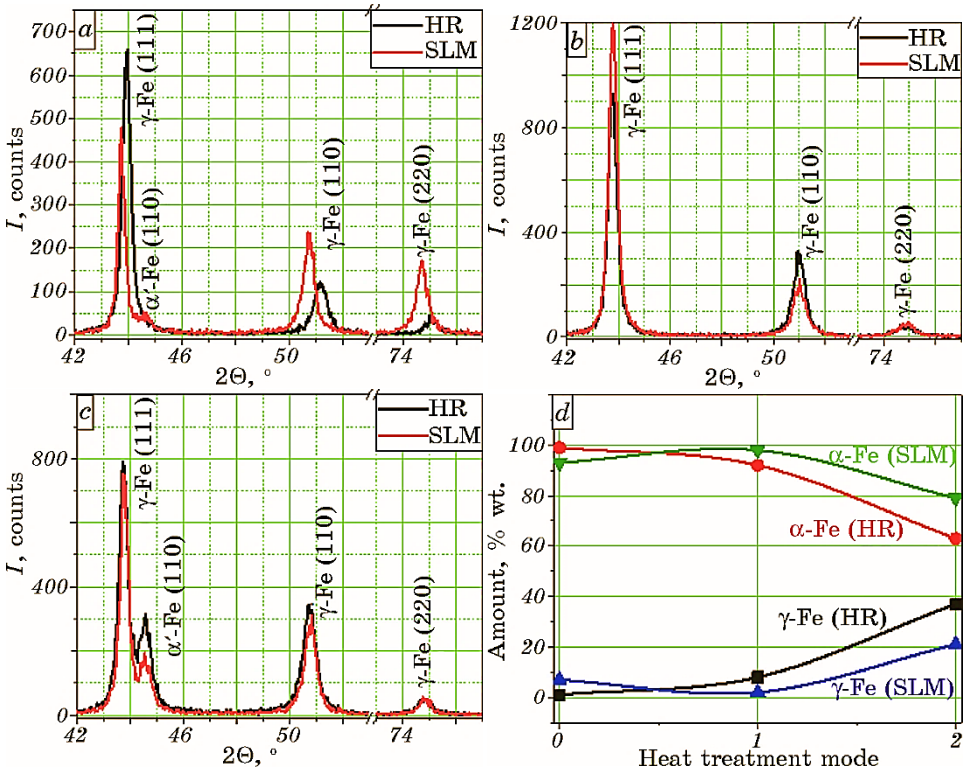


Fig. 3. XRD patterns of AISI 316 stainless steel produced by selective laser melting and hot rolling: as-received state (*a*), after annealing (*b*), after water quenching (*c*), and quantitative phase composition after different production and treatment routes (*d*).

distribution is accompanied by a reduction in residual stresses, indicating significant microstructural and stress-state changes during heat treatment. The γ-phase also predominates in the hot-rolled material after annealing.

The most significant phase composition modification occurs after water quenching (Fig. 3, *c*). In the both cases, the amount of α-phase increases while the fraction of austenite decreases accordingly. However, the rate of these changes strongly depends on the fabrication route. In the hot-rolled specimen, the α-phase fraction increases to 37%, whereas the γ-phase content decreases to 63%. In turn, for the SLM specimen, these changes are less pronounced: the α-phase content is of 21%, while the γ-phase fraction remains at 79%. This fact indicates higher stability of the austenitic structure in the material produced by selective laser melting.

Thus, substantial differences in the phase composition of AISI 316

steel depending on the fabrication route are achieved after the heat-treatment stage. The material produced by selective laser melting demonstrates higher stability of the austenitic phase and a lower tendency to phase transitions, whereas the hot-rolled steel is characterized by a higher α-phase fraction after heat treatment and higher sensitivity to subsequent deformation strengthening.

Since the phase composition, structural defectiveness and internal-stress level determine the response of the material to external deformation, the efficiency of ultrasonic impact treatment can also be expected to depend strongly on the structural state formed during heat treatment stage. Therefore, the next step of the study examined the effect of ultrasonic impact treatment and the combined effect of heat treatment and UIT on microhardness, surface morphology, phase composition, coherent scattering domain size and residual stresses of AISI 316 steel produced by selective laser melting and hot rolling.

Figure 4 shows the change in microhardness of AISI 316 steel after different treatment regimes.

All T0, T1 and T2 specimens exhibit a nonmonotonic change in microhardness with increasing UIT duration. For specimens not subjected to heat treatment (T0), the microhardness varies in an oscillatory manner with UIT time. For the SLM case, the hardness increases rapidly to a maximum of 6.5 GPa after 80 s, and then sharply decreases to 4.5 GPa at 120 s, with the following increase up to 6.4 GPa at 210 s and final decrease to 5 GPa. For the HR specimen (T0), strengthening occurs in two stages: up to 6.5 GPa after 60 s of UIT and up to 7.6 GPa after 120 s, followed by a sharp decrease in hardness to 4.5 GPa. This behaviour can be associated with efficient accumulation of crystal-lattice defects, refinement of structural features and formation of a

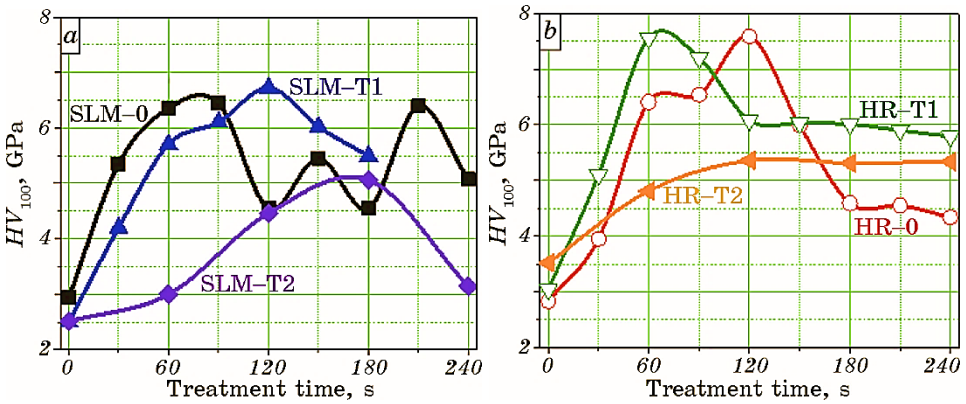


Fig. 4. Microhardness of AISI 316 stainless steel produced by selective laser melting (SLM, *a*), and hot rolling (HR, *b*) as a function of ultrasonic impact treatment duration.

strain-hardened surface layer at the initial stages of UIT, followed by the onset of relaxation processes.

After annealing according to the T1 and T2 regimes, the initial microhardness values of the SLM specimens decrease relative to the T0 state due to relaxation of internal stresses and partial structural recovery. At the following stage, UIT leads to significant increase in microhardness. For the SLM–T1 condition, the strengthening maximum is delayed compared to T0 and reaches 6.7 GPa after 120 s of the treatment, followed by a gradual decrease. The HR–T1 condition is potentially the most stable: the hardness rapidly increases to 7.6 GPa after only 60 s of the treatment and remains at a high level of 6.0–6.4 GPa up to 240 s.

After water quenching (T2), the microhardness behaviour differs depending on the production procedure. The SLM–T2 sample shows the poorest stability. Strengthening proceeds very slowly, reaching only 5.06 GPa at a UIT duration of 180 s, and decreases to 3.1 GPa at the final stage of the treatment (240 s), which is an indicator of complete annealing and recrystallization. The hot-rolled stainless steel (HR–T2) is characterized by a monotonic increase in microhardness already at the initial stages of UIT, with a maximum value of 5.3 GPa after 120 s, followed by stabilization at this.

Comparison of thermal and deformation effects on the microhardness of stainless steel produced by selective laser melting and hot rolling allows to found that the HR steel exceeds the SLM steel in maximum strengthening capacity: the maximum microhardness of HR material reaches 7.6 GPa (T0 and T1 conditions), while, for SLM, it does not exceed 6.7 GPa (T1 condition). The higher maximum microhardness of hot-rolled specimens, especially after annealing, associated with more effective strain hardening and formation of a finely dispersed substructure during UIT. In contrast, SLM specimens show a smaller increase in microhardness during UIT, caused by the specific cellular–dendritic structure and residual stresses formed during additive manufacturing.

Regarding the treatment duration required to achieve the maximum hardness, the hot-rolled steel (HR–T1) responds much faster, reaching its peak after 60 s of ultrasonic impact treatment, whereas the SLM–T1 specimen requires 120 s to attain a comparable strengthening effect. It can be concluded that for AISI 316 steel produced by both SLM and HR, annealing with a furnace cooling (T1) is considerably more effective for subsequent ultrasonic strengthening since it creates prerequisites for phase or dispersion strengthening. In contrast, water quenching (T2) makes the matrix excessively prone for rapid recrystallization during UIT.

Figure 5 demonstrates the effect of ultrasonic impact treatment (UIT) on the surface morphology of selective laser melted and hot-

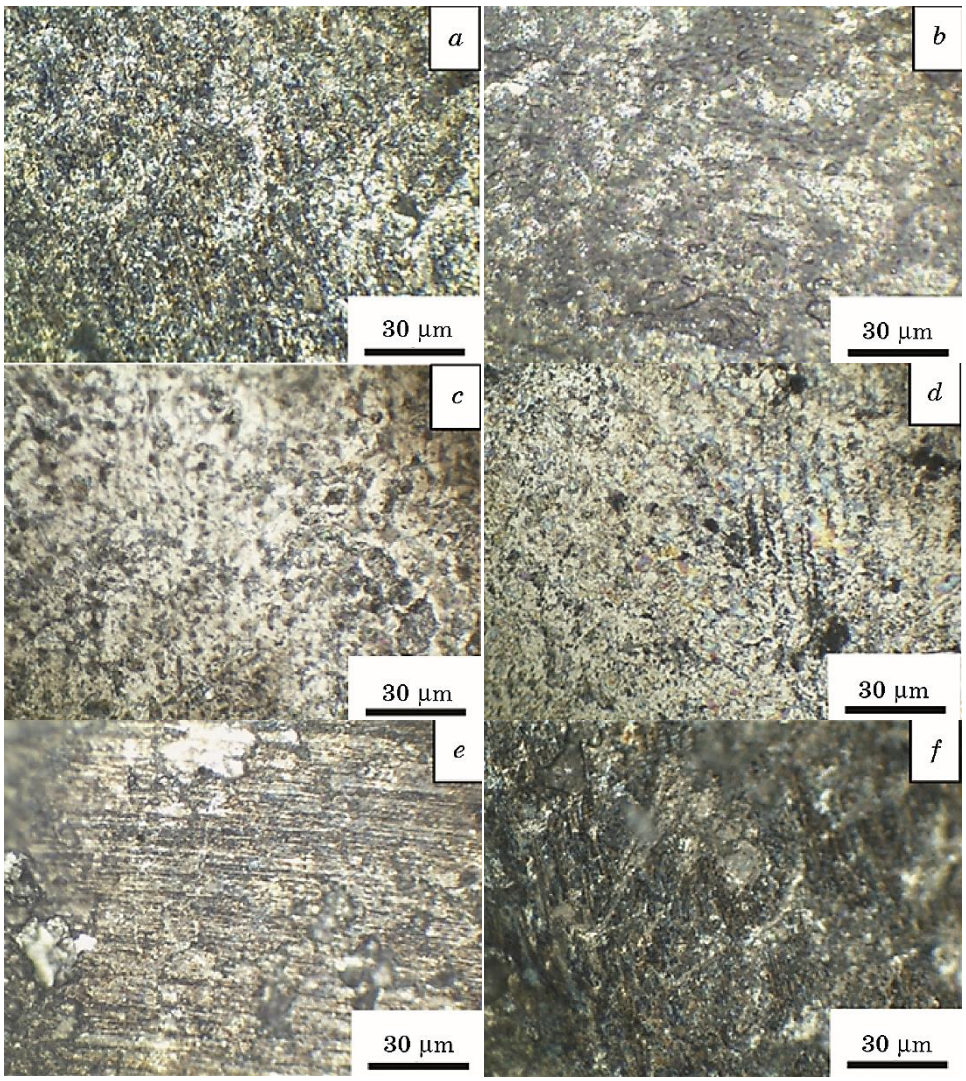


Fig. 5. Surface morphology of AISI 316 stainless steel produced by selective laser melting (*a*, *c*, *e*) and hot rolling (*b*, *d*, *f*) after heat treatment and UIT with duration that provides the maximum microhardness (Fig. 4): T0 + UIT (*a*, *b*), annealing, T1 + UIT (*c*, *d*), water quenching, T2 + UIT (*e*, *f*).

rolled AISI 316 steel in the as-received state and after heat treatment, with all specimens shown after the UIT duration that produced the maximum increase in microhardness.

The SLM specimens have a specific highly dispersed initial structure, including submicron solidification cells and remnants of the melt-track boundaries, which respond differently to deformation de-

pending on the heat treatment. In the T0 + UIT condition, a very fine, heterogeneous surface morphology is observed. The high initial defect density after 3*D* printing restricts dislocation motion. Thus, the deformation relief after UIT is strongly fragmented and rough, without pronounced linear features. T1 annealing partly relieves internal stresses and homogenizes the structure. After T1 + UIT, the surface appears more uniformly deformed and exhibits somewhat larger microrelief features, suggesting a more extensive plastic flow during UIT. After T2 + UIT, a fundamental change in morphology is observed. A directional texture with numerous parallel deformation traces (slip bands) is clearly visible on the surface. Water quenching brings the steel to a highly plastic austenitic state, allowing the metal to deform intensively under the impacts of the UIT striker and to form a pronounced textured relief.

The conventionally deformed metal is characterized by a more macroscopically homogeneous initial structure and different grain morphology. In the T0 + UIT condition, the surface appears as a heavily work-hardened rolled structure. Ultrasonic treatment produces a chaotic fine-grained relief caused by superposition of UIT-induced plastic deformation of the matrix already deformed by rolling. After T1 annealing, recrystallization occurs and the hardening induced by rolling is removed. Subsequent UIT of this stress-relieved surface forms a relatively uniform, smooth microrelief with distinct boundaries of local plastic-deformation regions. The quenched rolled steel surface after UIT shows pronounced structural fragmentation. Visually, it appears the darkest and most finely dispersed, indicating formation of an ultrafine or nanostructured sublattice in the near-surface layer because of a high degree of deformation of quenched austenite.

Figure 6 presents the XRD analysis results. The fragments of the XRD patterns (Fig. 6, *a*, *b*) contain typical reflections from austenite γ-Fe(111), martensite α′-Fe(110) and γ-Fe(200). After UIT, the intensity of the α′-Fe(110) peak gradually increases, especially for the hot-rolled material, indicating development of the $\gamma \rightarrow \alpha'$ deformation-induced martensitic transformation under cyclic impact loading. For the SLM specimens, the changes in the peak intensity are less pronounced, signalizing a higher stability of the austenitic structure.

For the SLM material (Fig. 6, *c*), the CSD size gradually decreases from ≅ 32 nm and ≅ 22 nm for γ-Fe and α′-Fe, respectively, to 12 nm and 6 nm. For the hot-rolled material (Fig. 6, *d*), the CSD size of the γ-phase decreases from 17 to 12 nm during the initial stages of treatment and then increases to 30 nm with increasing treatment duration. The CSD size of the α′-phase remains nearly unchanged up to 180 s before also increasing to approximately 30 nm. These changes reflect the evolution of the coherently diffracting domain structure during UIT and are consistent with the accumulation of lattice defects at the initial treat-

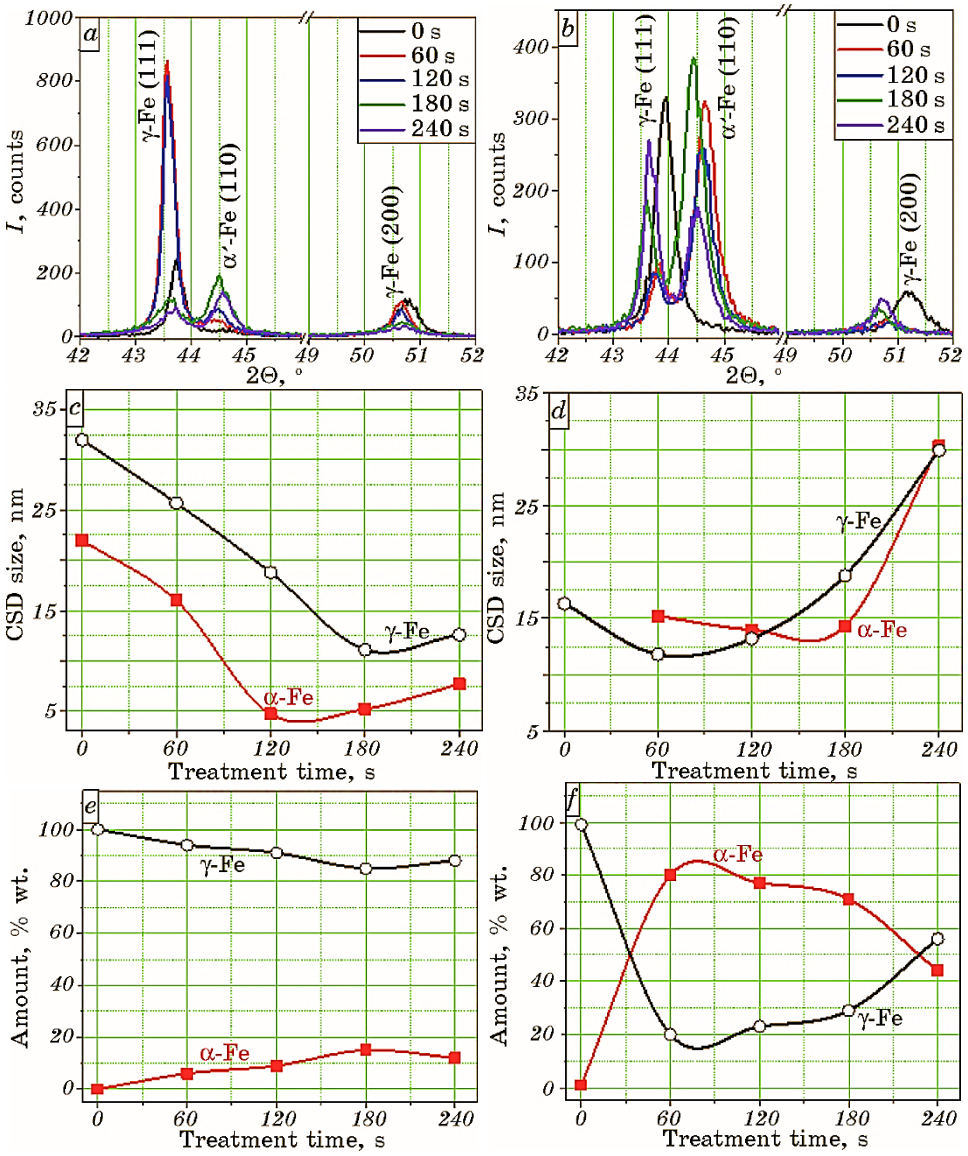


Fig. 6. Fragments of XRD patterns (*a*, *b*), CSD size (*c*, *d*), and quantitative phase composition (*e*, *f*) as a function of ultrasonic impact treatment of AISI 316 stainless steel produced by selective laser melting (*a*, *c*, *e*) and hot rolling (*b*, *d*, *f*).

ment stages, followed by their rearrangement during continued deformation.

For the SLM material (Fig. 6, *e*), the austenitic phase remains domi-

nant throughout the treatment cycle; its content decreases only from 99 to 82%. A different behaviour is observed for the hot-rolled material (Fig. 6, *f*). After only 60 s of UIT, the γ-phase fraction decreases sharply from 99% in the initial state to 20%. The phase composition then stabilizes, indicating considerably lower austenite stability after hot rolling and a high susceptibility to deformation-induced martensitic transformation.

For the SLM material (Fig. 7), the level of compressive residual stresses rapidly increases after UIT. The maximum value is reached after 60 s and is approximately –250 MPa. Subsequently, the stresses gradually relax to about –88 MPa after 240 s. In the hot-rolled material (Fig. 7), the initial state is characterized by tensile stresses; UIT produces compressive stresses in the surface layer after 180 s of treatment at a level of –100 GPa.

Formation of compressive stresses is accompanied by intensive martensitic transformation and strengthening of the surface layer.

These results agree well with the microhardness measurements. For the SLM specimens, the increase in microhardness after UIT is mainly associated with accumulation of compressive residual stresses and dislocation strengthening, while the contribution of martensitic transformation remains limited due to the high austenite stability. For the hot-rolled material, the dominant strengthening mechanism is the in-

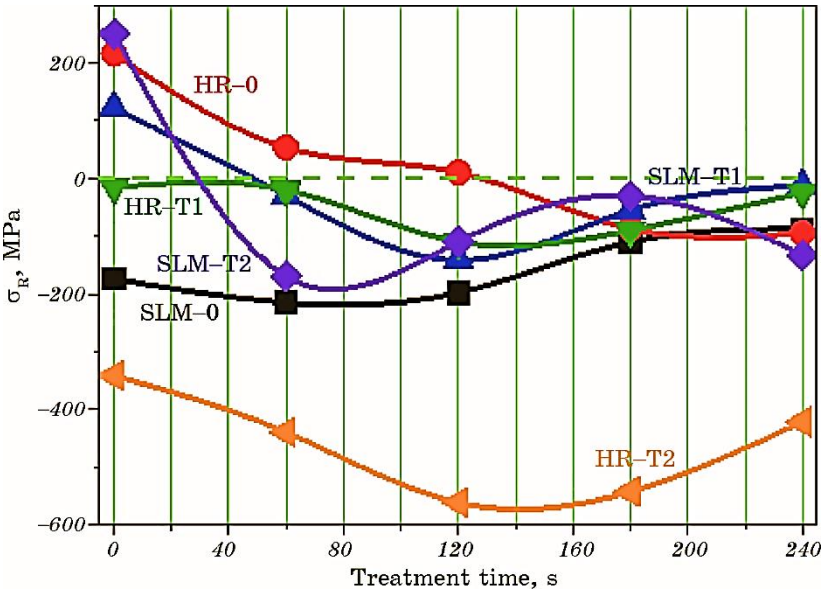


Fig. 7. Residual stress evolution as a function of ultrasonic impact treatment duration for AISI 316 stainless steel produced by selective laser melting and hot rolling.

tensive $\gamma \rightarrow \alpha'$ deformation-induced transformation, accompanied by a sharp increase in the martensite fraction and formation of compressive stresses. This is why the structural and microhardness changes after UIT are much more pronounced for the hot-rolled material compared to the AISI 316 stainless steel produced by selective laser melting.

Figure 8 shows XRD patterns, calculated changes in quantitative phase composition, coherent scattering domain size and first-order stresses for AISI 316 stainless steel produced by SLM and HR after annealing and subsequent ultrasonic impact treatment. The XRD patterns (Fig. 8, *a*, *b*) reveal diffraction peaks corresponding to austenite γ-Fe(111) and (200), as well as deformation-induced martensite α′-Fe(110). With increasing UIT duration, the intensity of the α′-Fe reflections gradually increases, suggesting the progressive $\gamma \rightarrow \alpha'$ deformation-induced martensitic transformation. Simultaneously, diffraction peak broadening is observed, indicating a reduction in the size of coherently diffracting domains and/or an increase in lattice mi-

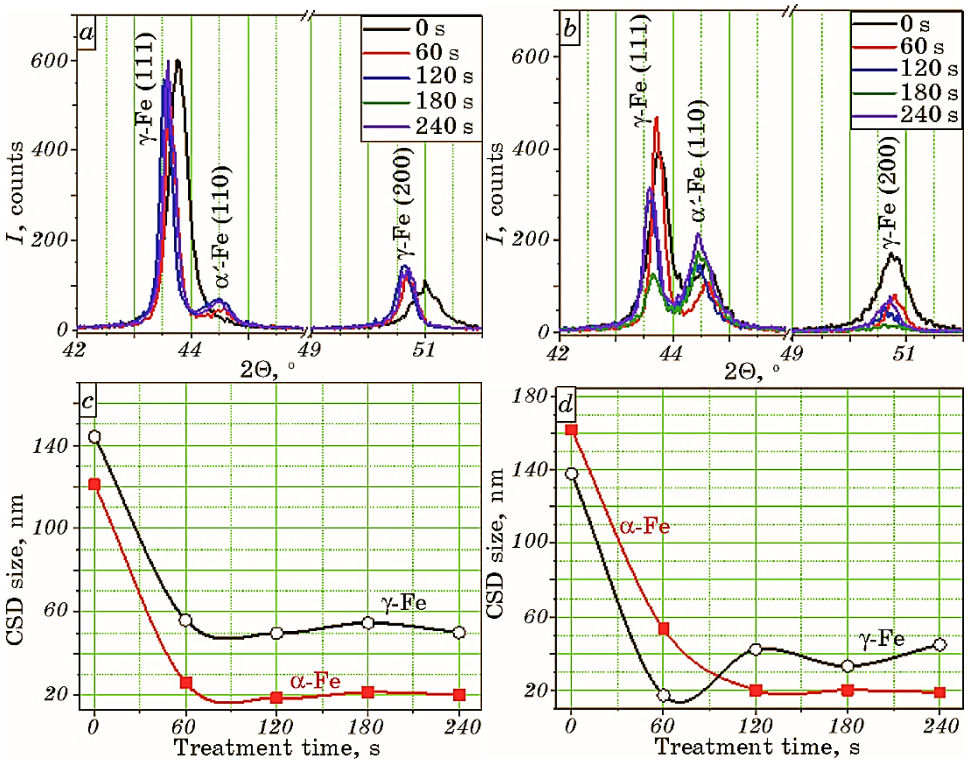
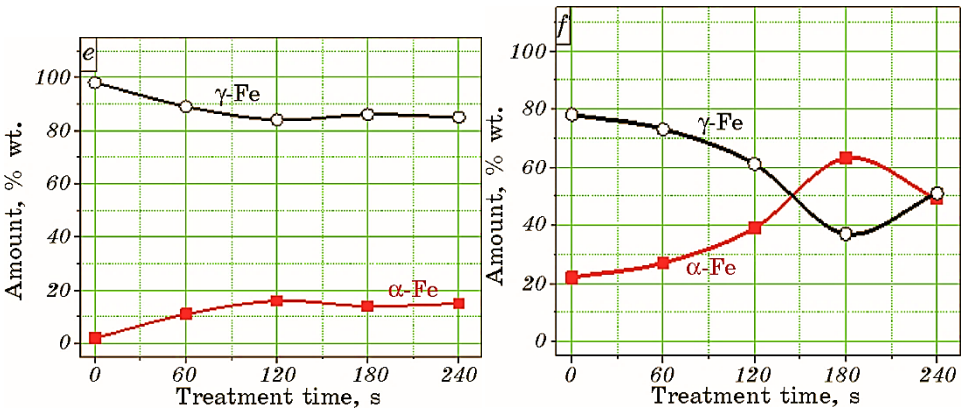


Fig. 8. Fragments of XRD patterns (*a*, *b*), change in CSD size (*c*, *d*), and change in quantitative phase composition (*e*, *f*) in AISI 316 stainless steel produced by selective laser melting (*a*, *c*, *e*) and hot rolling (*b*, *d*, *f*) after annealing (T1) and ultrasonic impact treatment.



Continuation of Fig. 8.

crostrain associated with plastic deformation of the surface layer.

For SLM AISI 316 steel (Fig. 8, *c*), the CSD size of the austenitic γ-Fe phase sharply decreases from ≅ 145 nm in the initial state to 55 nm after only 60 s of UIT. Further increase in treatment duration does not cause additional CSD refinement. For α′-martensite in the initial state, a somewhat smaller CSD size of ≅ 125 nm is observed; after UIT during 60 s, as for γ-Fe, the CSD size also sharply decreases.

For HR AISI 316 steel (Fig. 8, *d*), the CSD-size variation at the initial deformation stages is similar: the CSD sizes of γ-Fe and α′-Fe decrease sharply from 140 nm and 162 nm in the initial state to 18 nm and 58 nm after 60 s of UIT. Increasing the UIT duration leads to a gradual increase in the γ-Fe CSD size to 40 nm, whereas the α′-Fe CSD size continues to decrease and remains at ≅ 20 nm after 120 s of the treatment.

The quantitative phase analysis results (Fig. 8, *e*, *f*) show a gradual decrease in the γ-phase fraction and a corresponding increase in the α′-martensite content with increasing UIT duration for both fabrication routes of AISI 316 stainless steel.

For the SLM specimens (Fig. 8, *e*), the austenite content decreases from ≅ 95% to ≅ 80%, while for the HR material (Fig. 8, *f*) α′-phase formation is much more intensive: the γ-phase content decreases from ≅ 79% to ≅ 38% after 180 s of UIT. The higher amount of the formed α′-phase indicates a higher tendency of the rolled structure to form martensite.

The first-order residual stresses in AISI 316 stainless steel produced by selective laser melting and hot rolling after annealing and subsequent ultrasonic impact treatment are shown in Fig. 7. For the SLM steel after T1 annealing, tensile stresses of ≅ 250 MPa are registered. After UIT, compressive stresses with a maximum value of ≅ 150 MPa

are formed in the surface layer after 120 s of the treatment, followed by the partial relaxation. For HR specimens, minimum stress values are also observed near 120 s of the treatment; however, their absolute magnitude is somewhat lower ($\cong$ 120 MPa) and further treatment decreases the level of compressive stresses.

Figure 9 presents the XRD results for AISI 316 stainless steel after water quenching (HT-2) and subsequent ultrasonic impact treatment. The evolution of quantitative phase composition, CSD size, and first-order stresses as a function of deformation-treatment duration is shown.

The fragments of the XRD patterns (Fig. 9, *a*, *b*) identify (111) and (200) diffraction peaks from the austenitic γ-Fe phase and (110) peak from martensitic α′-Fe. With increasing UIT duration, the intensity of the α′-Fe(110) diffraction peak increases, indicating development of the $\gamma \rightarrow \alpha'$ deformation-induced transformation.

For SLM AISI 316 steel, the austenite to martensite transformation

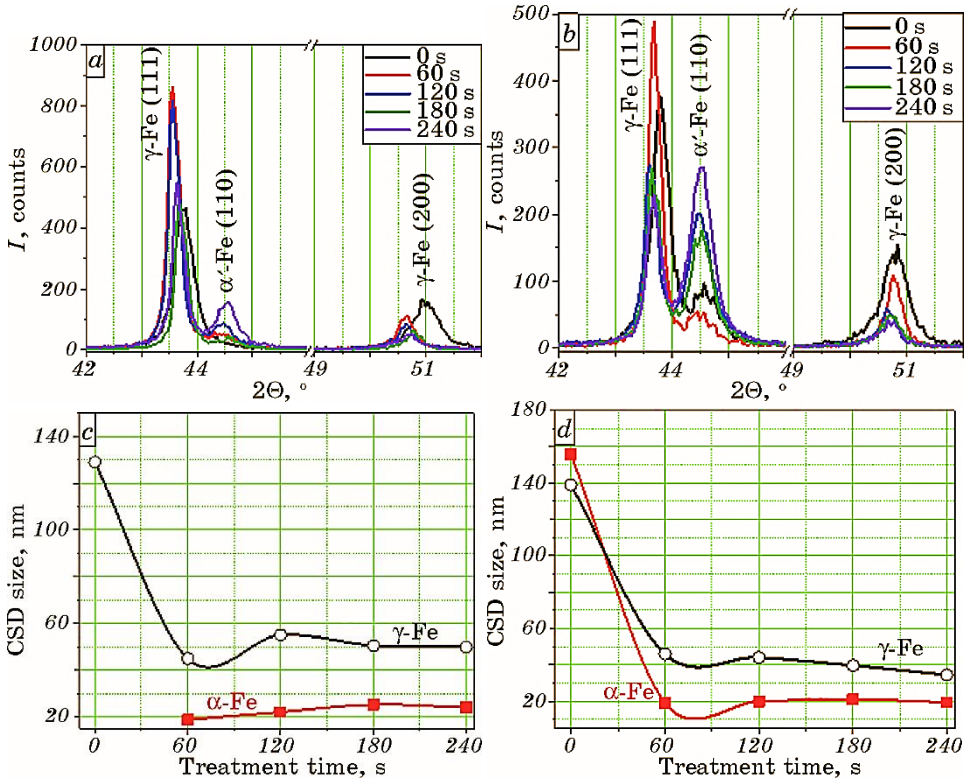
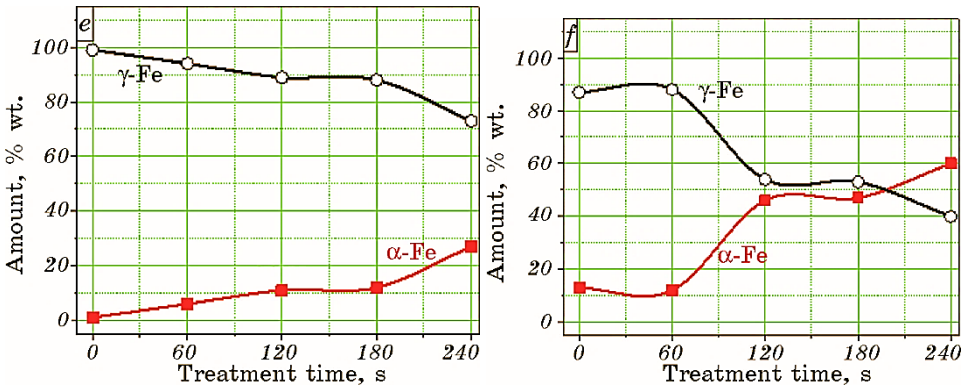


Fig. 9. Fragments of XRD patterns (*a*, *b*), change in CSD size (*c*, *d*), and change in quantitative phase composition (*e*, *f*) in AISI 316 stainless steel produced by selective laser melting (*a*, *c*, *e*) and hot rolling (*b*, *d*, *f*) after water quenching (T2) and ultrasonic impact treatment.



Continuation of Fig. 9.

occurs less intensively compared to the HR steel, indicating a lower tendency of the structure after water quenching (HT–2) to undergo martensitic transformation under deformation.

For the SLM specimen after water quenching (Fig. 9, *c*), the CSD size of austenitic γ-Fe sharply decreases from ≅ 130 nm in the initial state to 45 nm after 60 s of treatment. Further increase in treatment duration does not lead to a significant decrease in CSD size. The CSD size of α′-Fe remains substantially smaller (≅ 25 nm) and does not change with increasing treatment duration. For HR AISI 316 steel (Fig. 9, *d*), the CSD-size variation during UIT is similar.

The quantitative phase composition of AISI 316 stainless steel produced by different routes was determined from the XRD results (Fig. 9, *e*, *f*). For the both fabrication routes, after water quenching (T2) and ultrasonic impact treatment, the γ-Fe content decreases with increasing UIT duration. For the SLM specimens (Fig. 9, *e*), the γ-phase content decreases from ≅ 99% to ≅ 76% after 240 s of UIT. The process occurs gradually, indicating relatively high austenite stability after water quenching. In the hot-rolled specimens (Fig. 9, *f*), martensitic transformation is much more intensive: the γ-phase fraction decreases from 86% to 40% after 240 s of the treatment.

UIT after water quenching induces compressive residual stresses in the surface layer (Fig. 7). For the SLM specimens, tensile residual stresses of approximately 230 MPa are present after water quenching; after 60 s of UIT, they change sign and become compressive (–185 MPa). With further increasing treatment duration, the residual stress values change in a non-monotonic manner, which may be associated with local heating and stress relaxation during continued deformation. For the hot-rolled AISI 316 steel, this effect is considerably more pronounced: compressive residual stresses exceed –550 MPa after 120 s of UIT, indicating severe plastic deformation of the surface layer.

These results show that, after water quenching, subsequent ultrasonic impact treatment causes formation of deformation-induced α'-Fe martensite, reduction of the CSD size of the austenitic phase at the initial stages of UIT and accumulation of compressive residual stresses.

At the same time, SLM-produced AISI 316 steel exhibits higher austenite stability, while the HR material is characterized by more intensive martensitic transformation and formation of higher compressive stresses.

4. CONCLUSIONS

AISI 316 stainless steel produced by selective laser melting exhibited higher stability of the austenitic γ-phase during UIT, manifested by a less pronounced $\gamma \rightarrow \alpha'$ deformation-induced martensitic transformation and a different microhardness evolution compared with the hot-rolled material. This behaviour is attributed to the cellular-dendritic microstructure and residual stresses characteristic of the SLM process.

Hot-rolled specimens are characterized by a much more intensive martensitic transformation during UIT, accompanied by a substantial increase in the α'-phase fraction and formation of higher compressive residual stresses. These factors provide the maximum microhardness values after 120 s of the treatment. At the same time, after the optimal UIT duration exceeded, partial stress relaxation and phase-composition stabilization are observed; this slows slowing down the further strengthening.

Analysis of coherent scattering domain size changes showed that short-term UIT reduces the CSD size of the γ-phase, indicating refinement of the coherently diffracting domains during the initial stages of plastic deformation.

Combining water quenching with UIT increases the susceptibility of the material to deformation-induced martensitic transformation and promotes the formation of higher compressive residual stresses. This effect is more pronounced for the hot-rolled material. In SLM specimens, austenite remains more stable even after water quenching, confirming the distinct microstructural characteristics of additively manufactured AISI 316 stainless steel.

Thus, the efficiency of ultrasonic impact treatment is governed by the initial structural state of the material. Hot-rolled AISI 316 steel shows reveal more intensive deformation strengthening and martensitic transformation after UIT, whereas while the steel produced by selective laser melting is characterized by higher austenite stability and slower kinetics of changes in phase composition, microhardness and residual stresses.

This work was performed within the framework of budget-funded

project No. 2701f of Igor Sikorsky Kyiv Polytechnic Institute 'Scientific foundations of ultrasonic impact and additive technologies for manufacturing highly loaded UAV components with improved range' (No. 0124U001001).

AUTHORS' CONTRIBUTIONS

S. M. Voloshko conceived the study, contributed to the development of the research methodology, supervised the experimental work, interpreted the results, and critically revised the manuscript. I. A. Vladymyrskyi contributed to the conceptualization of the study, analysis and interpretation of the experimental results, and critical revision of the manuscript. M. I. Anyakin contributed to the preparation of the specimens, implementation of the processing procedures, and analysis of the experimental results. N. A. Shapovalova performed microstructural characterization, processed and analysed the experimental data, and contributed to the preparation of the manuscript. M. M. Voron contributed to the preparation and characterization of the investigated materials and to the analysis and interpretation of the microstructural results. A. P. Burmak designed the experimental program, performed and analysed the x-ray diffraction, microhardness, and residual-stress measurements, interpreted the obtained results, prepared the figures, and wrote the original draft of the manuscript. All authors discussed the results, contributed to the revision of the manuscript, and approved its final version.

REFERENCES

1. Z. Huang, J. Zhang, Z. Ma, S. Yuan, and H. Yang, *Appl. Sci.*, **14**, Iss. 22: 10196 (2024).
2. *Stainless Steels* (Ed. J. R. Davis) (ASM International: 1994).
3. J. Singh, V. Il'yenko, and J. P. Oliveira, *Sci. Technol. Weld. Join.*, **30**, Iss. 3: 220 (2025).
4. B. Szubzda, A. J. Antończak, P. E. Kozioł, Ł. Łazarek, B. Stępak, K. Łęcka, A. Szmaja, and M. Ozimek, *IOP Conf. Ser.: Mater. Sci. Eng.*, **113**: 012017 (2016).
5. A. S. Lima, A. M. Nascimento, H. F. G. Abreu, and P. de Lima-Neto, *J. Mater. Sci.*, **40**: 139 (2005).
6. P. Marshall, *Austenitic Stainless Steels: Microstructure and Mechanical Properties* (Springer: 1984).
7. A. Amininejad, R. Jamaati, and S. J. Hosseinipour, *Trans. Indian Inst. Metals*, **74**: 1799 (2021).
8. Y. Xiong, Y. Yue, T. He, Y. Lu, F. Ren, and W. Cao, *Materials*, **11**, Iss. 9: 1557 (2018).
9. F. K. Yan, G. Z. Liu, N. R. Tao, and K. Lu, *Acta Mater.*, **60**, Iss. 3: 1059 (2012).
10. H. A. Rezaei, M. S. Ghazani, and B. Eghbali, *Mater. Sci. Eng. A*, **736**: 364 (2018).
11. L. Zheng, H. Zang, Y. Liu, Y. Xiao, Y. Cong, Z. Cheng, G. Chen, Z. Xing, J. Pan,

Q. Jiang, W. Chen, K. Yamanouchi, H. Xu, and R. Li, *Light Sci. Appl.*, **14**: 352 (2025).
12. Y. B. Lei, Z. B. Wang, B. Zhang, Z. P. Luo, J. Lu, and K. Lu, *Acta Mater.*, **208**: 116773 (2021).
13. Z. B. Wang, J. Lu, and K. Lu, *Acta Mater.*, **53**: 2081 (2005).
14. K. Wang, N. Lin, Q. Liu, Q. Shi, Z. Liu, Q. Zeng, Y. Yu, D. Li, and Y. Wu, *J. Mater. Res. Technol.*, **38**: 5486 (2025).
15. Y. Wang, X. Shu, S. Wei, C. Liu, W. Gao, R. A. Shakoor, and R. Kahraman, *J. Alloys Compd.*, **630**: 189 (2015).
16. D. Zeng, S. Yang, and Z. D. Xiang, *Appl. Surf. Sci.*, **258**, Iss. 12: 5175 (2012).
17. J. L. Marulanda, F. J. Pérez, and A. Remolina-Millán, *J. Phys.: Conf. Ser.*, **466**: 012009 (2013).
18. E. Villabona, F. Veiga, P. J. Rivero, V. Uralde, and A. Suárez, *Steel Res. Int.*, **96**, Iss. 10: 2400976 (2025).
19. M. A. Bevan, A. A. H. Ameri, D. East, D. C. Austin, A. D. Brown, P. J. Hazell, and J. P. Escobedo-Diaz, *Characterization of Minerals, Metals, and Materials* (Eds. S. Ikhmayies, B. Li, J. S. Carpenter, J. Li, J.-Y. Hwang, S. N. Monteiro, D. Firrao, M. Zhang, Z. Peng, J. P. Escobedo-Diaz, C. Bai, Y. E. Kalay, R. Goswami, and J. Kim) (Springer: 2017), p. 577.
20. S. Behera, M. Patel, P. K. Dwivedi, R. Velayutham, A. Gaurav, and J. Murugesan, *J. Mater. Eng. Perform.*, **35**: 1873 (2026).
21. C. A. Sumanariu, C. G. Amza, F. Baciu, M. I. Vasile, and A. I. Nicoara, *Materials*, **17**, Iss. 19: 4808 (2024).
22. B. V. Efremenko, Y. G. Chabak, L. Falat, V. G. Efremenko, A. Amanov, A. M. Syrotyuk, and E. V. Tsvetkova, *Physicochem. Mech. Mater.*, **62**, Iss. 1: 17 (2026).
23. B. N. Mordyuk, G. I. Prokopenko, M. A. Vasylyev, and M. O. Iefimov, *Mater. Sci. Eng. A*, **458**, Iss. 1–2: 253 (2007).
24. B. V. Efremenko, Y. G. Chabak, A. Amanov, V. G. Efremenko, O. Milkovič, E. V. Tsvetkova, I. M. Olejnik, and A. V. Dzherenova, *J. Nano- Electron. Phys.*, **17**, No. 5: 05019 (2025).
25. *Alt-Print, 316L Data Sheet*.
26. A. P. Burmak, M. M. Voron, S. M. Voloshko, S. I. Sydorenko, I. A. Vladymyrs'kyy, S. I. Konorev, B. M. Mordyuk, and M. O. Vasyl'yev, *Metallofiz. Noveishie Tekhnol.*, **47**, No. 8: 827 (2025).
27. S. P. Chenakin, B. M. Mordyuk, N. I. Khripta, and V. Y. Malinin, *Metallofiz. Noveishie Tekhnol.*, **45**, No. 9: 1109 (2023).
28. Y. Zhang, L. Peng, Y. Wang, and C. Ye, *Proc. CIRP*, **123**: 481 (2024).
29. V. Kumar, N. K. Kumbhar, M. D. Joshi, Y.-R. Ma, I. Singh, and S. S. Hosmani, *Mater. Sci. Technol.*, **40**, Iss. 17: 1268 (2024).
30. T. Gundgire, S. Santa-aho, T. Rautio, A. Järvenpää, and M. Vippola, *J. Mater. Process. Technol.*, **323**: 118229 (2024).
31. M. Geľatko, M. Hatala, F. Botko, and R. Vandžura, *Materials*, **17**, Iss. 10: 2270 (2024).
32. I. Morozova, C. Kehm, A. Obrosov, Y. Yang, K. U. M. Miah, E. Uludintceva, S. Fritzsche, S. Weiß, and V. Michailov, *J. Mater. Eng. Perform.*, **32**: 4295 (2023).
33. M. Geľatko, M. Hatala, F. Botko, R. Vandžura, J. Hajnyš, M. Šajgalík, and J. Török, *Materials*, **16**, Iss. 19: 6461 (2023).

Metallophysics and Advanced Technologies
Металофіз. новітні технол.
Metallofiz. Noveishie Tekhnol.
2026, vol. 48, No. 8, pp. 889–906
https://doi.org/10.15407/mfint.48.08.0889
Reprints available directly from the publisher

© 2026 G. V. Kurdyumov Institute for Metal Physics,
National Academy of Sciences of Ukraine
Published by license under
the G. V. Kurdyumov Institute for Metal Physics–
N.A.S. of Ukraine Publishers imprint.
Printed in Ukraine.

PACS numbers: 46.50.+a, 62.20.F-, 81.20.Hy, 81.20.Wk, 81.40.Ef, 81.40.Lm, 83.50.Uv

Gradient Metals' Microstructure Change under Severe Plastic Deformation: A Review

I. E. Volokitina, A. V. Volokitin, T. D. Fedorova, E. N. Reshotkina, and G. M. Zhumanazarova

Karaganda Industrial University,
30 Republic Ave.,
KZ-101400 Temirtau, Republic of Kazakhstan

Research of gradient-structure conditions in metals is rapidly developing area of materials science providing opportunities for creation of materials with unique properties. Long products such as bars and wires are of special interest here as combination of harder surface layer and softer inner part within them allows optimizing a number of mechanical properties. Such gradient shift provides higher durability due to hard outer layer, efficient load distribution across the section, reducing stress concentration in critical points and, more importantly, increasing overall product plasticity. In case of sudden impact, *e.g.*, a hit, softer inner layer may absorb the energy, preventing breakdown. This review study looks into various methods of obtaining gradient metals, mainly based on severe plastic deformation. Their influence on metal-materials' microstructure and properties as well as most efficient areas of application for some of them are studied.

Key words: gradient metals, severe plastic deformation, microstructure.

Дослідження умов ґрадієнтної структури металів є галуззю матеріялознавства, що швидко розвивається та відкриває можливості для створення матеріялів з унікальними властивостями. Особливий інтерес тут представляють довгі вироби, такі як прутки та дріт, оскільки поєднання твердого поверхневого шару та м'якої внутрішньої частини дає змогу оптимізувати

Corresponding author: Irina Yevgenievna Volokitina
E-mail: i.volokitina@alservice.kz

Citation: I. E. Volokitina, A. V. Volokitin, T. D. Fedorova, E. N. Reshotkina, and G. M. Zhumanazarova, Gradient Metals' Microstructure Change under Severe Plastic Deformation: A Review, *Metallofiz. Noveishie Tekhnol.*, **48**, No. 8: 889–906 (2026). DOI: 10.15407/mfint.48.08.0889

© Publisher PH 'Akademperiodyka' of the NAS of Ukraine, 2026. This is an open access article under the CC BY-ND license (https://creativecommons.org/licenses/by-nd/4.0)

ряд механічних властивостей. Такий ґрадієнтний зсув забезпечує вищу міцність завдяки твердому зовнішньому шару, ефективному розподілу навантаження по перерізу, зменшенню концентрації напружень у критичних точках і, що більш важливо, підвищенню загальної пластичности виробу. У разі раптового впливу, наприклад удару, м'який внутрішній шар може ввібрати енергію, запобігаючи руйнуванню. У цьому оглядовому дослідженні розглядаються різні методи одержання ґрадієнтних металів, головним чином, на основі сильної пластичної деформації. Вивчається їхній вплив на мікроструктуру та властивості металевих матеріялів, а також найбільш ефективні області застосування деяких з них.

Ключові слова: ґрадієнтні метали, сильна пластична деформація, мікроструктура.

(Received 25 February, 2025; in final version, 13 May, 2025)

1. INTRODUCTION

Gradient materials are specific group of materials distinguished by smooth controlled change of chemical composition or microstructure properties by volume. This is not random non-homogeneity but specially created gradient intentionally imbedded in material structure in order to achieve specific properties. Unlike traditional homogeneous materials, whose properties are consistent throughout the volume, gradient materials express gradual shift from one phase or composition to another one. This approach provides massive opportunities for creation of materials with unique properties unachievable with traditional methods [1–3].

The notion of gradient materials was mentioned in international scientific periodicals for the first time in history in 1972, when Massachusetts Institute of Technology published results of a brainstorm by metallurgist M. B. Bever [4, 5]. Although Bever's study was financed by USA's Advanced Research Project Agency, immediate activities did not follow. Only ten years later, gradient metal alloys program in Michigan Technical University in Houghton, MI resulted in a number of publications and reports in conferences. Meanwhile, national program of commercial supersonic space shuttle development started in Japan; thermal barrier coating development for this ambitious project became an objective for an enormous research program and gradient material studies. First results were published only in Japanese, then occasionally in other international periodicals and conferences. The program quickly took off and had impressive results, which were shown in 50 of 70 reports in First International Symposium in Sendai in 1990. At the same time, some laboratories in Germany, Switzerland, France, Belgium, and Finland started independent studies, including ones on gradient material structure.

Gradient-materials' area of use is incredibly wide, including metals, ceramics, polymers, composites and even biomaterials [6–11]. For example, gradient can be used in metal alloys for mechanical strength and durability increase. Take an example of casehardened steel: surface layer is enriched with carbon, which provides high strength and durability, while the inner layer remains plastic and impact viscosity. This smooth transition between hard and soft layer prevents cracking and increases overall reliability of the detail. Similar effect is achieved with steel nitridation, where nitrogen diffuses into surface layer, forming nitride phases increasing corrosion resistance and wearability.

Welding seams, although not always designed as gradient materials, often show gradients of composition and microstructure due to welding process peculiarities. Alloy elements segregation, uneven phase distribution and grain size change are possible, which may significantly influence seams' mechanical properties. Special welding and further treatment technologies are used to minimize these negative effects.

Ceramic materials also can be modified using gradient technology. For example, creation of porosity gradient allows controlling material strength and thermal conductivity. Higher porosity may be necessary in some areas for less weight, lower porosity to provide necessary strength in other areas of component [12].

Material surface hardening using ion exchange or ion implantation is another example of successful gradient technology application. Ion implantation allows implementing alloy element atoms into surface layer of material, creating concentration gradient. This leads to surface physical-mechanical properties change, for example, strength and durability increase [13].

Semi-conductor technologies include multiple examples of gradient structures. Classical p–n-transition in diodes and transistors is basically a gradient structure with smooth change of charge carriers' concentration. More modern semi-conductor devices use much more complex gradient structures to control current and voltage properties [14].

Gradient-materials' application in materials science is caused by inability of most monolithic materials to resist different types of loads simultaneously. This includes mechanical (rupture, compression, bending, fatigue), thermal (high or low temperatures, temperature gradients), chemical (corrosion, oxidation, aggressive environments) and even radiation loads. Engineering objective becomes more complicated considering additional criteria such as environmental safety, raw material availability and cost, reuse and recycle possibilities, and, in case of medical or bioengineering use, biocompatibility.

Gradient materials suggest fundamentally different approach. Instead of rapid transition from one material to another, a smooth transition in properties from core to coating is created [15–17]. This is achieved through controlled change of material chemical composition,

structure or microstructure in the intended direction. This approach allows minimizing inner tensions at the separation line and provides strong cohesion between different zones of the material. As a result, high reliability and longevity of the whole structure are achieved. Various methods are used for gradient-materials' creation: spraying, diffusion sintering, selective laser sintering, *etc*. Method selection depends on specific material and required properties. Gradient transition may deal with not only chemical composition but also microstructure (for example, grain size), which allows to manage material mechanical properties more flexibly. Gradient-materials' study is a promising area of contemporary material science allowing creating highly reliable and durable components for various engineering areas. Further research is concentrated on developing new methods of gradient materials creation, their properties modelling and structure optimization to achieve maximum efficiency in specific areas of application [18–20].

In conclusion, it can be said that gradient materials are promising area in material science bringing new possibilities for creation of materials with unique pre-designed properties outperforming those of traditional materials. Continuous technology development allows creating even more complex and efficient gradient structures, expanding their area of application in different spheres of science and engineering. Research in this area continues, leading the way to new discoveries and innovations.

2. OBTAINING GRADIENT MICROSTRUCTURE THROUGH SEVERE PLASTIC DEFORMATION METHODS

Contemporary technologies allow managing properties' anisotropy intentionally in such processes as drawing and rolling. Change of tense-deformed state may create functional gradients of properties, which is especially important for creation of materials, which should possess various properties depending on terms of use. For example, in aircraft and vehicle industry, it is important to have materials capable of taking high loads in some areas and remain light and flexible in others [21].

Recent years have seen active development of severe plastic deformation (SPD) methods with size reduction of microstructure in specific areas of processed material [22–30]. These methods allow improving materials' strength properties significantly at a sufficient level of plastic deformation. Besides, it should be notes that, with development of nanotechnologies and nanolevel processing methods, possibilities of materials' structure and properties management vary even more. This creates new ways of creating high-functional materials, which can be used in various areas, from medicine to electronics.

SPD technologies have a number of attractive features allowing to obtain materials with ultrafine-grain structure and improved mechan-

ical properties, such as higher strength, hardness, and plasticity [31–35]. At first sight, it seems that SPD should become commonly used, considering its advantages. However, its wider practical use is limited by a number of significant obstacles.

One of main reasons is necessity to apply ultrahigh pressure (5–6 GPa and higher) to achieve desired gradient ultrafine-grain structure. Such pressures create extreme equipment load, causing its faster wearing and, subsequently, higher production costs. Development and application of stronger long-life instruments capable of resisting such loads is one of key objectives for wider SPD use. Research in this area includes development of new instrumental materials, use of innovative coatings and perfection of press equipment structures [36–39].

The second serious barrier is lack of available practice-oriented reference literature describing SPD principles and methods. Lack of detailed manuals and recommendations on technological processes development impairs SPD implementation in industry. Engineers lack information to develop optimal processing modes, selection of proper equipment and product quality control. Effort is required to arrange knowledge on SPD, create learning guides, write review articles and organize special extension courses for engineering and technical personnel.

The third limiting factor is necessity to reconsider all technical-economical concept of production and sales of products obtained using SPD. Despite better properties, ultrafine-grain materials may require changes of existing technological chains, which cause higher expenses. This requires complex analysis of costs and benefits from SPD implementation considering not only equipment and instruments cost but also potential rise of product quality and competitiveness.

Manufacturers' conservatism and unwillingness to give up tried-and-tested technological processes also stops wide use of SPD. Transition to new technology is always connected to risks and requires significant investments. To overcome this obstacle, massive awareness-building effort should be done among manufacturers in showing SPD advantages providing consulting assistance with new technologies implementation.

2.1. Methods for Obtaining Limited Length Billets

There are many ways to obtain gradient microstructure in limited length billets through methods. The most popular method of obtaining gradient microstructure is high-pressure torsion (HPT), where shearing deformation occurs in flat cylindrical samples. In the process sample is placed between two punches and deformed by rotating one punch or rotating both punches in opposite directions (Fig. 1, left) [40, 41].

In the first version, (unlimited) sample may flow radially between punches. Radial deformation here is limited by only internal friction

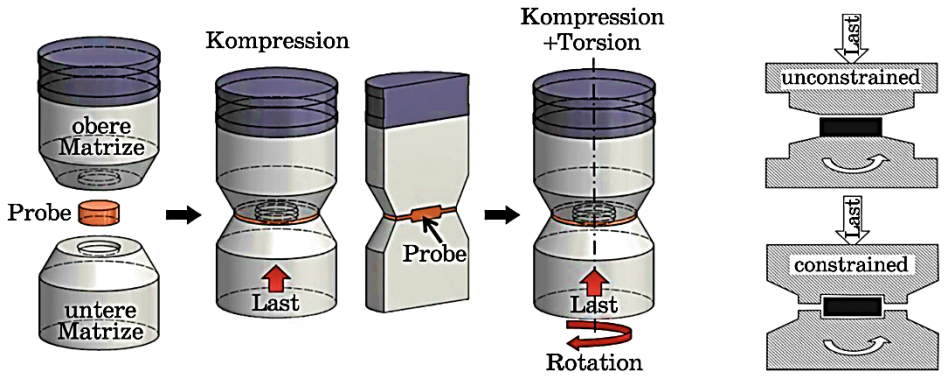


Fig. 1. High-pressure torsion: instruments and operating principle (left, [40]), and difference between 'limited' and 'unlimited' HPT (right, [41]).

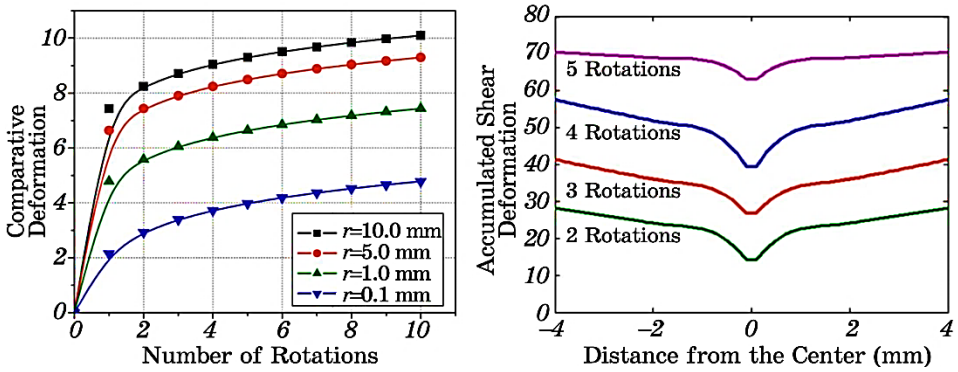


Fig. 2. Comparative deformation (left [41]) and accumulated shear deformation (right [42]) depending on radius and number of rotations.

and friction between the sample and the punch. In this version, sample thickness reduces and diameter increases. Sample thickness in 'limited' version is constant throughout the process. Thus, a distinctive radial deformation gradient occurs depending on number of rotations (Fig. 2).

Accumulated shear deformations rapidly increase radially from disc centre at first, but at longer distances become more linear. Formed microstructures show these gradients in grain size and shape [41].

At the beginning of HPT, as a rule, laminated structures are formed which turn into equiaxial structures as deformation increases due to grain fragmentation, starting from the edge of sample. Average grain size also initially grows from the edge to the centre of the sample. At enough elongation, saturated grain size is reached, when further deformation does not cause structural changes. Thus, highly homogeneous microstructures may be obtained in HPT samples after enough ro-

tations [41, 43].

Another widespread method is equal-channel angular pressing (ECAP). Its idea is the following: a billet is extruded through fitting rig along two channels with the same cross sections crossing at 90–135°. After each pass, the billet is rotated along its axis by 180° (Fig. 3). Deformational impact of ECAP creates various defects of alloy crystals, changing material microstructure. As a result, there is consecutive decrease of grain size due to formation of grid of small-angle boundaries and, then, large-angle boundaries. The advantage is that ECAP can be repeated several times without billet size change, and applied tension can be increased to any level.

Besides, critical shear instability may be caused by deformation direction change, for example, when switching from regular shear (at ECAP) to variable loading with axial compression–extension (at fatigue) (Fig. 4, *b*). Depending on grain boundaries stability in shear

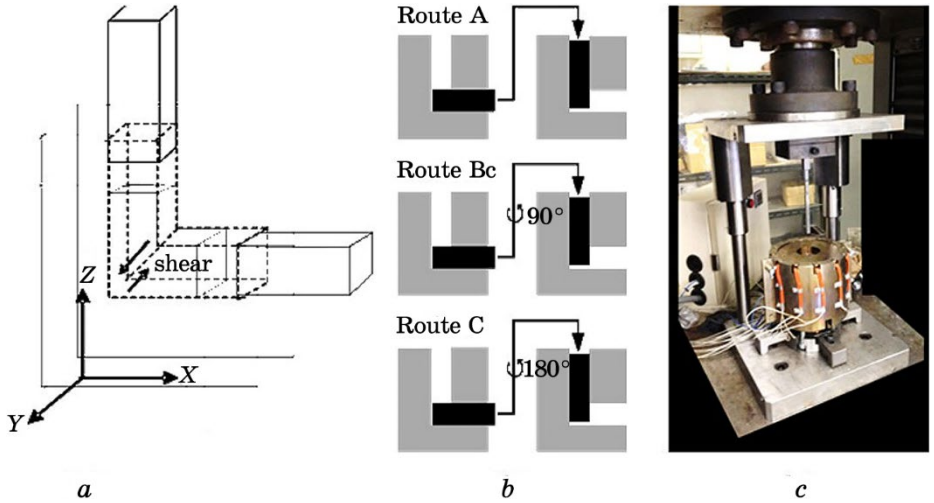


Fig. 3. Equal-channel angular pressing layout [44].

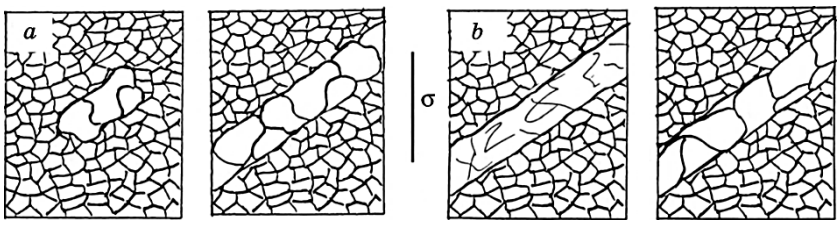


Fig. 4. Alternative models of shear bands formation in UFG materials: local grain coarsening spreading along the shear (*a*); shear band formation through deformation mode change and following coarsening [45] (*b*).

band grain coarsening caused by deformation may occur.

2.2. Methods of Obtaining Long Billets

However, the abovementioned methods practically cannot be used to obtain long billets in industrial conditions. Thus, research of gradient-structure conditions in metal materials is a rapidly developing area of contemporary material science. Long products such as bars and wires, where combination of hard surface layers and soft core provides unique set of mechanical properties, are of special interest. Such architecture allows increasing wearability significantly, evenly distribute loads across bar section and, subsequently, increase overall plasticity and breakdown resistance. This is especially important for details working under high friction or impact loads.

'Conform' method based on SPD principles is used in electrotechnical industry for making heavy-duty copper busbars and cables with higher conductivity [46–48]. Nanostructured implants obtained using SPD are used in medicine and show increased biocompatibility and better acceptability in human body that is promising way for creation of more effective and safer medical products. In addition, there has been research of SPD use in aerospace industry for creation of light and strong materials for aircraft construction as well as automobile manufacturing for creation of details with higher wearability. SPD opportunities are enormous, and further research in this area may lead to creation of new materials with unique properties and expansion of this technology area of application [49, 50].

Main way of metal pressure treatment used in contemporary technological processes of wire making is drawing performed in one-piece die. This process is a key technological operation where two main tasks are solved: obtaining wire with set shape and size and forming required physical-mechanical properties, which define quality and functionality of the final product. For solving the first task size of initial billet (wire rod) should be carefully selected, intermediate billet size should be defined, and drawing transitions for each section should be calculated. This allows optimizing technological process and providing high preciseness of obtained product. Another aspect is choice of proper equipment and tools, which must correspond to set parameters and provide process stability.

The second task is to define steel grade, which will be used in the drawing process and to set optimal values of reduction per pass and overall reduction. These parameters are necessary to achieve set physical-mechanical properties regulated by corresponding state standards and technical conditions. It should be noted that wire properties such as strength, plasticity and corrosion resistance directly depend on choice of steel grade and processing conditions.

However, despite all achievements in drawing, obtaining ultrafine-grain structure providing high physical-mechanical properties of wire using traditional drawing in one-piece die appears to be impossible. This is related to quasi-monotonic character of deformation limiting the ability to achieve required material properties. As a result, researchers and engineers started looking for alternative processing methods that could overcome these limitations.

A classic example of gradient-structure formation is non-monotonic shear deformation during drawing with controlled shear [27, 28]. In case of using low-carbon steel, this method allows to create structure gradient from coarse-grain core to nanostructure surface layers possessing ultrahigh microhardness. Experiments have proven multifold wearability increase for such processed products compared to initial material. However, it should be noted that gradient-structure formation is just one of tools of managing properties. Gradient interaction with other effects such as texturing, phase transformation and chemical composition change opens new possibilities for fine-tuning of local material properties.

Significant potential in this area is shown by dynamic strain ageing (DSA). DSA is seen at severe plastic deformation leading to formation of ultrafine-grain and nanostructural states [51, 52]. Simultaneously with grain size decrease, there is material strength and hardness increase, which is related to point defects and dislocations build-up; this prevents dislocations movement. Combination of gradient-structure formation methods and DSA allows creating products with gradually changing properties from nano- to macrolevel. For example, a product with nanostructural durable surface layer changing into more plastic coarse-grain core, which provides higher impact viscosity.

Managing gradient structure and DSA opens prospects for creation of functional materials with set properties. For example, composite materials where gradient structure improves adhesion between components or a product with controlled cracking resistance, where gradient transitions facilitate crack-propagation energy dissipation. Besides, development of gradient structure methods modelling and computer design allows optimizing technological processes and predicting future material properties. Further research should be aimed at study of various deformation process parameters' (temperature, deformation speed, deformation rate) impact on gradient-structure formation and DSA display as well as development of new control methods and measurement of local properties in gradient-structure materials. In the longer term, this will allow to create high-efficient and durable products for various industries from machinery to aerospace and medicine.

Annealing is used in some cases to restore material plasticity, even if it means less gain in strength characteristics at SPD stage. Depending on specific case, further thermal treatment may simply restore ma-

terial, while another one may cause local recrystallization.

Influence of such annealing is shown in Fig. 5 with types of microstructures and changes in microhardness of non-alloyed copper samples deformed by 8 passes of hot ECAP and then annealed at different temperatures [53].

This tendency shows significant drop of microhardness between 210°C and 250°C. Flow curves between initial copper state and after 8 passes of ECAP show rise of strength properties to the detriment of plasticity, but annealing at 200°C for 20 minutes after SPD shows simultaneous rise of strength and plasticity properties, which is unusual for annealing treatment effect. In authors' opinion, this can be explained by formation of small recrystallized grains with fewer dislocations than in initial grains, but their small size facilitates macroscopic increase of flow stress.

Another promising process allowing obtaining gradient microstructure in bars is cross rolling and one of its types—radial-shear rolling (RSR) patented in Ref. [54]. Its difference from cross rolling is rolling of one-piece bar through three-roll layout with large feeding angles. Unlike well-known processes such as equal-channel angle pressing and Bridgman anvil deformation, RSR has a number of advantages, including lower deformation force, no limits for billet length and ability of rolling with significant elongation ratio without destruction.

Radial shear rolling differs from other metal pressure treatment in the fact that it does not only provide high quality of final product but also allows reducing its production costs significantly. In the process of radial shear rolling, typical spiral macrostructure formation occurs, which is explained by specific force and kinematic conditions appearing during technological tool impact on the billet. Due to this, differ-

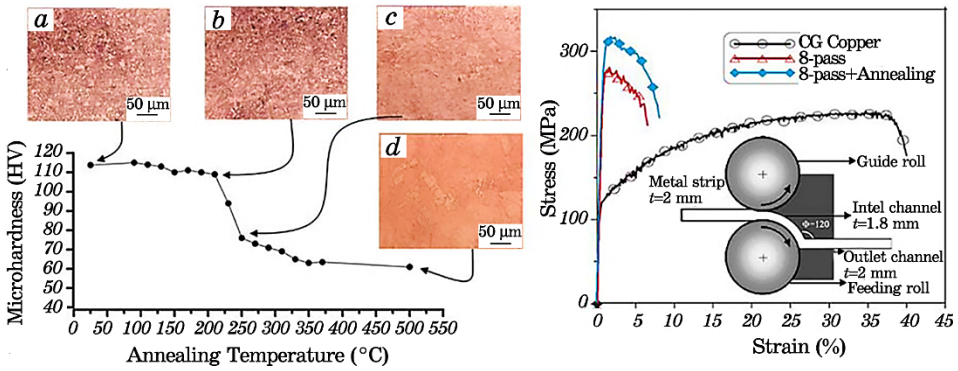


Fig. 5. Influence of annealing temperature on non-alloyed copper after 8 passes of hot ECAP: microphotographs and change of microhardness depending on temperature (*a*) change of flow stress after annealing at 200°C for 20 minutes (*b*) [53].

ent metal layers movement trajectories with different pitch and movement angle of screw lines display complex patterns. As a result, apart from general material structure reduction, there is layer-by-layer orientation of reduced structure, where each layer obtains its own unique movement trajectory, which in its turn influences mechanical properties of obtained product [55, 56].

At RSR, deformation zone follows state of stress close to all-round compression with high shear deformations. In outer layer, each small trajectory-oriented element is exposed to compression deformation along billet radius (diameter), deformation along movement direction and, respectively, stretching deformation across the screwing trajectory (Fig. 6). Metal structural composition elements obtain form of isotropic particles of high dispersion ability separated from each other. Tendency towards formation of structured banded orientation and reticulation caused by general billet elongation is thus suppressed. Such metal deformation conditions do not exist in any known stationary bar-making process. Overall, along the billet volume, metal helicoidal egress within the groove along set trajectories with slowing of surface layers and speed-up of core ones creates volumetric macroshear effect. Macroshear deformations are extremely favourable for non-defect plastic deformation of metal and facilitate significant increase of billets' technological deformability [54].

Authors of the study [58] have shown obtained gradient microstructure of bar section (Fig. 7). However, this method can be used only for deformation of limited length bars, as the authors of Ref. [59] have noted, RSR uses very expensive planetary stands.

Study [60] performed experimental research of RSR technological possibilities for obtaining small-diameter titanium-alloy rods with gradient microstructure from small diameter ingots. Influence of rolling patterns and thermal deformation conditions on macro- and microstructure of obtained ingots and mechanical properties was studied. Production layout, which was experimentally proven at RSR stands,

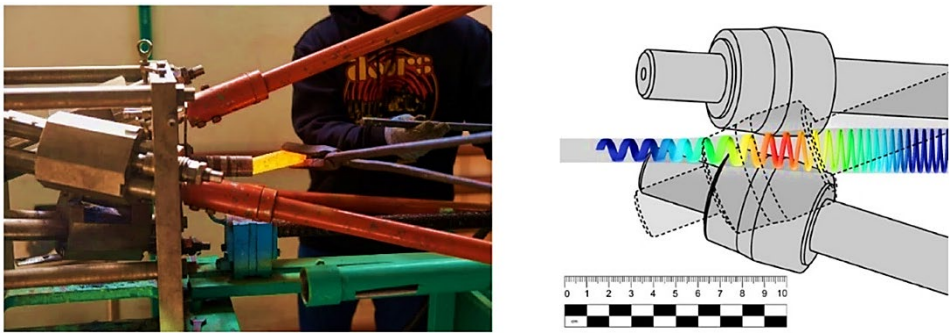


Fig. 6. Radial-shear rolling overview [57].

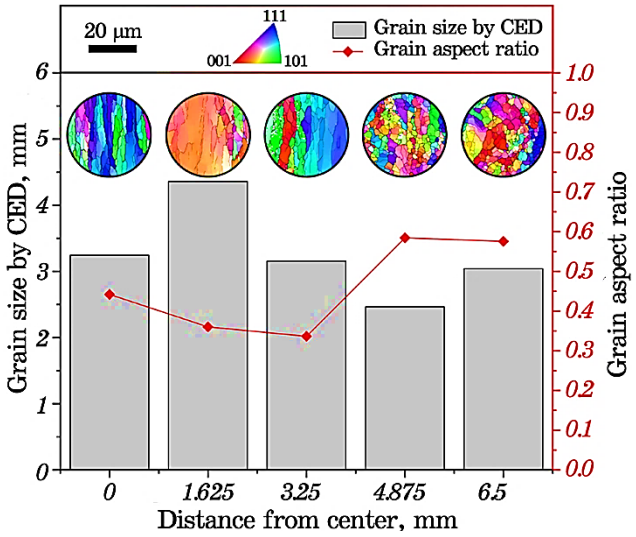


Fig. 7. EBSD study of the gradient microstructures of rolled bar longitudinal sections [58].

can be suggested as foundation for high-technological minirolling line with flexible production plan.

There are studies considering possibilities of combining RSR and drawing [61], since use of traditional drawing as final operation after various SPD processes allows to eliminate all drawbacks (geometrical roughness, pores, *etc.*) of preliminary deformation [15, 26].

Study [26] looks into evolution of copper wires' microstructure and mechanical properties during deformation in rotating equal-channel echelon matrix followed by drawing. As a result of deformation, ultrafine-grain gradient microstructure with high share of large-angle boundary grains was obtained. Use of such strengthened wire in construction will allow reducing structure weight due to smaller diameter.

Study [15] developed new way of wire deforming—'pressing-drawing', which is more effective than previously known ways of obtaining metal with ultrafine-grain structure. The example of tough-pitch copper deformed using pressing–drawing process shows that combination of ECAP and traditional drawing leads to formation of structure with fine homogeneous equiaxial grain with mostly large-angle boundary. These results could be achieved using shear deformations occurring in equal-channel matrix, which caused formation of material structure different from one formed through traditional methods.

As an alternative solution to improve metal deformation process, study [55] suggested innovative combination of radial shear rolling and traditional drawing. This technology forms a unique combination,

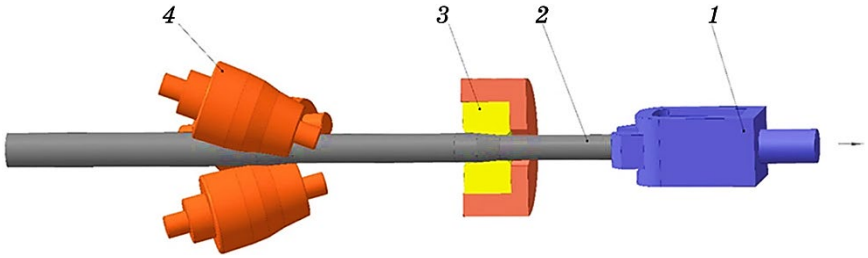


Fig. 8. Rolling and drawing process overview [55].

which allows increasing metal treatment significantly. The process begins from rod rolling through cone-shaped rollers positioned at 120° to each other (Fig. 8). This specific configuration provides even deformation spreading throughout material volume, which, in its turn, promotes structure homogeneity improvement. This is especially important for obtaining high-quality metal products with set properties.

Besides, combination of radial shear rolling and drawing allows reducing overall treatment time significantly. This happens due to the fact that both processes, namely, deformation and rod profile formation, are done simultaneously. This approach speeds up production process and reduces energy and material costs.

During simultaneous rod drawing through rollers and drawing-block there are tension stresses, which, as studies have shown, reduce force required for drawing. This is caused by formation of screw-shaped dents on rod surface after radial shear-rolling step. These dents do not touch drawing-block during drawing, which reduces overall force by 15–17%. This significant force reduction eases the process and increases equipment lifetime [62].

Rod deformation is done using gripping unit, which carefully and effectively provides rod movement through both deforming units. In the gap between these two units, rod torsion occurs that additionally improves mechanical properties of the final product.

As a result of such deformation, gradient microstructure with improved mechanical properties is formed in the rod (Fig. 9).

Thus, suggested solution combines advantages of both radial-shear rolling and traditional drawing, which allows optimizing metal treatment process, improve product quality and reduce costs. Implementation of this technology may bring significant changes in metallurgical industry and open new possibilities for high-quality metal-products' making.

Studies and experience accumulated over the recent years show that radial-shear rolling combines advantage of traditional methods and ability of intense grain-size reduction, even nanoparticles' dispersion and controlled microstructure gradient state.

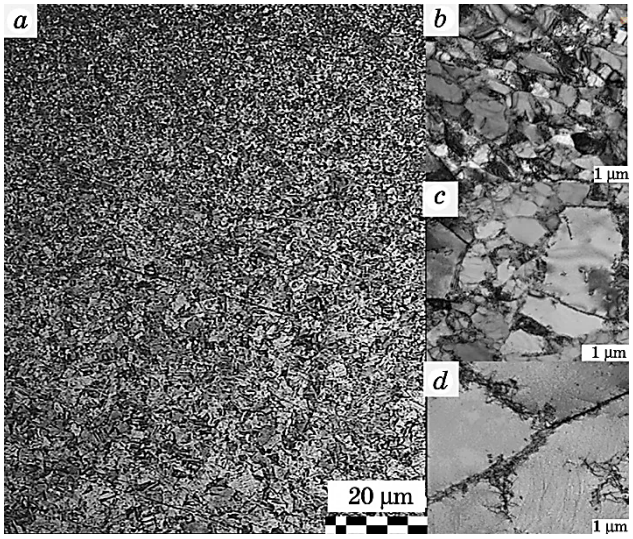


Fig. 9. Rod microstructure after deformation: rod section optical image (*a*); surface area (*b*); neutral area (*c*); central area (*d*) [62].

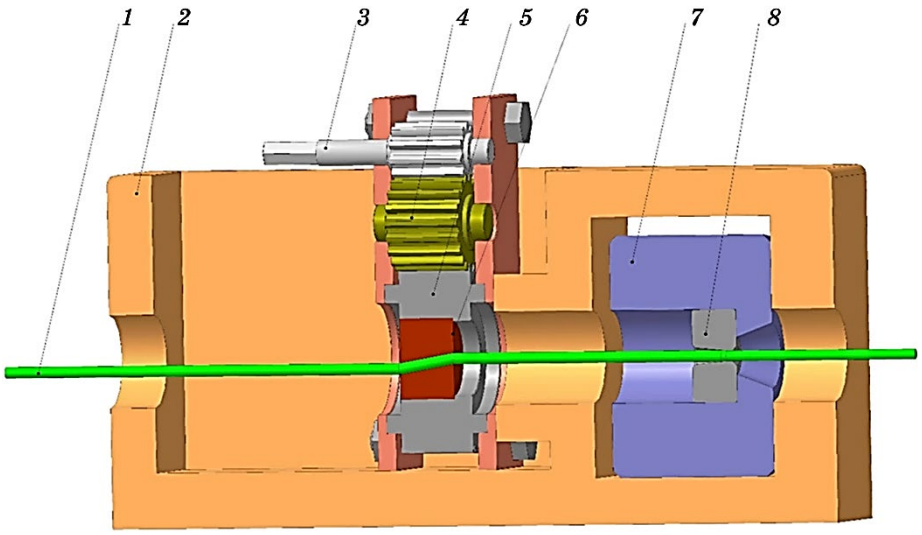


Fig. 10. Wire deformation overview [63].

Research presented in the study [63] looks into evolution of copper wires' microstructure and mechanical properties during deformation in rotating equal-channel echelon matrix followed by drawing (Fig. 10). As a result of performed experiments, ultrafine-grain gradient microstructure with high share of large-angle boundary grains

(Fig. 11) was obtained. This discovery is important for construction industry, as use of such strengthened wire in construction will allow reducing structure weight due to smaller diameter, which in its turn may lead to material saving and better operational characteristics.

Combination of cross rolling and following pressing in angle equal-channel matrix allows to implement stressed–strained state with intense shear of surface metal layers during screw rolling in first deformation zone and combination of intense shear deformation of angular pressing and torsion in second deformation zone. In this case, central part of the billet, which was not fully treated in the first deformation zone, is intensely treated in the second deformation zone through another procedure—in echelon ECA matrix. This creates good conditions for formation of ultrafine-grain structure throughout the whole round billet. Besides, study of angular pressing and torsion parameters is of interest. Technically, this is a process of continuous pressing with billet torsion elements inside the matrix, which increases level of cumulative defor-

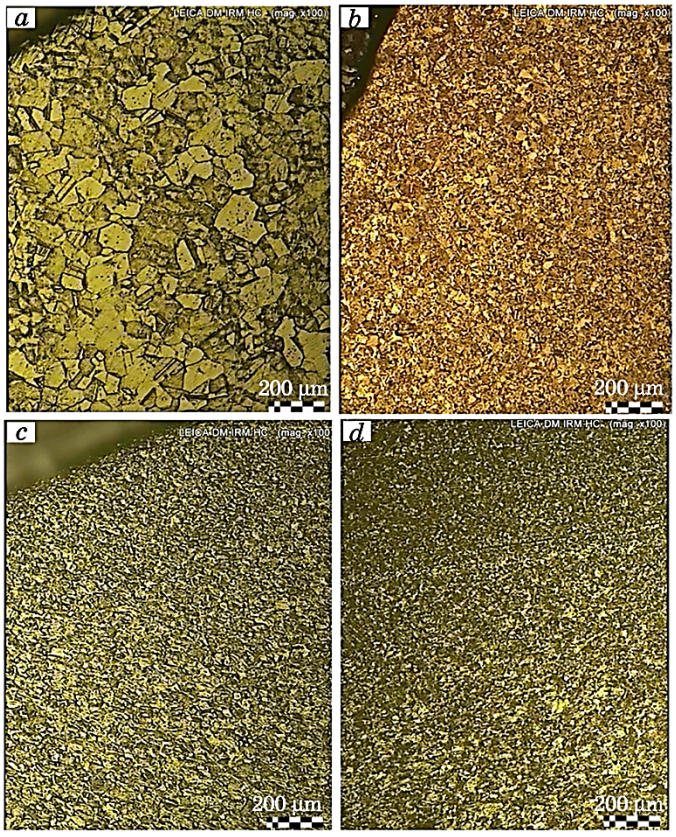


Fig. 11. Copper wire microstructure after three deformation cycles.

mation throughout billet volume and facilitates central-area treatment. Same as in method [38], less homogeneous torsion deformation is covered by more homogeneous and intense shear deformation at ECA pressing, which evens out occurring non-homogeneity after torsion.

Combination of cross rolling and following pressing in angle equal-channel matrix allows to implement stressed–strained state with intense shear of surface metal layers during screw rolling in first deformation zone and combination of intense shear deformation of angular pressing and torsion in second deformation zone. In this case, central part of the billet, which was not fully treated and elongated in the first deformation zone, is intensely treated in the second deformation zone through another procedure—in echelon ECA matrix. This creates good conditions for formation of ultrafine-grain structure throughout the whole round billet.

3. CONCLUSION

Combining gradient structures and thermal treatment brings new possibilities for material properties improvement. Thermal treatment, such as annealing and tempering, may significantly change metal microstructure, which in combination with gradient properties allows achieving optimal combination of strength, plasticity and wearability. This is especially important for components working under heavy loads and temperatures. Thus, analysis of contemporary energy-saving technologies of obtaining metals and alloys with gradient structure and ability of combining them with thermal treatment is an important and promising area of research. This area not only promotes creation of efficient durable materials but also accepts challenges of contemporary industry requiring implementation of innovative and sustainable solutions. In the future, further development of this area can be expected, which will lead to creation of new high-quality metal products with unique properties demanded in various industries.

Funding: This research has been/was/is funded by the Science Committee of the Ministry of Science and Higher Education of the Republic of Kazakhstan (Grant No. AP19678974).

REFERENCES

1. I. E. Volokitina, A. V. Volokitin, M. A. Latypova, V. V. Chigirinsky, and A. S. Kolesnikov, *Prog. Phys. Met.*, **24**, No. 1: 132 (2023).
2. P. Wang, L. Zhao, J. Liu, M. D. Weir, X. Zhou, and H. H. K. Xu, *Bone Research*, **2**: 14017 (2014).
3. I. Volokitina, A. Volokitin, E. Panin, and B. Makhmutov, *Symmetry*, **16**, No. 9: 1174 (2024).
4. M. B. Bever and P. E. Duwez, *Mater. Sci. Eng.*, **10**: 1 (1972).

5. M. Shen and M. B. Bever, *J. Mater. Sci.*, **7**: 741 (1972).
6. A. Bychkov and A. Kolesnikov, *Metallogr., Microstruct., Anal.*, **12**, No. 3: 564 (2023).
7. M. Danilenko and V. Gorban, *Mater. Sci. Forum*, **503**: 787 (2006).
8. V. Bhavar, P. Kattire, S. Thakare, and S. Patil, *IOP Conf. Ser.: Mater. Sci. Eng.*, **229**: 012021 (2017).
9. S. Ramakrishna, J. Mayer, E. Wintermantel, and K. Leong, *Compos. Sci. Technol.*, **61**, No. 9: 1189 (2001).
10. B. Sapargaliyeva, A. Agabekova, G. Ulyeva, A. Yerzhanov, and P. Kozlov, *Case Studies in Construction Materials*, **18**: e02162 (2023).
11. I. E. Volokitina, *J. Chem. Technol. Metall.*, **57**, No. 3: 631 (2022).
12. J. Jauk, H. Vašatko, L. Gosch, K. Ristoski, J. Füssl, and M. Stavric, *Ceramics*, **6**: 2243 (2023).
13. S. Grigoriev, A. Metel, M. Volosova, and Y. Melnik, *Mech. Ind.*, **16**: 711 (2015).
14. W. Shockley, *The Bell System Technical Journal*, **28**: 3 (1949).
15. I. E. Volokitina and A. V. Volokitin, *Metallurgist*, **67**: 232 (2023).
16. I. E. Volokitina, A. V. Volokitin, and E. A. Panin, *Prog. Phys. Met.*, **23**, No. 4: 684 (2022).
17. N. Zhangabay, B. Sapargaliyeva, U. Suleimenov, K. Abshenov, A. Utelbayeva, A. Kolesnikov, K. Baibolov, R. Fediuk, D. Arinova, B. Duissenbekov, A. Seitkhanov, and M. Amran, *Materials*, **15**: 5732 (2022).
18. I. Volokitina, A. Volokitin, A. Denissova, and Y. Kuatbay, and Y. Liseitsev, *Case Studies in Construction Materials*, **19**: e02346 (2023).
19. D. A. Sinitsin, A. E. M. M. Elrefaei, A. O. Glazachev, D. V. Kuznetsov, A. A. Parfenova, E. I. Kayumova, and I. V. Nedoseko, *Construction Materials and Products*, **6**, No. 6: 2 (2023).
20. A. Nurumgaliyev, T. Zhuniskaliyev, V. Shevko, Y. Mukhambetgaliyev, B. Kelamanov, Y. Kuatbay, A. Badikova, G. Yerekeyeva, and I. Volokitina, *Sci. Rep.*, **141**: 7456 (2024).
21. A. D. Korotaev, A. N. Tyumentsev, I. Y. Litovchenko, *Phys. Met. Metall.*, **90**: 36 (2000).
22. A. V. Volokitin, I. E. Volokitina, and E. A. Panin, *Prog. Phys. Met.*, **23**, No. 3: 411 (2022).
23. I. E. Volokitina, *Prog. Phys. Met.*, **3**, No. 24: 593 (2023).
24. I. Volokitina, A. Volokitin, E. Panin, T. Fedorova, D. Lawrinuk, A. Kolesnikov, A. Yerzhanov, Z. Gelmanova, and Y. Liseitsev, *Case Studies Construct. Mater.*, **19**: 02609 (2023).
25. A. Volokitin and E. Panin, *Metallogr. Microst. Anal.*, **11**, No. 4: 673 (2022).
26. B. Sapargaliyeva, A. Agabekova, S. Syrlybekkyzy, L. Nurshakhanova, F. Nurbaeva, A. Kolesnikov, G. Sabyrbayeva, A. Izbassar, O. Kolesnikova, Y. Liseitsev, and S. Vavrenyuk, *Case Studies Construct. Mater.*, **19**: e02256 (2023).
27. A. Volokitin and D. Kuis, *J. Chem. Technol. Metallurgy.*, **56**: 643 (2021).
28. M. Hawryluk, J. Ziemba, and P. Sadowski, *Materials Science*, **50**: 74 (2017).
29. E. V. Galieva, V. A. Valitov, R. Ya. Lutfullin, and A. A. Bikmukhametova, *Defect Diffus. Forum*, **385**: 150 (2018).
30. I. E. Volokitina, *Metal Sci. Heat Treat.*, **63**: 163 (2021).
31. S. Lezhnev, A. Naizabekov, and E. Panin, *Procedia Eng.*, **81**: 1499 (2014).
32. S. Lezhnev and A. Naizabekov, *Procedia Eng.*, **81**: 1505 (2014).

33. G. Kurapov, E. Orlova, and A. Turdaliev, *J. Chem. Technol. Metallurgy.*, **51**, No. 4: 451 (2016).
34. H. Tian, H. L. Suo, O. V. Mishin, Y. B. Zhang, D. Jensen, and J.-C. Grivel, *J. Mater. Sci.*, **48**: 4183 (2013).
35. R. Yuan, *Acta Mechanica*, **234**: 4147 (2023).
36. A. Naizabekov and E. Panin, *J. Mater. Eng. Perform.*, **28**: 1762 (2019).
37. S. Lezhnev and E. Panin, *Advanced Materials Research*, **814**: 68 (2013).
38. A. Naizabekov, A. Arbuz, S. Lezhnev, and E. Panin, *Phys. Scr.*, **94**, No. 10: 105702 (2019).
39. S. Ramesh Kumar, K. Gudimetla, B. Tejaswi, and B. Ravisankar, *Trans. Indian. Inst. Met.*, **70**: 639 (2017).
40. D. J. Lee, E. Yoon, D.-H. Ahn, B. H. Park, H. W. Park, L. J. Park, Y. Estrin, and H. S. Kim, *Acta Mater.*, **76**: 281 (2014).
41. A. P. Zhilyaev, T. R. McNelley, and T. G. Langdon, *J. Mater. Sci.*, **42**: 1517 (2007).
42. Y. Estrin, A. Molotnikov, C. H. J. Davies, and R. Lapovok, *J. Mech. Phys. Solids*, **56**: 1186 (2008).
43. A. Vorhauer and R. Pippan, *Scr. Mater.*, **51**: 921 (2004).
44. M. Rifai, H. Miyamoto, and H. Fujiwara, *Metals*, **4**: 55 (2014).
45. H. Mughrabi and H. W. Höppel, *Int. J. Fatigue*, **32**: 1413 (2010).
46. S. Atefi, M. H. Parsa, D. Ahmadkhaniha, C. Zanella, and H. R. Jafarian, *J. Mater. Res. Technol.*, **21**: 1614 (2022).
47. X. Pang, Y. Zeng, S. Li, Z. Li, P. Shen, B. Zhang, and W. Deng, *J. Mater. Res. Technol.*, **23**: 4479 (2023).
48. V. Ayati, M. H. Parsa, and H. Mirzadeh, *Adv. Eng. Mater.*, **18**: 319 (2016).
49. M. Kawasaki, B. Ahn, H. J. Lee, A. P. Zhilyaev, and T. G. Langdon, *J. Mater. Res.*, **31**: 88 (2015).
50. X. L. Wu, P. Jiang, and L. Chen, *Mater. Res. Lett.*, **2**, No. 4: 185 (2014).
51. G. Aleshin, G. Raab, and I. Kodirov, *Key Eng. Mater.*, **743**: 191 (2017).
52. S. Zhao, C. Meng, F. Mao, and G. Gottstein, *Acta Mater.*, **76**: 54 (2014).
53. A. Habibi and M. Ketabchi, *Materials and Design*, **34**: 483 (2012).
54. S. P. Galkin, *Method of Screw Rolling*: Patent 2293619 RF. МПК B21B, 19/00; NITU MISiS - No. 2006110612/02, applied for 2007. 04.04.2006; publ. 20.02.2007 (Bulletin of Inventions, No. 5) (2007).
55. I. Volokitina, A. Volokitin, and E. Panin, *J. Mater. Res. Technol.*, **31**: 2985 (2024).
56. I. E. Volokitina and A. V. Volokitin, *Metallofiz. Noveishie Tekhnol.*, **46**, No. 9: 850 (2024).
57. A. Arbuz, A. Panichkin, F. Popov, A. Kawalek, K. Ozhmegov, and N. Lutchenko, *Metals*, **14**, No. 1: 53 (2024).
58. A. Arbuz, A. Kawalek, A. Panichkin, K. Ozhmegov, F. Popov, and N. Lutchenko, *Materials*, **16**: 7547 (2023).
59. V. A. Kharitonov and M. Usanov, *Metallurgist*, **57**, Nos. 11–12: 1015 (2014).
60. B. V. Karpov, P. V. Patrin, S. P. Galkin, E. A. Kharitonov, and I. B. Karpov, *Metallurgist*, **61**: 884 (2018).
61. S. Lezhnev, A. Naizabekov, D. Kuis, A. Kasperovich, and E. Panin, *30th Anniversary International Conference on Metallurgy and Materials (May 26–28, 2021, Brno, Czech Republic)*, p. 193.
62. I. Volokitina, A. Volokitin, and B. Makhmutov, *Symmetry*, **16**, No. 8: 997 (2024).
63. A. Volokitin, I. Volokitina, M. S. Sonmez, A. Denissova, and Z. Gelmanova, *Symmetry*, **16**, No. 11: 1515 (2024).

Metallophysics and Advanced Technologies
Металофіз. новітні технол.
Metallofiz. Noveishie Tekhnol.
2026, vol. 48, No. 8, pp. 907–918
https://doi.org/10.15407/mfint.48.08.0907
Reprints available directly from the publisher

© 2026 G. V. Kurdyumov Institute for Metal Physics,
National Academy of Sciences of Ukraine
Published by license under
the G. V. Kurdyumov Institute for Metal Physics–
N.A.S. of Ukraine Publishers imprint.
Printed in Ukraine.

PACS numbers: 06.60.Vz, 46.50.+a, 61.72.Ff, 61.72.Hh, 62.20.M-, 81.20.-n, 81.40.Np

Influence of Ti 6Al 4V Alloy Microstructure and Processing Parameters of Hot Deformation (Forging) on the Formation of Cup-Shaped Product

O. M. Ivasyshyn, H. A. Bahlyuk*, V. I. Bondarchuk, S. F. Kyrylyuk*, and P. Ye. Markovs'kyy

G. V. Kurdyumov Institute for Metal Physics, N.A.S. of Ukraine,
36, Academician Vernadsky Blvd.,
UA-03142 Kyiv, Ukraine
**I. M. Frantsevich Institute for Problems of Materials Science, N.A.S. of Ukraine,*
3, Omeljan Pritsak Str.,
UA-03142 Kyiv, Ukraine

The influence of the microstructure type of the titanium Ti–6Al–4V alloy on the formation of a cup-shaped part by two-stage hot plastic deformation by forging is studied. As found, surface cracks in a strictly localized region form in the case of a globular $\alpha+\beta$ microstructure, whereas this is not observed in a microstructure with unrecrystallized plastic particles of the α-phase. A scheme explaining such a locking action of the α-phase plates is proposed, and performed finite-elements' simulation has established the occurrence of a complex stress state in this area, which causes the nucleation of surface cracks.

Key words: titanium, Ti–6Al–4V alloy, microstructure, hot deformation, forging, stresses.

Досліджено вплив типу мікроструктури титанового стопу Ti–6Al–4V на формування чашоподібної деталі двостадійним гарячим пластичним деформуванням куванням. Було виявлено, що у випадку ґлобулярної $\alpha+\beta$-

Corresponding author: Pavlo Yevhenovych Markovs'kyy
E-mail: pmark@imp.kiev.ua

Citation: O. M. Ivasyshyn, H. A. Bahlyuk, V. I. Bondarchuk, S. F. Kyrylyuk, and P. Ye. Markovs'kyy, Influence of Ti–6Al–4V Alloy Microstructure and Processing Parameters of Hot Deformation (Forging) on the Formation of Cup-Shaped Product, *Metallofiz. Noveishie Tekhnol.*, **48**, No. 8: 907–918 (2026). DOI: 10.15407/mfint.48.08.0907

© Publisher PH 'Akademperiodyka' of the NAS of Ukraine, 2026. This is an open access article under the CC BY-ND license (https://creativecommons.org/licenses/by-nd/4.0)

мікроструктури утворюються поверхневі тріщини у строго локалізованій області, тоді як у мікроструктурі з некристалізованими пластичними частинками α-фази цього не спостерігається. Запропоновано схему, що пояснює таку замикальну дію пластин α-фази, а проведене моделювання методом скінченних елементів встановило виникнення складного напруженого стану в цій області, що викликає зародження поверхневих тріщин.

Ключові слова: титан, стоп Ti–6Al–4V, мікроструктура, гаряче деформування, кування, напруження.

(Received 17 July, 2026; in final version, 22 July, 2026)

1. INTRODUCTION

Titanium alloys are ones of the most important structural materials for a wide range of applications due to the unique combination of their properties—high specific strength and ductility, fatigue characteristics, corrosion resistance, and non-magnetism [1–3]. In addition, these alloys are characterized by good processability; to obtain the desired properties, they are subjected to various types of deformation and heat treatment [2–4]. These treatments can be divided into treatments for the purpose of creating a certain internal phase composition and microstructure (which determines the mechanical characteristics of the material) and treatments that form a specific product. Often, the optimal parameters and modes of these two types of treatments do not coincide. For example, to obtain the considered most optimal globular (equiaxed) microstructure in titanium alloys, thermomechanical treatment with compression ratios of more than 80% is required, carried out at temperatures lower than the β-transition temperature [3, 5]. At the same time, to simplify the processes of shaping in various types of deformation (from rolling to pressing and forging) and to use effectively equipment and tools, it is desirable to carry out deformation processing at the highest possible temperatures. The latter approach critically spoils the microstructure of titanium alloys, catastrophically reducing their properties, firstly plasticity [5, 6]. At the same time, it is impossible to state unequivocally that titanium alloys have one universal microstructure for all cases and practical applications. For example, the highest strength characteristics are possessed by alloys with highly dispersed inclusions of the primary α-phase obtained by quenching from temperatures of a single β-phase field and subsequent aging [1, 7], while the resistance to crack propagation and high-temperature creep is better in a coarse-grained lamellar microstructure [1, 6, 8]. The present work is concerned with the study of the influence of the structural features of the microstructure of the Ti–6 Al–4V [wt.%] alloy on its hot deformability in the manufacture of such a relatively simple, but widely used in real practice object as a ‘cup’.

2. MATERIAL AND EXPERIMENTAL PROCEDURE

Two ∅30 mm rods (Fig. 1, *a*) of commercial Ti–6Al–4V [wt.%] alloy produced by different companies were used as initial material to produce 'cup' shaped object (Fig. 1, *b*) by means of two-step hot forging. One of these rods has bi-modal type of microstructure type consisting of primary α-globules and fine mixture of lamellae secondary α + β in all locations—in the centre and near the rod edge (Fig. 2, *a*, *b*). The second one is characterized by similar bimodal microstructure in the centre (Fig. 2, *c*), but not completely recrystallized microstructure with laminated in longitudinal direction α- and β-phases in the zone near the edge of the rod (Fig. 2, *d*).

Hot forging of the samples of the rods with both microstructures was performed in two steps. In the first step, after heating at 920°C for 30 min, the outer hemispherical shape of the forged peace was formed with a die. Moreover, in the second, the inner cavity was formed using a reverse extrusion scheme of deformation. At least 5 forged pieces were produced from each type of the rods.

The manufactured forgings were first examined over their entire surface to detect possible defects. Cracks were found on the outer surface of products made from the rod with microstructure 1, while products made from the rod with microstructure 2 had no defects. The article containing surface defects was then cut (as shown in Fig. 3) for a detailed study of the microstructure and its relationship with crack formation. Microstructural studies were performed using scanning electron microscopy (SEM, using TESCAN Vega 3 microscope) on sec-

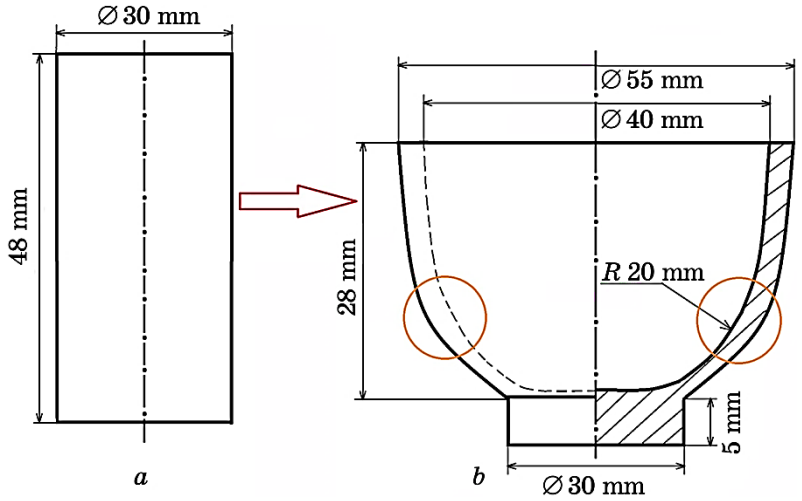


Fig. 1. Schematic presentation of the initial rod (*a*) and final shape of the forged piece (*b*).

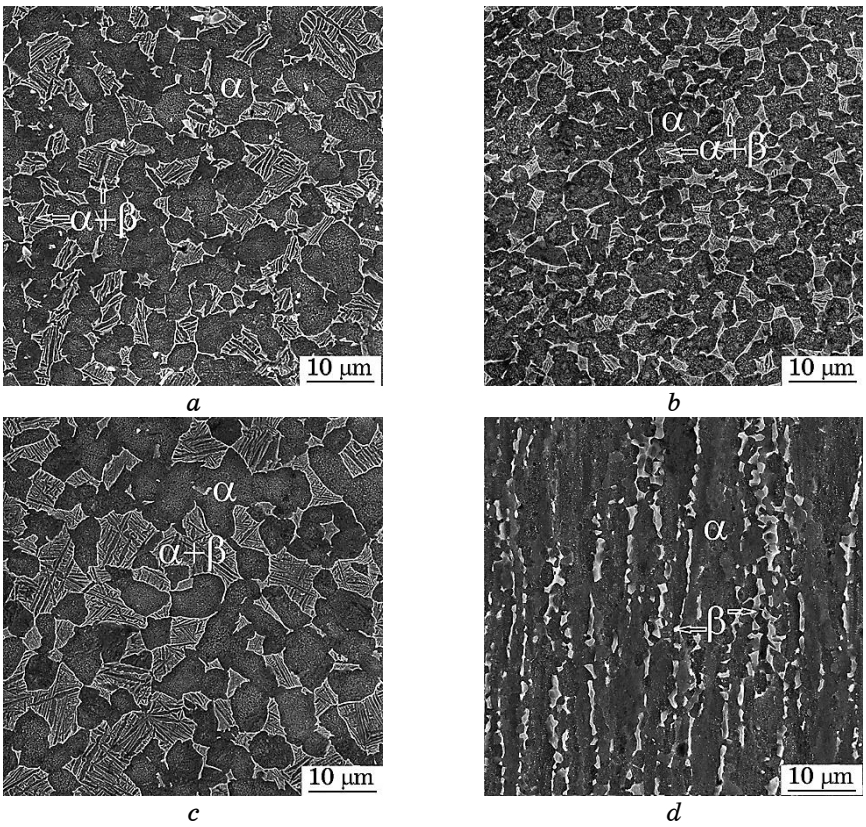


Fig. 2. Microstructure of the 1st (*a*, *b*) and the 2nd (*c*, *d*) ∅30 mm rods in the initial state in the centre (*a*, *c*) and near the edge (*b*, *d*). (SEM, SE).

tions prepared according to the standard method for this alloy in its etched with Kroll solution state [9].

To explain the influence of hot deformation conditions on the localization of stresses and deformations during the formation of forged pieces, a finite element simulation was carried out by means of the finite element method [10] using the DEFORM 2D/3D software. Based on the modelling results, the deformed state was established and the distribution of effective strain ε_i in the forging volume at various transitions was analysed:

$$\varepsilon_i = \frac{\sqrt{2}}{3}\int_0^t \sqrt{(\dot{\varepsilon}_z - \dot{\varepsilon}_r)^2 + (\dot{\varepsilon}_z - \dot{\varepsilon}_\varphi)^2 + (\dot{\varepsilon}_r - \dot{\varepsilon}_\varphi)^2 + \frac{3}{2}\dot{\gamma}_{rz}^2}\, dt\,, \tag{1}$$

$$\dot{\varepsilon}_z = \frac{\partial V_z}{\partial z},\ \dot{\varepsilon}_r = \frac{\partial V_r}{\partial r},\ \dot{\varepsilon}_\varphi = \frac{V_r}{r},\ \dot{\gamma}_{rz} = \frac{1}{2}\left(\frac{\partial V_r}{\partial z} + \frac{\partial V_z}{\partial r}\right), \tag{2}$$

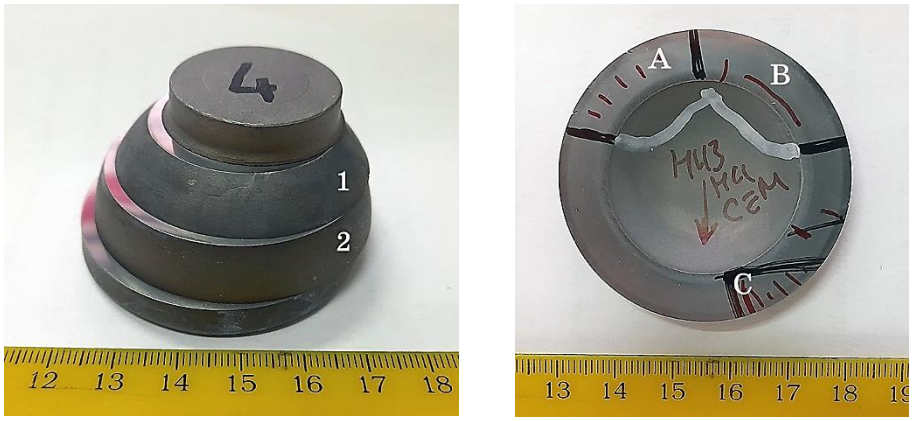
where V_r and V_z are radial and axial components of the velocity vector.

3. RESULTS AND DISCUSSION

3.1. Study of Microstructure after Hot Deformation

During the initial visual examination, cracks were found in areas (A), (B) and (C) indicated in Fig. 3, *b* and Fig. 4, *a*. In two areas marked as (A) and (C), cracks are visible, directed tangentially at an angle of approximately 45° from the outer surface into the depths of the forged peace (1–4 in Fig. 4, *a*). The presence of such cracks in the products is a fact, causing their complete rejection. All these cracks had practically the same character and appearance. Details of the microstructure of a typical crack 4 are shown in Fig. 4, *b*–*e*. In Figure 4, *b*, it can be seen that the crack extends to a depth of approximately 2 mm from the surface. At its most superficial edge (Fig. 4, *c*—locations (A) and (B) are identical), traces of plastic deformation are visible in the areas both around the crack itself (marked by arrow *1*) and at the outer surface of the forging (arrow *2*). However, in the deeper zone at the tip of the crack (Fig. 4, *c*), it is already clearly visible that it grew along a narrow channel of a highly deformed structure, which is very similar to the adiabatic shear band (ASB [11], marked with an arrow). Moreover, this ASB extends dipper into the deformed material (Fig. 4, *e*).

An adiabatic shear band is a narrow region in a material, often a metal, where intense shear deformation occurs under high strain rates, leading to a rapid temperature rise that is not dissipated to the surroundings. The formation of ASB involves complex microstructural



a *b*

Fig. 3. General view of the divisional ones of the forged pieces (*a*) and its cross-section in the layer (1), where the surface cracks were discovered (*b*).

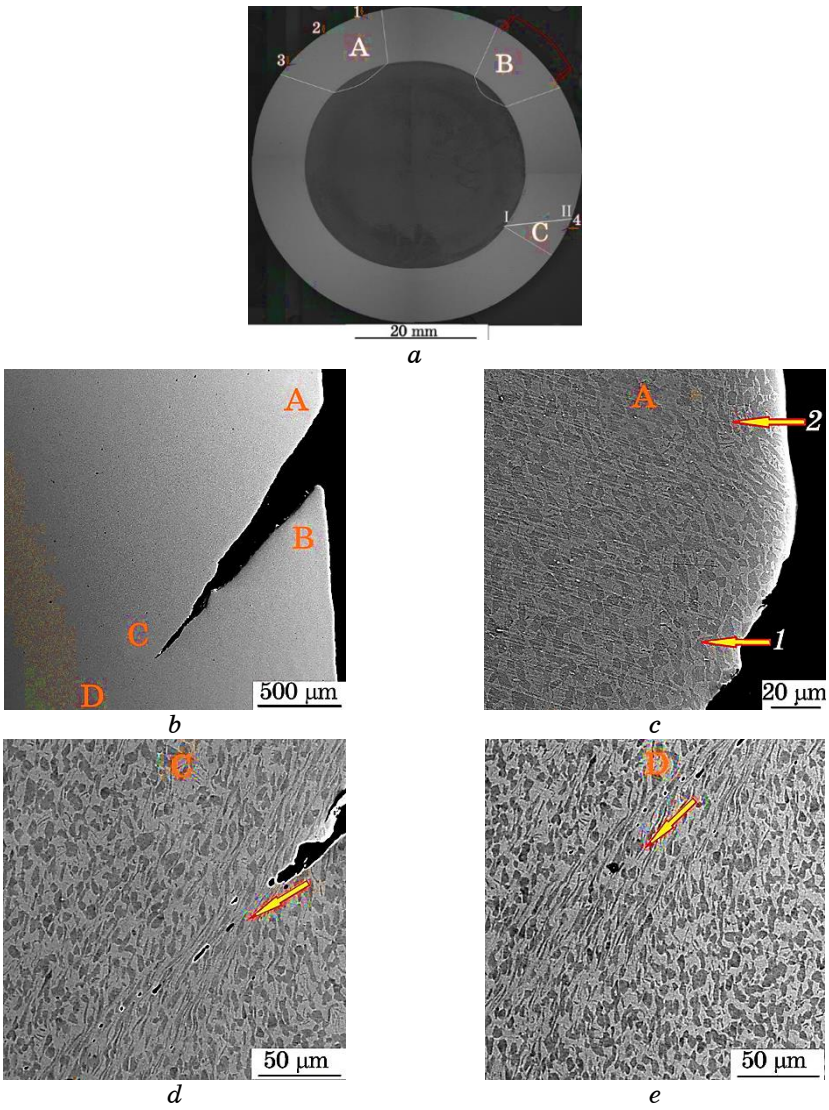


Fig. 4. General view (*a*) of section 1 (from Fig. 3, *b*), and microstructure of the crack 4 (*b*–*e*) in the different locations indicated in (*b*). Arrows in (*c*–*e*) indicate elements of microstructure discussed (SEM, BSE).

changes, such as dynamic recrystallization, which contribute to the observed material softening [11, 12].

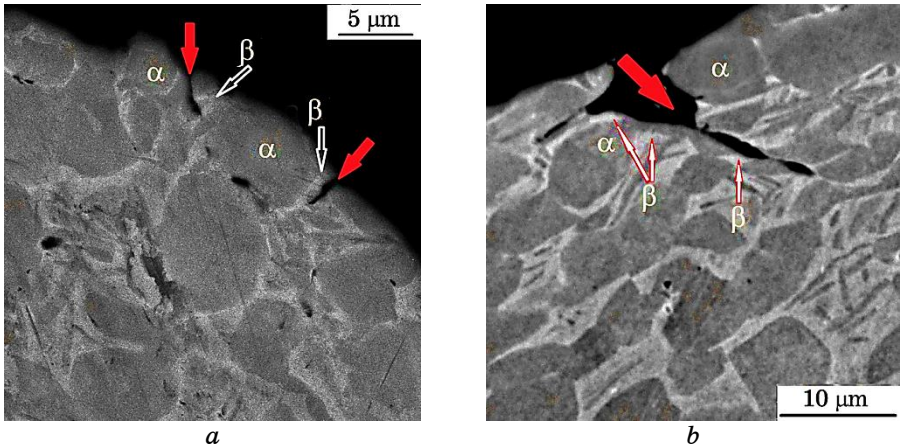
These results of microstructural studies explain the nature of the formation of such deep cracks in the microstructure of the 1st type due to the localization of deformation in certain areas of the surface with the formation of adiabatic shear bands. The special nature of such ASB

[13] leads to strong local heating of the material and its weakening, which causes cracking. Nevertheless, these results do not explain how the initial stage of the origin of such cracks occurs. In addition, this does not explain the fact that, in the microstructure of the 2nd type with a banded structure of phases in the near-surface layers, cracks do not arise.

To solve this problem, additional studies were carried out in other areas to detect smaller cracks, those at the earliest stage of crack initiation. Such cracks (Fig. 5) were found in area (B) shown in Fig. 4, *a*. In Fig. 5, *a*, *b*, it is evident that small cracks originate in the surface layer itself at the boundaries between the stronger particles of the α-phase [8] and the softer interlayers of the β-phase. Further, with increasing load, such cracks continue to spread in depth along the same 'weakened' interphase α/β boundaries. A similar phenomenon, in principle, was observed earlier, mainly in the case of the spread of fatigue cracks under alternating loading [14].

In the forged pieces obtained from rods with the second type of microstructure, no cracks were found. However, analysing the above results, one can come to a fairly well founded conclusion that even if such a microcrack can form on the surface, then, as can be seen in Fig. 2, *d*, there will be no such 'weakened' α/β-interphase boundary in front of it.

Instead, the tip of the microcrack will rest against a plate of stronger α-phase, which will lie across its path. A comparison of these situations is shown in the form of a conditional diagram in Fig. 6. It is obvious that, for the propagation of cracks deeper inside the forging body (shown in Fig. 4), the nucleation of such small cracks on the surface is



a *b*

Fig. 5. Small (initial) cracks on the surface of forgings processed with 1st microstructure rod. Red arrows indicate direction of cracks (SEM, BSE).

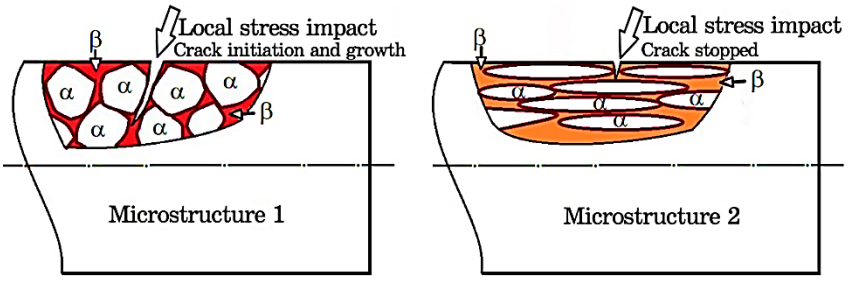


Fig. 6. Scheme illustrating influence of microstructure in the surface layers on surface cracks propagation.

a necessary condition.

3.2. Modelling of Deformation

The results of modelling the temperature fields and the deformed state of the forging volume during each of the two deformation transitions confirm the hypothesis regarding the deformation nature of the local temperature changes (Figs. 7–10). First of all, it should be noted that the deformation production of a product of this shape is carried out in two stages: first, by forming an intermediate bell-shaped product from a cylindrical blank (Fig. 7, *a*), and then by forming an internal cavity inside it (Fig. 7, *b*).

As can be seen from Fig. 7, *a*, already at the first forging operation, in which the open-die forging scheme is implemented in most of the forging volume, preheated to 920°C, deformation heating of the material occurs, which is accompanied by an increase in temperature to

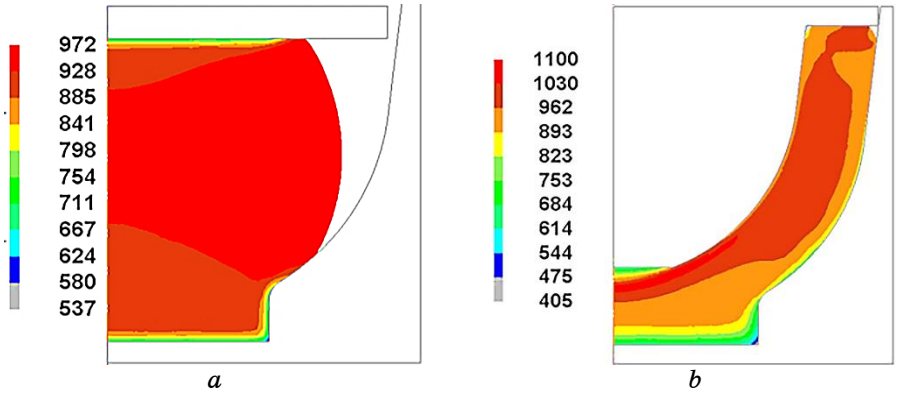


Fig. 7. Distribution of temperature fields in the forging volume after the first (*a*) and second (*b*) forging operations.

more than 970°C in local zones subjected to greater deformations.

In the second forging transition, the temperature of the lower (cylindrical) part of the forging and the peripheral layers of the spherical part of its surface, due to contact with the colder working surface of the die, decreased to 750–820°C in the cylindrical part and to 890–960°C on the lateral spherical part (Fig. 7, *b*).

The deformation nature of temperature changes in local zones of the forging is confirmed by the results of modelling the effective strain distribution across its cross-section (Fig. 8), which correlates quite closely with the nature of the temperature distribution. As can be seen in Fig. 8, *a*, the highest values of effective strain are observed in the central zone of the forging during the first pass and decrease in the radial direction towards the peripheral areas. In contrast, the lower cylindrical zone of the forging is marked by the minimum values of effective strain.

At the same time, in the peripheral region of the forging, bordering the transition zone from cylindrical to spherical surfaces, there is a narrow region of increased deformation (indicated by an arrow), directed tangentially at an angle of approximately 45° from the outer surface into the depths of the forged peace (Fig. 8, *a*). Its location and direction are similar to the area and direction of cracks in the forging, as shown in Fig. 3 and Fig. 4.

However, taking into account the fact that the effective strain is a scalar quantity, which is considered as a generalized indicator of deformations [15] to identify the causes of the cracks formation on the surface of forgings, it is obviously also necessary to have information on the distribution of radial and axial deformations over the volume of the forging at different stages of deformation. Thus, the analysis of the patterns of radial deformation fields distribution shows, that, similarly to the pattern of the effective strain, already at the first stage of

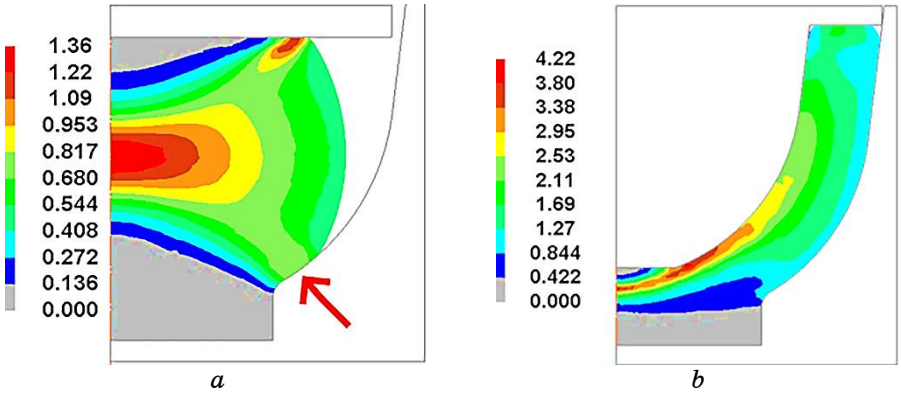


Fig. 8. Distribution of effective strain fields in the forging volume after the first (*a*) and second (*b*) forging operations.

the process in the peripheral region of the forging at the boundary of the transition from cylindrical to spherical surfaces, a narrow zone of increased level of radial deformations with a positive sign (arrow) is also formed, which corresponds to tensile deformations.

The level of the values in this zone after the first transition is in the range of 0.30–0.38 (Fig. 9, *a*); however, during the forging process at the second transition, they gradually decrease from 0.21–0.36 (Fig. 9, *b*) to a value close to zero (Fig. 9, *c*, *d*).

The noted effect of reducing the level of the values at the second transition is due to the 'wedge-forming' action of the punch when it is pressed into the forging body, at which the rate of radial deformation of local volumes located in the zone of action of the punch acquires a significantly negative value, *i.e.*, compression deformations are realized.

Obviously, the hypothesis given regarding the mechanism of crack occurrence from the point of view of the deformed state of the forging can be considered debatable referring to the significantly larger values of tensile radial deformations in the central zone of the forging (direct-

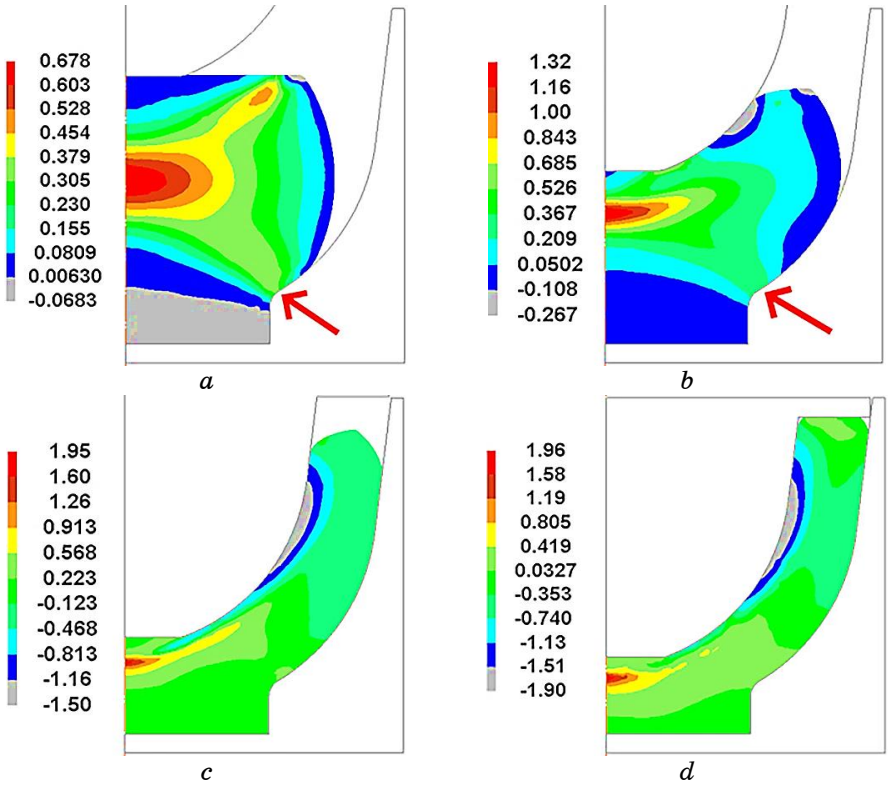


Fig. 9. Distribution of radial deformation fields in the forging volume after the first (*a*) and second (*b*–*d*) forging operations.

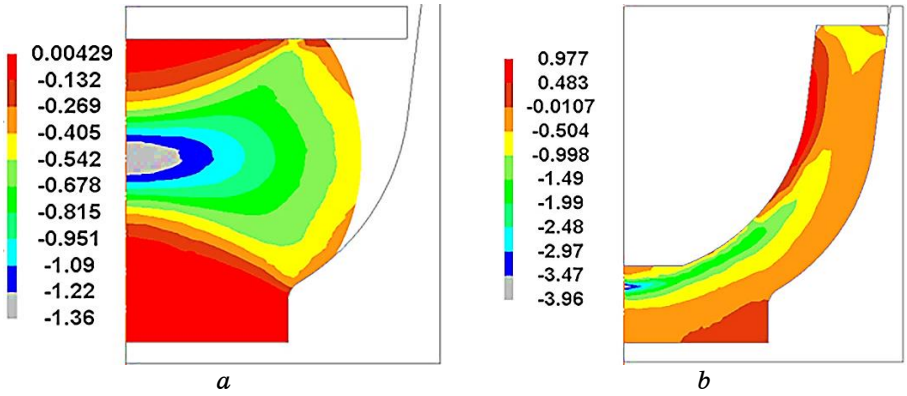


Fig. 10. Distribution of axial deformation fields in the forging volume after the first (*a*) and second (*b*) forging operations.

ly under the punch), reaching the values of 1.2–1.6 and more, in which, nevertheless, cracks are not observed. However, the assessment of the values of axial deformations ε_z under the punch shows that, in this zone, they reach negative values up to –1.5––1.9 (which indicates a significantly compressive nature of the deformations). This fully compensates for the tensile radial deformations and makes it impossible for the material to crack in this zone.

In contrast, the value of ε_z on the side surface of the forging in the area of crack formation, although it has a negative value (of about –0.011) (Fig. 10), approaches zero in magnitude, which in no way can compensate for significant tensile deformations.

4. CONCLUSION

Thus, the results of the microstructure study clearly demonstrated that the formation of surface cracks in a strictly localized region occurs in the case of the initial alloy microstructure of the globular type, which was previously considered the best in terms of mechanical properties. However, in contrast to this, the microstructure with incompletely globularized phases showed no such cracking. Based on a detailed study of the microstructure of surface layers and the nature of the initiation and propagation of such cracks in them, a scheme was proposed that shows the inhibitory effect of lamellar particles of the stronger α-phase on the growth of a such surface cracks.

To explain the somewhat unexpected location of formation of such cracks, a finite element simulation of such hot deformation was carried out. Based on the obtained data, a hypothesis is proposed regarding the mechanism of crack formation on the side surface of the forg-

ing from the point of view of their deformed state. It is based on the formation of noticeable tensile deformations in this zone during the forging process, while local axial deformations approach zero in magnitude, which in no way compensates for tensile deformations.

Part of this work was performed in G. V. Kurdyumov Institute for Metal Physics, N.A.S. of Ukraine within the framework of the project 060/23 funded by the National Academy of Sciences of Ukraine.

AUTHORS' CONTRIBUTIONS

O. M. Ivasyshyn provided general guidance for the research, set tasks, discussed the results, and participated in writing the article, H. A. Bahlyuk analysed the modelling results and prepared their description for publication, V. I. Bondarchuk performed microstructural investigations, S. F. Kyrylyuk performed computer modelling of hot deformation processes for titanium alloy and prepared graphic materials for further analysis, P. E. Markovs'kyy performed structural experiments, summarized the results of experimental studies and modelling, wrote the draft of the article and participated in its final revision.

REFERENCES

1. G. Lütjering and J. C. Williams, *Titanium* (2nd ed.) (Berlin–Heidelberg–New York: Springer: 2007).
2. M. Peters, J. Kumpfert, C. H. Ward, and C. Leyens, *Adv. Eng. Mater.*, **5**, No. 6: 419 (2003).
3. M. Niinomi, *Metall. Mater. Trans. A*, **33**: 477 (2002).
4. T. L. Jones, K. Kondoh, T. Mimoto, N. Nakanishi, and J. Umeda, *Key Eng. Mater.*, **551**: 118 (2013).
5. P. E. Markovsky, *Metallofiz. Noveishie Tekhnol.*, **31**, No. 4: 511 (2009) (in Russian).
6. S. L. Semiatin, *Metall. Mater. Trans. A*, **51**: 2593 (2020).
7. O. M. Ivasishin, P. E. Markovsky, S. L. Semiatin, and C. H. Ward, *Mat. Sci. Eng. A*, **405**, Nos. 1–2: 296 (2005).
8. P. E. Markovsky and S. L. Semiatin, *Mater. Sci. Eng. A*, **528**, Nos. 7–8: 3079 (2011).
9. https://www.struers.com/en/Knowledge/Materials/Titanium
10. Sh. Kobayashi, S.-I. Oh, and T. Altan, *Metal Forming and the Finite-Element Method* (New York–Oxford: Oxford University Press: 1989).
11. S. P. Timothy, *Acta Metall.*, **35**, No. 2: 301 (1987).
12. P. E. Markovsky, J. Janiszewski, D. G. Savvakin, O. O. Stasiuk, K. Cieplak, P. Baranowski, and S. V. Prikhodko, *Materials and Design*, **223**: 111205 (2022).
13. Y. Guo, Q. Ruan, S. Zhu, Q. Wei, J. Lu, B. Hu, X. Wu, and Y. Li, *J. Mech. Phys. Solids*, **135**: 103811 (2020).
14. G. Lütjering, *Mater. Sci. Eng. A*, **243**, Nos. 1–2: 32 (1998).
15. V. M. Danchenko, V. O. Hrynkevich, and O. M. Golovko, *Teoriya Protsesiv Obrobky Metaliv Tyskom* [Theory of Processes of Metal Working by Pressure] (Dnipropetrovsk: Porogi: 2008) (in Ukrainian).